The Dynamic Modelling of Industrial Oxygen Gas Jet Assisted CO_2 Laser Cutting of Metal

by

Donald N. B. Ouyang ©

UNIVERSITY
of
GLASGOW

The Dynamic Modelling of Industrial Oxygen Gas Jet Assisted CO_2 Laser Cutting of Metal

Donald Ning Ben Ouyang ©

歐陽寧 字本©

B.Sc., M.Phil.

A thesis submitted to

the Department of Mechanical Engineering

University of Glasgow

in fulfillment of the requirement for

the Degree of Doctor of Philosophy

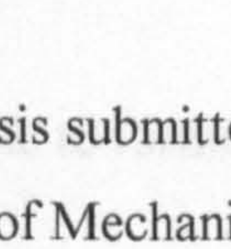

UNIVERSITY
of
GLASGOW

Laser and Optical System Engineering Center

June 1998

學海無涯

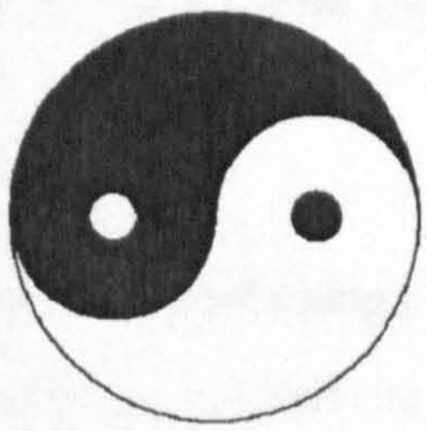

No Limit To Knowledge

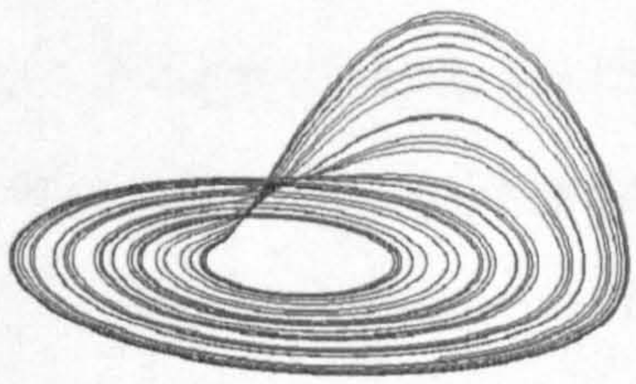

勤是徑

Abstract

The objective of this work is to generalize the predictions of the laser cutting performance, in particular, of the kerf surface quality. The dynamic modelling for the reactive jet gas assisted laser cutting of metals is focused at the dynamic formation and development of the flow of the molten metal layer in the kerf and its multiple interactions with the laser beam, the gas jet and the substrate metallic solid. The most relevant physical mechanisms are mathematically modelled:

- Dynamic balances of mass, momentum and energy for the flowing molten metal layer;
- Momentum interaction between the gas jet and the liquid at the gas / liquid interface;
- Oxidisation reaction at the gas / liquid interface;
- Energy loss producing the heat affect zone (HAZ) at the liquid / solid interface;
- Dynamic absorption of the laser power by the workpiece;

The structure of the differential governing equations for the theoretical laser cutting system reflects the fact that the individual physical mechanisms interact with each other through the time-dependent variables. The most relevant variables are treated as time-dependent while the others are treated as time-independent:

- $\delta_l(t)$, the thickness of the liquid film at the bottom of the kerf;
- $T_l(t)$, the surface temperature of the liquid at the gas / liquid interface;
- $V_e(t)$, the fusion front velocity at the liquid / solid interface along cutting direction;
- $y(t)$, the displacement of the fusion front relative to the laser beam front;
- $P_{l,abs}(t)$, the absorption of the laser power by the workpiece.

The set of the differential governing equations for the theoretical laser cutting system are derived; it consists of 5 or 4 coupled, 1st-order, nonlinear differential equations. The physical boundary conditions are also derived. The program based on the 4th-order Runge-Kutta method is designed in C to numerically solve the differential governing equations with their physical boundary conditions.

The mathematical analysis of the differential governing equations shows that the cutting system is sensitive to the given initial conditions, i.e., $\delta_l(0)$, $T_l(0)$, $V_e(0)$, $y(0)$ and $P_{l,abs}(0)$, even in the limited time. In the long run, the differential governing equations are controlled by the principles of Chaos theory for the set of more than 3 coupled, 1st-order, nonlinear differential equations.

The comparison of a theoretical laser cutting system and a practical laser cutting system is analyzed by experimentally measuring the laser power and the beam translation velocity. A variety of the measured striations and local kerf widths are demonstrated.

It is concluded that the theoretical laser cutting system, in which the operating parameters such as the laser power and the beam translation velocity are constant, is essentially chaotic; the unexpected variations of the operating parameters in the practical laser cutting system add more complexity into the chaotic nature. Both the theoretical calculations and the experimental measurements reveal the nature of the generation of the striations: the variable $\delta_l(t)$ with respect to time produces the local striations with variable periodicity and thus variable local kerf widths. The striations can be nearly periodic, intermittent with variable periodicity and stochastic. The optimized kerf surface quality can be predicted by adjusting the operating parameters to achieve the nearly periodic variation of $\delta_l(t)$ accompanied with the smallest phase space comprised of the 5 time-dependent variables.

Acknowledgment

During my research work as well as the preparation of this thesis, so many things have happened. They at times seemed as though they would never end...

It is my privilege to thank my first supervisor, Prof. Chris Chatwin (University of Sussex) for his continuous interest and enthusiastic encouragement. His initial suggestions to this research direction provided me with a good opportunity to challenge myself towards the understanding of the physical mechanisms in the reactive gas jet assisted CO_2 laser cutting process. His caring, trusting and supportive attitude to my academic work and personal life for nearly 2 years should be greatly acknowledged.

The research project gradually matured during the period with the second supervisor, Prof. Brian F. Scott. I appreciate very much the research work which he recommended to me - the Ph.D. thesis by P. Dutta. His critical supervision has strongly influenced me for over two and half years. Some of his suggestions are acknowledged. The academic arguments with him have given me a life-long lesson: to create by learning. I appreciate the value of these beyond that which I could express here.

I am extremely grateful to the head of Mechanical Engineering Department (University of Glasgow), Prof. John Hancock, for his caring attitude towards the completion of this thesis. His academic experience and kind advice gave me the confidence in the speedy preparation of this thesis. The constructive advice from Post-graduate Tutor, Dr. Ian Watson, should also be gratefully acknowledged.

This research work which involves the theoretical derivations, the numerical methods and the experimental work is intensive. My special acknowledgment is due to Mr. Ian Peden for his enthusiastic help and valuable discussions, in particular, in C/C++ programming and computer software used. I should thank Mr. George Forkler and Mr. Brian Robb for their active corporation in the related experimental work.

Throughout my research work, many discussion and information received from inquires are very appreciated: Dr. M. Vicanek (Technische University, Germany); Prof. D. Schuocker (University of Technology, Austria); Prof. W. Duley (University of Waterloo, Canada); Dr. A. M-Y Huang (Vivitec Co. Ltd., Taiwan).

I should gratefully acknowledge the Glasgow University Scholarship and British ORS award, without which this research work in such a well-known university would have not been possible. I am also extremely grateful for the financial support from my previous company, Dong-Xiong Arc Furnace Ltd., Dong-Xiong Group, China. The friendship and compassion from its boss, Mr. B. N. Yuan, vividly support me throughout this research work in Great Britain.

My special gratitude goes to Mr. Lewis Robertson (manager, Mechanical Engineering Department), Mr. Paul Kennedy (lecturer, mechanical design), Mrs. Geroldine Mahmood (lecturer, tourism management), Ms. Joan Perry (Ph.D. candidate), who have checked the written language in this thesis respectively. I am extremely grateful to Mr. J. J. Wu (Ph.D. candidate) who has checked the mathematical derivations and calculations in this thesis. Without their genuine assistance, I can never be confident to submit this thesis.

Last but not at least, I would deeply acknowledge my wife and my parents for their sincere love and endless patience, which has been encouraging me to do my best through all those years for whatever I have done and wherever I have been.

I certify herewith that, except where the specific references in the text are made in respect with the work of others, the contents of this thesis are original and have not been submitted to any other academic institutes. This thesis is the result of my own work and I would be solely responsible for all the consequent conclusions.

...

I am going to turn off my computer for the completion of this research project, like a solider putting down his gun... Tomorrow will be better than today...

Donald Ning Ben Ouyang

Contents

Synopsis

Objectives

The overall objective of this research work is to generalise predictions of the laser cutting performance, in particular, of the kerf surface quality. Because the kerf surface quality is characterised by striations, the interest is focused at the dynamic formation / development of the flowing molten metal layer in the kerf. By defining a theoretical laser cutting system and applying the concept of control volume, it is expected to dynamically construct the balance equations of mass, momentum and energy in the control volume which always encloses the flowing molten metal layer in the kerf. In order to ascertain the specific entries into the 3 balance equations, as comprehensively as possible, there are 4 individual physical processes to be modelled:

(1) Momentum interaction between the gas and metallic liquid flows;

(2) Exothermic reaction between the gas and metallic liquid flows;

(3) Energy loss from the metallic liquid into the substrate metallic solid;

(4) Dynamic relation between the fusion front velocity and the beam front velocity.

As a result, a set of governing equations are expected to be able to dynamically model this theoretical laser cutting system in which the multiple interactions of the metallic liquid with the gas, the metallic solid and the laser beam occur. Mathematically, the 5 most concerned variables in respect with time, as follows, are expected to be numerically calculated:

$\delta_l(t)$: the thickness of molten metal layer at the bottom of the kerf;

$T_l(t)$: the surface temperature of molten metal layer at the gas / liquid interface;

$V_e(t)$: the fusion front velocity at the liquid / solid interface along cutting direction;

$y(t)$: the displacement of the fusion front relative to the laser beam front;

$P_{l,abs}(t)$: the laser power absorbed by the workpiece.

After the theoretical derivations, a programme, coded in C, is made to numerically solve the governing equations with their specific boundary conditions for the 5 time-dependent variables, simultaneously. The time evolution of the thickness of the molten metal layer, $\delta_l(t)$, reflects the dynamic nature of the theoretical laser cutting system.

In addition to the dynamic modelling, objective-oriented experimental tests are carried out. An X-Y table which can produce both constant cutting velocity (linear and circular cutting profiles) and accelerated / decelerated cutting velocity (spiral cutting profile) is designed to study the influence of the cutting velocity on the formation of striations in a practical laser cutting system.

Major conclusions

(1) The dynamic modelling has resulted in 3 sets of differential governing equations for the theoretical laser cutting system. These were found to be in the form of 5 or 4 coupled, 1st-order non-linear differential equations along with their specific boundary conditions for the 5 time-dependent variables. By simultaneously solving those equations, the dynamic nature of the laser cutting system can be clearly demonstrated.

(2) The type of the differential governing equations itself suggests that any practical laser cutting process is essentially chaotic. The recent amazing findings from Chaos theory can thus be employed to explain and predict the chaotic characteristics of kerf surface finishes, in particular, when the cutting time is long.

(3) The most concerned physical mechanisms underlying practical laser cutting processes can be concluded as follows:

* Two boundary layer flows exist and interact with each other at the gas / liquid interface. The shear stress is thus produced at the gas / liquid interface and it is predominantly responsible for the removal of the molten metal layer.

* The exothermic reaction contributes a considerable amount of energy, in addition to the absorbed laser power, to help heat up the workpiece. The exothermic energy entering into the metallic liquid film comes predominantly from the oxidisation reaction of the gas (O_2) and the metallic liquid (Fe), rather than that of the gas (O_2) and the metallic vapour (Fe).

* The molten metal layer, acting as a linear moving heat source, will incur the unavoidable heat conduction loss. It is also responsible for the retrieval of part of the heat conduction loss when it advances. Theoretically, however, due to the invalidity of pre-conditions when applying the moving heat source theory in the modelling, the heat conduction loss can be evaluated by the heat convection theory, i.e., the heat convected from the flowing molten metal layer into the liquid / solid interface can instead be calculated.

* Keeping V_c (cutting velocity) constant does not guarantee the constant value of V_e (fusion front velocity at the liquid / solid interface), simply because there is no physical bond between V_c and V_e in reality. The oscillation of V_e with respect to time is confirmed. This consequently changes the interacting area of the laser beam and the workpiece and thus influences the absorption of laser power by the workpiece.

Originality

(1) A 2-dimensional-based, dynamic model concerning the reactive jet gas assisted laser cutting of metals has been constructed in this thesis. As far as the author is aware, to date, this is the first, most comprehensive, dynamic model in the research communities of laser materials processing. Dynamic solutions rather than static ones are thus naturally expected, i.e., the 5 most concerned time-dependent variables, $\delta_l(t)$, $T_l(t)$, $V_e(t)$, $y(t)$ and $P_{l,abs}(t)$, as defined above, can be simultaneously simulated in respect of cutting time. For example, the periodicity of striations can be calculated by analysing the periodicity of $\delta_l(t)$.

(2) The sets of differential governing equations for the theoretical laser cutting system have been derived and they are comprised of 5 or 4 coupled, 1st-order, non-linear differential equations. The detailed boundary conditions for the governing equations have been derived based on both physical and mathematical grounds; they must be satisfied in every step of

time evolution. Chaos theory certifies that the theoretical laser cutting system, governed by the differential governing equations, is essentially chaotic.

(3) The measured striations demonstrate that the chaotic nature is embedded in a practical laser cutting system where any unstable factors in, for example, the laser power and cutting velocity will add to more complexity in the laser cutting mechanism. Essentially, the chaotic striations are unavoidably generated (including nearly periodic striations) regardless of how constant all the operating parameters are adhered to. Both the theoretical calculations and the experimental measurements reveal the dynamic nature of the striations: the variable $\delta_1(t)$ with respect to time produces the local striations with variable periodicity and thus variable local kerf widths. The optimised operating parameters for good cuts (nearly periodic fine striations) can be theoretically predicted by achieving the nearly periodic variation of $\delta_1(t)$ together with the smallest phase space comprised of the 5 time-dependent variables.

Nomenclature

a $2a$ defined as the width of focused laser beam at $1/e^2$ points of the intensity profile ($m.$)

b $2b$ defined as the width of throat of jet gas ($m.$)

CV control volume which encloses the molten metal layer at any time

C_{exo} combustion efficiency coefficient defined as: $\dot{m}_{exo} = C_{exo} \cdot \delta_l(t)$ $(kg/(m \cdot s))$

$(\frac{c_f}{2})_{g,w}$ local skin friction coefficient, applied at gas side of gas / liquid interface

$(\frac{c_f}{2})_{l,w}$ local skin friction coefficient, applied at liquid side of gas / liquid interface

$(\frac{c_f}{2})'_{l,w}$ local skin friction coefficient, applied at liquid side of liquid / solid interface

c_h Stanton number

$(c_h)_{g,w}$ local Stanton number at the gas / liquid interface

$(c_h)_{l,w}$ local Stanton number at the liquid / solid interface

c_p specific heat $(J/kg\cdot^oK)$

$c_{p,g}$ specific heat of gas at around T_g $(J/kg\cdot^oK)$

$c_{p,g,w}$ specific heat of gas at around T_m $(J/kg\cdot^oK)$

$c_{p,s}$ specific heat of solid Fe at around T_m $(J/kg\cdot^oK)$

$c_{p,l}$ specific heat of liquid Fe at around T_m $(J/kg\cdot^oK)$

D thickness of metal specimen to be cut ($m.$)

$\dot{e}_{in}$ energy rate carried by the mass in solid phase into the CV ($W.$)

$\dot{e}_{exo}$ exothermic reaction energy release rate entering into the CV ($W.$)

$\dot{e}_{out}$ energy rate carried by the mass in liquid phase flowing out of the CV ($W.$)

$\dot{e}_{loss}$ rate of energy loss from the CV into the solid metal ($W.$)

$\dot{e}_{cond}$ rate of heat conduction from the liquid / solid interface into the solid metal ($W.$)

$\dot{e}_{conv}$ rate of heat convection from the gas / liquid interface to liquid / solid interface ($W.$)

$\dot{e}_{cool}$ rate of cooling of the liquid by the gas jet ($W.$)

$\dot{e}_{CV}$ rate of change of energy stored in the CV ($W.$)

F_{δ_l} derived differential governing equation for $\delta_l(t)$ in Eqs.81,82,83, $F_{\delta_l} = \frac{d}{dt}\left[\delta_l(t)\right]$

$F_{P_{l,abs}}$ derived differential governing equation for $P_{l,abs}(t)$ in Eqs.81, $F_{P_{l,abs}} = \frac{d}{dt}\left[P_{l,abs}(t)\right]$

F_y derived differential governing equation for $y(t)$ in Eqs.81,82,83, $F_y = \frac{d}{dt}\left[y(t)\right]$

F_{V_e} derived differential governing equation for $V_e(t)$ in Eqs.81,82,83, $F_{V_e} = \frac{d}{dt}\left[V_e(t)\right]$

F_{T_l} derived differential governing equation for $V_e(t)$ in Eqs.81,82,83, $F_{T_l} = \frac{d}{dt}\left[T_l(t)\right]$

$\dot{g}_{cool}$ heat flux convected from the liquid into the gas (W/m^2)

$\dot{g}_{cond}$ heat flux convected from the liquid into the solid (W/m^2)

h_f enthalpy of fusion of Fe at ambient pressure (J/kg)

h enthalpy (J/kg)

h_g enthalpy of gas in free stream (J/kg)

$h_{g,w}$ enthalpy of gas at T_l (J/kg)

$\Delta H\big|_T$ enthalpy of reaction at T, for the chemical reaction identified $(J/kg\ of\ Fe)$

I_0 power intensity at the centre of the beam waist (W/m^2)

$I_{(r)}$ Gaussian profile of the laser power intensity in Y direction, defined as:

$$I_{(r)} = \frac{1}{e^{2\left(\frac{r}{a}\right)}} I_0,\ 0 \le r \le a\ (W/m^2)$$

k_s thermal diffusivity of solid Fe at around T_m (m^2/s)

k_{exo} ratio of the liquid entering the exothermic reaction to the liquid leaving the CV, defined as: $k_{exo} = \frac{\dot{m}_{exo}}{\dot{m}_{out}},\ 0 < k_{exo} \le 1$

K_0 modified Bessel function of the second kind, zero order

K thermal conductivity $(W/m\cdot^\circ K)$

K_s thermal conductivity of solid Fe at around T_m $(W/m\cdot^\circ K)$

K_l thermal conductivity of liquid Fe at around T_m $(W/m\cdot^\circ K)$

K_g thermal conductivity of gas at T_g $(W/m\cdot^\circ K)$

$K_{g,w}$ thermal conductivity of gas at the wall temperature of $T_{g,w}$ $(W/m\cdot^\circ K)$

M_g Mach number of gas jet in the exit plane of the nozzle

M_{Fe} relative molar mass of Fe, $M_{Fe} = 55.85 \times 10^{-3}$ $(kg / mole)$

M_{FeO} relative molar mass of FeO, $M_{FeO} = 71.85 \times 10^{-3}$ $(kg / mole)$

M_{O_2} relative molar mass of O_2, $M_{O_2} = 32 \times 10^{-3}$ $(kg / mole)$

$\dot{m}_{in}$ mass rate of the solid metal moving into the CV (kg / s)

$\dot{m}_{out}$ mass rate of the molten metal flowing out of the CV (kg / s)

$\dot{m}_{out,max}$ possible maximum $\dot{m}_{out}$ at $\delta_l = \delta_{l,max}$ (kg / s)

$\dot{m}_{CV}$ mass change rate of the CV (kg / s)

$\dot{m}_{exo}$ mass rate of the molten metal entering exothermic reaction (kg / s)

p_0 stagnation pressure of gaseous O_2 (N / m^2)

p_a ambient pressure (N / m^2)

p_g static pressure of gas in free stream (N / m^2)

$p_{g,w}$ static pressure of gas at around T_m (N / m^2)

P_l total power of laser radiation in the beam waist $(W.)$

$P_{l,abs}$ absorption of laser power by the heated workpiece $(W.)$

$\dot{P}_{l,abs}$ rate of change of the absorbed laser power with respect to time t (W / s)

$(Pr)_g$ Prandtl number for gas

$(Pr)_l$ Prandtl number for liquid

$\dot{q}_{g,w}$ heat flux convected from the liquid into the gas, at gas / liquid interface (W / m^2)

$\dot{q}_{l,w}$ heat flux convected from the liquid into the solid, at liquid / solid interface (W / m^2)

r radius of focused laser beam measured from the centre, in Y, $0 \le r \le a$ $(m.)$

Re Reynolds number

$\Re$ universal gas constant, $\Re = 8.3144$ $(J / mole \cdot {}^0K)$

S co-ordinate reference in the negative direction of Y

s magnitude of co-ordinate in S $(m.)$

s_0 local liquid thickness varying with x $(m.)$

t time $(s.)$

T_a absolute ambient temperature $({}^0K)$

T_f average temperature of molten metal layer, defined as $T_f = \frac{T_m + T_l}{2}$ $({}^0K)$

T_l surface temperature of molten metal layer at gas / liquid interface (^0K)

$\dot{T}_l$ rate of change of T_l with respect to time t ($^0K / s$)

T_m temperature of fusion of Fe at around p_a, $T_m = 1808\,(^0K)$

T_v temperature of vaporisation of Fe at around p_a, $T_v = 3133\,(^0K)$

T_0 stagnation temperature of gaseous O_2, $T_0 = T_a$ (^0K)

T_g gas temperature in free stream (^0K)

$T_{g,w}$ gas temperature at the gas / liquid interface (^0K)

U_g gas velocity in free stream (m / s)

u velocity in X (m / s)

u_l velocity profile of molten metal flow (m / s)

u_0 surface velocity of molten metal layer at the bottom of gas / liquid interface (m / s)

$u_{0,max}$ maximum u_0 (m / s)

$u_{l,0}$ local surface velocity of molten metal layer at the gas / liquid interface (m / s)

$\bar{u}_{l,0}$ average value of $u_{l,0}$ along X (m / s)

V_c velocity of translation of laser beam along Y (m / s)

V_e velocity of propagation of fusion front along Y (m / s)

$V_{e,max}$ possible maximum V_e at $\delta_l = \delta_{l,max}$ (m / s)

$\dot{V}_e$ rate of change of V_e with respect to time t (m / s^2)

v velocity in S (m / s)

w average measured kerf width ($m.$)

X, Y rectangle co-ordinate reference fixed on CV with moving velocity V_e

y displacement of laser beam front relative to the liquid / solid interface

$\dot{y}$ rate of change of y with respect to time t (m / s)

α angle of the fusion front to horizontal plane (^{o})

ρ density (kg / m^3)

ρ_g gas density in free stream (kg / m^3)

$\rho_{g,w}$ gas density at the wall temperature of $T_{g,w}$ (kg / m^3)

ρ_l density of liquid Fe at around T_m (kg / m^3)

ρ_s density of solid metal Fe (kg / m^3)

δ_l thickness of metallic liquid boundary layer flow at the bottom ($m.$)

$\delta_{l,max}$ maximum δ_l when it varies with respect to time t ($m.$)

$\dot{\delta}_l$ rate of change of δ_l with respect to time t (m / s)

$\tau_{l,w}$ shear stress applied at the liquid side of gas / liquid interface (N / m^2)

$\tau'_{l,w}$ shear stress applied at the liquid side of liquid / solid interface (N / m^2)

$\tau_{g,w}$ shear stress applied at the gas side of gas / liquid interface (N / m^2)

μ dynamic viscosity ($N \cdot s / m^2$)

μ_g dynamic viscosity of gas in free stream ($N \cdot s / m^2$)

$\mu_{g,w}$ dynamic viscosity of gas at the wall temperature of $T_{g,w}$ ($N \cdot s / m^2$)

μ_l dynamic viscosity of liquid Fe at around T_m ($N \cdot s / m^2$)

ν kinetic viscosity (m^2 / s)

$\nu_{g,w}$ kinetic viscosity of gas at around T_m (m^2 / s)

γ specific heat ratio for O_2, $\gamma = 1.401$

subscript

g represents conditions out of gaseous boundary layer flow

l represents conditions inside liquid boundary layer flow

s represents conditions in solid metal at around T_m

w represents conditions along either gas / liquid interface or liquid / solid interface

List of Figures

Chapter 1. Introduction

In this chapter, the general objectives of the theoretical modelling are stated. A typical set-up of coaxial oxygen gas jet assisted CO_2 laser cutting of metals is introduced. Previous theoretical models are reviewed. Finally, the structure of this thesis is emphasised.

1-1. Objectives of this research work

The stability of the reactive gas jet assisted, continuous wave, CO_2 laser cutting of metals (mild steel sheet) is analysed with the purpose of identifying mechanisms responsible for discontinuities evident in kerf surfaces, i.e., striations, which affect the quality of the cut. A theoretical laser cutting system abstracted from practical laser cutting processes is built up to model the dynamic characteristics of the molten metal layer covering the liquid / solid interface during cutting, which results in the dynamic formation of striations in the kerf. In the theoretical laser cutting system (the cutting system, in short form), the most concerned variables are treated as time-dependent while all others (laser operating parameters and materials' physical properties) are taken as time-independent. The time-dependent variables are:

- the thickness of molten metal layer at the bottom of kerf, $\delta_l(t)$;
- the surface temperature of molten metal layer at the gas / liquid interface, $T_l(t)$;
- the velocity of propagation of fusion front, $V_e(t)$;
- the displacement of laser beam front relative to the liquid / solid interface, $y(t)$;
- the laser power absorbed by the heated workpiece, $P_{l,abs}(t)$;

Mathematically, the dynamic characteristics of the molten metal layer are interpreted by the time evolution of $\delta_l(t)$, $T_l(t)$, $V_e(t)$, $y(t)$ and $P_{l,abs}(t)$, respectively; they are expected to be discovered by solving the derived set of the governing equations for the cutting system.

A 2-dimentional quantitative physical model is established to dynamically characterise this cutting system, in which 4 individual mechanisms are taken into account:

(1) Momentum interaction between gas / metallic liquid flows.

The boundary layer theory concerning forced convection / external flows is employed. The governing differential equations for the gaseous boundary layer flow are solved by the Howarth-Dorodnitsyn transformation rather than Blasius one. The former method is able to describe an ideal gas flowing over a "flat plate" with higher temperature. The shear stress along the gas / liquid interface is thus calculated. The cooling effect by heat convection is evaluated by applying the modified Reynolds analogy.

(2) Exothermic reaction between gas / metallic liquid flows.

The energy release rate from the exothermic reaction has been experimentally testified to be comparable to the magnitude of laser power, e.g., *800 W.* as in Appendix 1 , and it helps heat up the workpiece in addition to the absorbed laser power. The generation mechanisms are to be analysed for 2 kinds of chemical reactions, i.e., the chemical reaction between the gaseous O_2 and liquid Fe with the product of FeO in liquid phase; the chemical reaction between the gaseous O_2 and vapour Fe with the product of gaseous FeO. The former mechanism is analysed based on the experiment-based conclusions by Powell, and the latter with the calculation method of Dutta and Scott, which was based on the boundary layer analysis for gases in chemical equilibrium (in Appendix 4). The theory of thermochemistry is employed to calculate the enthalpy of reaction with the heats of formation for elements and compounds from standard tables.

In calculating the rate of the mass fully participating in the chemical reaction between the gaseous O_2 and liquid Fe with the product of FeO in liquid phase, it is assumed that the oxidisation occurs only at the surface of molten metal layer, i.e., at the gas / liquid interface. Finally, the energy releases of exothermic reaction based on the 2 exothermic mechanisms above are to be numerically tested with the typical data in Appendixes 1-3.

(3) Energy loss from the molten metal layer into the substrate solid metal.

This has been conventionally realised as the heat conduction loss which produces the heat affected zone (HAZ) during laser cutting. The theoretical calculations were thus associated with the moving heat source theory. From the viewpoint of the mechanisms of heat transfer across the molten metal layer, the energy is convected from the gas / liquid interface to the liquid / solid interface, due to the flowing nature of the molten metal layer, and it is further conducted only in the metallic solid substrate. 3 kinds of evaluating methods based on the heat conduction theory and one based on the heat convection theory are reviewed, analysed and numerically tested. The retrieval of part of the heat conduction loss into the molten metal layer is also subject to analysis.

(4) The influence of the velocity of propagation of fusion front on the absorbed laser power

In previous theoretical models, the velocity of propagation of fusion front, or the liquid / solid interface velocity (V_e), is always treated as the same as the velocity of translation of laser beam (V_c) , i.e., $V_e = V_c$. In the dynamic modelling in this thesis, V_e is treated as one of the 5 time-dependent variables due to the fact that there is a lack of bond between V_e and V_c. The oscillation of V_e, e.g., around the constant value of V_c, is thus expected and this phenomenon will directly influence the displacement of the laser beam front relative to the liquid / solid interface, y, and thus the laser power absorbed by the heated workpiece.

The 4 individual physical processes above interact with each other in the cutting system and the multiple interactions should satisfy the conservation of mass, momentum and energy for the flowing molten metal layer. The concept of control volume (CV) which always encloses the molten metal layer in the kerf is to be applied for the 3 dynamic equilibrium descriptions. As a result, a set of governing differential equations are expected to be able to dynamically model the cutting system. To numerically solve them will produce the time evolution for 5 time-dependent variables, respectively. The detailed boundary conditions for the governing equation should be derived based on the mathematical and physical meanings, and be satisfied at each step of time evolution.

It is noted that the dynamic modelling is effective when, practically, a thin molten metal layer in dynamic balance is first generated. The transient process during which a keyhole is produced, enlarged and penetrated until the formation of the first molten metal layer at the beginning of a laser cutting process is not within the scope of the modelling. This is due to the fact that the erosion front is always found to be covered by a very thin film of molten metal layer during cutting, which is continuously generated from the metallic solid substrate and simultaneously blown away by the gas jet.

In addition to the dynamic modelling, objective-oriented experimental tests are carried out. An X-Y table which can produce both constant V_c (linear and circular cutting profile) and accelerated / decelerated V_c (spiral cutting profile) is designed to study the influence of the variation of V_c on the periodicity of striations in a practical laser cutting system.

1-2. Reactive gas jet assisted CO_2 laser cutting

As the basis for a variety of practical applications, a typical set-up of coaxial oxygen gas jet assisted CO_2 laser cutting of metals is schematically shown in Fig.1, where laser cutting power, e.g., around *1 kW*, is employed for the cutting of flat metal sheet, e.g., mild steel of *4* to *10 mm* thickness.

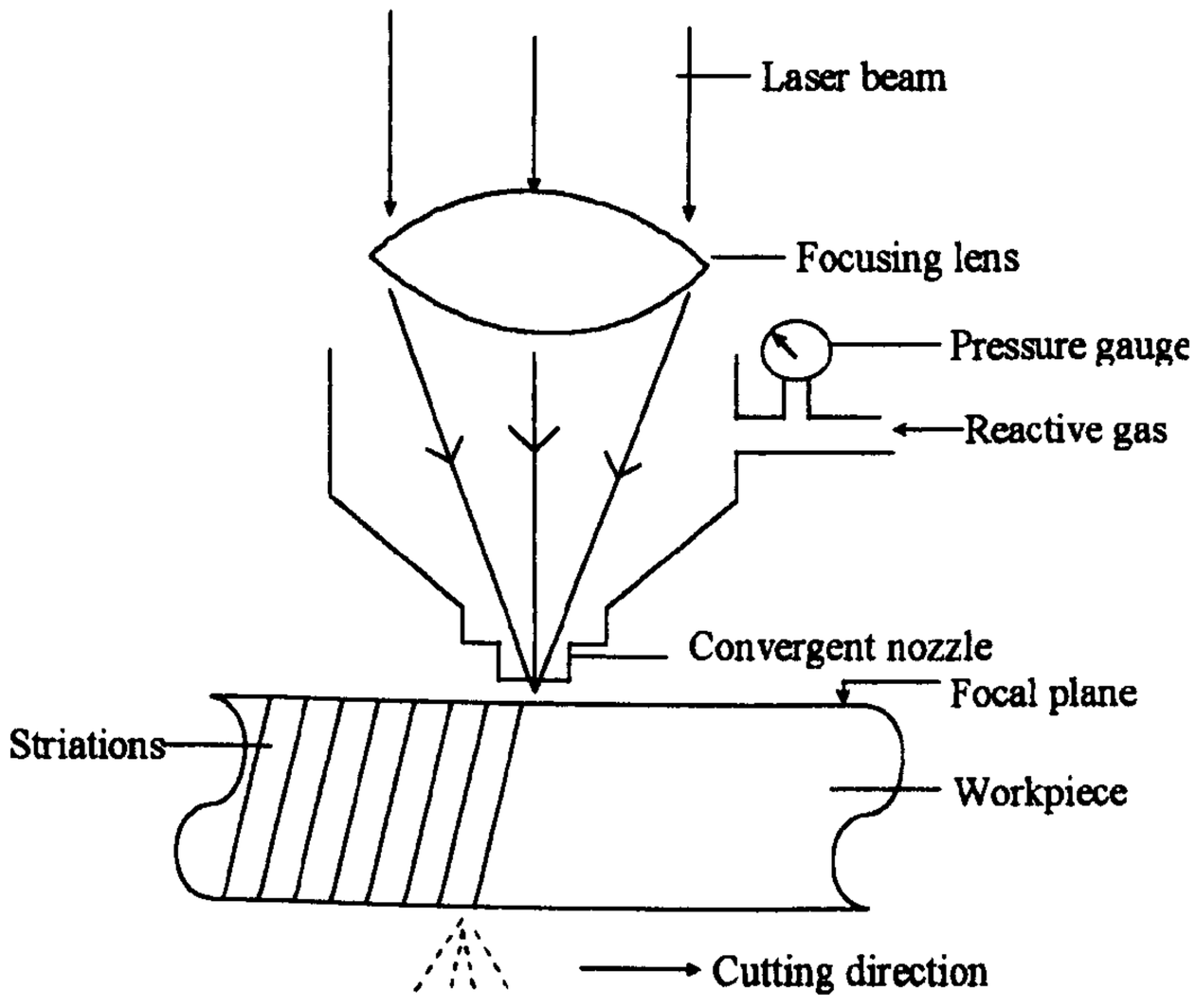

Figure 1. A schematic of coaxial oxygen gas jet assisted CO_2 laser cutting of metals

The basic mechanisms of laser cutting process in Fig.1 can be qualitatively described as follows:

- A certain intensity beam (*1 kW*) of infrared light (wavelength *10.6 μm* and parallel in nature) is generated by a CO_2 laser. The mode of laser beam is usually chosen as Gaussian distribution in continuous wave.
- A high-quality focusing lens is used to focus the beam onto the surface of the metallic workpiece.
- The focused beam heats the metal up and thus produces a tiny keyhole at their initial interaction. After the rapid transient process in which the keyhole becomes enlarged and deeper, a very localised molten metal layer throughout the depth of the sheet is generated.
- Two interactions occur simultaneously between the molten metal layer and oxygen gas jet. On one hand, the molten metal layer is ejected by the pressurised gas due to their momentum interaction. On the other hand, due to the oxidation of the molten metal layer, the chemical reaction between them generates its exothermic heat which greatly helps increase the efficiency of the cutting process.
- The newly produced thin melt is continuously removed and a cut kerf is thus generated.

The relative movement between the laser and the sheet is usually achieved by moving the sheet fixed on a CNC controlled X-Y table.

The reactive gas jet assisted CO_2 laser cutting, shown in Fig.1, is controlled by the multiple interactions of the flowing molten metal layer with the focused laser beam, the oxygen gas jet and the substrate solid metal. They are responsible for the dynamic formation and development of the local striations. This is shown in Fig.2.

The individual interaction mechanisms in Fig.2 can be summarised as follows:

- The "non-contact" interaction between the focused laser beam and heated workpiece. In the case that the absorption is high (nearly *1* for molten mild steel [2]) and the velocity of translation of laser beam (V_c) is constant, the energy absorbed by the molten metal layer is determined by the real interacting area of the focused laser beam and heated workpiece (as shown in Fig.2, for example, part of laser beam simply passes through the kerf and does not "contact" with the workpiece). The interacting area is in turn subject to the displacement of

laser beam front relative to the liquid / solid interface (y), due to the variable velocity of propagation of fusion front (V_e). This phenomenon is simply due to the lack of physical bond between V_e and V_c.

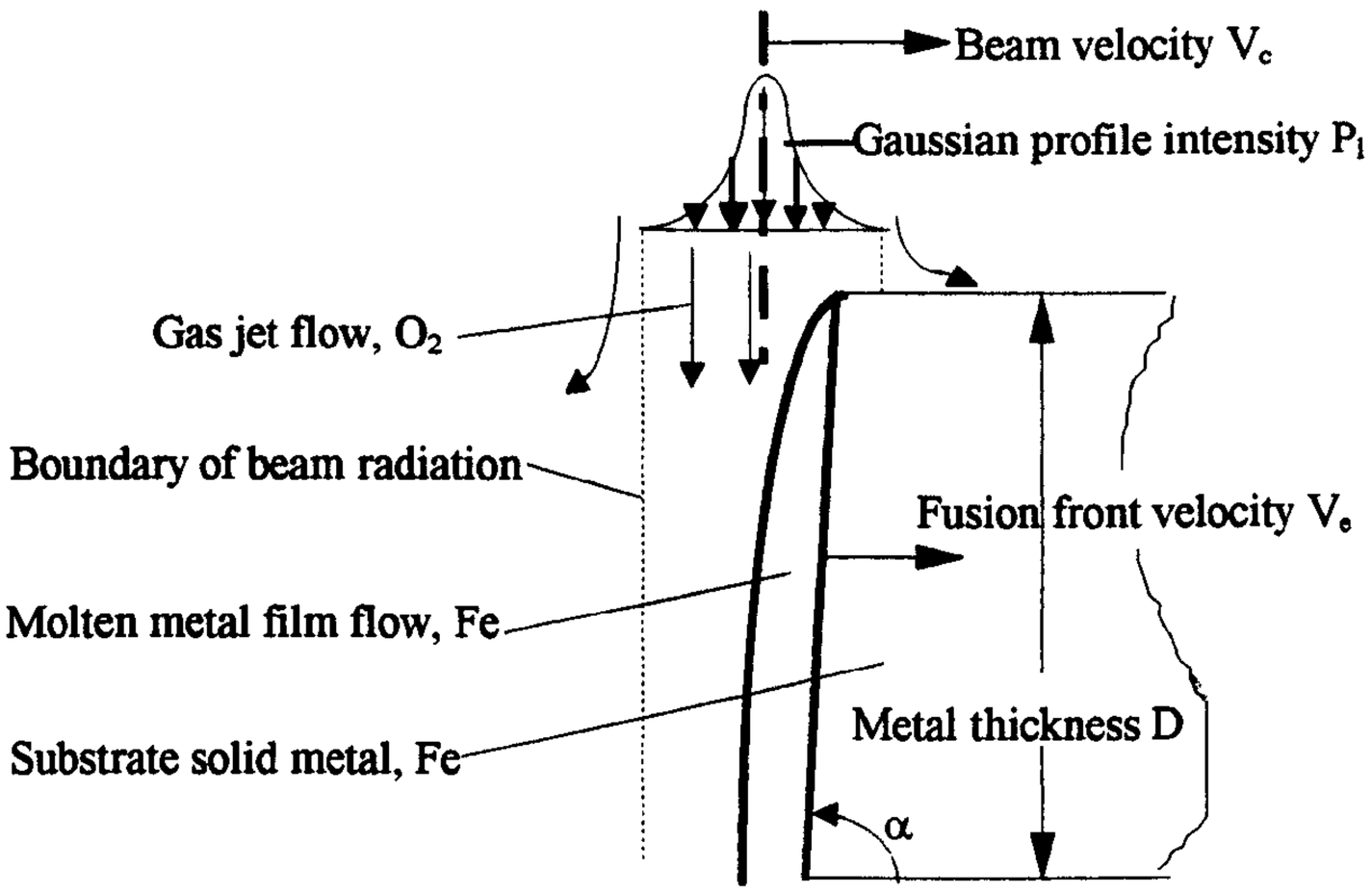

Figure 2. *In reactive gas jet assisted CO_2 laser cutting, laser beam, pressurised oxygen gas, molten metal layer and substrate solid metal interact each other. The combinations of these interactions are responsible for the dynamic formation and development of striations*

- Momentum transfer from the gas jet into the molten metal layer. The molten metal layer is ejected by the shear stress at the gas / liquid interface. The associated cooling effect of the gas jet is unavoidable.

- The exothermic reaction between the jet gas and the molten metal layer. Part of the molten metal mass, if not all, is oxidised and part of the exothermic reaction heat enters the molten metal layer adding to the absorbed laser energy.

- The interaction between the molten metal layer and the solid substrate. Along the liquid / solid interface, the energy is lost into the solid substrate by heat conduction and the mass transfer from the solid to the liquid occurs. A part of the heat conduction loss is retrieved when the heated solid metal is converted into the molten metal layer.

None of the mechanisms identified is susceptible to any precise theoretical modelling. It is more difficult to assess the combined effects of those individual mechanisms.

1-3. Literature Review of theoretical models

Due to unique advantages over conventional mechanical / thermal cutting techniques, the CO_2 laser cutting technology, since its early industrial application in 1971 [1], has been tremendously investigated by both academic communities and industry fields. Although industry has seen this cutting technology increasingly utilised with great commercial success, the laser cutting mechanism itself is not fully understood. For instance, different patterns of striations which are always found to be naturally generated on the cut edge of workpiece, e.g., mild steel, have not quantitatively been explained [P.80, reference 2].

A cut with no striations at all or homogeneously fine striations is expected in applications because the cut finish would be of better quality. The striations with variable periodicity in one cut or repeated cuts imply different edge roughness, i.e., different finish quality. The worst situation could also occur, i.e., the intermittence of cut and no cut at all. In large-scale automatic cutting processes, this directly results in higher post-process costs. Indeed, the striations themselves imply that the mechanism of laser cutting process is dynamic rather than steady, no matter how constant are the operating parameters such as laser power, gas pressure and laser cutting speed. In other words, a comprehensive dynamic model which could describe the dynamic formation / development of molten metal layer, with respect to time, is anticipated in order to reveal the combined effects of the multiple interactions which underlie and control the reactive gas jet assisted CO_2 laser cutting.

Modelling of the laser cutting mechanism was active in 1970s and 1980s but subsequently almost ceased. As concluded by Steen [P.85, reference 2], existing analytic models are limited in their ability to model details in real world problems. In particular, to date, no dynamic model exists which can describe the mechanism of formation and development of striations. Nevertheless, research has been conducted, from several standpoints, towards the gradual understanding of the laser cutting mechanism. In this section, some well-

established analytic models and academic endeavours are reviewed as an introductory understanding to the laser cutting mechanism.

One of the simplest models, e.g., by Steen [2], represents a primitive yet fundamental understanding of the laser cutting mechanism. This so-called "simple lumped heat model" is shown in Fig.3.

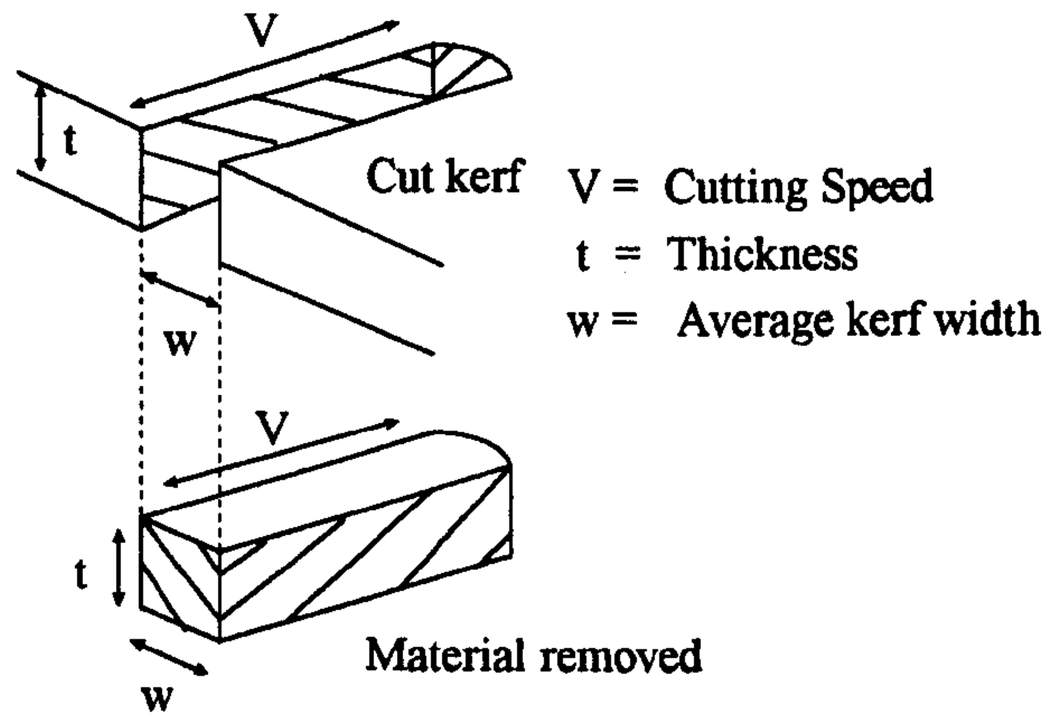

Figure 3. *A schematic of "simple lumped heat model" proposed by Steen [2]*

The cutting mechanism in Fig.3 is straightforward: once the penetration hole is made and the cutting starts from the edge, a sufficiently strong gas jet blows away the molten metal which has been heated in a certain block before leaving the kerf; this process is repeated and a cut is thus generated. It is clear that models of this type are too simple to describe the complicated cutting process.

Work by Dutta and Scott in 1975 [3] proposed a detailed analytic model, in which the molten metal layer was treated as a laminar boundary layer flow. Although the physical model looks simple (shown in Fig.4), several individual interactions such as momentum interaction, cooling effect, exothermic heat generation and heat conduction loss have been calculated systematically. The contribution to the understanding of laser cutting process can be concluded as follows.

- The cutting fusion front is assumed to be always covered by a thin molten metal film, which is essentially a boundary layer flow. The typical average thickness of molten metal

layer is calculated at the magnitude of *0.01 - 0.1 mm*. for the mild steel of thickness *of 2 - 3 mm*.. The surface quality of the kerf is expected to be strongly influenced by the stability of this film.

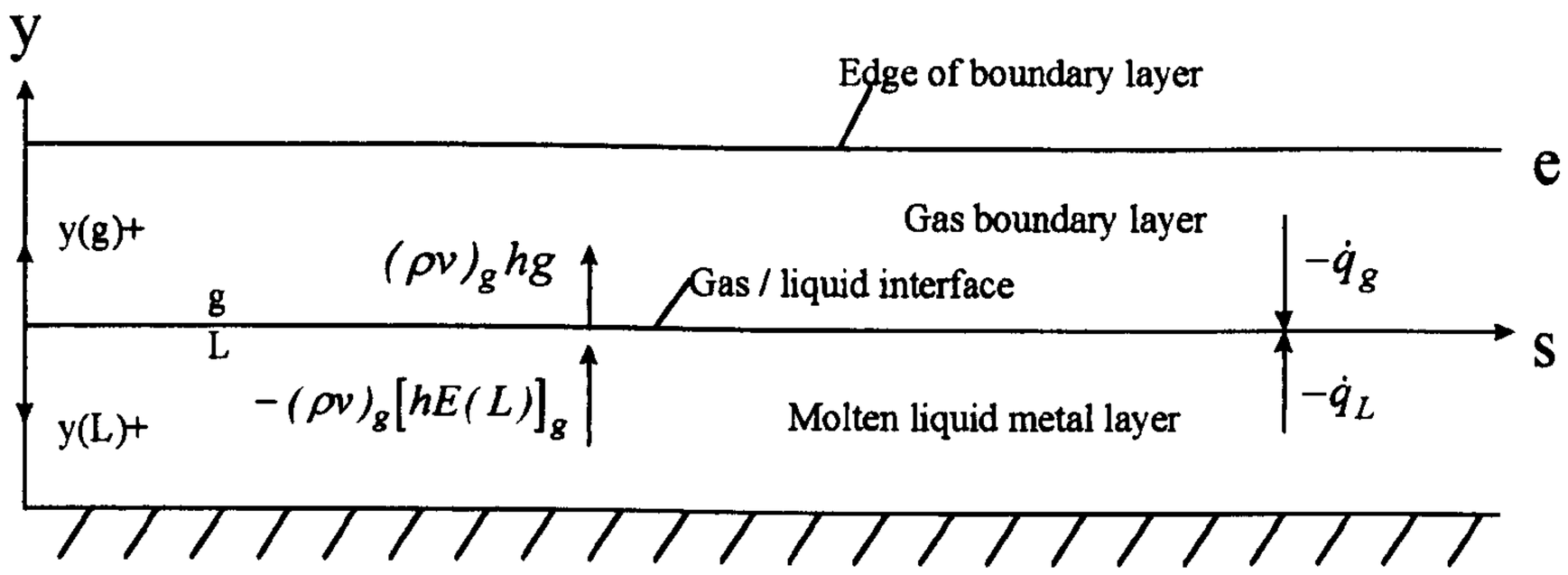

Figure 4*. Analytic model used by Dutta and Scott to quantitatively analyse individual interactions at the gas / liquid interface and the liquid / solid interface [3]*

- The momentum interaction occurs between the gaseous boundary layer flow and the metallic liquid boundary layer flow. The skin friction along the gas / liquid interface is calculated and confirmed to control the removal of the molten metal layer, rather than the pressure gradient in the kerf.

- Because there is so far no analytical solution to the 3-dimensional (3-D) Navier-Stokes equation, the modelling is essentially limited to the 2-D level. This 2-D analysis is justified by the fact that a typical measured kerf width, at the magnitude of *1 mm*., is much larger than a typical thickness of the molten metal layer of *0.01 - 0.1 mm*..

- The exothermic reaction is assumed to occur between the metallic vapour (*Fe*) and the oxygen gas (O_2) with the product of gaseous *FeO*. The exothermic reaction heat release is calculated based on the boundary layer analysis for gases in chemical equilibrium. This assumption overcomes the dilemma that, for example, if the oxidation is assumed to happen between the oxygen gas and the metallic liquid, the amount of the molten metal that is fully oxidised per unit time can not be determined.

Because this model seeks a steady state solution, the dynamic characteristics of multiple interactions during a laser cutting can not be reflected. It thus fails to explain the dynamic appearance of striations.

Focused on nearly periodic striations, Arata et al in 1979 made a qualitative explanation shown in Fig.5 [4], assuming a catch-up cycle between the constant cutting speed and the oscillating burning speed of the "erosion front".

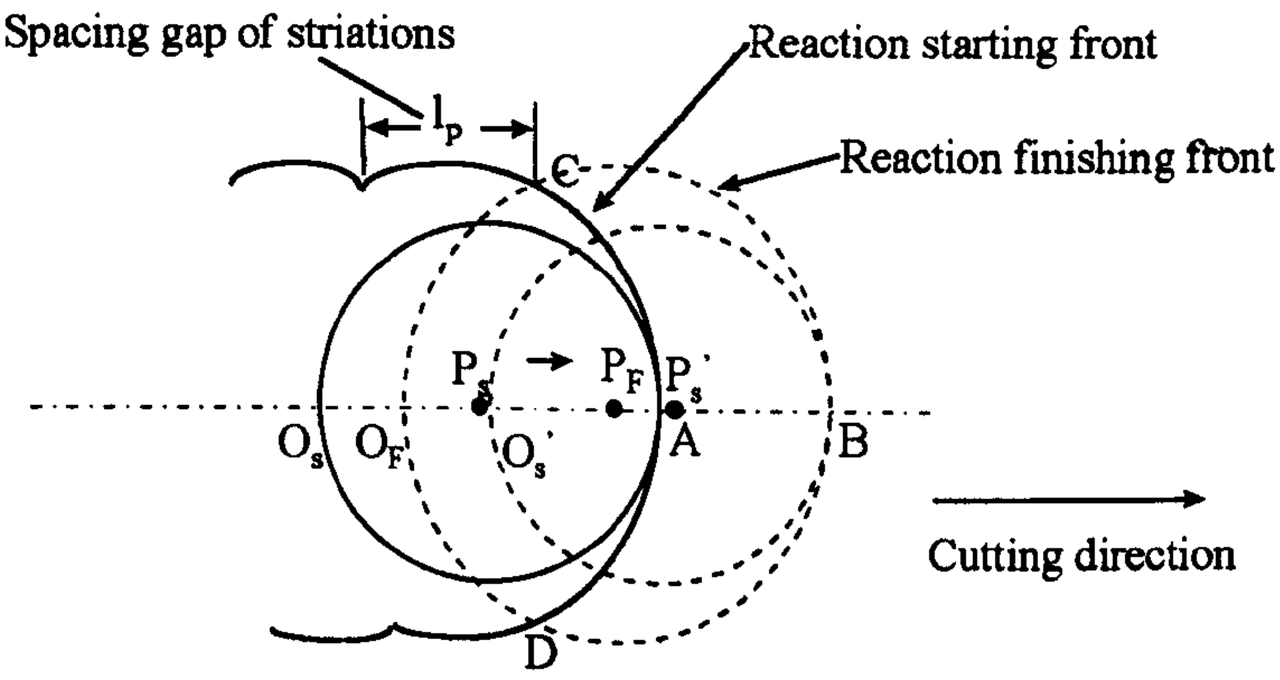

Figure 5. *A model proposed by Arata et al [4], qualitatively showing how nearly periodic striations are formed (top view)*

The most valuable parts of this research work towards the understanding of laser cutting mechanism may be their experimental findings by using a high speed camera and a radiation pyrometer, shown in Fig.6. The contribution can be concluded as follows:

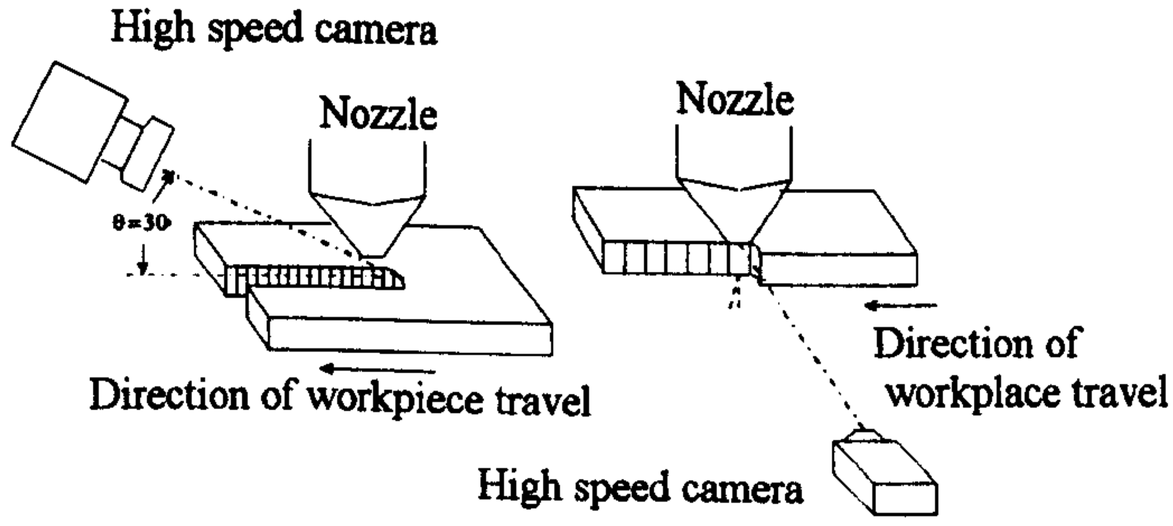

Figure 6. *A schematic of the arrangement of detectors, used by Arata et al, where a high speed camera is used to film the dimension of the cutting front and a radiation pyrometer to measure its temperature. (a) for normal cutting and (b) for edge cutting*

- The high speed movie pictures (the interval of each picture is 1/1000 seconds) suggest that, for an acceptable normal cut rather than a edge cut, the cutting front is always covered with a molten metal layer along the depth of the kerf. This experimental finding very much justifies the physical model where the "erosion front" is assumed to be covered with a thin molten metal flow.

- The temperature measurement suggests that, though it changes slightly along the depth of the kerf, the average temperature of cutting front is limited, i.e., between *1900* ^0K and *2400* ^0K, in the cutting of mild steel workpiece. This proves that the average cutting front temperature always stays high enough to maintain itself in liquid phase but can hardly reach the boiling temperature.

The work reported by Schuocker from 1983 to 1986 [5,6,7] made efforts to construct a dynamic analytic model. The physical model is shown in Fig.7.

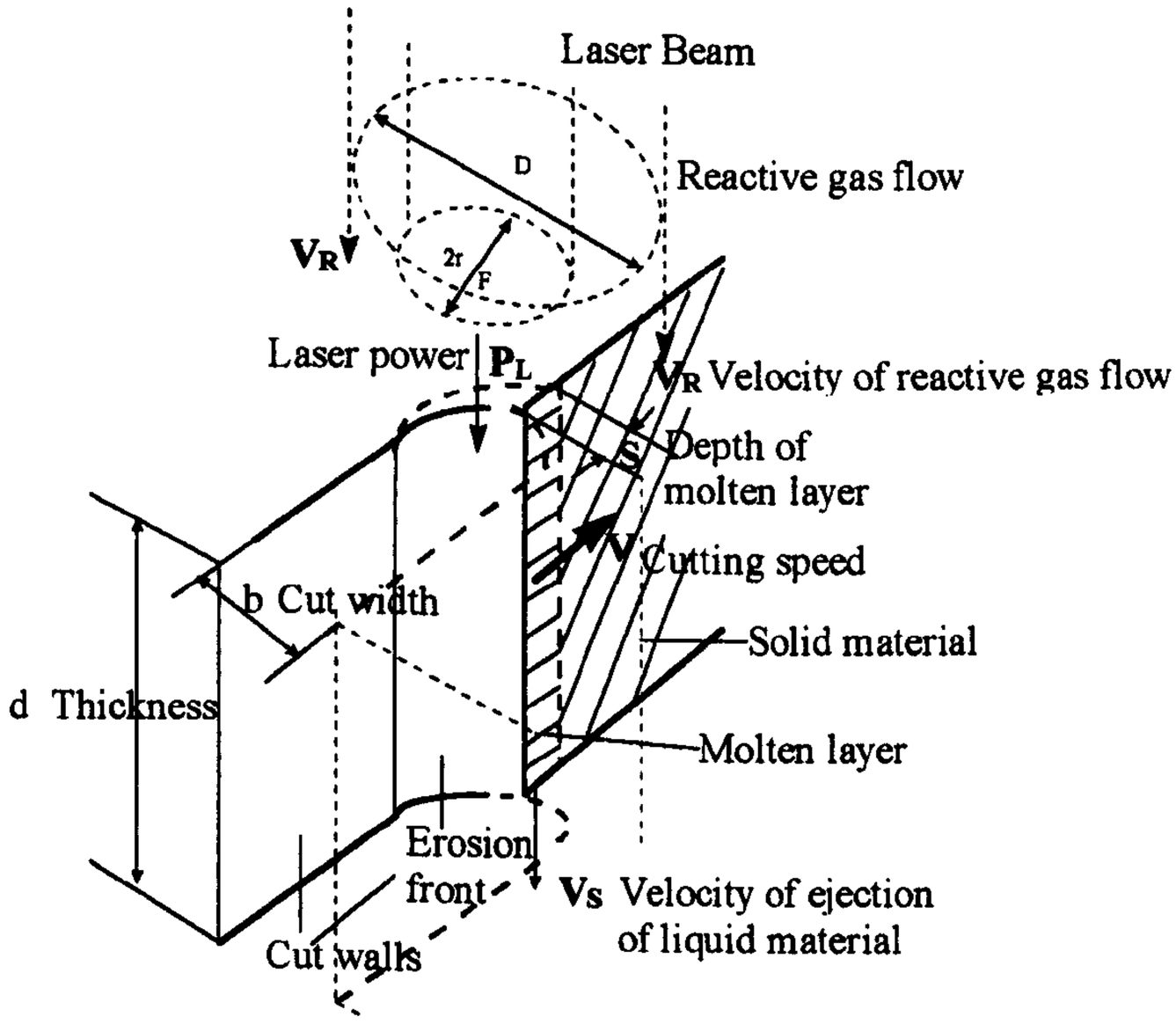

Figure7. *A schematic of cutting geometry suggested by Schuocker [5]*

From the macroscopic viewpoint, 5 steady-state balances are constructed in the molten metal layer, namely, the number of both reactive and pure metal particles in the melt; the momentum, the energy and the mass of the molten metal layer. Adding the heat conduction

equation for a moving point source, all the 6 equations identified are used to determine the 6 quantities, i.e., the thickness of the molten metal layer, the temperature of the melt, the densities of the pure metallic particles and reactive gas particles in the melt, the velocity of the ejection of the molten material at the lower surface of the workpiece and the cutting velocity [5].

This steady-state analytic model is then transformed into a dynamic description, assuming that, for instance, the laser power or chemical reaction energy, are time-dependent [6]. The former reason is due to the instability of laser power itself; the latter one is caused by the formation of turbulence in the gas flow. The dynamic mass and energy balances are thus built up, in which the thickness of the molten metal layer (S) and the temperature of the melt (T) are treated as time-dependent, too, together with the laser power and the chemical reaction energy. To solve those essentially non-linear differential equations, the treatment by the "small perturbation approximation" is used to produce linear differential equations, for example,

$S(t) = S_0 + S_1(t) \quad S_1 << S_0$;

$T(t) = T_0 + T_1(t) \quad T_1 << T_0$;

where, both T_0 and S_0 are constant with respect to time. Subsequently, the frequency of striations is evaluated by analysing the periodicity of $S(t)$ with respect to time.

The approach to construct this analytic model yields a set of differential equations by which the dynamic characteristics in cutting, in particular, the periodicity of striations, can be quantitatively studied. However, as introduced above, the reasons responsible for the dynamics are assumed to essentially come from the instabilities of the laser power and the chemical reaction energy gain. In other words, the dynamic analysis only depends on the artificial oscillations of the laser power and the chemical reaction energy gain.

The lesson drawn here is reflected in Chapter 2 where a theoretical laser cutting system is first of all defined and the governing differential equations are thereafter derived for it. All the input variables to this system, in particular, all the operating parameters including the laser power, are theoretically taken as constant with respect to time. As for the chemical reaction energy gain, the forced oscillating regularity is replaced by the mechanism analysis of exothermic reaction between the oxygen gas and the metallic liquid. In this case it is

expected to discover how the dynamic characteristics in cutting are generated due to the internal variables in the cutting system, rather than externalities such as the laser power.

Realising that the molten metal layer behaves as a thin film flow and its instability results in the striations, Vicneck et al in 1986 [8,9] analysed the flow of the molten metal layer by solving 2-D differential governing equations for the liquid flow. This endeavour was later extended to complexity by Weng et al in 1993 [10], which was based on the non-linear stability analysis for a film flow [11]. The boundary conditions for the film flow in each of them, however, exhibit weaknesses in describing the multiple interaction mechanisms along the gas / liquid interface and the liquid / solid interface.

In 1994, Lim and Chatwin suggested [12,13,14], for the first time, that the unstable striations, i.e., the intermittence of different periodicity of striations, could occur simply because of the chaotic nature of the so-called "non-linear laser cutting system", even when all of the operating parameters are constant with respect to time. Their conclusions are proved by the experiments; however, the theoretical modelling of the cutting system is simplified - it was mainly based on the analyses of the heat conduction in the molten metal layer [13]. This encouraging argument can be justified if the governing equations could be reasonably abstracted from the reality, e.g., the multiple interactions of the flowing molten metal layer in the kerf with the laser beam, the gas jet and the substrate metallic solid, as identified in Section 1-2, and further theoretically proved by Chaos theory in the subset of dynamic nonlinearity [15-19]. Good examples may be referred to the work by Baker and Gollub [18] concerning their chaotic findings in a forced pendulum system, and also by Slivsgaard and Ture [19] in their chaotic findings for an abstracted railway-vehicle system.

In conclusion, all the models introduced above, more or less, have indeed contributed into the knowledge of understanding the extremely complicated laser cutting mechanism, quantitatively or qualitatively, experimentally or analytically. They have laid down a solid basis for the author of this thesis to construct a quantitative, dynamic, mathematical model. More detailed contributions from several research backgrounds are to be mentioned in the relevant chapters where each individual mechanism underlying the laser cutting process is dealt with, along with arguments for the necessary assumptions in context.

1-4. Structure of this thesis

The structure of this thesis is shown in Fig.8.

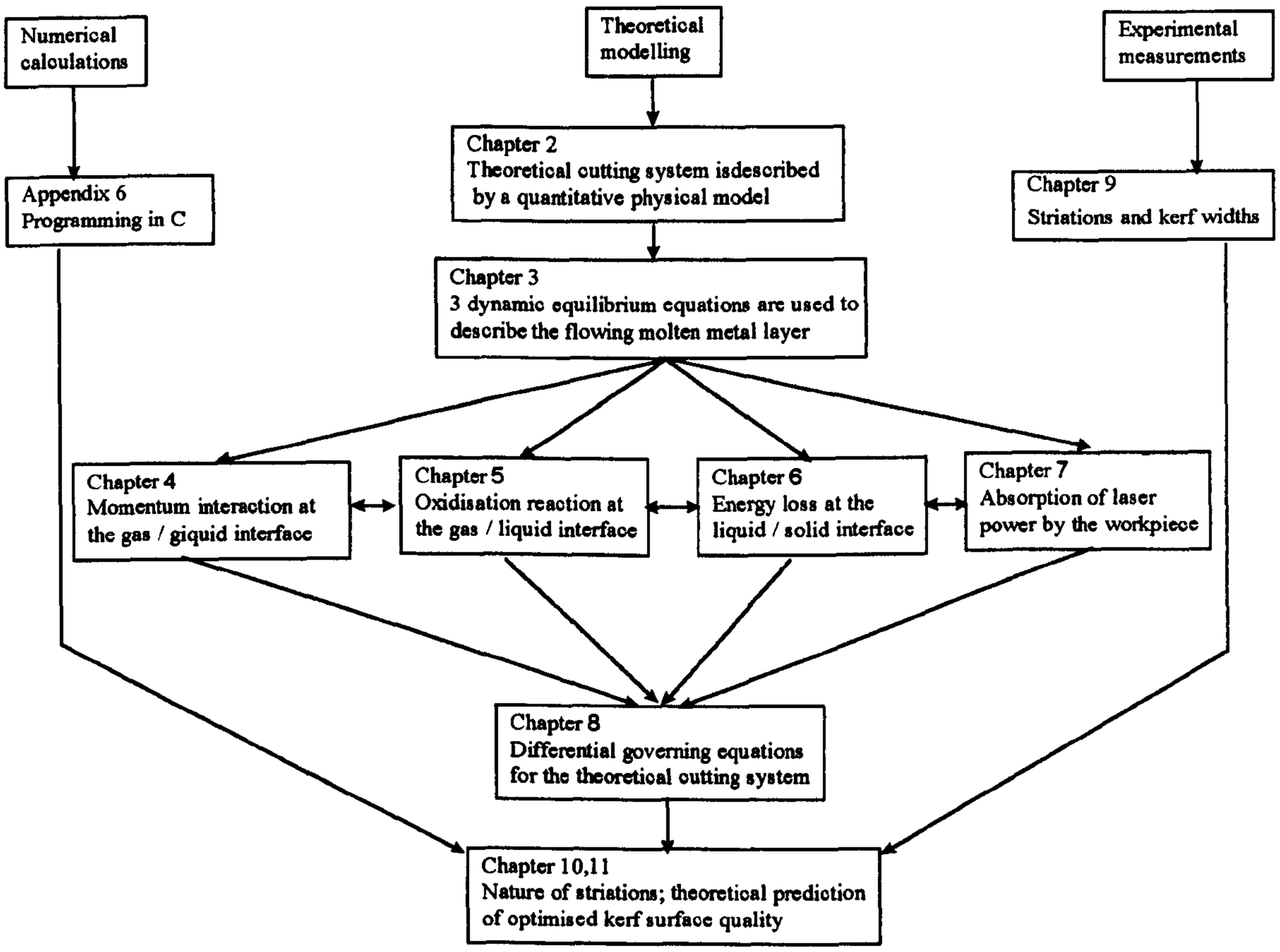

Figure 8. *The structure of the thesis*

A quantitative physical model is established in Chapter 2 and it is referred to throughout the theoretical derivation procedures given in Chapters 3 to 8. The concepts associated with the physical model, e.g., theoretical laser cutting system, control volume, time-dependent and time-independent variables in the system, are defined. The assumptions required by this physical model are argued and established over there. The effective scope of simulation of the dynamic model is finally clarified.

In Chapter 3, three dynamic equilibrium equations concerning continuity, momentum conservation and energy conservation in the control volume, which always encloses the molten metal layer in the kerf with respect to time, are quantitatively established.

Chapters 4 to 7 consider the 4 interacting mechanisms as described in Section 1-2. In Chapter 4, the momentum interaction between the cold, fast-flowing gas and hot, slow-moving metallic liquid is analysed based on the boundary layer flow theories. In Chapter 5, the exothermic reaction between the oxygen gas and the molten metal layer is investigated based on the thermo-chemistry theories. In Chapter 6, the continuous heat transfer from the metallic liquid into the substrate solid is analysed based on the heat conduction and heat convection theories. In Chapter 7, the absorption of laser power by the workpiece is modelled based on the geometrical analysis on the relative displacement between the front of laser beam and the "erosion front" of molten metal layer (the liquid / solid interface). At the end of those chapters, respectively, quantitative tests are presented, based on the typical data in Appendices 1 to 3, to exhibit the magnitudes of the derived unknowns.

Chapter 8 deals with the combined effects of the 4 interacting mechanisms which have been analysed in Chapters 3 to 7. The method to derive the sets of governing differential equations for the laser cutting system is demonstrated. The nature of those simultaneous equations is analysed thereafter. Examples of the numerical solutions to the differential governing equations which are based on the typical data in Appendices 1-3, are respectively shown to demonstrate their variations with respect to time. The dynamic formation and development of striations can quantitatively be illustrated by analysing the variation of the thickness of molten metal layer, $\delta_l(t)$.

In Chapter 9, the objective-oriented experimental tests are introduced. An X-Y table that can produce both constant V_c, for linear and circular cutting profiles, and accelerated / decelerated V_c, for spiral cutting profile, is designed to investigate the influence of the variation of V_c on the periodicity of striations in a practical laser cutting system. The different types of measured striations will be shown and analysed in this chapter.

In Chapter 10, all the individual conclusions from the different parts of this thesis will be discussed and generalised. It also provides some suggestions for the future research work. In Chapter 11, the major achievements in this thesis are stressed.

Appendixes provide useful information necessary for understanding specific derivations, data and numerical solutions. In Appendix 1, the set of typical operating parameters used in the O_2 jet gas assisted continuous wave CO_2 laser cutting of mild steel sheet is introduced. The data are treated as time-independent variables for the theoretical modelling throughout this thesis. In Appendix 2, the flow parameters in the free stream of the gas are calculated with the data in Appendix 1. In Appendix 3, the thermophysical properties (thermodynamic properties and transport properties) of oxygen gas, metallic liquid (iron) and metallic solid (iron) are listed with their reference sources. All of these are treated as time-independent variables in the theoretical modelling. In Appendix 4, the method to calculate the rate of exothermic heat to the molten metal layer, derived by Dutta and Scott [3], are introduced. In Appendix 5, the moving heat source theory and the applications for heat conduction in solids are introduced and analysed. In Appendix 6, a well-structured program in C source codes is listed. In Appendix 7, the characteristics of Lorenz's attractor are presented using the program in Appendix 6. In Appendix 8, more pictures of cutting results are shown.

Chapter 2. Theoretical laser cutting system

In this chapter, the theoretical laser cutting system is described by a quantitative physical model, as shown in Fig.9. It is referred to throughout the theoretical derivation procedures in Chapters 3-8. The concepts related to the physical model, e.g., control volume, time-dependent and time-independent variables are defined. The assumptions required by this physical model are argued and established. The effective scope of the dynamic modelling is finally clarified.

2-1. Definition of theoretical laser cutting system

In practical laser cutting processes, any unstable factors in laser operating parameters, e.g., oscillations in laser power or beam translation velocity, would to a greater or lesser extent affect the finish quality of kerf surface. A practical laser cutting system is the one into which any of its input variables, i.e., the stagnation pressure of gaseous O_2 (p_0), the stagnation temperature of gaseous O_2 (T_0), the total power of laser radiation in the beam waist (P_l), the velocity of translation of laser beam (V_c), can change with respect to time. The practical laser cutting system thus symbolises general laser cutting processes.

A theoretical laser cutting system is abstracted from the reality. It is defined as the system into which the inputs (p_0, T_0, P_l, V_c) are time-independent variables. It symbolises ideal laser cutting processes in which the operating parameters (p_0, T_0, P_l, V_c) are controlled as constantly as possible.

In this thesis, the dynamic modelling is constructed for the theoretical laser cutting system (the cutting system, in short form), rather than the practical laser cutting system. Therefore, the possible effects of the unstable factors in P_l, V_c, p_0 and T_0 in the practical laser cutting system are isolated from the dynamic formation and development of striations. The object

is thus to ascertain how the dynamic characteristics are related to the most relevant time-dependent variables, which are the internal unstable factors in the cutting system.

2-2. Time-dependent and time-independent variables

In the cutting system, all the variables are divided into time-dependent variables and time-independent variables. The time-dependent variables are chosen as follows:

- the thickness of molten metal layer at the bottom of kerf, $\delta_l(t)$;
- the surface temperature of molten metal layer at the gas / liquid interface, $T_l(t)$;
- the velocity of propagation of fusion front, $V_e(t)$;
- the displacement of laser beam front relative to the liquid / solid interface, $y(t)$;
- the laser power absorbed by the heated workpiece, $P_{l,abs}(t)$;

The operating parameters are chosen as time-independent variables:

- the stagnation pressure of gaseous O_2, p_0;
- the stagnation temperature of gaseous O_2, T_0;
- the total power of laser radiation in the beam waist, P_l;
- the velocity of translation of laser beam, V_c;

The thickness of workpiece, D, is even and thus treated as a time-independent variable.

The thermophysical properties (thermodynamic properties and transport properties) of the oxygen gas, metallic liquid (iron) and metallic solid (iron) are treated as time-independent variables, for example:

- the dynamic viscosity of gas and metallic Fe liquid, μ_g, $\mu_{g,w}$ and μ_l;
- the specific heat of gas and metallic Fe liquid, $c_{p,g}$, $c_{p,g,w}$ and $c_{p,l}$;
- the heat conductivity of metallic Fe liquid and metallic Fe solid, K_l and K_s;

- the density of gas, metallic Fe liquid and metallic Fe solid, ρ_g, $\rho_{g.w}$, ρ_l and ρ_s;
- the enthalpy of fusion of Fe, h_f;

In general, except the 5 most concerned variables identified above, which are treated as time-dependent variables and expected to be evaluated with respect to time, respectively, all the other variables associated with the modelling are taken as constant with respect to time.

2-3. Reference co-ordinates

A 3-D rectangular co-ordinates system is chosen as shown in Fig.9. Its origin locates at the start of the molten metal layer and moves at $V_e(t)$, i.e., at the same velocity as the liquid / solid interface. X co-ordinate is along the depth of the workpiece. Y co-ordinate is on the surface of the workpiece and along the beam translation direction. Z co-ordinate is along the kerf width. The dynamic modelling in this thesis is focused in the X-Y plane.

2-4. Control volume

A control volume is defined as such that it always encloses the molten metal layer in the kerf and moves with the reference co-ordinate system, shown in Fig.9. The concept of the control volume makes it possible to build up the dynamic equilibrium equations of mass, momentum and energy, quantitatively, for the flow of the molten metal layer existing in the kerf.

2-5. General assumptions for the cutting system

The physical model representing the cutting system is shown in Fig.9. The physical model shows the major variables applying at the control volume which encloses the molten metal layer, due to the multiple interactions around the molten metal layer. Its different simplified

forms will be illustrated, respectively, in analysing the individual interaction mechanisms, in Chapters 3 to 8.

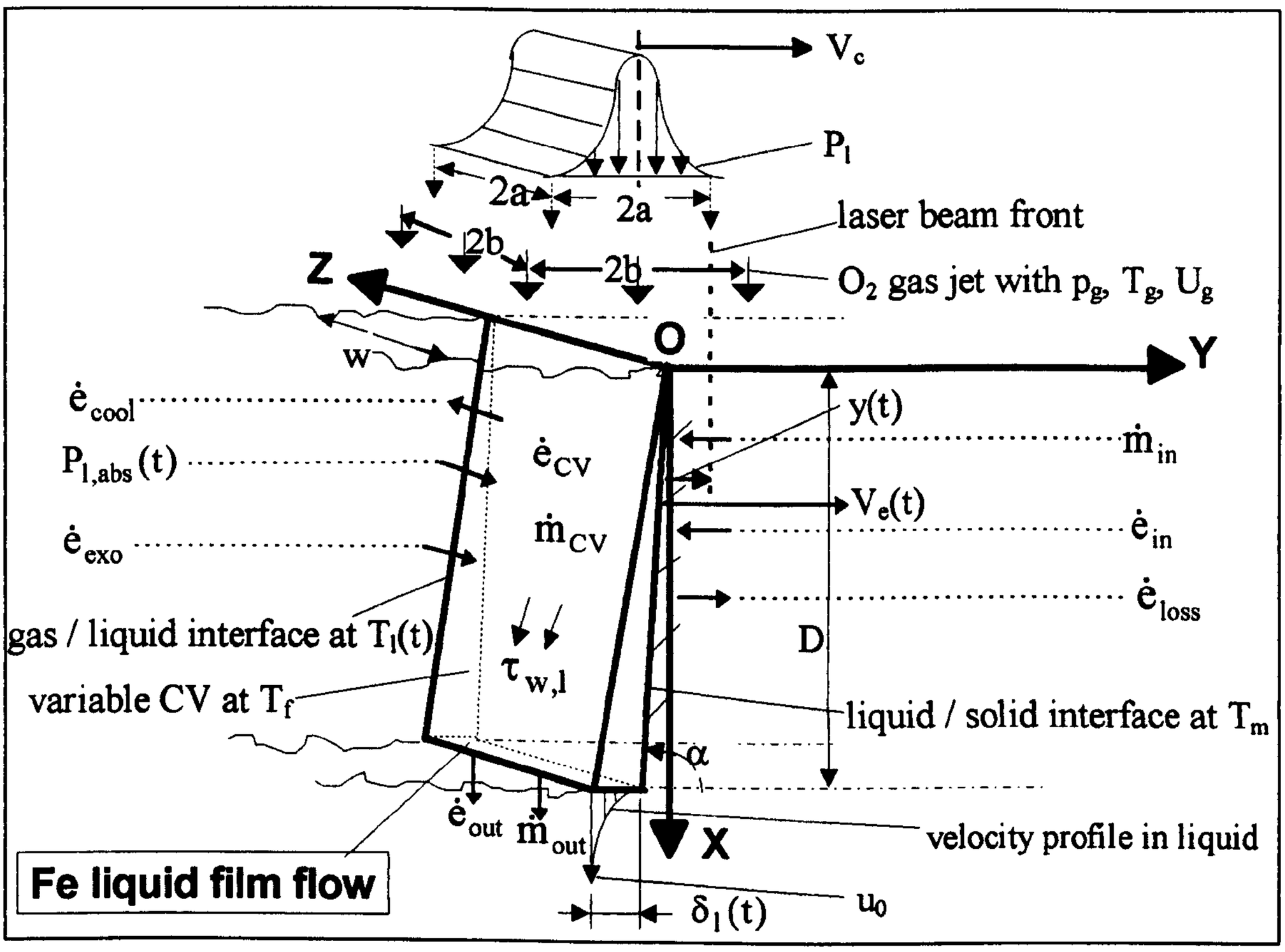

Figure 9. *The physical model illustrates the major variables applying at the molten metal layer. In the model, the metallic workpiece is fixed and the laser beam is translated at constant V_c while the liquid / solid interface moves at variable $V_e(t)$. X-Y plane is studied*

The basic assumptions for the physical model are established in this section and they are referred to throughout the theoretical derivations.

- The interface of the molten metal layer and the solid metal substrate (the liquid / solid interface) is an inclined plane at T_m. The interface of the molten metal layer and the gas jet (the gas / liquid interface) is an inclined plane at the variable temperature of $T_l(t)$. Both interfaces start from the origin of the reference system and move along Y at the variable velocity of $V_e(t)$. The liquid / solid interface has a constant angle, α, to Y.

- The control volume enclosing the molten metal layer in the kerf is wedge-shaped. Its one side is the liquid / solid interface and the other is the gas / liquid interface.

- The modelling is focused in the X-Y plane. The variations in Z, e.g., the cut width (w), are not considered. In the evaluations of typical derived quantities, the measured cut width is used for w, assuming that $2b > 2a = w$. The 2-D approach is due to the unavailability of theories, in particular, the analytic solutions to the 3-D differential momentum equation in Fluid Mechanics. Practically, it is fairly justified because δ_l in Y is far less than w in Z.

- The temperature of the molten metal layer is defined as the film temperature, i.e., $T_f = (T_l + T_m)/2$, where T_l is the surface temperature of the molten metal layer at the gas / liquid interface; T_m is the melting temperature at the liquid / solid interface.

- The pressurised gas is regarded as an ideal gas; the Mach number at the nozzle outlet is $M = 1$; the gas velocity in free stream, along the depth of kerf, is constant. Therefore, the gas flow parameters, i.e., p_0, T_0 and U_g, are constant along the depth of kerf.

In Appendix 1, a set of typical operating parameters in laser cutting, including p_0 and T_0, is listed for reference throughout this thesis. In Appendix 2, the useful gas flow parameters including U_g, are evaluated for reference.

- The focused laser beam is transformed into a square column with the sectional area of $2a \times 2a$: in Y, the energy density holds Gaussian profile; in X and Z, the energy density is even, respectively.

- The gas jet flow is transformed into a square column with the sectional area of $2b \times 2b$. In Y, if the gaseous column can not "see" the molten metal layer, the exothermic reaction is assumed to stop.

In analysing the individual interaction mechanisms, further assumptions associated with the contexts will be introduced, in addition to the assumptions above.

2-6. Effective scope of the theoretical modelling

Since attention is focused on the dynamic formation and development of striations, the theoretical modelling concentrates on the dynamic balances of mass, momentum and energy in the molten metal layer in the kerf. Therefore, the modelling is effective when, practically, a thin molten metal layer in dynamic balance is first generated. The transient process during which a keyhole is produced, enlarged and penetrated until the formation of the first molten metal layer at the beginning of a laser cutting process is not within the scope of the modelling, as shown in Fig.9. This is due to the fact that the fusion front, i.e., the liquid / solid interface, is always found to be covered by a very thin film of molten metal layer during laser cutting, which is continuously generated from the metallic solid substrate and simultaneously ejected by the gas jet.

Chapter 3. Dynamic equations for the flow of molten metal layer

In this chapter, the flow characteristics of the molten metal layer in the kerf are analysed, in Fig.10, by conserving the 3 balances in the control volume enclosing the molten metal layer, namely, the continuity, the energy equilibrium and the momentum equilibrium. They must, at any time, be satisfied simultaneously. In the derivations of related quantities, some of them can directly be expressed in association with the 5 time-dependent variables, i.e., $\delta_l(t)$, $T_l(t)$, $V_e(t)$, $y(t)$ and $P_{l,abs}(t)$. The others will be analysed and thus associated with the 5 time-dependent variables, later in Chapters 4-7, where the relevant interaction mechanisms are dealt with. It is noted that Fig.10 is a simplified form of Fig.9, which is referred to throughout this thesis.

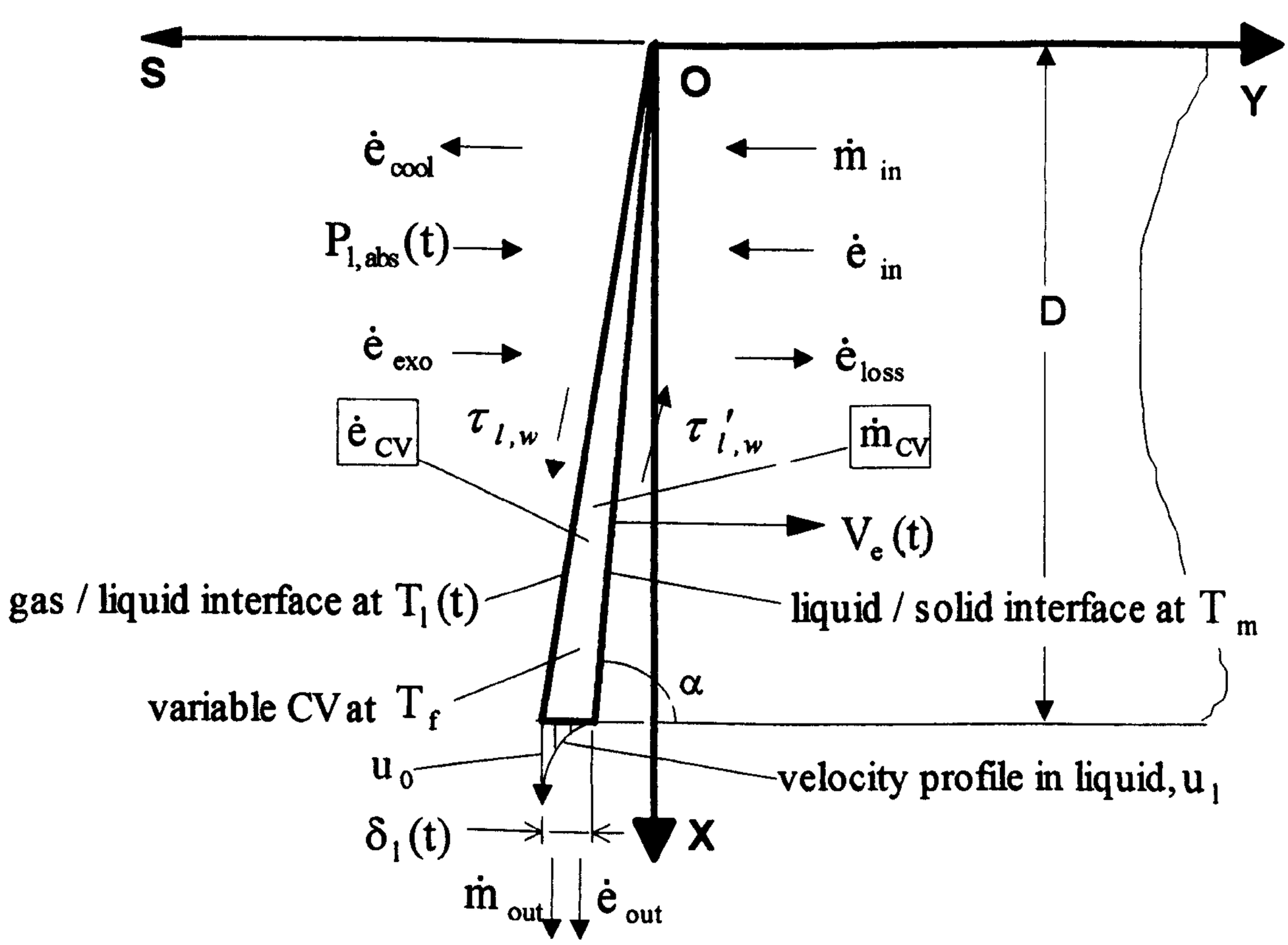

Figure 10. *In X-O-Y, the quantities around the wedge-shaped control volume enclosing the molten metal layer are exhibited. They must simultaneously satisfy the continuity, energy equilibrium and momentum equilibrium in the control volume, with respect to time*

3-1. Continuity in control volume

In Fig.10, if the vaporisation of the molten metal from the left side of the control volume is ignored, the continuity requires:

$$\dot{m}_{in} = \dot{m}_{out} + \dot{m}_{CV} \tag{1}$$

where $\dot{m}_{in}$: the mass rate of the solid metal moving into the CV ;

$\dot{m}_{out}$: the mass rate of the molten metal flowing out of the CV ;

$\dot{m}_{CV}$: the mass change rate of the CV ;

$\dot{m}_{in}$ is calculated as:

$$\dot{m}_{in} = \rho_s \cdot w \cdot D \cdot V_e(t) \tag{2}$$

thus, $\dot{m}_{in}$ is associated with the time-dependent variable, $V_e(t)$, and the time-independent variables, ρ_s, w and D. All the mathematical symbols have been listed in Nomenclature.

By the definition, $\dot{m}_{CV}$ is related to the 1st-order derivative of the time-dependent variable, $\delta_l(t)$, with respect to time, taking the control volume as wedge-shaped:

$$\dot{m}_{CV} = \frac{d}{dt}\left(\frac{1}{2} \cdot \rho_l \cdot w \cdot D \cdot \delta_l(t)\right) = \frac{1}{2} \cdot \rho_l \cdot w \cdot D \cdot \left(\frac{d}{dt}\left[\delta_l(t)\right]\right) \tag{3}$$

In Fig.10, $\dot{m}_{out}$ is essentially dependent on the velocity profile of the molten metal layer, u_l, at the bottom of CV, and the local thickness, $\delta_l(t)$. It is calculated as:

$$\dot{m}_{out} = \int_0^{\delta_l(t)} u_l \rho_l w(ds) \tag{4}$$

where, s denotes the co-ordinate in S, which is the magnitude in the negative direction of Y.

To calculate $\dot{m}_{out}$, the profile of u_l with respect to s should be known. Assuming that the molten metal layer is extremely thin and the removal of molten metal is dominantly by the shear stress applied by the fast-flowing gas at the gas / liquid interface, the flow of molten metal layer is treated as a quasi-shear-stress boundary layer flow*. In this case, the linear relationship between u_l and s is assumed; the shear stresses at the gas / liquid interface and the liquid / solid interface, $\tau_{l,w}$ and $\tau'_{l,w}$ as shown in Fig.10, are equal in magnitude but opposite in direction.

Further, the angle α, in Fig.10, is assumed at 90^o for the convenience of mathematical analysis**. Therefore, the liquid / solid interface is at X; $\tau_{l,w}$ is along the positive direction of X; $\tau'_{l,w}$ is along the negative direction of X. The analysis can be carried out in X-O-S co-ordinate system.

The boundary conditions for u_l are:

if $x = D$, $s = 0$, then $u_l = 0$;

if $x = D$, $s = \delta_l(t)$, then $u_l = u_0$;

u_l is thus calculated as:

$$u_l = \frac{u_0}{\delta_l(t)} \cdot s \quad \text{at } x = D \tag{5}$$

Contributing Eq.5 into Eq.4 gives:

$$\dot{m}_{out} = \int_0^{\delta_l(t)} \rho_l w \frac{u_0}{\delta_l(t)} s ds \tag{6}$$

---

* A pure shear-stress boundary-layer flow, or Couette flow, is produced when a viscous fluid between two parallel infinite plates is set into motion by the relative velocity of one of the walls. Experimentally it is often studied as the flow between two concentric cylinders when the spacing between the cylinders is small in comparison to the radii [20]. A Couette flow is characterised by (1) the velocity profile across the flow is linear; (2) the shear stresses applied by the two plates are equal in magnitude but opposite in direction.

** Taken as a time-independent variable in this thesis, α will be given the value slightly less than 90^o in the final construction of differential governing equations for the cutting system. The influence of α on the flow analyses of the molten metal layer is negligible.

where, u_0 is essentially related to $\delta_l(t)$ by $\tau_{l,w}$ and $\tau'_{l,w}$. This is analysed in Section 3-2.

3-2. Momentum conservation in control volume

The momentum conservation for the molten metal layer describes the fact that the velocity profile, u_l, is controlled by the forces applying at its surface. Treating the flow of the molten metal layer as a quasi-shear-stress boundary-layer flow, as analysed in Section 3-1, the momentum conservation for CV enclosing the liquid in the kerf requires:

$$(\tau_{l,w})_x = -(\tau'_{l,w})_x = \mu_l(\frac{du_l}{ds})_x = (\mu_l \frac{u_l}{s})_x \quad \text{at } x \in (0, D] \tag{7}$$

where, u_l is the function of both x and s. $(\tau_{l,w})_x$ is the shear stress applying at the left side of CV by the fast-flowing jet gas.

Eq.7 applies to every cross section in the flow of molten metal layer, in particular, at the bottom of the kerf. Introducing Eq.5 into Eq.7, the shear stress at $x = D$, $(\tau_{l,w})_{x=D}$, can be related to u_0 and $\delta_l(t)$:

$$(\tau_{l,w})_{x=D} = -(\tau'_{l,w})_{x=D} = \mu_l \frac{u_0}{\delta_l(t)} \tag{8}$$

Therefore, $\dot{m}_{out}$ can be calculated by introducing Eq.8 into Eq.6:

$$\dot{m}_{out} = \int_0^{\delta_l(t)} \left(\frac{\rho_l w}{\mu_l} (\tau_{l,w})_{x=D} \right) s \cdot ds \tag{6'}$$

Eq.6' is used to calculate $\dot{m}_{out}$ which is associated with $\delta_l(t)$. $(\tau_{l,w})_{x=D}$ will be derived to be time-independent in Chapter 4, where the gaseous boundary layer flow is analysed for the momentum interaction at the gas / liquid interface.

3-3. Energy conservation in control volume

It is seen that, in Fig.10, assuming the energy loss associated with the vaporisation of the molten metal from the left side of the control volume is ignored, the energy conservation in CV requires:

$$\dot{P}_{l,abs} + \dot{e}_{exo} + \dot{e}_{in} = \dot{e}_{out} + \dot{e}_{loss} + \dot{e}_{cool} + \dot{e}_{CV} \tag{9}$$

where, $P_{l,abs}(t)$: the laser power absorbed by the heated workpiece;

$\dot{e}_{exo}$: the exothermic reaction energy release rate entering into the CV ;

$\dot{e}_{in}$: the energy rate carried by the mass in solid phase into the CV ;

$\dot{e}_{out}$: the energy rate carried by the mass in liquid phase flowing out of the CV ;

$\dot{e}_{loss}$: the rate of the energy loss from the CV into the solid metal;

$\dot{e}_{cool}$: the rate of cooling of the liquid by the gas jet;

$\dot{e}_{CV}$: the rate of change of energy stored in the CV ;

If the temperature reference is at $0\ ^{o}K$; the kinetic energy is neglected in comparison to the internal energy when the mass moves into and out of CV, respectively, $\dot{e}_{in}$ is calculated:

$$\dot{e}_{in} = \dot{m}_{in} \cdot c_{p,s} \cdot T_m \tag{10}$$

Combining Eq.10 and Eq.2 gives:

$$\dot{e}_{in} = c_{p,s} \cdot \rho_s \cdot w \cdot D \cdot T_m \cdot V_e(t) \tag{11}$$

Taking the process of fusion at T_m into account, $\dot{e}_{out}$ is similarly calculated:

$$\dot{e}_{out} = \dot{m}_{out}(c_{p,l} \cdot T_f + h_f) \tag{12}$$

where, h_f denotes the heat of fusion for iron. T_f is the average temperature of the molten metal layer, defined as:

$$T_f = \frac{T_m + T_l(t)}{2} \tag{13}$$

Contributing Eq.6' and Eq.13 into Eq.12 gives:

$$\dot{e}_{out} = \left[\int_0^{\delta_l(t)} \left(\frac{\rho_l w}{\mu_l}(\tau_{l,w})_{x=D}\right) s \cdot ds\right] \cdot \left[c_{p,l} \cdot \frac{T_m + T_l(t)}{2} + h_f\right] \tag{14}$$

It is seen that, in Eq.11 and Eq.14, $\dot{e}_{in}$ is related to $V_e(t)$ and $\dot{e}_{out}$ is related to $\delta_l(t)$ and $T_l(t)$. $(\tau_{l,w})_{x=D}$ will be evaluated in Chapter 4.

The rate of change of energy stored in the CV, $\dot{e}_{CV}$, is calculated by the definition:

$$\begin{aligned}\dot{e}_{CV} &= \frac{d(e_{CV})}{dt} = \frac{d}{dt}\left\{\left[\frac{1}{2}\cdot\rho_l\cdot w\cdot D\cdot\delta_l(t)\right]\cdot\left[c_{p,l}\cdot T_f(t)+h_f\right]\right\} \\ &= \frac{1}{2}\cdot\rho_l\cdot w\cdot D\cdot c_{p,l}\cdot T_f(t)\cdot\frac{d}{dt}\left[\delta_l(t)\right]+\frac{1}{2}\cdot\rho_l\cdot w\cdot D\cdot h_f\cdot\frac{d}{dt}\left[\delta_l(t)\right] \\ &+\frac{1}{2}\cdot\rho_l\cdot w\cdot D\cdot c_{p,l}\cdot\delta_l(t)\cdot\frac{d}{dt}\left[T_f(t)\right]\end{aligned} \tag{15}$$

It is seen that $\dot{e}_{CV}$ is related to $\delta_l(t)$, $T_l(t)$ and their 1st-order derivatives with respect to time. The other quantities required in Eq.9 will be determined later in Chapters 4-7.

Chapter 4. Interaction of gas and liquid flows

This chapter analyses the interaction between the cold, fast-flowing gas jet and the hot, slow-moving metallic liquid film, along the gas / liquid interface. During the interaction, the momentum of the gas is transferred to the liquid, through the shear stress, $\tau_{l,w}$, that drives the liquid to flow out of the kerf; at the same time, the heat is convected from the liquid into the gas, making the gas cooling effect unavoidable.

The gaseous boundary layer develops at the gas / liquid interface. This phenomenon is analysed by solving the 2-D differential governing equations for a laminar boundary layer flow, based on Howarth-Dorodnitsyn's method and Von Karman's skin friction relationship [20]. As a result, the shear stress applied at the gas side at the gas / liquid interface ($\tau_{g,w}$) and the gas cooling effect ($\dot{e}_{cool}$) are derived. The shear stress applied at the liquid side at the gas / liquid interface is eventually derived, by $\tau_{l,w} = -\tau_{g,w}$, which is required in Eq.6' and Eq.14 in Chapter 3.

The maximum surface velocity of the liquid, $u_{0,max}$, is analysed with Lock's solution for the momentum interaction of 2 parallel laminar boundary layer flows [21]. $u_{0,max}$ occurs only when there is "no slip" between the 2 flows at the gas / liquid interface. It is used to discover the possible range of $\delta_l(t)$, i.e., $\delta_{l,max}$. $\delta_l(t) \in (0, \delta_{l,max}]$ must be adhered to at each step of time evolution.

Finally, the derived quantities are evaluated with the typical data in Appendixes 1-3.

4-1. Differential governing equations for gaseous boundary layer flow

The interaction between the cold, fast-flowing gas jet and the hot, slow-moving metallic liquid film along the gas / liquid interface is theoretically treated in Fig.11, where a gaseous

boundary layer flow develops along the gas / liquid interface. The skin friction occurs at the gas / liquid interface.

It is noted that X-O-Y and X-O-S reference systems in Fig.11 are the same as those in Fig.9 and Fig.10.

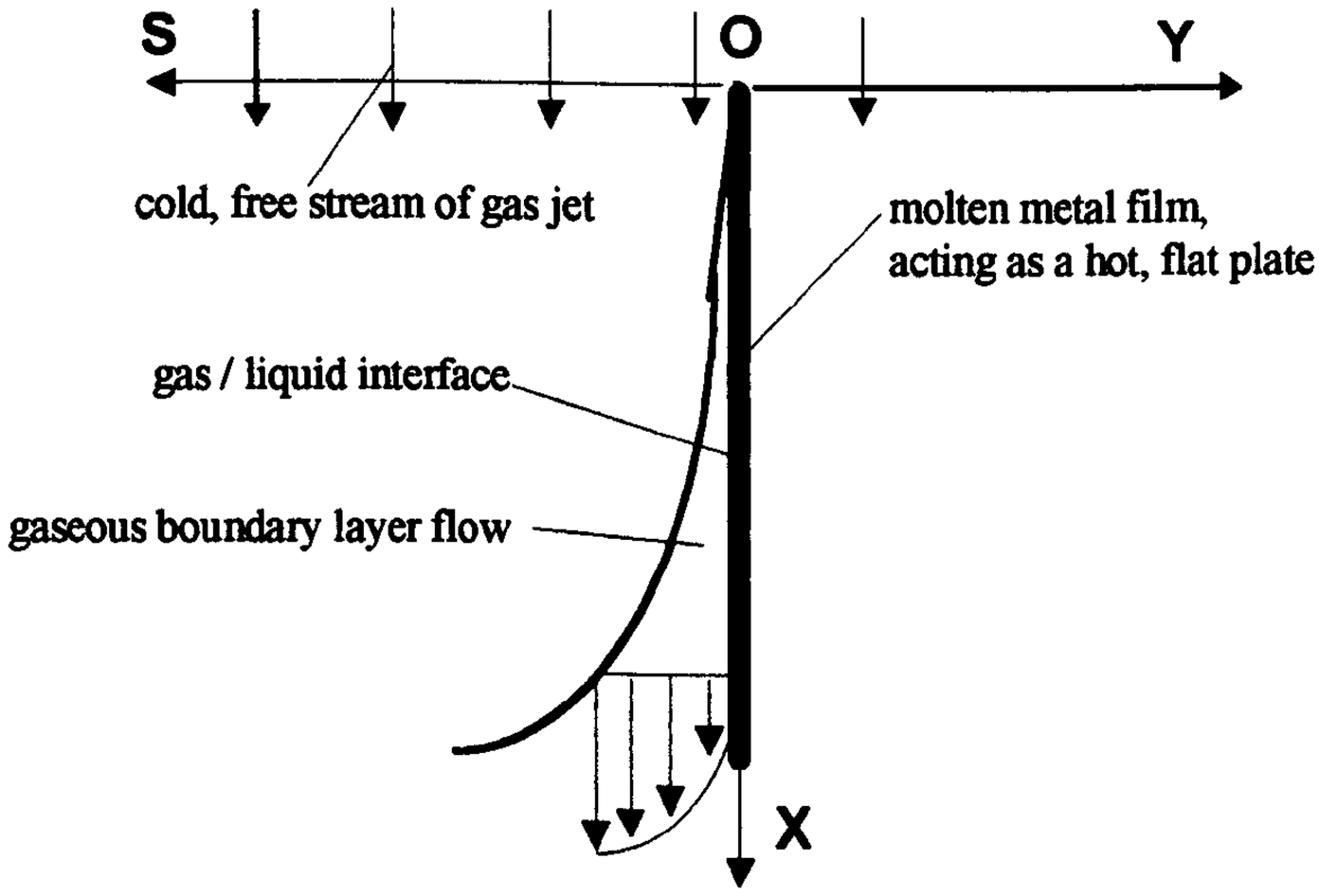

Figure 11. *The gas at T_g and U_g flows fast onto the molten metal layer acting as a "hot flat plate" at $T_l(t)$ and $u_{l.0}$. The plate is taken as fixed, due to $U_g >> u_{l.0}$. In the free stream, T_g, U_g and ρ_g, are constant along X*

In Fig.11, the gaseous boundary layer flow is treated as a laminar flow*. Empirically, this is justified by the Reynolds number for a forced external convection flow [20,22]:

$$Re = \frac{\rho_g \cdot U_g \cdot x}{\mu_g} \tag{16}$$

where, $(Re)_{critical} = 3 \times 10^5 - 5 \times 10^5$ [P.304, reference 22]. If $Re < (Re)_{critical}$, a laminar flow is defined; if $Re > (Re)_{critical}$, a turbulent flow is expected.

* With typical data in Appendixes 1-3, it can be seen: when $x = D$, $Re_{max} = 5.87 \times 10^3 << (Re)_{critical}$. It is justified that the gaseous boundary layer is treated as a laminar flow rather than a turbulent one.

The 2-D differential governing equations for the gaseous laminar boundary layer flow are as follows *, in X-O-S reference system:

$$\frac{\partial}{\partial x}(\rho u)+\frac{\partial}{\partial s}(\rho v)=0 \tag{17}$$

$$\rho u\frac{\partial u}{\partial x}+\rho v\frac{\partial u}{\partial s}=\frac{\partial}{\partial s}(\mu\frac{\partial u}{\partial s}) \tag{18}$$

$$\rho u\frac{\partial h}{\partial x}+\rho v\frac{\partial h}{\partial s}=\frac{\partial}{\partial s}[\frac{\mu}{Pr}\frac{\partial h}{\partial s}+\mu(1-\frac{1}{Pr})\frac{\partial(u^2/2)}{\partial s}] \tag{19}$$

with the boundary conditions:

if $x=0$ and $s>0$ then $u=U_g$;

if $x>0$ and $s\to\infty$ then $u\to U_g$;

if $x>0$ and $s=0$ then $u=0$;

where, u, v denote the local velocities in X and S in Fig.11, respectively, in the gaseous laminar boundary layer flow; ρ the local density; μ the local dynamic viscosity; h the local total enthalpy. Pr denotes Prandtl number of the gas, defined as:

$$Pr=\frac{\mu\cdot c_p}{K} \tag{20}$$

where, K denotes the heat conductivity of the gas; c_p the specific heat in constant pressure of the gas.

* The fundamental theory may be referred to Page 8-54 in [20]. This set of differential governing equations can directly be derived from the more generally studied problem where a gas flow in chemical equilibrium is investigated.

To solve Eqs.17-19, simultaneously, the concept of "boundary layer similarity" should be applied to transform the original partial differential equations into the ordinary differential equations*. The Howarth-Dorodnitsyn's transformation of the independent variables, from x and s to ζ and η, is applied in solving Eqs.17-19. The treatment is able to deal with an ideal gas flowing over a "flat plate" at higher temperature**, which is the case shown in Fig.11. The physical properties are therefore treated as changeable.

The new independent variables are constructed as:

$$\zeta = U_g \mu_{g,w} \rho_{g,w} x \ ; \ \eta = \sqrt{\frac{U_g}{\nu_{g,w} x}} \int_0^s \frac{\rho}{\rho_{g,w}} ds \tag{20}$$

where, the subscript w represents the reference condition for the specific properties at the wall of the boundary layer; U_g is the free stream velocity along X; $\nu_{g,w}$ the kinetic viscosity of the gas at the wall; $\mu_{g,w}$ the dynamic viscosity of the gas at the wall; $\rho_{g,w}$ the density of the gas at the wall; By introducing Eq.20 into Eqs.17-19, the transformed differential governing equations become:

$$(C_r f'')' + \frac{1}{2} f f'' = 0 \tag{21}$$

$$(\frac{C_r g'}{Pr})' + \frac{1}{2} f g' + \frac{U_g^{\ 2}}{h_g} [C_w (1 - \frac{1}{Pr}) f f'']' = 0 \tag{22}$$

---

* The idea of "boundary layer similarity" was discovered by Prandtl and is the most essential element of boundary layer theory [20]. One of the famous solutions is the Blasius' treatment which concerns the fluid with constant properties.

** The detailed derivations may be referred to Page 8-65 in [20].

where, $f' = \frac{u}{U_g}$; $g = \frac{h}{h_g}$; $C_r = \frac{\mu\rho}{\mu_g\rho_g}$; $\frac{\partial}{\partial\eta}(\ ) = (\ )'$. h_g denotes the enthalpy of the gas in the free stream. The subscript r represents the reference condition for the properties taken at the edge of the boundary layer. In Eqs.22, the "flat plate" wall has been assumed at uniform surface temperature. Correspondingly, the transformed boundary conditions are:

if $\eta = 0$ then $f = f' = 0$ and $g = h_{g,w} / h_g$;

if $\eta \to \infty$ then $f' \to 1$ and $g \to 1$;

Assuming C_r and Pr are constant, the local skin friction coefficient, $(\frac{c_f}{2})_{g,w}$, is derived:

$$(\frac{c_f}{2})_{g,w} = \frac{0.332}{\sqrt{(Re)_g}} \frac{\mu_{g,w}\rho_{g,w} / \mu_g\rho_g}{\sqrt{C_r}} = (\frac{c_f}{2})_i \frac{\mu_{g,w}\rho_{g,w} / \mu_g\rho_g}{\sqrt{C_r}} \tag{23}$$

where, $(\frac{c_f}{2})_i$ represents the skin friction coefficient corresponding to a constant property boundary layer at the same local length Reynolds number.

The local heat transfer coefficient or the local Stanton number, c_h, is calculated by the modified Reynolds' analogy:

$$(c_h)_{g,w} = (\frac{c_f}{2})_{g,w}\left[(Pr)_g\right]^{-2/3} \tag{24}$$

The Von Karman's skin friction relationship, expressed in Eq.25, is used to calculate C_r in Eq.23, assuming that the local physical properties at the wall would control the local skin friction law and heat convection law when their variations occur:

$$C_r = \frac{\mu_{g,w}\rho_{g,w}}{\mu_g\rho_g} \tag{25}$$

Contributing Eq.25 into Eq.23 gives:

$$(\frac{c_f}{2})_{g,w} = (\frac{c_f}{2})_i \sqrt{\frac{\rho_{g,w}\mu_{g,w}}{\rho_g \mu_g}} = \frac{0.332}{\sqrt{\rho_{g,w}U_g x / \mu_{g,w}}} \qquad (23')$$

and,

$$(c_h)_{g,w} = \frac{0.332}{\sqrt{\rho_{g,w}U_g x / \mu_{g,w}}}\left[(Pr)_g\right]^{-2/3} \qquad (24')$$

Knowing $(\frac{c_f}{2})_{g,w}$ in Eq.23, the local skin friction or shear stress, $\tau_{g,w}$, which is applied by the "flat plate" onto the gas side of the gas / liquid interface is calculated:

$$\tau_{g,w} = -(\frac{c_f}{2})_{g,w}\rho_{g,w}U_g{}^2 = -\frac{0.332\rho_{g,w}U_g{}^2}{\sqrt{\rho_{g,w}U_g x / \mu_{g,w}}} \qquad (26)$$

where, the negative sign denotes that $\tau_{g,w}$ is in the negative direction of X.

Knowing $(c_h)_{g,w}$ in Eq.24, the heat flux convected from the hot "flat plate" into the gas, $\dot{q}_{g,w}$, is calculated:

$$\dot{q}_{g,w} = (c_h)_{g,w}\rho_{g,w}U_g(h_{g,w} - h_g) = \frac{0.332\rho_{g,w}U_g[c_{p,g,w}T_i(t) - c_{p,g}T_g]}{\sqrt{\rho_{g,w}U_g x / \mu_{g,w}}}\left[(Pr)_g\right]^{-2/3} \qquad (27)$$

4-2. Shear stress applied at the molten metal layer

At the gas / liquid interface, in Fig.11, Newton's law of action and counteraction applies, as in Eq.28, regardless of whether a relative "slip" exists between the fast-flowing gas and the slow-moving metallic liquid:

$$(\tau_{l,w})_x = -(\tau_{g,w})_x \tag{28}$$

where, $\tau_{l,w}$: the shear stress applied at the liquid side of gas / liquid interface;

$\tau_{g,w}$: the shear stress applied at the gas side of gas / liquid interface;

Knowing the magnitude and the direction of $(\tau_{g,w})_x$, from Eq.26, $(\tau_{l,w})_x$ is calculated by combining Eq.28 and Eq.26:

$$(\tau_{l,w})_x = \frac{0.332\rho_{g,w}U_g^{\ 2}}{\sqrt{\rho_{g,w}U_g x / \mu_{g,w}}} \tag{29}$$

where, the direction of $\tau_{l,w}$ is along X; it changes when x varies. If $x = D$, the shear stress applied by the gas at the bottom of the surface of the molten metal liquid, at the interface of gas / liquid, $(\tau_{l,w})_{x=D}$, is calculated as:

$$(\tau_{l,w})_{x=D} = \frac{0.332\rho_{g,w}U_g^{\ 2}}{\sqrt{\rho_{g,w}U_g D / \mu_{g,w}}} \tag{30}$$

It is observed that, by Eq.30, $(\tau_{l,w})_{x=D}$ only depends on the physical properties of the gas at around T_l as well as the free stream velocity of the gas. Since they are time-independent, $(\tau_{l,w})_{x=D}$ is essentially a time-independent variable.

Knowing $(\tau_{l,w})_{x=D}$ in Eq.30, it is possible to evaluate $\dot{m}_{out}$ by Eq.6' and $\dot{e}_{out}$ by Eq.14, as shown in Fig.10 in Chapter 3. Contributing Eq.30 into Eq.6' gives:

$$\dot{m}_{out} = \left(0.166\frac{w\rho_l}{\mu_l}\frac{\rho_{g,w}U_g^{\ 2}}{\sqrt{\rho_{g,w}U_g D / \mu_{g,w}}}\right)\cdot\left[\delta_l(t)\right]^2 \tag{6''}$$

Similarly, contributing Eq.30 into Eq.14 gives:

$$\dot{e}_{out} = \left(0.166 \frac{w\rho_l}{\mu_l} \frac{\rho_{g,w} U_g^{\,2}}{\sqrt{\rho_{g,w} U_g D / \mu_{g,w}}} \right) \cdot \left[c_{p,l} \frac{T_m + T_l(t)}{2} + h_f \right] \cdot \left[\delta_l(t) \right]^2 \qquad (14')$$

As expected, $\dot{m}_{out}$ is associated with the time-dependent variable, $\delta_l(t)$, by Eq.6''; $\dot{e}_{out}$ is related to the time-dependent variables, $\delta_l(t)$ and $T_l(t)$, by Eq.14'. They will be used and contributed into Eq.1 and Eq.9, respectively, in Chapter 8.

4-3. Cooling effect of fast-flowing gas

In Section 4-1, the term of $\dot{q}_{g,w}$, by Eq.27, suggests that the cooling effect of the fast-flowing gas exists at the gas / liquid interface, from the hot metallic liquid into the cold gas. The convective heat rate, $\dot{e}_{cool}$, as shown in Fig.10 in Chapter 3, is calculated as follows, assuming α is nearly 90^0:

$$\dot{e}_{cool} = \int_0^D \dot{q}_{g,w}(w \cdot dx) = 0.664 \frac{w\rho_{g,w} U_g \left[c_{p,g,w} T_l(t) - c_{p,g} T_g \right]}{\sqrt{(\rho_{g,w} U_g) / (D\mu_{g,w})}} \cdot \left[(Pr)_g \right]^{-2/3} \qquad (31)$$

Eq.31 shows that $\dot{e}_{cool}$ is associated with the time-independent variable, $T_l(t)$. Pr for the gas is taken as a constant when the temperature varies, as listed in Appendix 3; it is thus chosen at the free stream temperature. $\dot{e}_{cool}$ will be used and contributed into Eq.9, in Chapter 8.

4-4. Maximum surface velocity of the molten metal layer

The interaction of the gas and the liquid is characteristic of Eq.28, i.e., $(\tau_{l,w})_x = -(\tau_{g,w})_x$, at the gas / liquid interface. The surface velocity of the liquid, $u_{l,0}$, is always bounded by the local shear stress, $(\tau_{l,w})_x$, and the local liquid thickness, s_0; it varies with x and reaches to the maximum, i.e., $u_{l,0} = u_0$ at $x = D^*$. u_0 is essentially associated with $\delta_l(t)$ by:

$$u_0 = \frac{0.332\rho_{g,w}U_g^{\,2}}{\mu_l\sqrt{\dfrac{\rho_{g,w}U_g D}{\mu_{g,w}}}}\delta_l(t) \tag{32}$$

It is seen that, normally, the relative "slip" between the gas and the liquid flows could happen, up to $x = D$. If the condition of "no slip" is reached at the gas / liquid interface, in addition to the condition of $(\tau_{l,w})_x = -(\tau_{g,w})_x$, u_0 would reach the maximum limit, $u_{0,max}$. The possible range of u_0 is thus expressed as:

$$0 \le u_0 \le u_{0,max} \tag{33}$$

It is noted that the generation of $u_{0,max}$ depends on the "no slip" condition at the gas / liquid interface; the real value of u_0 is always related to $\delta_l(t)$ by Eq.32. The theoretical description for the momentum interaction between the gas and the liquid is shown in Fig.12, in which the reference system is the same as in Figs.9-11.

---

* This can be mathematically expressed by combining Eq.7 and Eq.29, taking $\frac{x}{s_0} = \frac{D}{\delta_l(t)}$ into account:

$$u_{l,0} = \frac{0.332\rho_{g,w}U_g^{\,2}}{\mu_l\sqrt{\dfrac{\rho_{g,w}U_g}{\mu_{g,w}}\left[\dfrac{D}{\delta_l(t)}\right]}}\sqrt{s_0}\,.$$

It demonstrates that, at a certain time, $u_{l,0}$ will increase when s_0 increases by increasing x. In particular, u_0 is associated with $\delta_l(t)$ when $s_0 = \delta_l(t)$ at $x = D$.

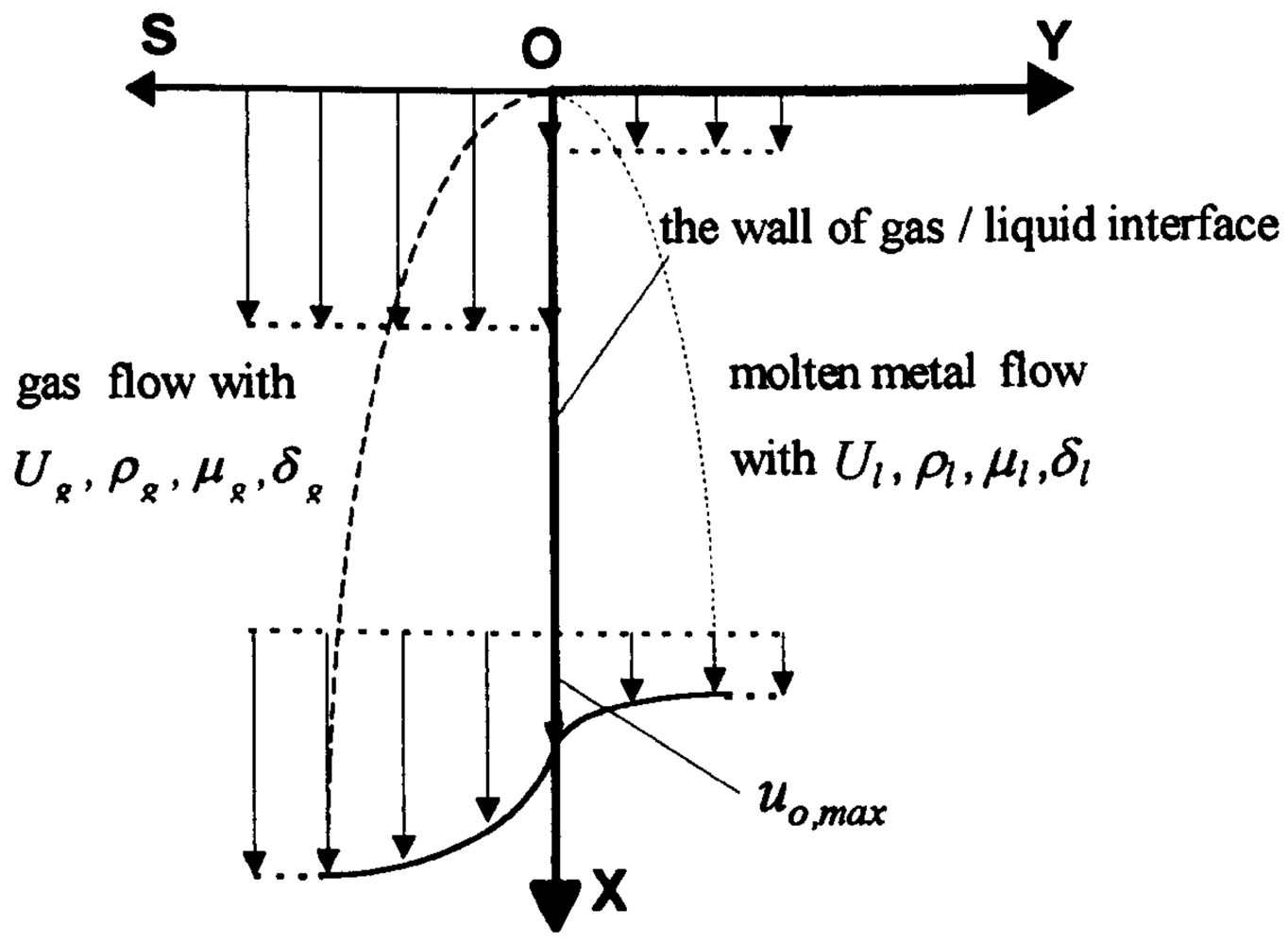

***Figure 12**. The momentum interaction of 2 parallel laminar boundary layer flows exists at the gas / liquid interface, by Lock [21]. They first meet at O with different velocities and 2 boundary layers develop, respectively. If x is long enough, there is "no slip" between the 2 flows; the interface velocity reaches to $u_{0,max}$*

For the 2 parallel laminar boundary layer flows in Fig.12, the theoretical solutions derived by Lock [21] are as follows, assuming that the "no slip" occurs if x is large enough:

$$\text{if } \lambda > 0, \text{ then } \frac{\delta}{\mu} = \left(\frac{1+\lambda}{2 \cdot \lambda \cdot \rho \cdot \mu}\right)^{\frac{1}{2}} \tag{34}$$

$$\text{if } \lambda = 0, \text{ then } \frac{\delta}{\mu} = (\rho \cdot \mu)^{\frac{-1}{3}} \tag{35}$$

$$\frac{u_{0,max}}{U_g} = c = \frac{\lambda + (\delta / \mu)}{1 + (\delta / \mu)} \tag{36}$$

where, in Eqs.34-36, $\delta = \frac{\delta_l}{\delta_g}$; $\lambda = \frac{U_l}{U_g}$; $\mu = \frac{\mu_l}{\mu_g}$; $\rho = \frac{\rho_l}{\rho_g}$.

δ_l, δ_g : the boundary layer thickness for the gas and the liquid, respectively;

U_l, U_g : the free stream velocity for the gas and the liquid, respectively;

μ_l, μ_g : the dynamic viscosity for the gas and the liquid, respectively;

ρ_l, ρ_g : the density for the gas and the liquid, respectively;

Taking $U_l = 0$ and thus $\lambda = 0$, It is seen that $\rho\mu >> 1$. By combining Eq.35 and Eq.36, the maximum interface velocity, $u_{0,max}$, where the "no slip" condition is reached, is derived:

$$u_{0,max} \cong U_g \cdot (\frac{1}{\rho \cdot \mu})^{\frac{1}{3}} = U_g \cdot (\frac{\rho_g \cdot \mu_g}{\rho_l \cdot \mu_l})^{\frac{1}{3}} \tag{37}$$

Eq.37 can be modified to take into account the influence of temperature on the properties of the gas:

$$u_{0,max} = U_g \cdot (\frac{\rho_{g,w} \cdot \mu_{g,w}}{\rho_l \cdot \mu_l})^{\frac{1}{3}} \tag{38}$$

The analogy between Eq.37 and Eq.38 is based on the assumption that the local physical properties at the gas / liquid interface would control the local skin friction law and the heat convection law when their variations occur*.

Eq.37 shows that $u_{0,max}$ only depends on the properties of the gas and liquid, and the free stream velocity of the gas. u_0 could reach to $u_{0,max}$ only if x is large enough that the "no slip" condition at that point is reached, along the gas / liquid interface. When $u_0 = u_{0,max}$, $\delta_l(t)$ will correspondingly reach to the maximum, $\delta_{l,max}$. By introducing Eq.32 and Eq.38 into Eq.33; taking $\delta_l(t) \neq 0$ into account, the possible range of $\delta_l(t)$ is derived:

* The assumption was intuitively made by Von Karman. The treatment by Lock for the 2 boundary layer flows assumes constant properties including temperature. By comparing the similarity of theoretical results between the Blasius' problem and the Howarth-Dorodnitsyn's problem as introduced in Section 4-1, the analogy between Eq.37 and Eq.38 is made to better describe the phenomenon where the physical properties of the gas would change, due to the high temperature at the gas / liquid interface.

$$0 < \delta_l(t) \leq \frac{1}{0.332}\sqrt{\frac{D}{U_g}}\frac{\rho_l^{(\frac{-1}{3})}\mu_l^{(\frac{2}{3})}}{\rho_{g,w}^{(\frac{1}{6})}\mu_{g,w}^{(\frac{1}{6})}} = \delta_{l,max} \tag{39}$$

It is seen that the analysis of the maximum surface velocity of molten metal layer, $u_{0,max}$, is necessary because $u_{0,max}$ will produce the maximum $\delta_l(t)$, by Eq.39. Although $\delta_l(t)$ is left variable with respect to time, it is essentially limited within the scope, $\delta_l(t) \in (0, \delta_{l,max}]$. As the boundary condition for $\delta_l(t)$, Eq.39 must be adhered to at each step of time evolution.

4-5. Evaluation of derived quantities

To complete this chapter, the derived quantities associated with the mechanism of the momentum interaction at the gas / liquid interface are evaluated based on the typical data in Appendices 1-3. The same data will be used for evaluations throughout Chapters 5-8 to maintain the consistency.

Maximum shear stress applied at the liquid side of the gas / liquid interface

The shear stress applied at the liquid side of the gas / liquid interface, $\tau_{l,w}$, is calculated by Eq.29. It is observed that $\tau_{l,w}$ only depends on the situation of the gas and varies with respect to x. At the bottom of the kerf, $x = D$,

$(\tau_{l,w})_{x=D} = 89.923 (N / m^2)$.

Heat cooling effect by the gas

The heat cooling rate by the gas, $\dot{e}_{cool}$, is calculated by Eq.31. Associated with $(\tau_{l,w})_x$, it only depends on the situation of the gas. Taking the boundary condition for $T_l(t)$ into account:

$$T_m \leq T_l(t) < T_v \tag{40}$$

$\dot{e}_{cool}$ is calculated by introducing Eq.40 into Eq.31:

$\dot{e}_{cool} \geq 17.06\,(W)$.

Maximum surface velocity of the liquid at the gas / liquid interface

The maximum surface velocity of the liquid at the gas / liquid interface, $u_{0,max}$, is only dependent on the properties of the gas and the liquid at the wall temperature, respectively. It is calculated by Eq.38:

$u_{0,max} = 2.43\,(m/s)$.

By Eq.33, the surface velocity of the liquid at the bottom of the kerf, u_0, is bounded:

$0 < u_0 \leq 2.43\,(m/s)$.

Maximum thickness of the molten metal layer

The thickness of the metallic liquid film at the bottom of the kerf, $\delta_l(t)$, is essentially associated with the local surface velocity of the liquid at the gas / liquid interface, u_0, by Eq.32. If u_0 reaches to $u_{0,max}$, $\delta_l(t)$ reaches to the maximum, correspondingly, by Eq.39:

$\delta_{l,max} = 0.105 \times 10^{-3}\,(m.)$.

By Eq.39, the boundary condition for $\delta_l(t)$ is:

$0 < \delta_l(t) \leq 0.105 \times 10^{-3}\,(m.)$.

Maximum removal rate of the liquid

The removal of the molten metal layer occurs at the bottom of the kerf. The removal rate, $\dot{m}_{out}$, is calculated by Eq.6'', taking $\delta_{l,max} = 0.105 \times 10^{-3}\,(m.)$:

$0 < \dot{m}_{out} \leq 2.014 \times 10^{-3}\,(kg/s)$.

4-6. Justification of theoretical treatment of liquid

The possible range of $\delta_l(t)$, e.g., $0 < \delta_l(t) \leq 0.105\,(mm)$, justifies heavily that the flow of the molten metal layer, in Chapter 3, has been treated as a quasi-shear-stress boundary-layer flow with linear velocity profiles at every section of the flow (except $x = 0$). The magnitude of $\delta_l(t)$ is also supported by several authors [2,3,5,8,10].

The fact that $\delta_l(t)$ in Y is far less than the average measured kerf width, w, in Z, certifies that the 2-D modelling, in X-Y plane, is very effective in describing the 3-D practical laser cutting system.

Chapter 5. Exothermic reaction between oxygen gas and metallic liquid

This chapter deals with the exothermic reaction mechanism between the oxygen gas and the molten metal liquid. It is generally realised that, in the oxygen jet gas assisted CO_2 laser cutting of mild steel, the energy of the exothermic reaction entering the molten metal layer, $\dot{e}_{exo}$, is at the same magnitude as the focused laser power [P.213, reference 1], [3,5] *. Two possible chemical reactions are analysed, i.e., between O_2 and liquid Fe with their product in liquid phase, and between O_2 and gaseous Fe with their product in gaseous phase. The former is studied based on the experimental findings by Powell et al [1,31,32]. The latter is investigated with the method of calculation derived by Dutta and Scott [P.84, reference 3], which is listed in Appendix 4. Comparing the calculated value of $\dot{e}_{exo}$ with the focused laser power, P_l, using the data in Appendixes 1-3, the exothermic energy generated due to the chemical reaction of O_2 and vapour Fe is disregarded.

For the chemical equilibrium identified, the enthalpy of reaction, $\Delta H|_T$, is calculated with Hess' principle using the respective heats of formation from standard tables [30]. $\Delta H|_T$ essentially depends on $T_l(t)$ at which the oxidisation occurs at the gas / liquid interface.

The mass rate of the molten metal entering exothermic reaction, $\dot{m}_{exo}$, is evaluated on the assumption that all the atoms of liquid Fe existing only at the surface of the molten metal layer, at the gas / liquid interface, are fully oxidised; the exothermic heat generated enters the metallic liquid.

* The conclusion is supported by the experimental test in Chapter 9: if the oxygen gas is replaced by inert gases such as argon, using the data in Appendix 1, there are no possible cuts at all, regardless of how slow the cutting velocity is adjusted. The result is shown in Fig.28

Knowing $\Delta H\big|_T$ and $\dot{m}_{exo}$, the energy rate of the exothermic reaction entering the molten metal layer, $\dot{e}_{exo}$, is calculated by $\dot{e}_{exo} = \Delta H\big|_{T_l} \times \dot{m}_{exo}$, which is essentially associated with $\delta_l(t)$ and $T_l(t)$.

Finally, the derived quantities are evaluated with the data in Appendices 1-3.

5-1. Mechanism of chemical reaction

5-1-1. Chemical reaction of O_2 and liquid Fe

The analyses based on the experimental work, introduced by Powell *, suggest that the type of oxidisation reaction in cutting mild steel is expressed by the chemical equilibrium:

$$\frac{1}{2} \times (O_2) + 1 \times \{Fe\} = 1 \times \{FeO\} + \Delta H\big|_T \qquad (41)$$

where, the symbol ( ) denotes the gaseous phase; { } the liquid phase. $\Delta H\big|_{T_l(t)}$ denotes the enthalpy of reaction at $T_l(t)$.

Eq.41 reflects the mechanism of the exothermic reaction between the O_2 and liquid Fe: the major product is FeO in liquid phase, rather than Fe_2O_3 or Fe_3O_4. With the theory of thermochemistry [35], $\Delta H\big|_{T_l(t)}$ is determined with the heats of formation for two reactants and one product. The heats of formation are thermochemical properties and temperature-dependent. Due to the high temperature of the chemical reaction, the chemical equilibrium is assumed to be established as soon as the fresh reactants meet each other.

* By collecting the oxidised material as it leaves the bottom of the cut zone, the wet chemical analyses for the ejected particles are carried out. The analysis indicates that FeO is the major constituent of the oxide. The details are referred to [P.211-213, Reference 1]

5-1-2. Chemical reaction of O_2 and vapour Fe

Assuming that the chemical reaction occurs between the O_2 and the saturated metallic vapour of Fe with the product of FeO in gaseous phase, the work by Dutta and Scott [3] is able to calculate the rate of exothermic heat from the reaction zone of gases into the molten metal layer. The chemical equilibrium is described, correspondingly,

$$\frac{1}{2}\times(O_2)+1\times(Fe)=1\times(FeO)+\Delta H\big|_T \qquad (42)$$

where, two reactants and one product are in gaseous phase, denoted by ( ). The enthalpy of reaction from this chemical reaction at $T_l(t)$, $\Delta H\big|_{T_l(t)}$, can be calculated.

By theoretically solving the laminar boundary layer governing equations for ideal gases (O_2, vapour Fe and vapour FeO) in chemical equilibrium, the rate of exothermic heat from the reaction zone of gases into the molten metal layer, $\dot{e}_{exo}$, is calculated. In this case, the quantity ($\dot{m}_{exo}$) is assumed to be sufficient to supply a concentration of Fe vapour for the chemical equilibrium with the maximum concentrations of the reactants (O_2, Fe), which can be diffused and convected through the boundary layer of the gas mixture from the external free stream to the interface of the gas mixture and the metallic liquid *.

The method of calculation derived by Dutta is listed in Appendix 4. Based on the data in Appendixes 1-3, the typical value of $\dot{e}_{exo}$ is calculated and analysed.

---

* The details are referred to the Method of Calculation, in Chapter 5.6 in Dutta's PhD thesis [3]

5-2. Enthalpy of reaction

As analysed in Section 5-1-1, the enthalpy of reaction for the chemical equilibrium shown in Eq.41, $\Delta H\big|_{T_l(t)}$, only depends on the heats of formation for three participants at the reaction temperature of $T_l(t)$. It is calculated by Hess' principle [P.6, reference 30].

The heats of formation at the reference temperature, $T = 298\,(^oK)$, are listed below each participants with the original units [Table A, reference 30]:

$$\frac{1}{2} \times (O_2) + 1 \times \{Fe\} = 1 \times \{FeO\} + \Delta H\big|_T$$

heat of formation at $T = 298\,(^oK)$: $\quad 0 \qquad 0 \qquad -63.2$

units: $kCal / mole$

By Hess' principle, $\Delta H\big|_T$ at $T = 298\,(^oK)$ is calculated:

$$\Delta H\big|_{298K} = 1 \times (-63.2) - \frac{1}{2} \times (0) - 1 \times (0) = -63.2 \ (kCal / mole\ of\ Fe)$$

$$= -4.74 \times 10^6 \ (J / kg\ of\ Fe) \tag{43}$$

where, the negative sign means that the chemical reaction system releases energy.

$\Delta H\big|_{T_l(t)}$ at $T_l(t) \geq 1800\,(^oK)$, is modified by Kirchhoff's equation, knowing $\Delta H\big|_{298K}$ in Eq.43 [P.9, reference 30]:

$$\Delta H\big|_{T_l(t)} = \Delta H\big|_{298K} + \int_{298}^{T_l(t)} \Delta C_p \cdot dT \tag{44}$$

where, ΔC_p is defined for the chemical equilibrium in Eq.41:

$$\Delta C_p = 1 \times C_p(FeO) - \frac{1}{2} \times C_p(O_2) - 1 \times C_p(Fe) \tag{45}$$

where, the heat capacities for 3 participants are (Tables C1, C2 in reference 30):

for Fe, $C_p(Fe) = 8.873 + 1.474 \times 10^{-3} \times T - 56.92 \times T^{\frac{-1}{2}}$ $(Cal / mole\ ^oK)$;

for O_2, $C_p(O_2) = 7.16 + 1.0 \times 10^{-3} \times T - 0.4 \times 10^5 \times T^{-2}$ $(Cal / mole\ ^oK)$;

for FeO, $C_p(FeO) = 11.66 + 2.0 \times 10^{-3} \times T - 0.67 \times 10^5 \times T^{-2}$ $(Cal / mole\ ^oK)$;

By contributing the data above into Eq.45, ΔC_p is discovered:

$$\Delta C_p = -0.795 + 0.026 \times 10^{-3} \times T - 0.47 \times 10^5 \times T^{-2} + 56.92 \times T^{\frac{-1}{2}} \qquad (45')$$

Combining Eq.45' and Eq.44 gives:

$$\Delta H\Big|_{T_l(t)} = -4.74 \times 10^6 + \int_{298}^{T_l(t)} (-59.586 + 1.945 \times 10^{-3} T - 35.227 \times 10^5 T^{-2} + 4266.211 T^{-0.5})dT \qquad (46)$$

where, the unit is: $J / kg\ of\ Fe$; the result in negative value denotes the oxidisation releases the heat. Eq.46 shows that $\Delta H\Big|_{T_l(t)}$ is essentially temperature-dependent *.

* Let $T_l = 2000\ (^oK)$, for example, $\Delta H\Big|_{2000K} = -4.613 \times 10^6\ (J / kg\ of\ Fe)$. This result is supported by that recommended by Powell [P.213, reference 1], where $\Delta H\Big|_{2000K} = -4.612 \times 10^6\ (J / kg\ of\ Fe)$.

5-3. Mass rate of the molten metal entering exothermic reaction

For the chemical equilibrium, by Eq.41, identified for the oxidisation mechanism in the cutting system, the molten metal entering the exothermic reaction must be part of the iron removed from the cut zone. This fact can be mathematically interpreted as:

$$\dot{m}_{exo} = k_{exo} \cdot \dot{m}_{out} \quad , \; 0 < k_{exo} \leq 1 \tag{47}$$

where, $\dot{m}_{exo}$: the mass rate of the molten metal entering the exothermic reaction;

$\dot{m}_{out}$: the mass rate of the molten metal flowing out of the CV , as shown in Fig.9;

By contributing $\dot{m}_{out}$, by Eq.6'' in Chapter 4, into Eq.47, $\dot{m}_{exo}$ is associated with $\delta_l(t)$ and k_{exo} :

$$\dot{m}_{exo} = k_{exo} \cdot \left(0.166 \frac{w\rho_l}{\mu_l} \frac{\rho_{g,w} U_g^{\,2}}{\sqrt{\rho_{g,w} U_g D / \mu_{g,w}}} \right) \cdot \left[\delta_l(t) \right]^2 \tag{47'}$$

In Eq.47 or Eq.47', k_{exo} is still an unknown variable; it is expected to be associated with the 5 time-dependent variables, essentially *.

---

* As a first approximation, Powell [P.213, reference 1] evaluated the oxidisation heat, $\dot{e}_{exo} = \Delta H\big|_{T_l} \times \dot{m}_{exo}$, with $\dot{m}_{exo} = \frac{\dot{m}_{out}}{2}$, by assuming $k_{exo} = 0.5$. Scientifically, for the dynamic modelling in this thesis, $\dot{m}_{exo}$ is derived to be time-dependent.

It is intended to directly derive the relationship between $\dot{m}_{exo}$ and the 5 time-dependent variables, e.g., $\delta_l(t)$, as follows.

Assuming that the oxidisation only occurs at the surface of the molten metal layer, that is, only the atoms of liquid Fe existing at the surface of the molten metal layer have chances to meet fresh oxygen molecules, it is seen that $\dot{m}_{exo}$ is proportional to the average surface velocity of the molten metal layer, $\overline{u}_{l,0}$, at the gas / liquid interface *:

$$\dot{m}_{exo} \propto \overline{u}_{l,0} \tag{48}$$

The local surface velocity of molten metal layer at the gas / liquid interface, $u_{l,0}$, varies with x; this has been derived in the footnote in Page 37, i.e.,

$$u_{l,0} = \frac{0.332\rho_{g,w}U_g^{\,2}}{\mu_l\sqrt{\frac{\rho_{g,w}U_g}{\mu_{g,w}}\left[\frac{D}{\delta_l(t)}\right]}}\sqrt{s_0} = \frac{0.332\rho_{g,w}U_g^{\,2}}{\mu_l\sqrt{\frac{\rho_{g,w}U_g}{\mu_{g,w}}\cdot\left[\frac{D}{\delta_l(t)}\right]}}\sqrt{x} \text{ , and } \frac{x}{s_0} = \frac{D}{\delta_l(t)} \tag{49}$$

$\overline{u}_{l,0}$ is defined as:

$$\overline{u}_{l,0} = \frac{1}{D}\int_0^D u_{l,0}dx \tag{50}$$

* For the extremely thin layer of thickness $l_{surface}$, up to the magnitude of the atomic diameter of iron, at the liquid surface, its average velocity is $\overline{u}_{l,0}$. $\dot{m}_{exo}$ is calculated: $\dot{m}_{exo} = (w\, l_{surface}\, \rho_l)\,\overline{u}_{l,0}$. The assumption that the oxidisation only occurs at the surface of molten metal layer yields: $l_{surface}$ = atomic diameter of iron. In this case, $\dot{m}_{exo}$ is proportional to $\overline{u}_{l,0}$.

Contributing Eq.49 into Eq.50 and letting $u_{l,0} = u_0$ when $x = D$, $\overline{u}_{l,0}$ is related to u_0 :

$$\overline{u}_{l,0} = \frac{2}{3} u_0 \tag{51}$$

Combining Eq.48 and Eq.51 yields:

$$\dot{m}_{exo} \propto \overline{u}_{l,0} \propto u_0 \tag{52}$$

Eq.52 shows that $\dot{m}_{exo}$ is proportional to the surface velocity of the molten metal layer at the bottom of the gas / liquid interface, u_0. Further, u_0 is in linear relation with the local thickness of the molten metal layer, $\delta_l(t)$, as is proved by letting $u_{l,0} = u_0$ when $x = D$, by Eq.49. So, $\dot{m}_{exo}$ can be found to be proportional to $\delta_l(t)$, eventually,

$$\dot{m}_{exo} \propto u_0 \propto \delta_l(t) \tag{53}$$

Eq.53 can be mathematically interpreted as follows, by introducing the constant, C_{exo},

$$\dot{m}_{exo} = C_{exo} \cdot \delta_l(t) \tag{53'}$$

where, C_{exo} is defined as the combustion efficiency coefficient. Keeping in mind that C_{exo} is essentially a time-independent constant, the significance and the calculation of C_{exo} are discussed in the next section. As soon as C_{exo} is determined, the mass rate of the molten metal entering the exothermic reaction, $\dot{m}_{exo}$, can be directly related to $\delta_l(t)$, by Eq.53'.

5-4. Significance of combustion efficiency coefficient, C_{exo}

By Eq.53', the combustion efficiency coefficient, C_{exo}, holds two characteristics. On one hand, C_{exo} must satisfy the dynamic energy balance around the molten metal layer (Eq.9) with respect to time, through $\dot{m}_{exo}$. When the energy balance starts with the specific initial conditions for the 5 time-dependent variables, C_{exo} is correspondingly determined at the start of time. Therefore, it is initial-condition-dependent. On the other hand, C_{exo} stays the same with respect to time after it is determined by the given initial conditions. Essentially, in conclusion, C_{exo} is an initial-condition-dependent, time-independent variable for the cutting system*. The nature of C_{exo} makes the treatment for it different from the other time-independent variables, listed in Appendixes 1-3.

Knowing the method to calculate C_{exo}, $\dot{m}_{exo}$ is associated with $\delta_l(t)$, by Eq.53'. The derivation process is independent of the definition of k_{exo}, in Eq.47'. The interest may be further to answer the question raised at the beginning of this section: how k_{exo} can be evaluated if Eq.47 or Eq.47' is used to calculate $\dot{m}_{exo}$**.

This is carried out by comparing Eq.53' with Eq.47' to relate k_{exo} to C_{exo} and $\delta_l(t)$:

---

* Being an initial-condition-dependent, time-independent variable, C_{exo} is mathematically determined as: for dynamic energy balance, in Eq.9, which is generalised as:
$\frac{dT_l(t)}{dt} = F_{T_l}\left(C_{exo},\ \delta_l(t),\ T_l(t),\ V_e(t),\ y(t),\ P_{l,abs}(t)\right)$, where F_{T_l} represents the derived function by Eq.9.
Letting $\frac{dT_l(t)}{dt} = 0$ for the given initial condition: $\delta_l(0),\ T_l(0),\ V_e(0),\ y(0)$ and $P_{l,abs}(0)$, C_{exo} can be calculated. Keeping this value constant in each step of time evolution, the differential governing equations including the energy equation can be numerically solved for the 5 time-dependent variables. The details are referred to in Chapter 8

** Conceptually, Eq.47 is easy to understand: $\dot{m}_{exo}$ is only part of $\dot{m}_{out}$ and k_{exo} simply means the ratio of $\dot{m}_{exo}$ to $\dot{m}_{out}$. This concept has always been used in major research [1,2,7,23], where, as a first approximation, taking a certain value for k_{exo}, e.g., $k_{exo} = 0.5$ by Powell [P.213, reference 1], is the usual way to calculate $\dot{m}_{exo}$ and thus $\dot{e}_{exo}$.

$$k_{exo}\delta_l(t) = C_{exo} \cdot \left(0.166 \frac{w\rho_l}{\mu_l} \frac{\rho_{g,w} U_g^{\ 2}}{\sqrt{\rho_{g,w} U_g D / \mu_{g,w}}} \right)^{-1} \tag{54}$$

In Eq.54, the right side of the equation is a new time-independent variable, which can be determined as soon as the cutting system starts from the initial dynamic balances. It can be concluded that k_{exo}, by Eq.47', is inversely proportional to the thickness of the molten metal layer, $\delta_l(t)$. For the steady-state modelling, e.g., in the previous work [1,2,3,5,23], taking $\delta_l(t)$ as time-independent variable yields constant k_{exo}, with respect to time. In this case, k_{exo} can still be calculated by Eq.54.

5-5. Exothermic reaction energy release, $\dot{e}_{exo}$

It is intended in this thesis to use C_{exo} to calculate the rate of exothermic reaction energy release, $\dot{e}_{exo}$, rather than k_{exo}. Combining Eq.46 and Eq.53' yields,

$$\begin{aligned} \dot{e}_{exo} &= \Delta H\big|_{T_l(t)} \times \dot{m}_{exo} \\ &= C_{exo} \times \delta_l(t) \times [-4.74 \times 10^6 + \\ &\int_{298}^{T_l(t)} (-59.586 + 1.945 \times 10^{-3} T - 35.227 \times 10^5 T^{-2} + 4266.211 T^{-0.5}) dT] \quad (W.) \end{aligned} \tag{55}$$

where, $\dot{e}_{exo}$ is in the unit of watt. Eq.55 shows that $\dot{e}_{exo}$ is essentially associated with 2 time-independent variables, $\delta_l(t)$ and $T_l(t)$. It is to be contributed into Eq.9.

5-6. Evaluation of derived quantities

At the completion of this chapter, the derived quantities associated with the mechanism of the oxidisation reaction at the gas / liquid interface are evaluated, based on the typical data in Appendices 1-3. Some data evaluated in Chapter 4-5 are used.

Enthalpy of reaction

The enthalpy of reaction, $\Delta H\big|_{T_l(t)}$, for the chemical equilibrium in Eq.41,

$$\frac{1}{2}\times(O_2)+1\times\{Fe\}=1\times\{FeO\}+\Delta H\big|_T$$

is calculated by Eq.46,

$$\Delta H\big|_{T_l(t)} = -4.74\times10^6 + \int_{298}^{T_l(t)}(-59.586+1.945\times10^{-3}T-35.227\times10^5\,T^{-2}+4266.211T^{-0.5})dT$$

at $T_l(t)=T_m=1808\ (^oK)$, $\Delta H\big|_{T_l(t)} = 4.621\times10^3$

at $T_l(t)=1900\ (^oK)$, $\Delta H\big|_{T_l(t)} = 4.621\times10^3$

at $T_l(t)=2000\ (^oK)$, $\Delta H\big|_{T_l(t)} \le 4.613\times10^3$

at $T_l(t)=2100\ (^oK)$, $\Delta H\big|_{T_l(t)} \le 4.609\times10^3$

at $T_l(t)=2200\ (^oK)$, $\Delta H\big|_{T_l(t)} \le 4.606\times10^3$

at $T_l(t)=2300\ (^oK)$, $\Delta H\big|_{T_l(t)} \le 4.602\times10^3$

...

It is seen that, although $\Delta H\big|_{T_l(t)}$ is temperature-dependent, the variation of $\Delta H\big|_{T_l(t)}$ at $T_l(t) = 1808 - 2300\ (^oK)$ is negligible in comparison with the base value of $\Delta H\big|_{T_l(t)}$. It is thus precise enough to take:

$$\Delta H\big|_{T_l(t)} = \Delta H\big|_{2000K} = -4.613 \times 10^6\ (J / kg\ of\ liquid\ Fe) \qquad (46')$$

when $T_l(t)$ practically varies around $2000\ (^oK)$. Eq.46' is to be used in calculating $\dot{e}_{exo}$, instead of Eq.46.

Mass rate of the molten metal entering exothermic reaction

The mass rate of the molten metal entering exothermic reaction, $\dot{m}_{exo}$, can be calculated by either Eq.47' through k_{exo}, or by Eq.53' through C_{exo}. The relation of k_{exo} and C_{exo} is by Eq.54. Because of the nature of C_{exo} (initial-condition-dependent, time-independent), the intention here is to evaluate the maximum $\dot{m}_{exo}$ by Eq.47':

$$\dot{m}_{exo} = k_{exo} \cdot \left(0.166 \frac{w\rho_l}{\mu_l} \frac{\rho_{g,w} U_g^{\ 2}}{\sqrt{\rho_{g,w} U_g D / \mu_{g,w}}} \right) \cdot \left[\delta_l(t)\right]^2 , \quad 0 < k_{exo} \le 1$$

Letting $k_{exo} = 1$ and $\delta_l(t) = \delta_{l,max} = 0.105 \times 10^{-3}\ (m.)$, from Section 4-5; using the other data in Appendixes 1-3, the maximum $\dot{m}_{exo}$ is:

$0 < \dot{m}_{exo} \le 2.014 \times 10^{-3}\ (kg / s)$

Exothermic reaction energy release

The exothermic reaction energy release, $\dot{e}_{exo}$, is calculated by Eq.55:

$$\dot{e}_{exo} = \Delta H\big|_{T_l(t)} \times \dot{m}_{exo}$$

Taking $0 < \dot{m}_{exo} \leq 2.014 \times 10^{-3}\ (kg / s)$ and

$\Delta H\big|_{T_l(t)} = \Delta H\big|_{2000K} = -4.613 \times 10^{6}\ (J / kg\ of\ liquid\ Fe)$, by Eq.46',

into account, $\dot{e}_{exo}$ is:

$0 < \dot{e}_{exo} \leq 9.29 \times 10^{3}\ (W.)$

5-7. Justification of theoretical treatment of oxidisation reaction

The exothermic reaction mechanism between the oxygen gas and the molten metal liquid has been analysed for two possible chemical reactions, i.e.,

$$\frac{1}{2} \times (O_2) + 1 \times \{Fe\} = 1 \times \{FeO\} + \Delta H\big|_T \qquad (41)$$

and,

$$\frac{1}{2} \times (O_2) + 1 \times (Fe) = 1 \times (FeO) + \Delta H\big|_T \qquad (42)$$

For Eq.41, the calculation with the typical data shows that, when $k_{exo} = 1$, the maximum value of $\dot{e}_{exo}$ could reach $9.29 \times 10^{3}\ (W.)$. k_{exo} is essentially variable with $\delta_l(t)$; it can be determined by the introduction of C_{exo} which is initial-condition-dependent but time-independent. The determination of C_{exo} will be shown in Chapter 8. Variable k_{exo} makes it possible for $\dot{e}_{exo}$ to be within the magnitude of P_l, as expected.

For Eq.42, the calculated results listed in Appendix 4 suggest that the oxidisation heat generated due to the chemical reaction of O_2 with vapour Fe can be ignored.

Chapter 6. Energy loss from liquid into solid

The energy loss from the molten metal layer into the substrate solid, along the liquid / solid interface, is studied in this chapter. In a practical laser cutting system, it is responsible for the phenomenon of heat affected zone (HAZ). In the physical model in Fig.9, the rate of the energy loss at the liquid / solid interface is denoted as $\dot{e}_{loss}$.

The mechanism of the heat transfer at the liquid / solid interface is analysed, i.e., how the heat flow goes from the surface of the liquid at $T_l(t)$, at the gas / liquid interface, into the surface of the solid at T_m, at the liquid / solid interface. The theories of heat conduction and heat convection are applied. The calculation of $\dot{e}_{loss}$ is carried out based on the heat convection theory for boundary layer flows, rather than the heat conduction theory. Several calculating methods based on the moving heat source theory, which is essentially related to the heat conduction in solids, are listed in Appendix 5 for reference. The justification of the theoretical treatment of the energy loss at the liquid / solid interface is made by comparing the calculating results of $\dot{e}_{loss}$ with the typical data listed in Appendixes 1-3.

6-1. Heat transfer mechanism at liquid / solid interface

The heat transfer from the molten metal layer into the substrate solid at the liquid / solid interface is shown in Fig.13, where, in X-O-Y system, the flow of the molten metal layer has been taken as a quasi-shear-stress boundary layer flowing over the "flat plate" made of substrate metallic solid at T_m in Chapter 3-2. On the left side of the liquid / solid interface, the heat is convected to the liquid / solid interface due to the temperature difference of $\left[T_l(t) - T_m\right]$, identified as $\dot{e}_{conv}$. On the right side of the liquid / solid interface, the same amount of heat is conducted from the interface into the infinity due to the temperature difference of $\left[T_m - T_a\right]$, identified as $\dot{e}_{cond}$.

Although the heat transfer mechanisms on two sides of the liquid / solid interface are different, their relationship can be ascertained by Newton's law:

at $y = 0$, $T = T_m$,

$$\dot{e}_{conv} = \dot{e}_{cond} = -(wD)K_s(\frac{dT}{dy})_{y=0} \tag{56}$$

Eq.56 states that the total heat convected from the gas / solid interface to the liquid / solid interface is due to conduction in the solid. $\dot{e}_{loss}$ is thus calculated as:

$$\dot{e}_{loss} = \dot{e}_{conv} = \dot{e}_{cond} = -(wD)K_s(\frac{dT}{dy})_{y=0} \quad \text{at } y = 0 \tag{57}$$

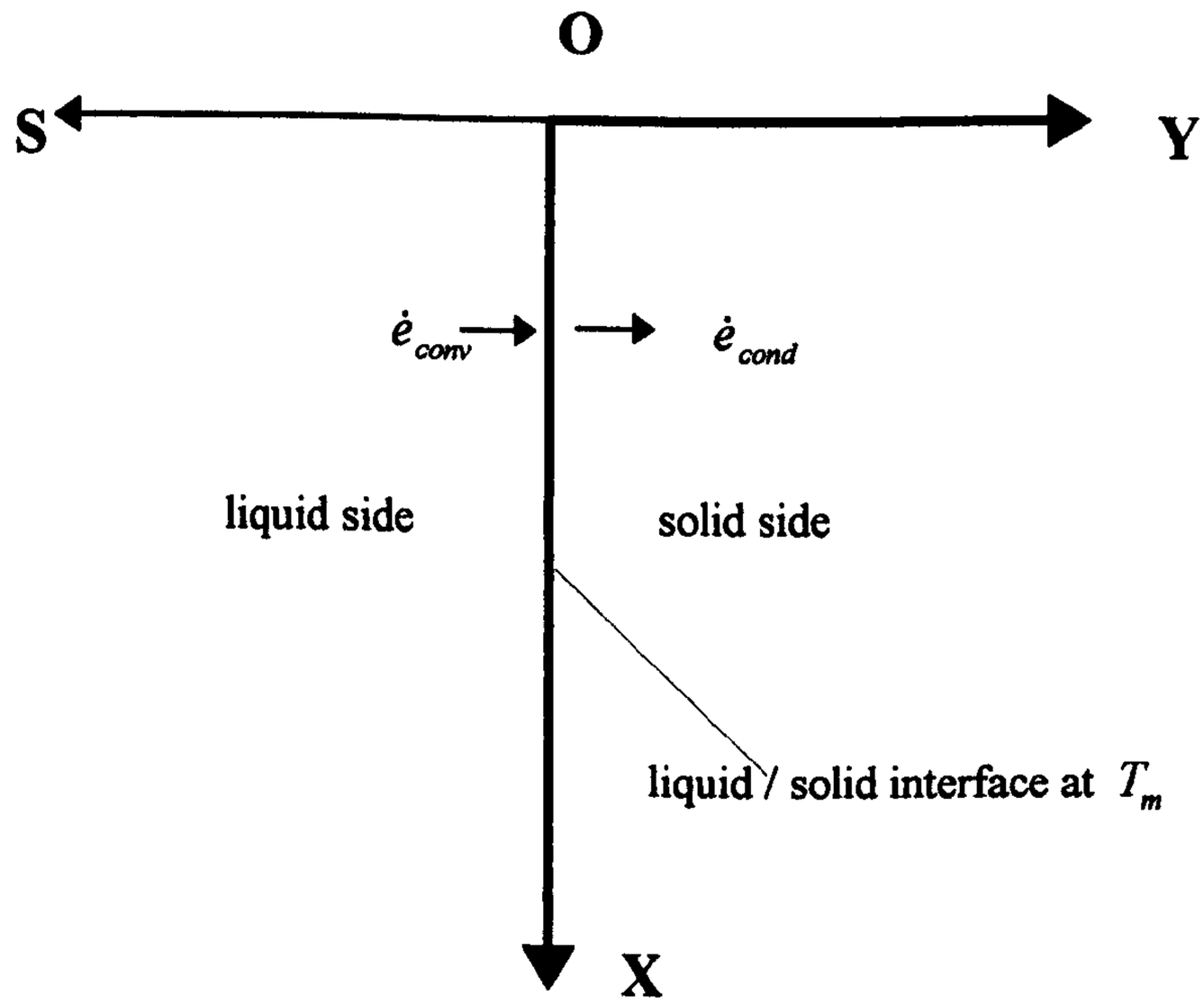

Figure 13. *The heat transfer mechanisms on two sides of the liquid / solid interface are different: on the left side, the heat convection exists; on the right side, the heat conduction exists. At* $y = 0$, $\dot{e}_{loss} = \dot{e}_{conv} = \dot{e}_{cond}$

It is noted that, if one tries to calculate $\dot{e}_{loss}$ by analysing $\dot{e}_{cond}$, it is crucial to evaluate $(\frac{dT}{dy})$ at $y = 0$ carefully. In this chapter, $\dot{e}_{conv}$ is analysed, instead, taking the molten metal

layer as a quasi-shear-stress boundary layer flow. In this case, $\dot{e}_{loss}$ can be discovered by Eq.57.

6-2. Heat convection from metallic liquid flow into substrate solid

In X-O-S co-ordinate system in Fig.13, taking the flow of molten metal layer as a quasi-shear-stress boundary layer flow over the "flat plate" made of the substrate solid, the local heat transfer coefficient, $(c_h)_{l,w}$, is calculated by the modified Reynolds' analogy *:

$$(c_h)_{l,w} = (\frac{c_f}{2})'_{l,w}[(Pr)_l]^{(-2/3)} = \frac{0.332}{\sqrt{\rho_l \bar{u}_{l,0} x / \mu_l}}(\frac{\mu_l c_{p,l}}{K_l})^{(-2/3)} \quad (58)$$

where, $(\frac{c_f}{2})'_{l,w}$: the local skin friction coefficient, applied at the liquid side of the liquid / solid interface, $(\frac{c_f}{2})'_{l,w} = \frac{0.332}{\sqrt{\rho_l \bar{u}_{l,0} x / \mu_l}}$;

$(Pr)_l$: Prandtl number for the liquid, $(Pr)_l = (\frac{\mu_l c_{p,l}}{K_l})$;

$\bar{u}_{l,0}$: the average value of $u_{l,0}$ along X, $\bar{u}_{l,0} = \frac{2}{3}u_0$ by Eq.51 **;

ρ_l : the density of liquid at around T_m;

K_l : the heat conductivity of liquid at around T_m;

$c_{p,l}$: the specific heat of liquid at around T_m;

---

* The characteristics of this liquid boundary layer are described by the governing differential equations of mass, momentum and energy. Similar to the treatment of gaseous boundary layer, introduced in Chapter 4, Blasius' solutions are applied, which concern the laminar boundary layer with constant physical properties (density and viscosity) [P.8-56, reference 20]

** $\bar{u}_{l,0}$ is, by the definition, taken as the reference velocity for the liquid boundary layer flow; normally, it is taken as the maximum velocity of the flow at the edge of the boundary layer [P.8-56, reference 20].

By the definition, the flux of heat convection from the liquid boundary layer to the wall of liquid / solid interface is:

$$\dot{q}_{l,w} = \frac{0.332\rho_l \bar{u}_{l,0} c_{p,l}[T_l(t) - T_m]}{\sqrt{\rho_l \bar{u}_{l,0} x / \mu_l}} \left(\frac{\mu_l c_{p,l}}{K_l}\right)^{(-2/3)} \tag{59}$$

where, $T_l(t)$: the surface temperature of molten metal layer at the gas / liquid interface;

T_m : the temperature of fusion of liquid at around p_a, $T_m = 1808\,(^0K)$;

The rate of heat convection, $\dot{e}_{conv}$, is thus evaluated by integrating Eq.59 along the kerf depth in X:

$$\dot{e}_{conv} = \int_0^D \dot{q}_{l,w}(w \cdot dx) = 0.664 \frac{w\rho_l \bar{u}_{l,0} c_{p,l}[T_l(t) - T_m]}{\sqrt{(\rho_l \bar{u}_{l,0})/(D\mu_l)}} \left(\frac{\mu_l c_{p,l}}{K_l}\right)^{(-2/3)} \tag{60}$$

Combining $\dot{e}_{conv}$ by Eq.60 and $\bar{u}_{l,0} = \frac{2}{3}u_0$ by Eq.51 into Eq.57, $\dot{e}_{loss}$ is thus derived,

$$\dot{e}_{loss} = 0.664\sqrt{\frac{2}{3}} \frac{w\rho_l u_0 c_{p,l}[T_l(t) - T_m]}{\sqrt{(\rho_l u_0)/(D\mu_l)}} \left(\frac{\mu_l c_{p,l}}{K_l}\right)^{(-2/3)} \tag{57'}$$

As the surface velocity of the molten metal layer at the bottom of gas / liquid interface, u_0 , is essentially associated with $\delta(t)$, by Eq.32,

$$u_0 = \frac{0.332\rho_{g,w} U_g^{\,2}}{\mu_l \sqrt{\frac{\rho_{g,w} U_g D}{\mu_{g,w}}}} \delta_l(t) \tag{32}$$

Combining Eq.32 and Eq.57' yields,

$$\dot{e}_{loss} = 0.312 w D^{\frac{1}{4}} \left[\rho_l^{\frac{1}{2}} c_{p,l} \left(\frac{\mu_l c_{p,l}}{K_l}\right)^{\frac{-2}{3}}\right] \left[\rho_{g,w}\mu_{g,w} U_g^3\right]^{\frac{1}{4}} \left[T_l(t) - T_m\right] \sqrt{\delta_l(t)} \tag{57''}$$

Eq.57'' shows that $\dot{e}_{loss}$ is essentially associated with 2 time-dependent variables, $\delta_l(t)$ and $T_l(t)$. It will be used and contributed into Eq.9 in Chapter 8.

6-3. Evaluation of derived quantities

In this section, the derived quantities associated with the mechanism of heat convection on the liquid side at the liquid / solid interface are evaluated, using the typical data in Appendices 1-3. The derived quantities associated with the mechanism of heat conduction on the solid side at the liquid / solid interface can be referred to in Appendix 5, using the same typical data.

The rate of energy loss from the molten metal layer into the substrate solid, $\dot{e}_{loss}$ $(W.)$, is calculated by Eq.57'':

$$\dot{e}_{loss} = 0.312wD^{\frac{1}{4}}\left[\rho_l^{\frac{1}{2}}c_{p,l}\left(\frac{\mu_l c_{p,l}}{K_l}\right)^{\frac{-2}{3}}\right]\left[\rho_{g,w}\mu_{g,w}U_g^3\right]^{\frac{1}{4}}\left[T_l(t)-T_m\right]\sqrt{\delta_l(t)}$$

The typical data from Appendices 1-3 are listed as follows:

$w = 2\times10^{-3}\,(m.)$; $D = 6\times10^{-3}\,(m.)$;

$\rho_l = 7.86\times10^{3}\,(kg/m^3)$; $c_{p,l} = 664.8\,(J/kg\cdot{}^oK)$;

$\mu_l = 3.9\times10^{-3}\,(N\cdot s/m^2)$; $K_l = 41.8\,(W/m\cdot{}^oK)$;

$\mu_{g,w} = 7.03\times10^{-5}\,(N\cdot s/m^2)$;

$U_g = 301.6\,(m/s)$;

$\rho_{g,w} = 0.228\,(kg/m^3)$ at $T_m = 1808\,(^0K)$;

Taking $T_l(t) = 2000\,(^0K)$; $\delta_{l,max} = 0.105\times10^{-3}\,(m.)$, in Chapter 4-5; $\dot{e}_{loss}$ is discovered: $\dot{e}_{loss} = 589.2\ (W.)$.

$\dot{e}_{loss}$ is discovered: $\dot{e}_{loss} = 589.2\ (W.)$.

It is noted that, when $0 < \delta_l(t) \leq \delta_{l,max}$ and $T_l(t)$ varies around $2000\ (^0K)$, with respect to time, $\dot{e}_{loss}$ is the same magnitude as the focused laser power, $P_l = 800\,(W)$.

6-4. Justification of theoretical treatment of heat transfer at liquid / solid interface

The analyses of the mechanisms of heat transfer through the liquid / solid interface, making the heat loss ($\dot{e}_{loss}$) unavoidable, suggest that $\dot{e}_{loss}$ can be approached by calculating $\dot{e}_{conv}$, due to the heat convection on the liquid side at the liquid / solid interface, or calculating $\dot{e}_{cond}$, due to the heat conduction on the solid side at the liquid / solid interface. In previous research [3,5,23,35], the heat conduction characteristics are focused. The calculating methods are usually associated with the moving heat source theory [33,34].

As shown in Appendix 5, the fundamental theory derived by Carslaw and Jaeger [Section 10.7, reference 34], in X-O-Y in Fig.13,

$$T_{(y)} = \frac{\dot{e}_{loss}}{2\pi K_s D} \cdot exp(\frac{V_e y}{2k_s}) \cdot K_0(\frac{V_e y}{2k_s}) \quad \text{when } y \neq 0 \qquad \text{(A5-3)}$$

requires $y \neq 0$, mathematically. Physically, however, its application requires that: $T_{(y \to 0)} = T_m$, in Eq.A5-3, because T_m only exists at the liquid / solid interface, i.e., $y = 0$.

For this reason, the calculation of $\dot{e}_{loss}$ in this thesis is carried out by evaluating $\dot{e}_{conv}$. The test of $\dot{e}_{loss}$ with the typical data in Appendices 1-3, by Eq.57'', supports the reasonability of the theoretical treatment, simply by comparing $\dot{e}_{loss} = 589.2\ (W.)$ with $P_l = 800\,(W)$.

Chapter 7. Dynamic absorption of laser power

In this chapter, the dynamic absorption of the laser power (P_l) by the workpiece, identified as $P_{l,abs}(t)$, is studied by analysing the relative displacement between the laser beam front and the fusion front at the liquid / solid interface, identified as $y(t)$. In the theoretical laser cutting system, as shown in Fig.9, $y(t)$ can vary with respect to time, simply because there is no physical bond between the laser beam at V_c and the fusion front velocity at $V_e(t)$. The analyses of the mechanism of dynamic absorption of laser power are thus to identify the interrelations of the time-dependent variables, i.e., $P_{l,abs}(t)$, $y(t)$, $V_e(t)$, assuming that P_l and V_c are constant with respect to time, respectively.

The ideal 3-D laser power with Gaussian profile is transformed into the 2-D model to fit the interest in X-O-Y plane: along Y, the power intensity is in Gaussian profile; along Z, it is even, as shown in Fig.9.

The derived quantities are tested with the typical data in Appendices 1-3. The theoretical treatment of $P_{l,abs}(t)$, $y(t)$ and $V_e(t)$ will be analysed in comparison with the steady-state analyses in previous work.

7-1. Mechanism of dynamic absorption of laser power

The "non-contact" interaction between the focused laser beam and the workpiece can be shown in Fig.14. If P_l is constant, the absorption of the laser power, $P_{l,abs}$, depends on the absorptivity *of the heated workpiece to the CO_2 laser light of wavelength $10.6\,\mu m.$, and the intersecting area of the laser beam and the workpiece.

* Experiments show that the absorptivity of mild steel to CO_2 laser light increases when the surface temperature gets higher: it is only *3%* at room temperature, showing extremely high reflectivity to the laser light; At $T_m = 1808(^{\circ}K)$, it goes up to the greatest, *97%* [1,25]

Assuming the absorptivity of mild steel at T_m is unity, it is seen that $P_{l,abs}$ only depends on the intersecting area of the laser beam and the workpiece, as shown in Fig.14.

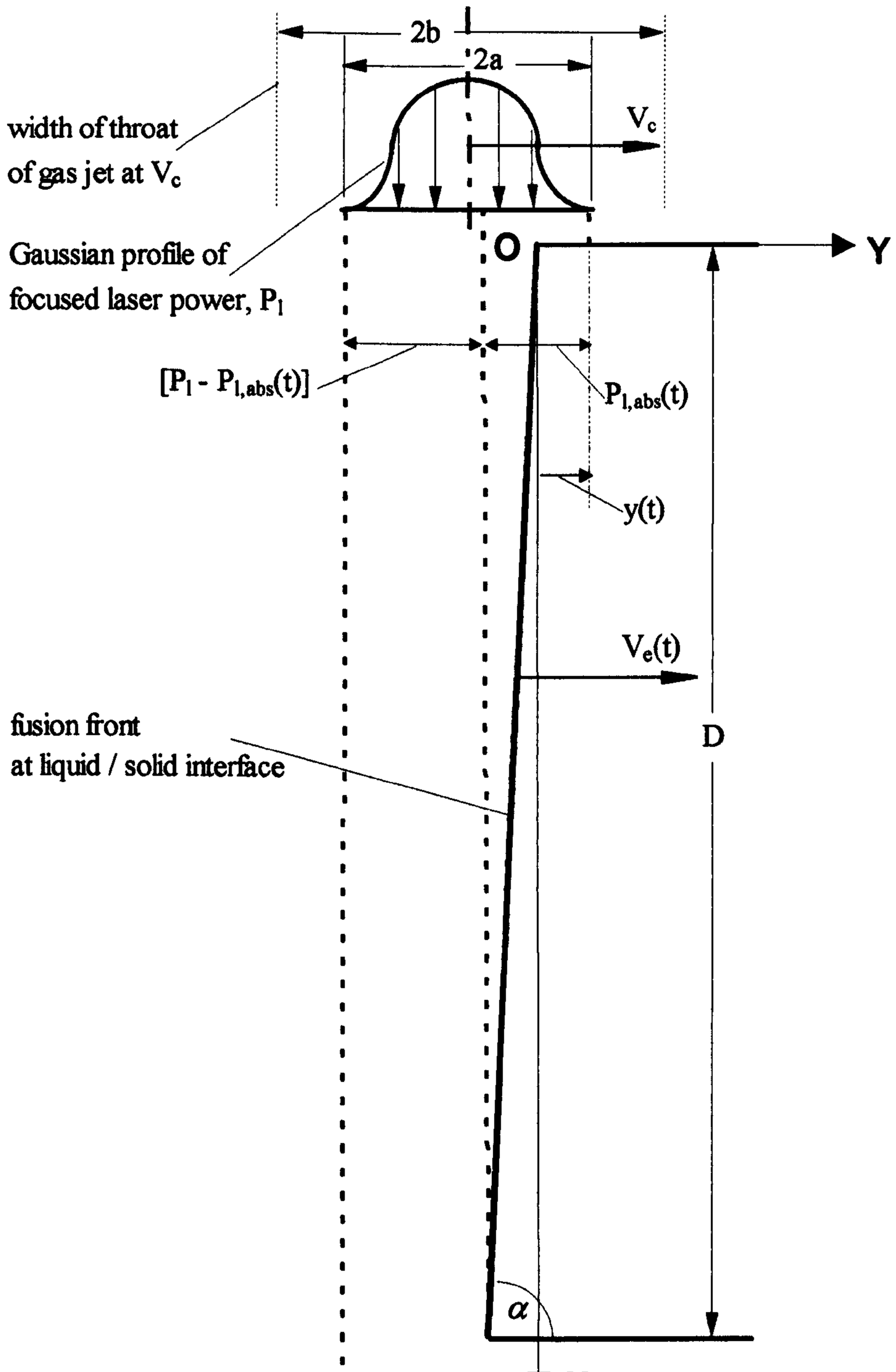

Figure 14. *Dynamic absorption of laser power by the workpiece due to the "non-contact" intersection. When $V_e(t)$ oscillates around V_c with respect to time, $y(t)$ varies. This makes $P_{l,abs}(t)$ vary with respect to time, too. X-O-Y system is the same as in Fig.9*

The underlying reason for the dynamic absorption of laser power by the workpiece is due to the fact that there is no physical bond between the fusion front at $V_e(t)$ and the laser beam light at V_c. Therefore, keeping V_c constant with respect to time does not guarantee the fusion front, at the liquid / solid interface, to propagate constantly. The velocity of the fusion front is thus treated as one of the 5 time-dependent variables in this thesis. It is expected that $V_e(t)$ would oscillate around V_c with respect to time. Fig.14 shows clearly that the change of $V_e(t)$ directly produces the changes of $y(t)$ and $P_{l,abs}(t)$, respectively.

7-2. 2-D Gaussian profile of laser power intensity

In accordance with the 2-D nature of the dynamic modelling throughout this thesis, i.e., in X-O-Y, the focused laser power is assumed as a 2-D model, as shown in Fig.9 and Fig.14:

- in Y, the power intensity holds Gaussian profile; in X and Z, it is even;
- the dimension in any section vertical to X is a square: $2a \times 2a$ (m^2);
- $2a = w$ $(m.)$;

By the assumptions, the power intensity of P_l in Y is,

$$I_{(r)} = \frac{I}{e^{2\left(\frac{r}{a}\right)}} I_0 \tag{61}$$

where, r: the radius from the beam centre, in Y; $0 \le r \le a$ $(m.)$;

I_0: the power intensity at the beam centre (W / m^2);

The total laser power is defined as,

$$P_l = 2\int_0^a \left[I_{(r)} 2a\right](dr) \tag{62}$$

Combining Eq.61 and Eq.62, I_o can be found out,

$$I_o = \frac{e^2}{2(e^2-1)} \cdot \frac{P_l}{a^2} \tag{63}$$

By contributing Eq.63 into Eq.61, the assumed laser power intensity is,

$$I_{(r)} = \left(\frac{e^2}{2(e^2-1)} \cdot \frac{P_l}{a^2} \right) \cdot \frac{1}{e^{2\left(\frac{r}{a}\right)}} \tag{64}$$

It is seen that, by Eq.64, given P_l and a, the power intensity, $I_{(r)}$, is the function of r. It assumes that, at the beam centre, $I_{(0)} = I_0$; at the beam front, $I_{(a)} = 0.13533 I_0$.

7-3. Influence of fusion front velocity on laser power absorption

Assuming that the focused laser beam is vertical to the surface of the workpiece and the thickness of the molten metal film is negligible in comparison with a, as shown in Fig.14, it can be observed that the magnitude of $\left[y(t) + D \cdot \cos\alpha\right]$ represents the absorption of laser power by the workpiece, $P_{l,abs}(t)$; the magnitude of $\left[2a - y(t) - D \cdot \cos\alpha\right]$ represents the energy which is not absorbed by the workpiece, $\left[P_l - P_{l,abs}(t)\right]$. $P_{l,abs}(t)$ is thus calculated,

When, $a - D \cdot \cot\alpha \le y(t) \le 2a - D \cdot \cot\alpha$,

$r = y + D \cdot \cot\alpha - a \ge 0$,

$$P_{l,abs}(t) = \frac{P_l}{2} + \int_0^r \left[I_{(r)} 2a \right](dr) \tag{65}$$

Combining Eq.65 with Eq.64 gives,

$$P_{l,abs}(t) = \frac{P_l}{2} + \frac{e^2}{2(e^2-1)}\left\{1 - exp\left[2\frac{a - y(t) - D\cdot\cot\alpha}{a}\right]\right\}P_l \qquad (65')$$

When, $-D\cdot\cot\alpha \le y(t) \le a - D\cdot\cot\alpha$,

$r = a - y - D\cdot ctg\alpha \ge 0$,

$$P_{l,abs}(t) = \frac{P_l}{2} - \int_0^r \left[I_{(r)}2a\right](dr) \qquad (66)$$

Combining Eq.66 with Eq.64 gives:

$$P_{l,abs}(t) = \frac{P_l}{2} - \frac{e^2}{2(e^2-1)}\left\{1 - exp\left[2\frac{y(t) + D\cdot\cot\alpha - a}{a}\right]\right\}P_l \qquad (66')$$

When, $2a - D\cdot\cot\alpha \le y(t) \le 2a$,

$$P_{l,abs}(t) = P_l \qquad (67)$$

Eq.65', Eq.66' and Eq.67 reflect the fact that $P_{l,abs}(t)$ is associated with $y(t)$. $y(t)$ is the co-ordinate of the front of the focused laser beam in Y. The boundary condition for $y(t)$ in each step of time evolution can be generalised as,

$$-D\cdot\cot\alpha \le y(t) \le 2a \qquad (68)$$

for,

$$0 \le P_{l,abs}(t) \le P_l \qquad (69)$$

If, $y(t) < -D\cdot\cot\alpha$ or $y(t) > 2a$, $P_{l,abs}(t) = 0$ is expected. The boundary conditions for $y(t)$ and $P_{l,abs}(t)$ derived in this section will be applied and discussed in Chapter 8.

Further, it is intended to ascertain the relationship among $y(t)$, $V_e(t)$ and V_c, in Fig.14,

$$\frac{d}{dt}\left[y(t)\right] = V_c - V_e(t) \tag{70}$$

The dynamic absorption of laser power is derived by differentiating Eq.65' and Eq.66' with respect to $y(t)$, respectively, and then combining them with Eq.70:

$$\begin{aligned}\frac{d}{dt}\left[P_{l,abs}(t)\right] &= \frac{d}{d\left[y(t)\right]}\left[P_{l,abs}(t)\right] \times \frac{d}{dt}\left[y(t)\right] \\ &= \frac{e^2}{(e^2-1)} \cdot \frac{P_l}{a} \cdot \frac{V_c - V_e(t)}{exp\left[2\dfrac{\left|y(t)+D\cdot\cot\alpha - a\right|}{a}\right]}\end{aligned} \tag{71}$$

where, the conditions are generally stated as:

$-D\cdot\cot\alpha \le y(t) \le 2a - D\cdot\cot\alpha$;

$0 \le P_{l,abs}(t) \le P_l$.

by the conditions for Eq.65' and Eq.66'.

When, $2a - D\cdot\cot\alpha \le y(t) \le 2a$, differentiating Eq.67 with respect to t yields:

$$\frac{d}{dt}\left[P_{l,abs}(t)\right] = 0 \tag{72}$$

where, the conditions are, of course, $2a - D\cdot\cot\alpha \le y(t) \le 2a$.

Generally, it is seen that the absorption of laser power by the workpiece, $P_{l,abs}(t)$, is associated with relative displacement between the fusion front and the focused laser beam front, $y(t)$, identified by,

- Eq.66' when, $-D\cdot\cot\alpha \le y(t) \le a - D\cdot\cot\alpha$;
- Eq.65' when, $a - D\cdot\cot\alpha \le y(t) \le 2a - D\cdot\cot\alpha$;
- Eq.67, when $2a - D\cdot\cot\alpha \le y(t) \le 2a$.

$y(t)$ is further associated with the difference of V_c and $V_e(t)$, identified by Eq.70. Hence, as expected, $P_{l,abs}(t)$, $y(t)$ and $V_e(t)$ are associated with each other, with respect to time.

7-4. Evaluation of derived quantities

As before, this section is to demonstrate the static values of the derived quantities with the typical data in Appendices 1-3.

Laser power intensity

This is calculated by Eq.64:

$$I_{(r)} = \left(\frac{e^2}{2(e^2-1)} \cdot \frac{P_l}{a^2}\right) \cdot \frac{1}{e^{2\left(\frac{r}{a}\right)}}$$

In appendix 1: $P_l = 800\ (W.)$; $w = 2 \times 10^{-3}\ (m.)$. So, $a = \frac{w}{2} = 1 \times 10^{-3}\ (m.)$.

$$I_{(r)} = \frac{462.61 \times 10^6}{e^{2\left(\frac{r}{a}\right)}}\ (W/m^2)$$

at the beam centre, $I_0 = I_{(r=0)} = 462.61 \times 10^6\ (W/m^2)$;

at the edge of the beam (along Y, front or rear): $I_{(r=a)} = 62.61 \times 10^6\ (W/m^2)$.

It is seen that the power intensity depends upon two factors, the focused area and the power intensity profile *, as expected.

* The laser power of Gaussian profile is expected in the applications of laser cutting of metals. Therefore, the ideal power intensity of Gaussian profile is assumed for the theoretical laser cutting system throughout this thesis. However, the laser power used in the experiment can only be, very roughly, treated as a 3-D Gaussian profile, as shown in Fig.18 in Chapter 9.

Absorption of laser power by workpiece

The absorption of laser power by the workpiece, $P_{l,abs}(t)$, is a time-dependent variable and it is calculated by Eq.65' or Eq.66' or Eq.67, depending on $y(t)$.

In Appendix 1: $a = \frac{1}{2}w = 1 \times 10^{-3}(m.)$; $\alpha = 85\ (^{\circ})$; $D = 6 \times 10^{-3}\ (m.)$; $P_l = 800(W.)$; the calculated results are:

- at $y(t) = -0.525 \times 10^{-3}\ (m.)$, by Eq.66', $P_{l,abs}(t) = 0\ (W.)$;
- at $y(t) = 0.0\ (m.)$, by Eq.66', $P_{l,abs}(t) = 116.3\ (W.)$;
- at $y(t) = 0.475 \times 10^{-3}\ (m.)$, by Eq.66' or Eq.65', $P_{l,abs}(t) = 400\ (W.)$;
- at $y(t) = 1.0 \times 10^{-3}\ (m.)$, by Eq.65', $P_{l,abs}(t) = 700.7\ (W.)$;
- at $y(t) = 1.475 \times 10^{-3}\ (m.)$, by Eq.65', $P_{l,abs}(t) = 800\ (W.)$;
- at $1.475 \times 10^{-3} \le y(t) \le 2 \times 10^{-3}\ (m.)$, by Eq.67, $P_{l,abs}(t) = 800\ (W.)$;

7-5. Justification of theoretical treatment of dynamic absorption of laser power

The dynamic absorption of the focused laser power, identified as $P_{l,abs}(t)$, is physically shown in Fig.14. It is focused at the influence of variable $y(t)$, due to the oscillation of variable $V_e(t)$ around V_c, on the absorption of the focused laser power by the workpiece. Consequently, $P_{l,abs}(t)$ is assumed to enter the liquid surface at the liquid / solid interface evenly.

In the simulation of $P_{l,abs}(t)$, the angle of the fusion front to horizontal plane, α, is taken into account. This is because, although the thickness of molten metal layer is negligible in comparison with a, the quantity of ($D \cdot cot\,\alpha$) can not be ignored, in comparison with a.

This is proved by the evaluations, above, with the typical data in Appendix 1. Even in the situation that $\alpha = 89\ (^{o})$, the quantity of $(D \cdot cot\,\alpha)$ can reach $0.105 \times 10^{-3}\ (m.)$.

In connection with the steady-state considerations in the previous major work [1,3,5,8,10, 12,23,25,35,36,37,38,39], where the assumptions ($V_e(t) = V_c$; $P_{l,abs}(t) = P_l$) were always made, the dynamic analyses in this thesis can be easily transferred into the steady-state analyses:

Let, $V_e(t) = V_c$,

by Eq.70, $\frac{d}{dt}(y) = V_c - V_e = 0$; so $y(t)$ is a constant;

Hence, let $y(t)$ be any constant in the scope $\left[(2a - cot\,\alpha),\ 2a\right]$,

by Eq.65' and Eq.67: $P_{l,abs}(t) = P_l$.

It is seen that, in order to better model the reality in the laser cutting of metals, in which there is a lack of forced physical connection between $V_e(t)$ and V_c, the dynamic approach as in Fig.14 is necessary. For this reason, the quantities $P_{l,abs}(t)$, $y(t)$ and $V_e(t)$ are treated as time-dependent variables for the theoretical laser cutting system. In this case, their dynamic characteristics are naturally observed by analysing their 1st-order derivatives with regard to time, respectively.

Chapter 8. Differential Governing equations

The nature of the theoretical laser cutting system as shown in Fig.9 in Chapter 2 is analysed with the derived differential governing equations. The construction of governing equations is based on the analyses in Chapters 2-7. The complicated mechanisms in the laser cutting of metals are characteristic of the combined interactions between the gas flow, the liquid flow, the substrate solid and the focused laser beam. This fact is reflected, mathematically, by combining the derived equations which are associated with the individual interactions in Chapters 4-7, respectively, according to the basic principles, i.e., the flowing molten metal layer in the kerf satisfying the dynamic balance equations of mass, momentum and energy, simultaneously.

The method to construct the differential governing equations is first demonstrated. The physical boundary conditions for the 5 time-dependent variables are analysed. The method to determine the special variable, C_{exo}, which is initial-condition-dependent but time-independent, derived in Chapter 5, is demonstrated. In association with C_{exo}, the nature of the differential governing equations are analysed, from the viewpoint of Chaos theory concerning a non-linear dynamic system.

Finally, a sample of the differential governing equations is shown, based on the typical data listed in Appendices 1-3. The dynamic solutions, i.e., $\delta_l(t)$, $T_l(t)$, $V_e(t)$, $y(t)$, $P_{l,abs}(t)$, varying with respect to time, are demonstrated. The numerical method can be referred to the C program in Appendix 6. The reason for doing the programming rather than using an existing software is stated.

8-1. 1st-order derivatives of time-dependent variables

In this section, it is intended to derive the rate of change, with respect to time, for the most concerned time-dependent variables, i.e., $\delta_l(t)$, $T_l(t)$, $V_e(t)$, $y(t)$, $P_{l,abs}(t)$, based on the previous analyses in Chapters 3-7.

8-1-1. The rate of change of $\delta_l(t)$, $\frac{d}{dt}\left[\delta_l(t)\right]$

The mass balance in *CV* enclosing the molten metal layer in the kerf must be dynamically satisfied at any time, by Eq.1, in Chapter 3:

$$\dot{m}_{in} = \dot{m}_{out} + \dot{m}_{CV} \tag{1}$$

where, $\dot{m}_{in}$ is calculated by Eq.2:

$$\dot{m}_{in} = \rho_s \cdot w \cdot D \cdot V_e(t) \tag{2}$$

$\dot{m}_{out}$ is derived as in Eq.6'' in Chapter 4:

$$\dot{m}_{out} = \left(0.166 \frac{w\rho_l}{\mu_l} \frac{\rho_{g,w} U_g{}^2}{\sqrt{\rho_{g,w} U_g D / \mu_{g,w}}} \right) \cdot \left[\delta_l(t)\right]^2 \tag{6''}$$

$\dot{m}_{CV}$ is calculated in Eq.3 in Chapter 3:

$$\dot{m}_{CV} = \frac{1}{2} \cdot \rho_l \cdot w \cdot D \cdot \left(\frac{d}{dt}\left[\delta_l(t)\right] \right) \tag{3}$$

Contributing Eqs.2, 3, 6'' into Eq.1 gives:

$$\rho_s \cdot D \cdot V_e(t) = 0.166 \frac{\rho_l}{\mu_l} \frac{\rho_{g,w} U_g{}^2}{\sqrt{\rho_{g,w} U_g D / \mu_{g,w}}} \left[\delta_l(t)\right]^2 + \frac{1}{2} \cdot \rho_l \cdot D \cdot \left(\frac{d}{dt}\left[\delta_l(t)\right] \right) \tag{1'}$$

Rearranging Eq.1' yields:

$$\frac{d}{dt}\left[\delta_l(t)\right] = 2\frac{\rho_s}{\rho_l} V_e(t) - \frac{0.332}{\mu_l} \frac{\rho_{g,w} U_g{}^2}{D\sqrt{\rho_{g,w} U_g D / \mu_{g,w}}} \left[\delta_l(t)\right]^2 \tag{73}$$

8-1-2. The rate of change of $P_{l,abs}(t)$, $\frac{d}{dt}\left[P_{l,abs}(t)\right]$

$P_{l,abs}(t)$ has been derived in Chapter 7; it is calculated by Eq.66', Eq.65' and Eq.67, up to the value of $y(t)$. Its 1st-order derivative is derived in Eqs.71, 72, depending on $y(t)$, too, by the conditions for Eq.65' and Eq.66'.

If, $-D\cdot\cot\alpha \le y(t) \le 2a - D\cdot\cot\alpha$;

and, $0 \le P_{l,abs}(t) \le P_l$,

$$\frac{d}{dt}\left[P_{l,abs}(t)\right] = \frac{e^2}{(e^2-1)}\cdot\frac{P_l}{a}\cdot\frac{V_c - V_e(t)}{exp\left[2\frac{\left|y(t)+D\cdot\cot\alpha-a\right|}{a}\right]} \tag{71}$$

If, $2a - D\cdot\cot\alpha \le y(t) \le 2a$,

and, $P_{l,abs}(t) = P_l$,

$$\frac{d}{dt}\left[P_{l,abs}(t)\right] = 0 \tag{72}$$

It is also noted that,

If, $y(t) < -D\cdot\cot\alpha$ and $y(t) > 2a$;

and, $P_{l,abs}(t) = 0$,

$$\frac{d}{dt}\left[P_{l,abs}(t)\right] = 0 \tag{74}$$

8-1-3. The rate of change of $y(t)$, $\frac{d}{dt}\left[y(t)\right]$

This has been derived in Eq.70 in Chapter 7,

$$\frac{d}{dt}\left[y(t)\right] = V_c - V_e(t) \tag{70}$$

It can be seen that, in Fig.14, the value of $y(t)$ determines both $P_{l,abs}(t)$, by Eqs.71, 72, 74, and $\dot{e}_{exo}$. Assuming $2b$ as the width of throat of jet gas which moves with the laser beam ($2b > 2a$), the influence of $y(t)$ on $\dot{e}_{exo}$ is described:

If, $y(t) > a + b$ and $y(t) < a - b$,

$$\dot{e}_{exo} = 0 \tag{75}$$

Whether $\dot{e}_{exo} \neq 0$ or $\dot{e}_{exo} = 0$ will be used as the critical condition for judging if the laser cutting can continue or not. Numerically, it is monitored by $y(t) \in \left[a - b,\ a + b\right]$.

8-1-4. The rate of change of $V_e(t)$, $\frac{d}{dt}\left[V_e(t)\right]$

By differentiating Eq.1' with respect to time; neglecting the second order infinitesimal quantity $\frac{d}{dt}\left\{\frac{d}{dt}\left[\delta_l(t)\right]\right\}$, in comparison with $\frac{d}{dt}\left[\delta_l(t)\right]$; combining it with Eq.73, it can be seen:

$$\frac{d}{dt}\left[V_e(t)\right] =$$

$$\frac{0.664}{D\mu_l}\left(\frac{\rho_{g,w}U_g{}^2}{\sqrt{\rho_{g,w}U_g D/\mu_{g,w}}}\right)\delta_l(t)\cdot V_e(t) - \left(\frac{0.332}{D\mu_l}\right)^2 \frac{\rho_l}{\rho_s}\left(\frac{\rho_{g,w}U_g{}^2}{\sqrt{\rho_{g,w}U_g D/\mu_{g,w}}}\right)^2 \left[\delta_l(t)\right]^3 \tag{76}$$

8-1-5. The rate of change of $T_l(t)$, $\frac{d}{dt}\left[T_l(t)\right]$

The energy balance in CV must be dynamically satisfied at any time, in Eq.9 in Chapter 3,

$$\dot{P}_{l,abs}(t) + \dot{e}_{exo} + \dot{e}_{in} = \dot{e}_{out} + \dot{e}_{loss} + \dot{e}_{cool} + \dot{e}_{CV} \tag{9}$$

In Eq.9, $P_{l,abs}(t)$ has been derived in Eqs.65', 66', 67, in Chapter 7, depending on the value of $y(t)$. It is noted that, only if: $-D\cdot cot\,\alpha \le y(t) \le 2a - D\cdot cot\,\alpha$, $\frac{d}{dt}\left[P_{l,abs}(t)\right]$ in Eq.71 is valid to calculate $P_{l,abs}(t)$. If $2a - D\cdot cot\,\alpha \le y(t) \le 2a$, it is seen, $P_{l,abs}(t) = P_l$; if $y(t) < -D\cdot cot\,\alpha$ or $y(t) > 2a$, it is seen, $P_{l,abs}(t) = 0$.

$\dot{e}_{exo}$ has been derived in Eq.55, in Chapter 5,

$$\dot{e}_{exo} = \Delta H\big|_{T_l(t)} \times \dot{m}_{exo}$$

$$= C_{exo} \times \delta_l(t) \times [-4.74 \times 10^6 +$$

$$\int_{298}^{T_l(t)} (-59.586 + 1.945 \times 10^{-3} T - 35.227 \times 10^5 T^{-2} + 4266.211 T^{-0.5})dT\,] \tag{55}$$

Taking the magnitude of $\Delta H\big|_{T_l(t)}$ in Eq.46' into account, Eq.55 is simplified as:

$$\dot{e}_{exo} = 4.613 \times 10^6 C_{exo} \delta_l(t) \tag{77}$$

$\dot{e}_{in}$ is calculated by Eq.11 in Chapter 3:

$$\dot{e}_{in} = c_{p,s} \cdot \rho_l \cdot w \cdot D \cdot T_m \cdot V_e(t) \tag{11}$$

$\dot{e}_{out}$ has been derived in Eq.14' from Chapter 4:

$$\dot{e}_{out} = \left(0.166 \frac{w\rho_l}{\mu_l} \frac{\rho_{g,w} U_g^{\ 2}}{\sqrt{\rho_{g,w} U_g D / \mu_{g,w}}}\right) \cdot \left[c_{p,l} \frac{T_m + T_l(t)}{2} + h_f\right] \cdot \left[\delta_l(t)\right]^2 \tag{14'}$$

$\dot{e}_{loss}$ has been derived in Eq.76 from Chapter 6:

$$\dot{e}_{loss} = 0.312 w D^{\frac{1}{4}} \left[\rho_l^{\frac{1}{2}} c_{p,l} \left(\frac{\mu_l c_{p,l}}{K_l}\right)^{\frac{-2}{3}}\right] \left[\rho_{g,w} \mu_{g,w} U_g^3\right]^{\frac{1}{4}} \left[T_l(t) - T_m\right] \sqrt{\delta_l(t)} \tag{57''}$$

$\dot{e}_{cool}$ has been derived in Eq.35 from Chapter 4:

$$\dot{e}_{cool} = \int_0^D \dot{q}_{g.w}(w \cdot dx) = 0.664 \frac{w\rho_{g,w} U_g \left[c_{p,g,w} T_l(t) - c_{p,g} T_g\right]}{\sqrt{(\rho_{g,w} U_g) / (D\mu_{g,w})}} \cdot \left[(Pr)_g\right]^{-2/3} \tag{31}$$

$\dot{e}_{CV}$ is calculated in Eq.15 in Chapter 3:

$$\begin{aligned} \dot{e}_{CV} &= \frac{1}{2} \rho_l w D c_{p,l} T_f(t) \frac{d}{dt}\left[\delta_l(t)\right] + \frac{1}{2} \rho_l w D h_f \frac{d}{dt}\left[\delta_l(t)\right] \\ &\quad + \frac{1}{2} \rho_l w D c_{p,l} \delta_l(t) \frac{d}{dt}\left[T_f(t)\right] \end{aligned} \tag{15}$$

Introducing Eq.13 into Eq.15 yields,

$$\begin{aligned} \dot{e}_{CV} &= \frac{1}{4} \rho_l w D c_{p,l} \left[T_m + T_l(t)\right] \frac{d}{dt}\left[\delta_l(t)\right] + \frac{1}{2} \rho_l w D h_f \frac{d}{dt}\left[\delta_l(t)\right] \\ &\quad + \frac{1}{4} \rho_l w D c_{p,l} \delta_l(t) \frac{d}{dt}\left[T_l(t)\right] \end{aligned} \tag{15'}$$

By contributing $P_{l,abs}(t)$ depending on the value of $y(t)$ by Eqs.71, 72, 74, and Eqs.77, 11 into the left side of Eq.9; Eqs.14', 57'', 31, 15 into the right side of Eq.9; then contributing Eq.73 into it, $\frac{d}{dt}\left[T_l(t)\right]$ is derived as follows, depending on the value of $y(t)$:

- when, $-D\cdot\cot\alpha \le y(t) \le 2a - D\cdot\cot\alpha$,

$$\frac{d}{dt}\left[T_l(t)\right] =$$

$$\left[\frac{4}{wD\rho_l c_{p,l}}\right]P_{l,abs}(t)\cdot\left[\delta_l(t)\right]^{-1} + \left[\frac{18.44\times10^6}{wD\rho_l c_{p,l}}\right]C_{exo} + \left[\frac{4c_{p,s}T_m}{c_{p,l}}\right]V_e(t)\cdot\left[\delta_l(t)\right]^{-1}$$

$$- \left[\frac{1.248}{\rho_l^{\frac{1}{2}}D^{\frac{3}{4}}}\left(\frac{\mu_l c_{p,l}}{K_l}\right)^{\frac{-2}{3}}\right]\left(\rho_{g,w}\mu_{g,w}U_g^3\right)^{\frac{1}{4}}\left[T_l(t)-T_m\right]\cdot\left[\delta_l(t)\right]^{\frac{-1}{2}}$$

$$- \left\{\frac{2.656}{\rho_l c_{p,l}}\frac{\rho_{g,w}U_g}{\sqrt{\rho_{g,w}U_g D/\mu_{g,w}}}\left[(Pr)_g\right]^{-2/3}\right\}\left[c_{p,g,w}T_l(t) - c_{p,g}T_g\right]\cdot\left[\delta_l(t)\right]^{-1}$$

$$- \left(\frac{2\rho_s}{\rho_l}\right)V_e(t)\cdot\left[T_m + T_l(t)\right]\cdot\left[\delta_l(t)\right]^{-1} - \left(\frac{4\rho_s h_f}{\rho_l c_{p,l}}\right)V_e(t)\cdot\left[\delta_l(t)\right]^{-1} \qquad (78)$$

- when, $2a - D\cdot\cot\alpha \le y(t) \le 2a$, $\frac{d}{dt}\left[P_{l,abs}(t)\right] = 0$, $P_{l,abs}(t) = P_l$,

$$\frac{d}{dt}\left[T_l(t)\right] =$$

$$\left[\frac{4P_l}{wD\rho_l c_{p,l}}\right]\cdot\left[\delta_l(t)\right]^{-1} + \left[\frac{18.44\times10^6}{wD\rho_l c_{p,l}}\right]C_{exo} + \left[\frac{4c_{p,s}T_m}{c_{p,l}}\right]V_e(t)\cdot\left[\delta_l(t)\right]^{-1}$$

$$- \left[\frac{1.248}{\rho_l^{\frac{1}{2}}D^{\frac{3}{4}}}\left(\frac{\mu_l c_{p,l}}{K_l}\right)^{\frac{-2}{3}}\right]\left(\rho_{g,w}\mu_{g,w}U_g^3\right)^{\frac{1}{4}}\left[T_l(t)-T_m\right]\cdot\left[\delta_l(t)\right]^{\frac{-1}{2}}$$

$$- \left\{\frac{2.656}{\rho_l c_{p,l}}\frac{\rho_{g,w}U_g}{\sqrt{\rho_{g,w}U_g D/\mu_{g,w}}}\left[(Pr)_g\right]^{-2/3}\right\}\left[c_{p,g,w}T_l(t) - c_{p,g}T_g\right]\cdot\left[\delta_l(t)\right]^{-1}$$

$$- \left(\frac{2\rho_s}{\rho_l}\right)V_e(t)\cdot\left[T_m + T_l(t)\right]\cdot\left[\delta_l(t)\right]^{-1} - \left(\frac{4\rho_s h_f}{\rho_l c_{p,l}}\right)V_e(t)\cdot\left[\delta_l(t)\right]^{-1} \qquad (79)$$

- when, $y(t) < -D \cdot \cot\alpha$ and $y(t) > 2a$, $\frac{d}{dt}\left[P_{l,abs}(t)\right] = 0$, $P_{l,abs}(t) = 0$,

$$\frac{d}{dt}\left[T_l(t)\right] =$$

$$\left[\frac{18.44 \times 10^6}{wD\rho_l c_{p,l}}\right] C_{exo} + \left[\frac{4c_{p,s}T_m}{c_{p,l}}\right] V_e(t) \cdot \left[\delta_l(t)\right]^{-1}$$

$$- \left[\frac{1.248}{\rho_l^{\frac{1}{2}} D^{\frac{3}{4}}} \left(\frac{\mu_l c_{p,l}}{K_l}\right)^{\frac{-2}{3}}\right] \left(\rho_{g,w}\mu_{g,w}U_g^3\right)^{\frac{1}{4}} \left[T_l(t) - T_m\right] \cdot \left[\delta_l(t)\right]^{\frac{-1}{2}}$$

$$- \left\{\frac{2.656}{\rho_l c_{p,l}} \frac{\rho_{g,w}U_g}{\sqrt{\rho_{g,w}U_g D / \mu_{g,w}}} \left[(Pr)_g\right]^{-2/3}\right\} \left[c_{p,g,w}T_l(t) - c_{p,g}T_g\right] \cdot \left[\delta_l(t)\right]^{-1}$$

$$- \left(\frac{2\rho_s}{\rho_l}\right) V_e(t) \cdot \left[T_m + T_l(t)\right] \cdot \left[\delta_l(t)\right]^{-1} - \left(\frac{4\rho_s h_f}{\rho_l c_{p,l}}\right) V_e(t) \cdot \left[\delta_l(t)\right]^{-1} \qquad (80)$$

- when, $y(t) > a + b$ and $y(t) < a - b$, it is assumed, by Eq.75, $\dot{e}_{exo} = 0$. In this case, it is seen that: $\dot{e}_{exo} = 0$; $P_{l,abs}(t) = 0$. Because the reactive laser cutting process is driven by the heats of both $P_{l,abs}$ and $\dot{e}_{exo}$, it is assumed that the energy balance in Eq.78, 79, 80, is invalid. The laser cutting process stops.

It is noted that Eq.79 represents the situation that the absorption of laser power does not vary, due to the angle α being slightly less than 90^o. Eq.80 represents the situation that there is no absorption of laser power and the cutting process is driven by the oxidisation heat, i.e., $P_{l,abs}(t) = 0$, $\dot{e}_{exo} \neq 0$. Hence, Eq.80 reflects the reality that the focused laser beam simply goes through the kerf because it is too far behind the fusion front.

8-2. Construction of differential governing equations

In general, when $-D\cdot\cot\alpha \le y(t) \le 2a - D\cdot\cot\alpha$, the differential governing equations for the theoretical cutting system, as shown in Fig.8, are made of Eqs.73, 71, 70, 76 and 78:

- $-D\cdot\cot\alpha \le y(t) \le 2a - D\cdot\cot\alpha$,

$$
\begin{cases}
\dfrac{d}{dt}\left[\delta_l(t)\right] = 2\dfrac{\rho_s}{\rho_l}V_e(t) - \dfrac{0.332}{D\mu_l}\dfrac{\rho_{g,w}U_g^{\,2}}{\sqrt{\rho_{g,w}U_gD/\mu_{g,w}}}\left[\delta_l(t)\right]^2 \\
\dfrac{d}{dt}\left[P_{l,abs}(t)\right] = \dfrac{e^2}{e^2-1}\dfrac{P_l}{a}\dfrac{V_c - V_e(t)}{exp\left[2\dfrac{\left|y(t)+D\cdot\cot\alpha-a\right|}{a}\right]} \\
\dfrac{d}{dt}\left[y(t)\right] = V_c - V_e(t) \\
\dfrac{d}{dt}\left[V_e(t)\right] = \dfrac{0.664}{D\mu_l}\dfrac{\rho_{g,w}U_g^{\,2}}{\sqrt{\dfrac{\rho_{g,w}U_gD}{\mu_{g,w}}}}\delta_l(t)\cdot V_e(t) - \left(\dfrac{0.332}{D\mu_l}\right)^2\dfrac{\rho_l}{\rho_s}\left(\dfrac{\rho_{g,w}U_g^{\,2}}{\sqrt{\rho_{g,w}U_gD/\mu_{g,w}}}\right)^2\left[\delta_l(t)\right]^3 \\
\dfrac{d}{dt}\left[T_l(t)\right] = \\
\qquad \left[\dfrac{4}{wD\rho_lc_{p,l}}\right]P_{l,abs}(t)\cdot\left[\delta_l(t)\right]^{-1} + \left[\dfrac{18.44\times10^6}{wD\rho_lc_{p,l}}\right]C_{exo} + \left[\dfrac{4c_{p,s}T_m}{c_{p,l}}\right]V_e(t)\cdot\left[\delta_l(t)\right]^{-1} \\
\qquad - \left[\dfrac{1.248}{\rho_l^{\frac{1}{2}}D^{\frac{3}{4}}}\left(\dfrac{\mu_lc_{p,l}}{K_l}\right)^{\frac{-2}{3}}\right]\left(\rho_{g,w}\mu_{g,w}U_g^3\right)^{\frac{1}{4}}\left[T_l(t)-T_m\right]\cdot\left[\delta_l(t)\right]^{\frac{-1}{2}} \\
\qquad - \left\{\dfrac{2.656}{\rho_lc_{p,l}}\dfrac{\rho_{g,w}U_g}{\sqrt{\rho_{g,w}U_gD/\mu_{g,w}}}\left[(Pr)_g\right]^{-2/3}\right\}\left[c_{p,g,w}T_l(t) - c_{p,g}T_g\right]\cdot\left[\delta_l(t)\right]^{-1} \\
\qquad - \left(\dfrac{2\rho_s}{\rho_l}\right)V_e(t)\cdot\left[T_m + T_l(t)\right]\cdot\left[\delta_l(t)\right]^{-1} - \left(\dfrac{4\rho_sh_f}{\rho_lc_{p,l}}\right)V_e(t)\cdot\left[\delta_l(t)\right]^{-1}
\end{cases}
\tag{81}
$$

When $2a - D \cdot \cot\alpha \le y(t) \le 2a$, the differential governing equations for the theoretical cutting system are made of Eqs.73, 70, 76 and 79:

- $2a - D \cdot \cot\alpha \le y(t) \le 2a$, $\dfrac{d}{dt}\left[P_{l,abs}(t)\right] = 0$, $P_{l,abs}(t) = P_l$,

$$
\begin{cases}
\dfrac{d}{dt}\left[\delta_l(t)\right] = 2\dfrac{\rho_s}{\rho_l}V_e(t) - \dfrac{0.332}{D\mu_l}\dfrac{\rho_{g,w}U_g^{\,2}}{\sqrt{\rho_{g,w}U_g D/\mu_{g,w}}}\left[\delta_l(t)\right]^2 \\
\dfrac{d}{dt}\left[y(t)\right] = V_c - V_e(t) \\
\dfrac{d}{dt}\left[V_e(t)\right] = \dfrac{0.664}{D\mu_l}\dfrac{\rho_{g,w}U_g^{\,2}}{\sqrt{\dfrac{\rho_{g,w}U_g D}{\mu_{g,w}}}}\delta_l(t)\cdot V_e(t) - \left(\dfrac{0.332}{D\mu_l}\right)^2\dfrac{\rho_l}{\rho_s}\left(\dfrac{\rho_{g,w}U_g^{\,2}}{\sqrt{\rho_{g,w}U_g D/\mu_{g,w}}}\right)^2\left[\delta_l(t)\right]^3 \\
\dfrac{d}{dt}\left[T_l(t)\right] =
\end{cases}
$$

$$
\left[\frac{4P_l}{wD\rho_l c_{p,l}}\right]\cdot\left[\delta_l(t)\right]^{-1} + \left[\frac{18.44\times10^6}{wD\rho_l c_{p,l}}\right]C_{exo} + \left[\frac{4c_{p,s}T_m}{c_{p,l}}\right]V_e(t)\cdot\left[\delta_l(t)\right]^{-1}
$$

$$
- \left[\frac{1.248}{\rho_l^{\frac{1}{2}}D^{\frac{3}{4}}}\left(\frac{\mu_l c_{p,l}}{K_l}\right)^{\frac{-2}{3}}\right]\left(\rho_{g,w}\mu_{g,w}U_g^3\right)^{\frac{1}{4}}\left[T_l(t) - T_m\right]\cdot\left[\delta_l(t)\right]^{\frac{-1}{2}}
$$

$$
- \left\{\frac{2.656}{\rho_l c_{p,l}}\frac{\rho_{g,w}U_g}{\sqrt{\rho_{g,w}U_g D/\mu_{g,w}}}\left[(Pr)_g\right]^{-2/3}\right\}\left[c_{p,g,w}T_l(t) - c_{p,g}T_g\right]\cdot\left[\delta_l(t)\right]^{-1}
$$

$$
- \left(\frac{2\rho_s}{\rho_l}\right)V_e(t)\cdot\left[T_m + T_l(t)\right]\cdot\left[\delta_l(t)\right]^{-1} - \left(\frac{4\rho_s h_f}{\rho_l c_{p,l}}\right)V_e(t)\cdot\left[\delta_l(t)\right]^{-1}
$$

(82)

When $a-b<y(t)<-D\cdot\cot\alpha$, $2a<y(t)<a+b$, the differential governing equations for the theoretical cutting system are made of Eqs.73, 70, 76 and 80:

- $a-b<y(t)<-D\cdot\cot\alpha$, $2a<y(t)<a+b$, $\dfrac{d}{dt}\left[P_{l,abs}(t)\right]=0$, $P_{l,abs}(t)=0$,

$$
\begin{cases}
\dfrac{d}{dt}\left[\delta_l(t)\right]=2\dfrac{\rho_s}{\rho_l}V_e(t)-\dfrac{0.332}{D\mu_l}\dfrac{\rho_{g,w}U_g^{\,2}}{\sqrt{\rho_{g,w}U_gD/\mu_{g,w}}}\left[\delta_l(t)\right]^2 \\
\dfrac{d}{dt}\left[y(t)\right]=V_c-V_e(t) \\
\dfrac{d}{dt}\left[V_e(t)\right]=\dfrac{0.664}{D\mu_l}\dfrac{\rho_{g,w}U_g^{\,2}}{\sqrt{\dfrac{\rho_{g,w}U_gD}{\mu_{g,w}}}}\delta_l(t)\cdot V_e(t)-\left(\dfrac{0.332}{D\mu_l}\right)^2\dfrac{\rho_l}{\rho_s}\left(\dfrac{\rho_{g,w}U_g^{\,2}}{\sqrt{\rho_{g,w}U_gD/\mu_{g,w}}}\right)^2\left[\delta_l(t)\right]^3 \\
\dfrac{d}{dt}\left[T_l(t)\right]=
\end{cases}
$$

$$
\left[\frac{18.44\times10^6}{wD\rho_lc_{p,l}}\right]C_{exo}+\left[\frac{4c_{p,s}T_m}{c_{p,l}}\right]V_e(t)\cdot\left[\delta_l(t)\right]^{-1}
$$

$$
-\left[\frac{1.248}{\rho_l^{\frac{1}{2}}D^{\frac{3}{4}}}\left(\frac{\mu_lc_{p,l}}{K_l}\right)^{\frac{-2}{3}}\right]\left(\rho_{g,w}\mu_{g,w}U_g^3\right)^{\frac{1}{4}}\left[T_l(t)-T_m\right]\cdot\left[\delta_l(t)\right]^{\frac{-1}{2}}
$$

$$
-\left\{\frac{2.656}{\rho_lc_{p,l}}\frac{\rho_{g,w}U_g}{\sqrt{\rho_{g,w}U_gD/\mu_{g,w}}}\left[(Pr)_g\right]^{-2/3}\right\}\left[c_{p,g,w}T_l(t)-c_{p,g}T_g\right]\cdot\left[\delta_l(t)\right]^{-1}
$$

$$
-\left(\frac{2\rho_s}{\rho_l}\right)V_e(t)\cdot\left[T_m+T_l(t)\right]\cdot\left[\delta_l(t)\right]^{-1}-\left(\frac{4\rho_sh_f}{\rho_lc_{p,l}}\right)V_e(t)\cdot\left[\delta_l(t)\right]^{-1}
\qquad \textbf{(83)}
$$

Eq.81, **Eq.82** and **Eq.83** are the differential governing equations for the theoretical cutting system, in Fig.9, depending on the value of $y(t)$, respectively. The characteristics of the solutions are related to the type of the simultaneous differential equations [15,18].

For further analyses, the type of the governing equations can be essentially generalised as follows:

- $-D \cdot \cot\alpha \le y(t) \le 2a - D \cdot \cot\alpha$,

$$\begin{cases} \dfrac{d}{dt}\left[\delta_l(t)\right] = F_{\delta_l}\left\{V_e(t),\ \delta_l(t)\right\} \\ \dfrac{d}{dt}\left[P_{l,abs}(t)\right] = F_{P_{l,abs}}\left\{V_e(t),\ y(t)\right\} \\ \dfrac{d}{dt}\left[y(t)\right] = F_y\left\{V_e(t)\right\} \\ \dfrac{d}{dt}\left[V_e(t)\right] = F_{V_e}\left\{V_e(t),\ \delta_l(t)\right\} \\ \dfrac{d}{dt}\left[T_l(t)\right] = F_{T_l}\left\{V_e(t),\ \delta_l(t),\ T_l(t),\ P_{l,abs}(t)\right\} \end{cases} \tag{81'}$$

- $2a - D \cdot \cot\alpha \le y(t) \le 2a$,

$$\begin{cases} \dfrac{d}{dt}\left[\delta_l(t)\right] = F_{\delta_l}\left\{V_e(t),\ \delta_l(t)\right\} \\ \dfrac{d}{dt}\left[P_{l,abs}(t)\right] = 0 \\ \dfrac{d}{dt}\left[y(t)\right] = F_y\left\{V_e(t)\right\} \\ \dfrac{d}{dt}\left[V_e(t)\right] = F_{V_e}\left\{V_e(t),\ \delta_l(t)\right\} \\ \dfrac{d}{dt}\left[T_l(t)\right] = F'_{T_l}\left\{V_e(t),\ \delta_l(t),\ T_l(t)\right\} \end{cases} \tag{82'}$$

- $a - b < y(t) < -D \cdot \cot\alpha$ and $2a < y(t) < a + b$,

$$\begin{cases} \dfrac{d}{dt}\left[\delta_l(t)\right] = F_{\delta_l}\left\{V_e(t),\ \delta_l(t)\right\} \\ \dfrac{d}{dt}\left[P_{l,abs}(t)\right] = 0 \\ \dfrac{d}{dt}\left[y(t)\right] = F_y\left\{V_e(t)\right\} \\ \dfrac{d}{dt}\left[V_e(t)\right] = F_{V_e}\left\{V_e(t),\ \delta_l(t)\right\} \\ \dfrac{d}{dt}\left[T_l(t)\right] = F''_{T_l}\left\{V_e(t),\ \delta_l(t),\ T_l(t)\right\} \end{cases} \tag{83'}$$

where, the symbols F_{δ_l}, $F_{P_{l,abs}}$, F_y, F_{V_e} and F_{T_l} (or F'_{T_l}, F''_{T_l}) represent different functions which are made of non-linear or linear combinations of 5 time-dependent variables, $\delta_l(t)$, $P_{l,abs}(t)$, $V_e(t)$, $y(t)$ and $T_l(t)$, respectively. It is noted that the functions F_{δ_l}, F_{T_l}, $F_{P_{l,abs}}$ (if it is not equal to zero) and F_{V_e} are non-linear functions.

In conclusion, the type of the derived differential governing equations for the theoretical cutting system in Fig.8, by Eqs.81, 82, 83, belongs to five (or four) coupled, simultaneous, 1st-order, non-linear differential equations.

8-3. Physical boundary conditions

The boundary conditions for the differential governing equations in Eqs.81, 82, 83 have two-fold meaning: mathematical and physical. Mathematically, given any initial conditions, i.e., $\delta_l(0)$, $P_{l,abs}(0)$, $V_e(0)$, $y(0)$ and $T_l(0)$, the set of differential governing equations could be solved numerically. Physically, in this case, the 5 time-dependent variables should be bounded within certain scopes according to their respective physical meanings. The physical boundary conditions should be satisfied in each step of time evolution. It can be seen that the physical boundary conditions cannot be applied by simply taking the required volume in the phase space of the solutions according to the limits of the physical boundary conditions, while the solutions are obtained only by applying the mathematical boundary conditions, i.e., the given initial conditions.

The physical boundary conditions are derived as follows.

- For $y(t)$, its physical boundary conditions are associated with $\dot{e}_{exc}$, in Eq.75. This fact is also reflected in Fig.14.

$$a - b \le y(t) \le a + b \tag{84}$$

Eq.84 is the most important boundary condition of all the 5 boundary conditions. When $y(t) > a + b$ and $y(t) < a - b$, $\dot{e}_{exo} = 0$, the laser cutting stops. Even under the condition of Eq.84, $P_{l,abs}(t)$ is strongly dependent on $y(t)$, as identified in Eq.81, 82, 83.

- For $P_{l,abs}(t)$, it is easy to understand:

$$0 \le P_{l,abs}(t) \le P_l \tag{85}$$

- For $\delta_l(t)$, its possible maximum occurs only when the surface velocity of the molten metal layer, u_0, reaches its possible maximum. $\delta_{l,max}$ has been derived in Eq.39,

$$0 < \delta_l(t) \le \delta_{l,max} = \frac{1}{0.166}\sqrt{\frac{D}{U_g}}\frac{\rho_l^{(\frac{-1}{3})}\mu_l^{(\frac{2}{3})}}{\rho_{g,w}^{(\frac{1}{6})}\mu_{g,w}^{(\frac{1}{6})}} \tag{39}$$

It is noted that if $\delta_l(t) = 0$, there is no metallic liquid and thus no cut at all.

- For $V_e(t)$, by its physical meaning it is expected: $0 \le V_e(t) \le V_{e,max}$. The value of $V_{e,max}$ only occurs when $\delta_{l,max}$ appears, with $\frac{d\delta_l(t)}{dt} = 0$ at $\delta_l = \delta_{l,max}$. In this case, the maximum value of $\dot{m}_{out}$ is calculated by Eq.6'' in Chapter 4:

$$\dot{m}_{out,max} = \left(0.166\frac{w\rho_l}{\mu_l}\frac{\rho_{g,w}U_g^{\,2}}{\sqrt{\rho_{g,w}U_g D/\mu_{g,w}}}\right)\cdot\left[\delta_{l,max}\right]^2 \tag{86}$$

By Eq.1 for the continuity of the liquid, $V_e(t)$ can be ascertained,

$$0 \le V_e(t) \le V_{e,max} = \frac{U_g}{0.166\rho_s\sqrt{\rho_{g,w}U_g D/\mu_{g,w}}}\frac{\rho_l^{(\frac{1}{3})}\mu_l^{(\frac{1}{3})}}{\rho_{g,w}^{(\frac{-2}{3})}\mu_{g,w}^{(\frac{1}{3})}} \tag{87}$$

- For $T_l(t)$: $T_m < T_l(t) < T_b$ (88)

In Appendix 3, it is seen that, $T_m = 1808(^oK)$, $T_b = 3133(^oK)$.

In conclusion, the boundary conditions for the differential governing equations are made of Eqs.84, 85, 39, 87, 88, as in Eq.89:

$$\begin{cases} a - b \le y(t) \le a + b \\ 0 < \delta_l(t) \le \dfrac{1}{0.332}\sqrt{\dfrac{D}{U_g}}\dfrac{\rho_l^{(\frac{-1}{3})}\mu_l^{(\frac{2}{3})}}{\rho_{g,w}^{(\frac{1}{6})}\mu_{g,w}^{(\frac{1}{6})}} \\ 0 \le P_{l,abs}(t) \le P_l \\ 0 \le V_e(t) \le \dfrac{U_g}{0.166\rho_s\sqrt{\rho_{g,w}U_g D/\mu_{g,w}}}\dfrac{\rho_l^{(\frac{1}{3})}\mu_l^{(\frac{1}{3})}}{\rho_{g,w}^{(\frac{-2}{3})}\mu_{g,w}^{(\frac{1}{3})}} \\ T_m < T_l(t) < T_b \end{cases} \quad \textbf{(89)}$$

8-4. Determination of C_{exo}

In the differential governing equations, by Eqs.81-83, C_{exo} remains unknown. According to its nature identified in Chapter 5-4, C_{exo} will remain constant during the dynamic energy balance with respect to time, as long as a dynamic balance starts with the certain set of initial conditions, i.e., $\delta_l(0)$, $P_{l,abs}(0)$, $V_e(0)$, $y(0)$ and $T_l(0)$. In other words, C_{exo} is a sensitive-to-initial-condition constant. By its nature, it can be calculated as follows:

Given any initial conditions, $\delta_l(0)$, $P_{l,abs}(0)$, $V_e(0)$, $y(0)$ and $T_l(0)$, let F_{T_l} (F'_{T_l} and F''_{T_l}) in the differential governing equations Eqs.81'-83', be equal to zero, i.e.,

- $-D\cdot\cot\alpha \le y(t) \le 2a - D\cdot\cot\alpha$,

$$F_{T_l}\left\{V_e(0),\ \delta_l(0),\ T_l(0),\ P_{l,abs}(0),\ C_{exo}\right\} = 0 \quad \textbf{(90)}$$

- $2a - D \cdot \cot\alpha \le y(t) \le 2a$,

$$F'_{T_l}\{V_e(0),\ \delta_l(0),\ T_l(0),\ C_{exo}\} = 0 \tag{91}$$

- $a - b < y(t) < -D \cdot \cot\alpha$ and $2a < y(t) < a + b$,

$$F''_{T_l}\{V_e(0),\ \delta_l(0),\ T_l(0),\ C_{exo}\} = 0 \tag{92}$$

Eqs.90-92 show the general treatment to determine C_{exo}, respectively. The method of calculation will be used in the numerical approach to solve the sets of differential governing equations identified in Eqs.81,82,83. It can be seen that C_{exo} is sensitive to the given initial conditions.

8-5. Numerical method for differential governing equations

So far, the differential governing equations for the theoretical laser cutting system shown in Fig.8 have been derived, by Eqs.81,82,83, depending on the scope of $y(t)$, respectively. They are bounded by the physical boundary conditions identified in Eq.89, in each step of time evolution. Given any initial conditions, i.e., $\delta_l(0)$, $P_{l,abs}(0)$, $V_e(0)$, $y(0)$ and $T_l(0)$, C_{exo} is determined by Eqs.90,91,92, depending on the scope of $y(t)$, respectively.

The type of the governing equations are generalised in Eqs.81',82',83', corresponding to Eqs.81,82,83, respectively. It is clear that Eq.81 belongs to the 5 coupled, 1st-order, non-linear, ordinary differential equations; Eq.82 and Eq.83 belong to the 4 coupled, 1st-order, non-linear, ordinary differential equations, respectively.

To solve the differential governing equations, a feasible numerical approach is necessary. Commercially, several software packages, e.g., *Mathematica*, *MathCad* and *NAG routine*, are able to numerically solve the sets of 1st-order differential equations. However, these software packages are difficult to incorporate with the special requirement, which is the

physical boundary conditions for the 5 time-dependent variables, in Eq.89, in this thesis. As analysed before, Eq.89 must be satisfied in each step of time evolution, as long as the simulation of the laser cutting process continues ($a - b \leq y(t) \leq a + b$).

In Appendix 6, a well-structured program coded in C is designed to solve Eqs.81,82,83 bounded by Eq.89. The algorithm is based on the 4th-order Runge-Kutta method *. The program has been tested with several simpler 1st-order non-linear differential equations.

8-6. An example of differential governing equations

With the typical data listed in Appendixes 1-3, which have been used for the evaluations of the derived quantities in Chapters 4-7, respectively, a sample of the differential governing equations for the theoretical laser cutting system in Fig.9 is demonstrated. It is to exhibit:

- the coefficients in the sets of differential governing equations are dependent on the laser operating parameters and the physical properties of the gas, the liquid and the solid;
- the sensitive-to-initial-conditions constant, C_{exo}, is determined by the initial conditions;
- the chaotic nature of the system are dependent on the choices of the coefficients and C_{exo};

Given the initial conditions: $y(0)$, $\delta_l(0)$, $P_{l,abs}(0)$, $V_e(0)$ and $T_l(0)$ at $t = 0$ $(s.)$, the differential governing equations are derived, respectively,

* The numerical method for integration of ordinary differential equations is beyond the topic of this thesis. The theory and programming may be referred to [P.707, reference 40]

- When $\begin{cases} -0.525\times10^{-3} \le y(t) \le 1.475\times10^{-3} & (m.) \\ 0 < \delta_l(t) \le 0.105\times10^{-3} & (m.) \\ 0 \le P_{l,abs}(t) \le 800 & (W.) \\ 0 \le V_e(t) \le 85.255\times10^{-3} & (m/s) \\ 1808 < T_l(t) < 3133 & (^\circ K) \end{cases}$

the differential governing equations,

$$\begin{cases} \dfrac{d}{dt}\left[\delta_l(t)\right] = 2.00356V_e(t) - 3.84286\times10^{6}\left[\delta_l(t)\right]^2 & (m/s) \\ \dfrac{d}{dt}\left[P_{l,abs}(t)\right] = 9.25214\times10^{5}\,\dfrac{0.015 - V_e(t)}{exp\left[2\times10^{3}\left|y(t) - 0.475\times10^{-3}\right|\right]} & (W/s) \\ \dfrac{d}{dt}\left[y(t)\right] = 0.015 - V_e(t) & (m/s) \\ \dfrac{d}{dt}\left[V_e(t)\right] = 7.68572\times10^{6}\,\delta_l(t)\cdot V_e(t) - 1.47413\times10^{13}\left[\delta_l(t)\right]^3 & (m/s^2) \\ \dfrac{d}{dt}\left[T_l(t)\right] = 6.37918\times10^{-2}\,P_{l,abs}(t)\cdot\left[\delta_l(t)\right]^{-1} + 2.94084\times10^{5}C_{exo} \\ \quad + 6.0593\times10^{3}V_e(t)\cdot\left[\delta_l(t)\right]^{-1} - 19.0872\left[T_l(t) - 1808\right]\cdot\left[\delta_l(t)\right]^{\frac{-1}{2}} \\ \quad - 5.80102\times10^{-7}\left[1.1647\times10^{3}\,T_l(t) - 2.29404\times10^{5}\right]\cdot\left[\delta_l(t)\right]^{-1} \\ \quad - 2.00356V_e(t)\cdot\left[1808 + T_l(t)\right]\cdot\left[\delta_l(t)\right]^{-1} - 1.6395\times10^{3}V_e(t)\cdot\left[\delta_l(t)\right]^{-1} & (^\circ K/s) \end{cases}$$

the sensitive-to-initial-conditions constant, C_{exo},

$$C_{exo} = \frac{-1}{2.94084\times10^{5}}\Big\{\, 6.37918\times10^{-2}\,P_{l,abs}(0)\cdot\left[\delta_l(0)\right]^{-1} + 6.0593\times10^{3}V_e(0)\cdot\left[\delta_l(0)\right]^{-1} - 19.0872\left[T_l(0) - 1808\right]\cdot\left[\delta_l(0)\right]^{\frac{-1}{2}} - 5.80102\times10^{-7}\left[1.1647\times10^{3}\,T_l(0) - 2.29404\times10^{5}\right]\cdot\left[\delta_l(0)\right]^{-1} - 2.00356V_e(0)\cdot\left[1808 + T_l(0)\right]\cdot\left[\delta_l(0)\right]^{-1} - 1.6395\times10^{3}V_e(0)\cdot\left[\delta_l(0)\right]^{-1} \Big\}$$

- When
$$\begin{cases} 1.475\times10^{-3} \le y(t) \le 2\times10^{-3} & (m.) \\ 0 < \delta_l(t) \le 0.105\times10^{-3} & (m.) \\ P_{l,abs}(t) = 800 & (W.) \\ 0 \le V_e(t) \le 85.255\times10^{-3} & (m/s) \\ 1808 < T_l(t) < 3133 & (^oK) \end{cases}$$

the differential governing equations:

$$\begin{cases} \dfrac{d}{dt}\left[\delta_l(t)\right] = 2.00356V_e(t) - 3.84286\times10^{6}\left[\delta_l(t)\right]^2 & (m/s) \\ \dfrac{d}{dt}\left[y(t)\right] = 0.015 - V_e(t) & (m/s) \\ \dfrac{d}{dt}\left[V_e(t)\right] = 7.68572\times10^{6}\,\delta_l(t)\cdot V_e(t) - 1.47413\times10^{13}\left[\delta_l(t)\right]^3 & (m/s^2) \\ \dfrac{d}{dt}\left[T_l(t)\right] = 51.0335\left[\delta_l(t)\right]^{-1} + 2.94084\times10^{5}C_{exo} \end{cases}$$

$$+\ 6.0593\times10^{3}V_e(t)\cdot\left[\delta_l(t)\right]^{-1} - 19.0872\left[T_l(t)-1808\right]\cdot\left[\delta_l(t)\right]^{\frac{-1}{2}}$$

$$-\ 5.80102\times10^{-7}\left[1.1647\times10^{3}T_l(t) - 2.29404\times10^{5}\right]\cdot\left[\delta_l(t)\right]^{-1}$$

$$-2.00356V_e(t)\cdot\left[1808+T_l(t)\right]\cdot\left[\delta_l(t)\right]^{-1} - 1.6395\times10^{3}V_e(t)\cdot\left[\delta_l(t)\right]^{-1} \qquad (^oK/s)$$

the sensitive-to-initial-conditions constant, C_{exo},

$$C_{exo} = \frac{-1}{2.94084\times10^{5}}\Big\{\ 51.0335\cdot\left[\delta_l(0)\right]^{-1}$$

$$+\ 6.0593\times10^{3}V_e(0)\cdot\left[\delta_l(0)\right]^{-1} - 19.0872\left[T_l(0)-1808\right]\cdot\left[\delta_l(0)\right]^{\frac{-1}{2}}$$

$$-\ 5.80102\times10^{-7}\left[1.1647\times10^{3}T_l(0) - 2.29404\times10^{5}\right]\cdot\left[\delta_l(0)\right]^{-1}$$

$$-2.00356V_e(0)\cdot\left[1808+T_l(0)\right]\cdot\left[\delta_l(0)\right]^{-1} - 1.6395\times10^{3}V_e(0)\cdot\left[\delta_l(0)\right]^{-1}\ \Big\}$$

- When $\begin{cases} -1\times10^{-3} < y(t) < -0.525\times10^{-3};\ 2\times10^{-3} < y(t) < 3\times10^{-3} & (m.) \\ 0 < \delta_l(t) \le 0.105\times10^{-3} & (m.) \\ P_{l,abs}(t) = 0 & (W.) \\ 0 \le V_e(t) \le 85.255\times10^{-3} & (m/s) \\ 1808 < T_l(t) < 3133 & (^oK) \end{cases}$

the differential governing equations,

$$\begin{cases} \dfrac{d}{dt}\left[\delta_l(t)\right] = 2.00356V_e(t) - 3.84286\times10^{6}\left[\delta_l(t)\right]^2 & (m/s) \\ \dfrac{d}{dt}\left[y(t)\right] = 0.015 - V_e(t) & (m/s) \\ \dfrac{d}{dt}\left[V_e(t)\right] = 7.68572\times10^{6}\,\delta_l(t)\cdot V_e(t) - 1.47413\times10^{13}\left[\delta_l(t)\right]^3 & (m/s^2) \\ \dfrac{d}{dt}\left[T_l(t)\right] = 2.94084\times10^{5}\,C_{exo} \end{cases}$$

$$+\ 6.0593\times10^{3}V_e(t)\cdot\left[\delta_l(t)\right]^{-1} - 19.0872\left[T_l(t)-1808\right]\cdot\left[\delta_l(t)\right]^{\frac{-1}{2}}$$

$$-\ 5.80102\times10^{-7}\left[1.1647\times10^{3}\,T_l(t) - 2.29404\times10^{5}\right]\cdot\left[\delta_l(t)\right]^{-1}$$

$$-2.00356V_e(t)\cdot\left[1808+T_l(t)\right]\cdot\left[\delta_l(t)\right]^{-1} - 1.6395\times10^{3}V_e(t)\cdot\left[\delta_l(t)\right]^{-1} \qquad (^oK/s)$$

the sensitive-to-initial-conditions constant, C_{exo},

$$C_{exo} = \frac{-1}{2.94084\times10^{5}}\Big\{\ 6.0593\times10^{3}V_e(0)\cdot\left[\delta_l(0)\right]^{-1} - 19.0872\left[T_l(0)-1808\right]\cdot\left[\delta_l(0)\right]^{\frac{-1}{2}}$$

$$-\ 5.80102\times10^{-7}\left[1.1647\times10^{3}\,T_l(0) - 2.29404\times10^{5}\right]\cdot\left[\delta_l(0)\right]^{-1}$$

$$-2.00356V_e(0)\cdot\left[1808+T_l(0)\right]\cdot\left[\delta_l(0)\right]^{-1} - 1.6395\times10^{3}V_e(0)\cdot\left[\delta_l(0)\right]^{-1}\ \Big\}$$

Given the initial conditions:

$$\begin{cases} y(t) = 1.12 \times 10^{-3} & (m.) \\ \delta_l(t) = 0.026 \times 10^{-3} & (m.) \\ P_{l,abs}(t) = 700 & (W.) \\ V_e(t) = 23.5 \times 10^{-3} & (m/s) \\ T_l(t) = 1900 & (^{\circ}K) \end{cases}$$

at $t = 0\ (s.)$. Fig.15 shows the respective variations of the 5 time-dependent variables with respect to time, within *50* seconds.

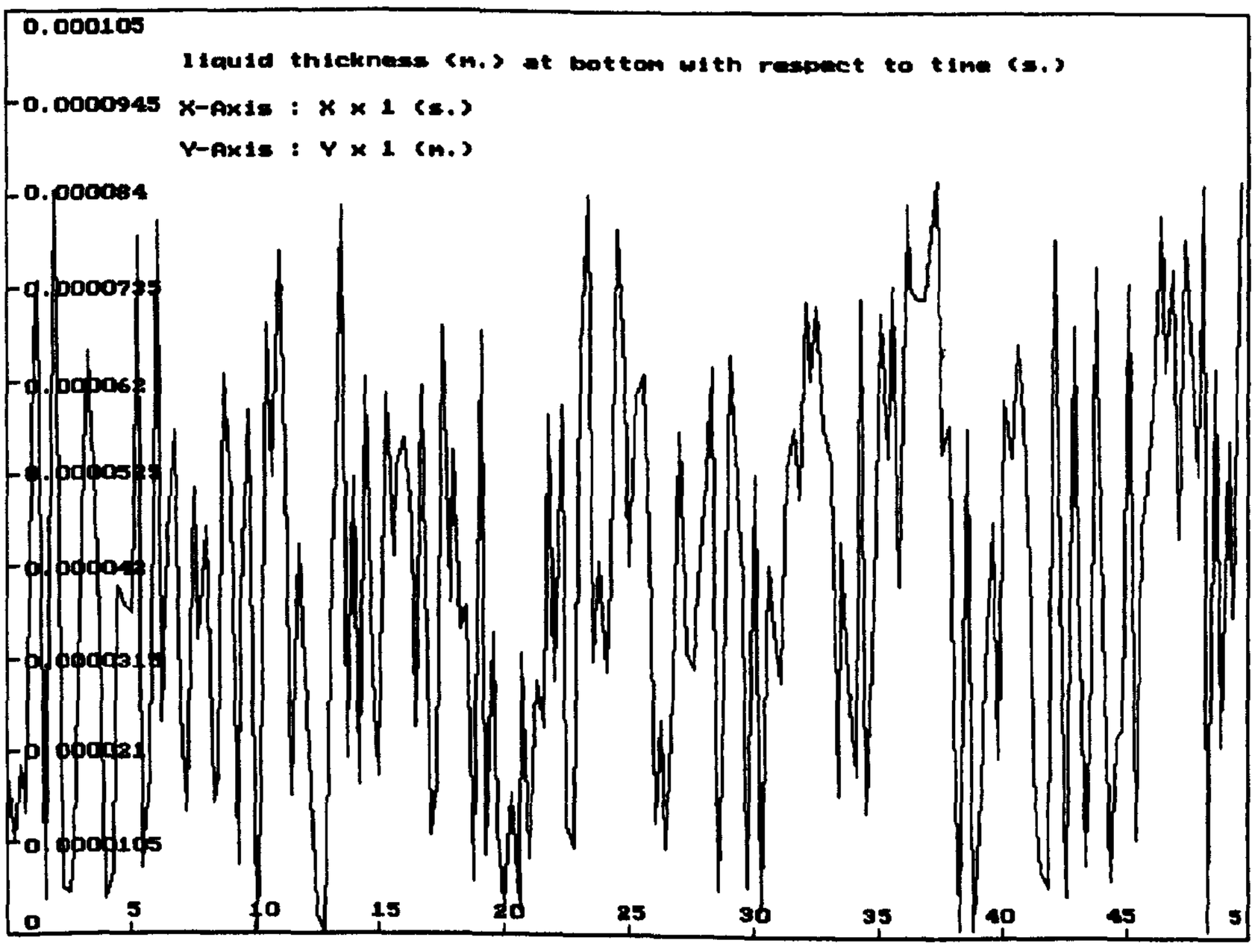

Figure 15 (a). *The thickness of the molten metal layer, $\delta_l(t)$, varies with respect to time (50 seconds)*

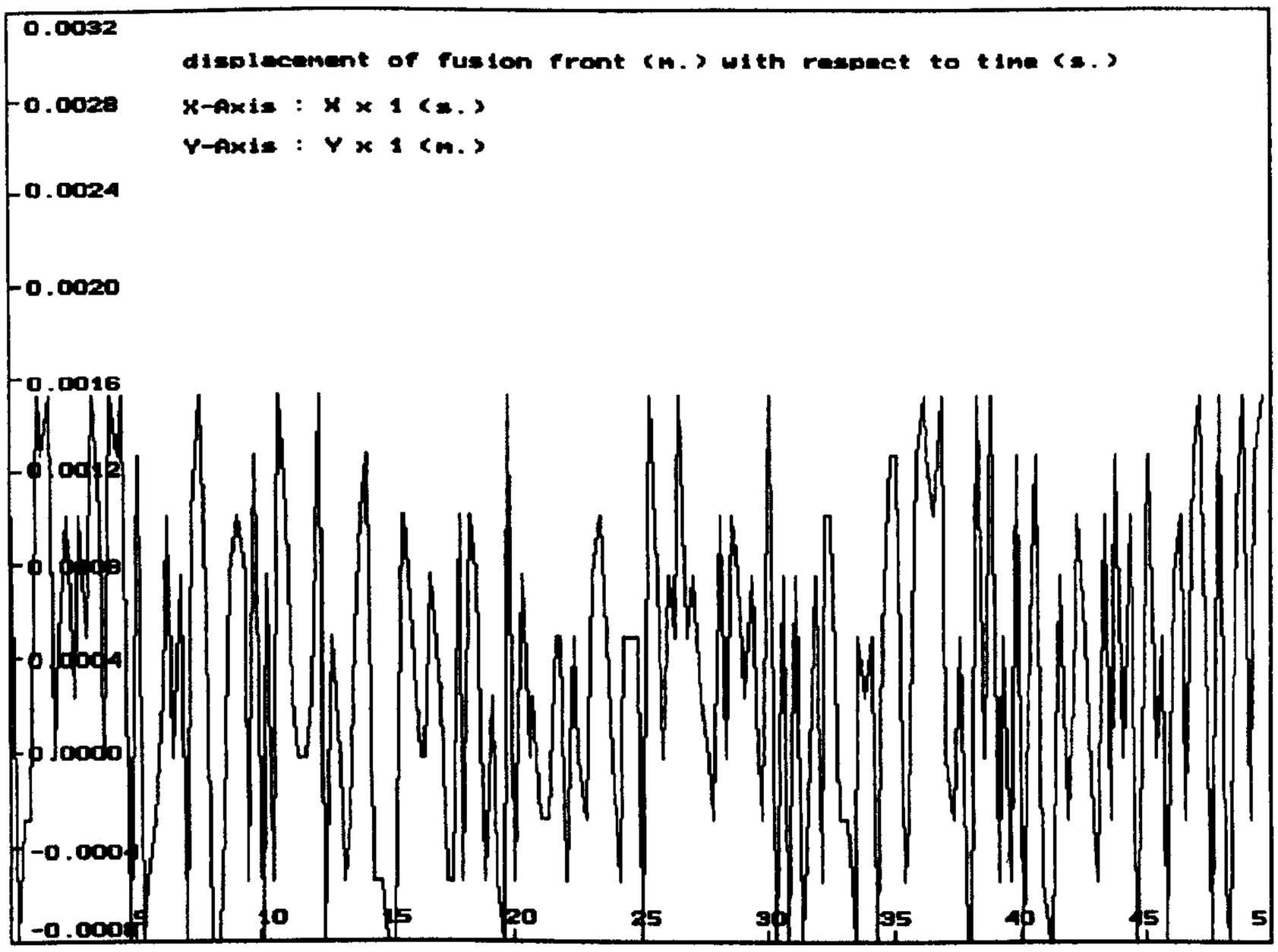

Figure 15 (b). *The displacement of laser beam front relative to the liquid / solid interface, $y(t)$, varies with respect to time (50 seconds)*

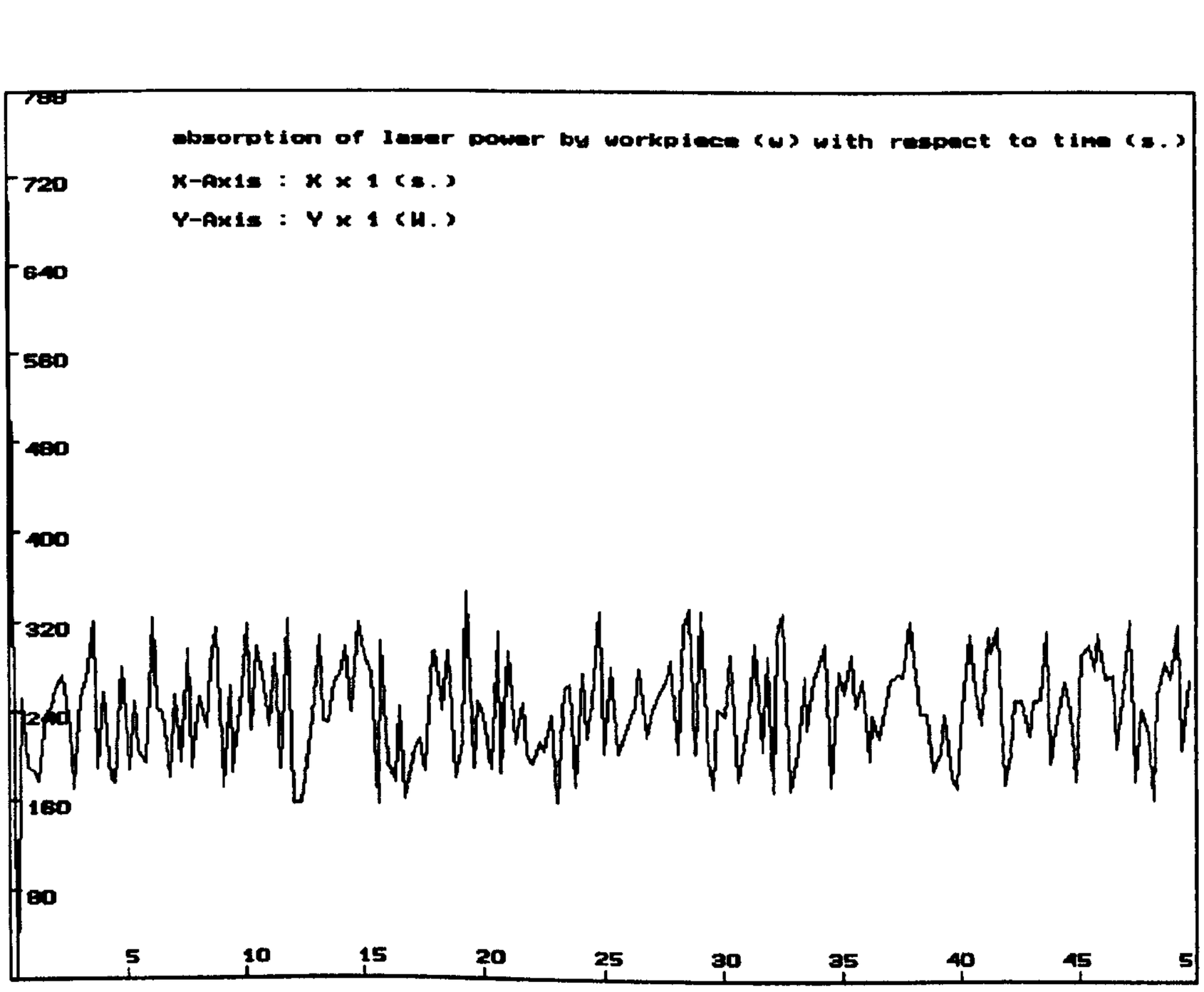

Figure 15 (c). *The absorption of laser power by the workpiece, $P_{l,abs}$, varies with respect to time (50 seconds)*

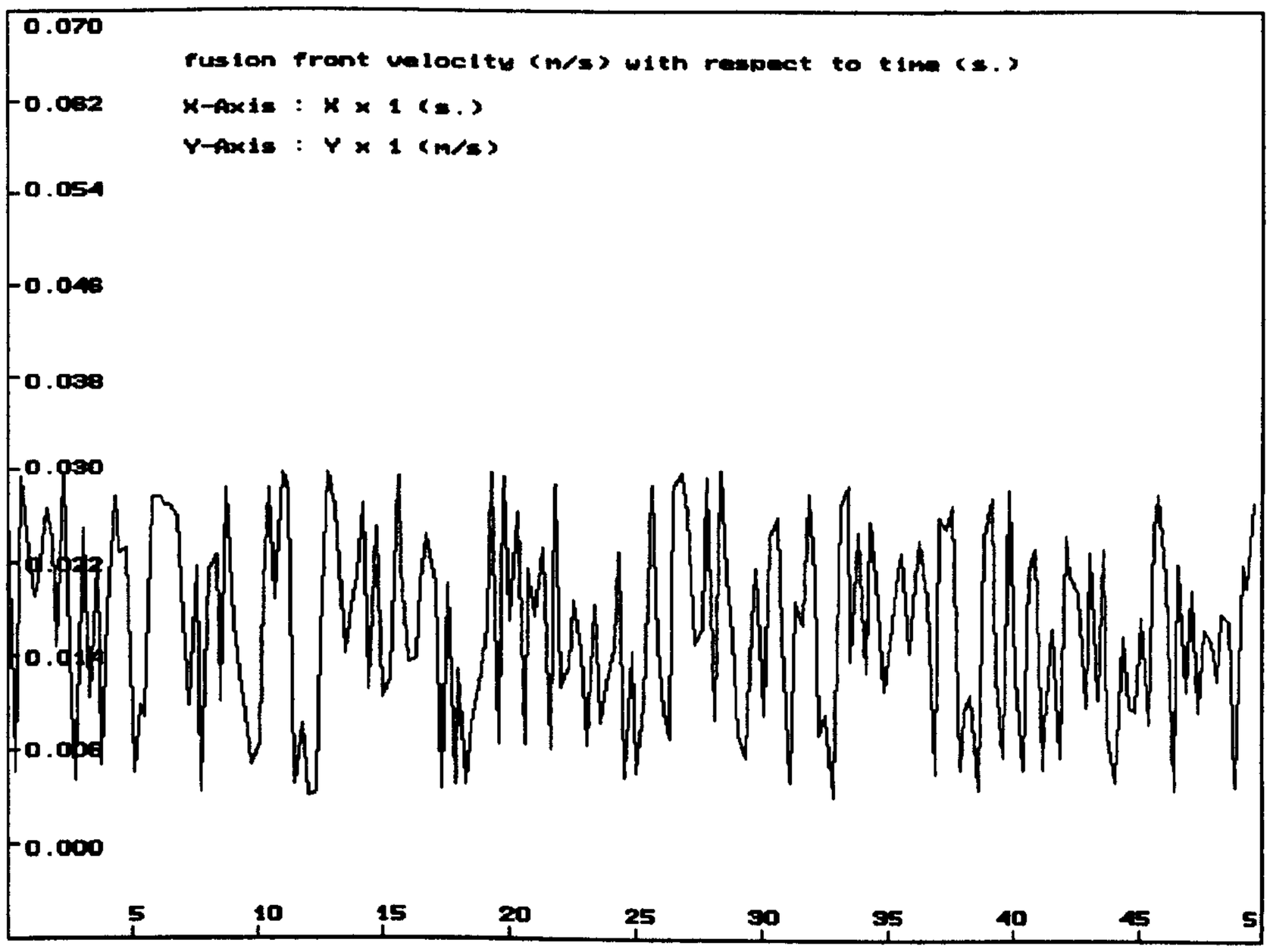

Figure 15 (d). *The velocity of propagation of fusion front, $V_e(t)$, varies with respect to time (50 seconds)*

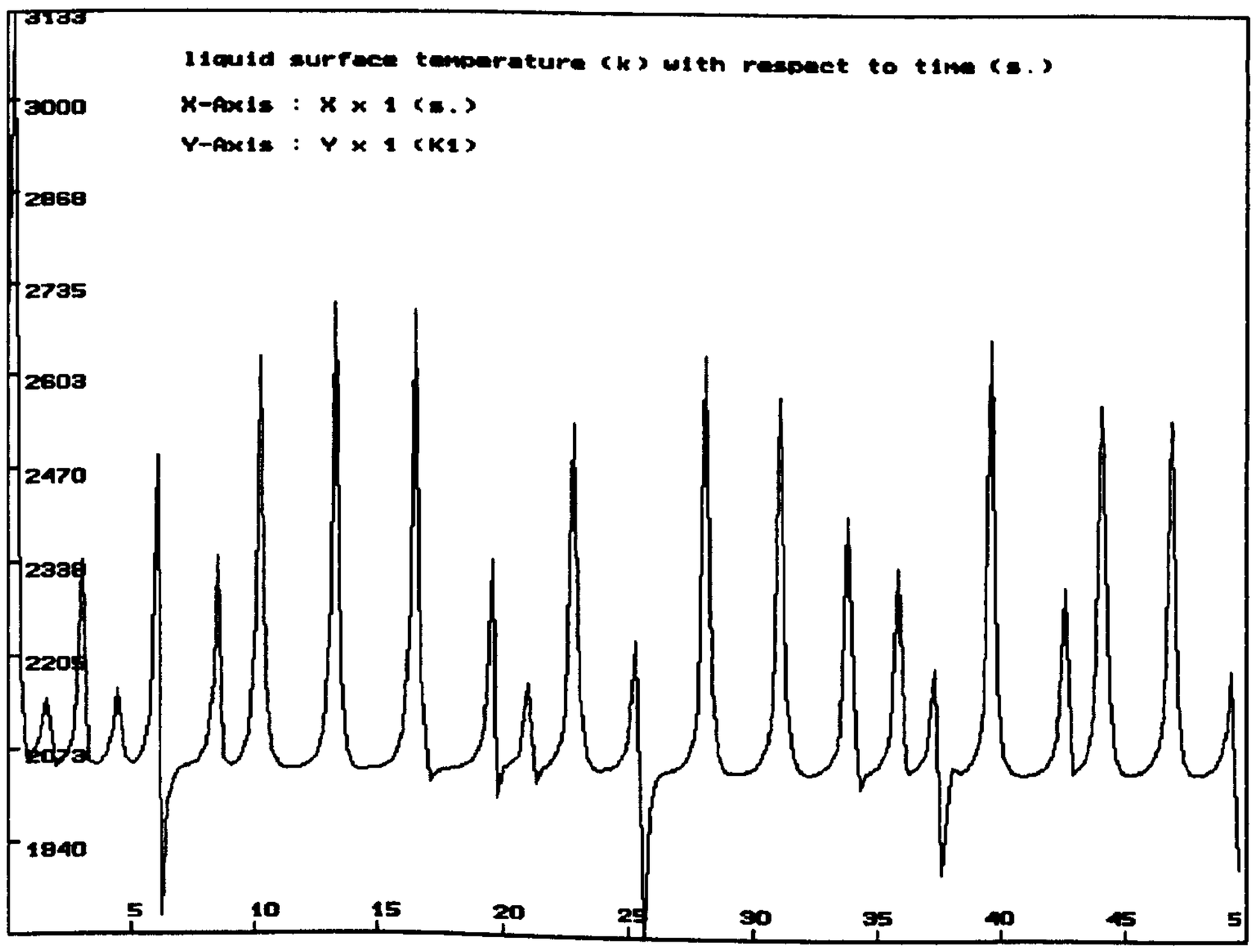

Figure 15 (e). *The surface temperature of molten metal layer at the gas / liquid interface, $T_l(t)$, varies with respect to time (50 seconds)*

Here is one more example. Given the initial conditions:

$$\begin{cases} y(t) = 0.35 \times 10^{-3} & (m.) \\ \delta_l(t) = 0.012 \times 10^{-3} & (m.) \\ P_{l,abs}(t) = 350 & (W.) \\ V_e(t) = 25 \times 10^{-3} & (m/s) \\ T_l(t) = 2000 & (^oK) \end{cases}$$

at $t=0\ (s.)$. Fig.16 shows the respective variations of the 5 time-dependent variables with respect to time, within *50* seconds.

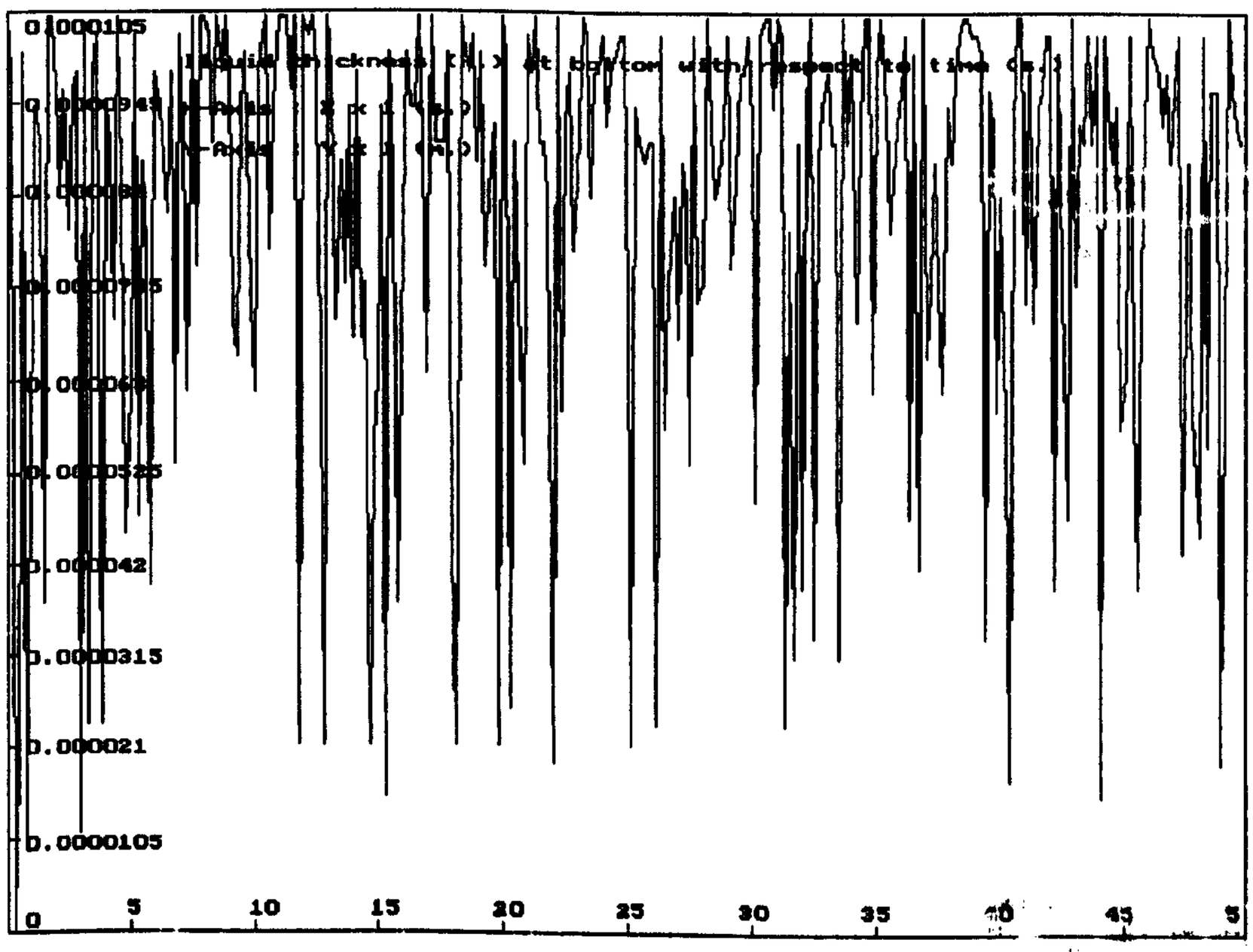

Figure 16 (a). *The thickness of the molten metal layer, $\delta_l(t)$, varies with respect to time (50 seconds)*

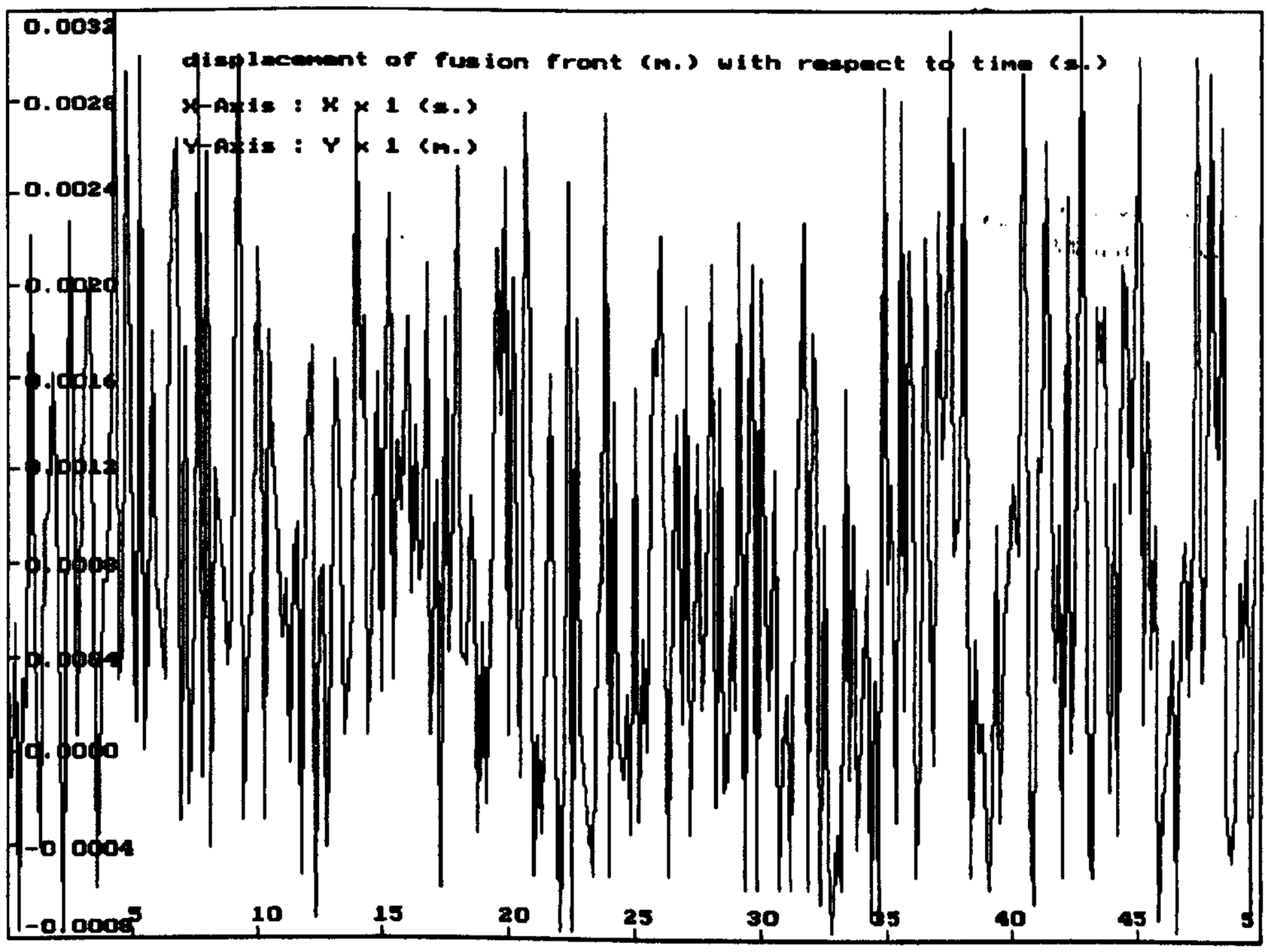

Figure 16 (b). *The displacement of laser beam front relative to the liquid / solid interface, $y(t)$, varies with respect to time (50 seconds)*

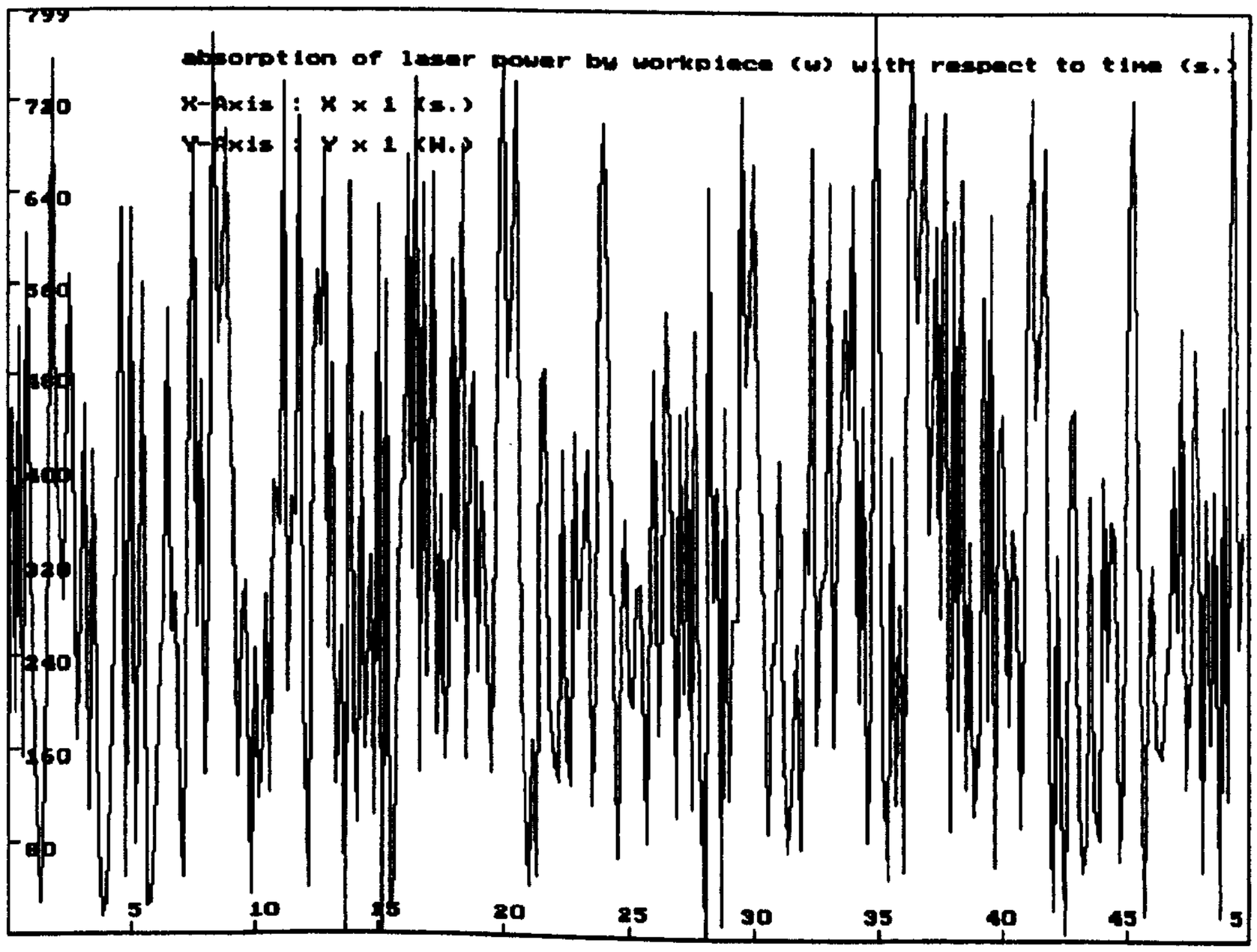

Figure 16 (c). *The absorption of laser power by the workpiece, $P_{l,abs}$, varies with respect to time (50 seconds)*

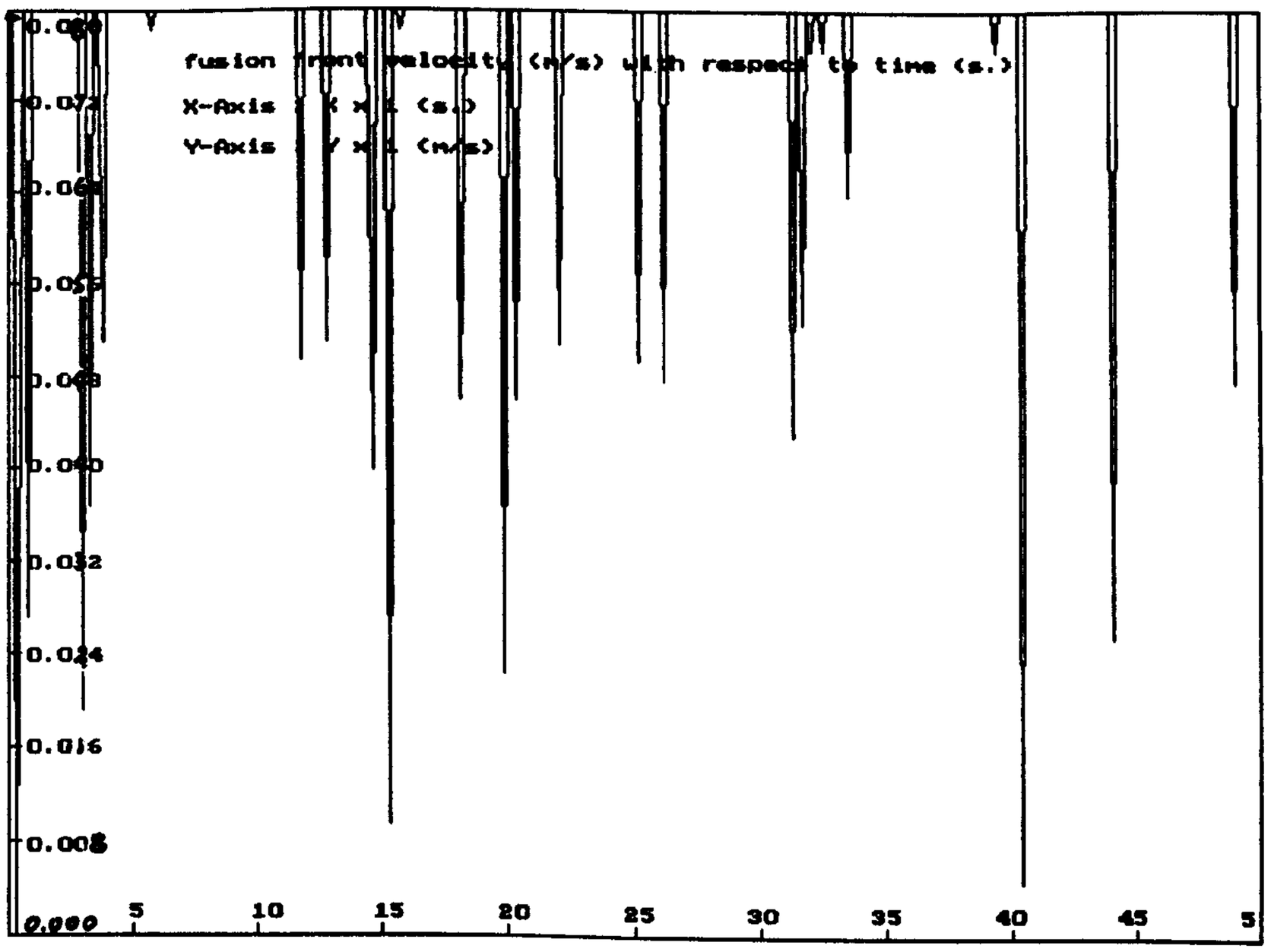

Figure 16 (d). *The velocity of propagation of fusion front, $V_e(t)$, varies with respect to time (50 seconds)*

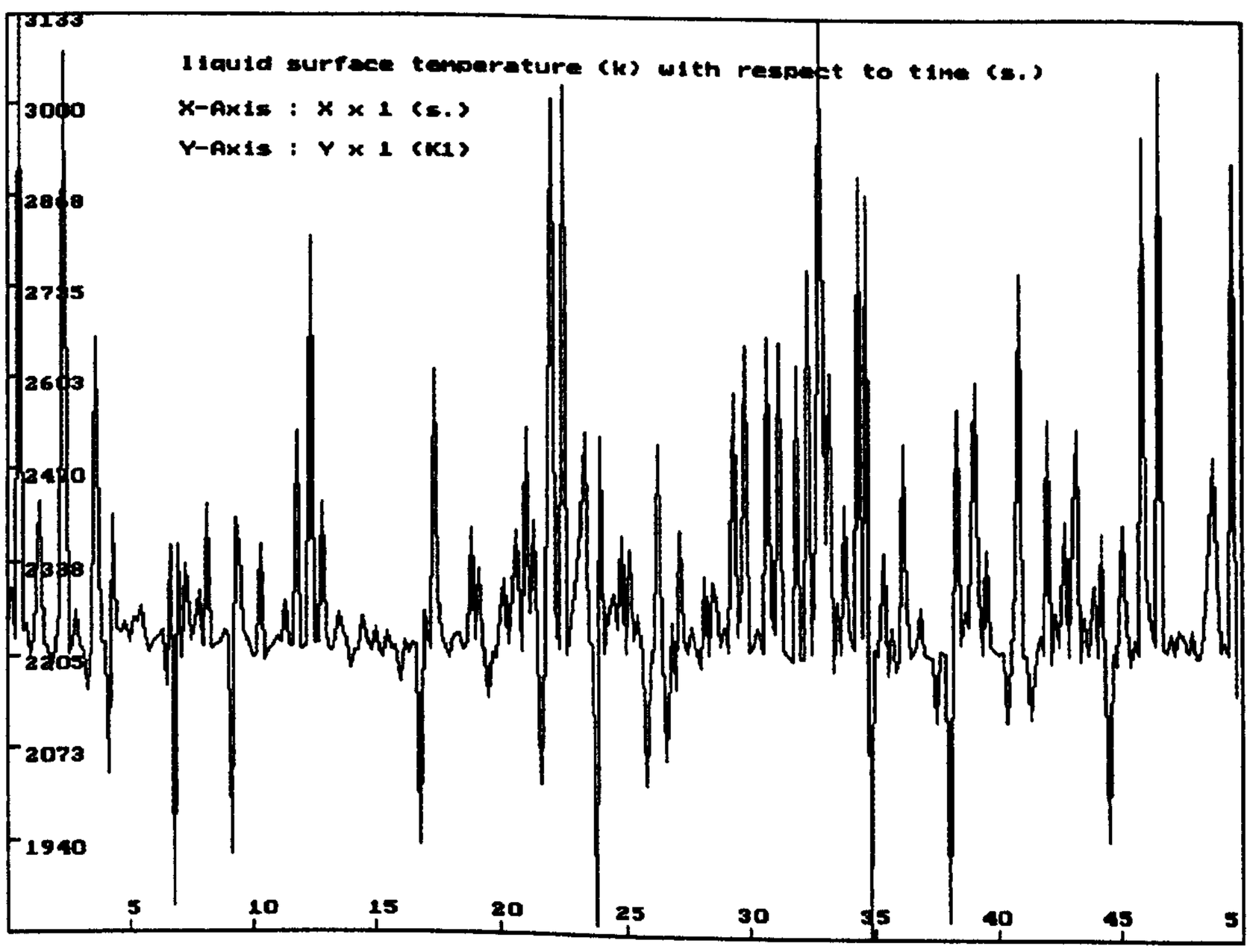

Figure 16 (e). *The surface temperature of molten metal layer at the gas / liquid interface, $T_l(t)$, varies with respect to time (50 seconds)*

Fig.15 and Fig.16 demonstrate only the 2 examples of many possible solutions. It is clear that, when the coefficients in the sets of differential governing equations are determined by giving the laser operating parameters and the physical properties of the gas, the liquid and the solid using the typical data listed in Appendixes 1-3, the possible solutions during the limited cutting time are still up to the initial conditions: $y(0)$, $\delta_l(0)$, $P_{l,abs}(0)$, $V_e(0)$ and $T_l(0)$ at $t = 0\ (s.)$ as well as the sensitive-to-initial-conditions constant, C_{exo}.

In general, the characteristics of the solutions in Fig.15 and Fig.16 can be concluded as follows:

The 5 time-dependent variables, namely, the thickness of the molten metal layer, $\delta_l(t)$; the absorption of laser power by the workpiece, $P_{l,abs}(t)$; the displacement of laser beam front relative to the liquid / solid interface, $y(t)$; the velocity of propagation of fusion front, $V_e(t)$; the surface temperature of the molten metal layer at the gas / liquid interface, $T_l(t)$, always vary with the cutting time. All the individual variables are normally characteristic of non-periodic oscillations. In this sense, the laser cutting process is described as dynamic rather than static.

In Fig.15(a), the time-averaged $\delta_l(t)$ is approximately $0.04\,(mm)$ and its varying range is approximately $0 < \delta_l(t) \le 0.092\,(mm)$. In Fig.15(b), the time-averaged $y(t)$ is roughly calculated at $0.38\,(mm)$ with its varying range: $-0.83 \le y(t) \le 1.58\,(mm)$. In Fig.15(c), the time-averaged $P_{l,abs}(t)$ is $241.3\,(W.)$ with $356 \le P_{l,abs}(t) \le 157\ (W.)$. In Fig.15(d), the time-averaged $V_e(t)$ is approximately $16.2\,(mm/s)$ with $31.8 \le V_e(t) \le 4.1\ (mm/s)$. In Fig.15(e), the time-averaged $T_l(t)$ is $1992\,(^0K)$ with $1890 \le T_l(t) < 3133\ (^0K)$.

The rationality of the theoretical solutions in Fig.15 may be qualitatively proved with the experimental data introduced in Appendix 1* and the findings by other researchers.

---

* The theoretical laser cutting system for which the differential governing equations are built is not the same as in the experiment. This can be referred to the tests in Chapter 9-2. It is therefore concluded that the time-averaged quantities from the theoretical laser cutting system can only qualitatively be checked with the corresponding data from the practical experiments

In Appendix 1, the velocity of translation of the laser beam along Y is $V_c = 15\ (mm/s)$. By comparing V_c ($15\ mm/s$) and the time-averaged $V_e(t)$ ($16.2\ mm/s$) in Fig.15(d), it is seen that the theoretical laser cutting process is very reasonable. As expected, the oscillation of $V_e(t)$ around V_c is verified.

Further, the time-averaged $T_l(t)$ of $1992(^0K)$ in Fig.15(e) is qualitatively supported by the experimental finding by Arata et al [4].

In comparison with the example in Fig.15 where the laser cutting process does not stop in the limited cutting time, i.e., $V_e(t) \neq 0$, Fig.16 demonstrates another example where the fusion front stops moving intermittently ($V_e(t) = 0$ or $V_e(t) = 85.26\ (mm/s)$). The time-averaged quantities of the 5 time-dependent variables are as follows. The time-averaged $\delta_l(t)$ is approximately $0.081(mm)$ with its varying range, $0 < \delta_l(t) \leq 0.105(mm)$. The time-averaged $y(t)$ is $0.78(mm)$ with its varying range, $-0.73 \leq y(t) \leq 3.2\ (mm)$. The time-averaged $P_{l,abs}(t)$ is $358\ (W.)$ with its varying range, $0 \leq P_{l,abs}(t) \leq 800\ (W.)$. The time-averaged $V_e(t)$ is $20.7\ (mm/s)$ with $0 \leq V_e(t) \leq 85.26\ (mm/s)$. In Fig.16(e), the time-averaged $T_l(t)$ is $2295(^0K)$ with its varying range, $1843 \leq T_l(t) < 3133\ (^0K)$.

The discontinuities in $V_e(t)$ shown in Fig.16(d) suggest that the fusion front does stop intermittently during the limited cutting time, i.e., $V_e(t) = 0$; it also intermittently stays at the maximum possible velocity, i.e., $V_e(t) = 85.26\ (mm/s)$. To keep the laser cutting process carrying on, the time-averaged $V_e(t)$ is $20.7\ (mm/s)$ and it is still comparable to the laser operating parameter, $V_c = 15\ (mm/s)$.

In general, the numerical calculations suggest that the respective variations of 5 time-independent variables are sensitive to the initial conditions, even when the coefficients in the differential governing equations are constant, assuming the thermophysical properties and the operating parameters in Appendices 1-3 are constant.

8-7. Chaotic nature of laser cutting system

The nature of the dynamic solutions, e.g., in Figs.15,16, of the differential governing equations for the theoretical laser cutting system, as shown in Fig.9, can be understood by Chaos theory in the subset of nonlinear dynamics [15,16,17,18,19]. As concluded by Baker [P.3, reference 18], the systems such as Eqs.81'-83' representing the differential governing equations Eqs.81-83 are often chaotic for some choices of the coefficients in the equations. The recent findings from Chaos theory help predict the optimized operating parameters.

One of the most significant developments in the pure mathematics community in this century may be Chaos theory, which is still being contributed to and established from different research communities. So far, one of the established branches has been able to deal with the so-called dynamic nonlinear systems which are controlled by the set of coupled first-order non-linear differential equations. The interests in chaos has rapidly grown since 1963 when Lorenz [15] published his numerical findings from the abstracted dynamic model of mass and heat convection, and discussed its implications for weather predictions *. His revolutionary achievement has since become one of icons in Chaos theory in respect of non-linear differential equations, as far as it is understood today [18]. Deep in the center of Lorenz's system the understanding of predictability or unpredictability for the nonlinear system has essentially provided a brand new approach to look at practical dynamic systems in science, engineering and mathematics. Lorenz's system, shown in Eq.93, is the set of 3 coupled 1st-order non-linear differential equations,

$$\left.\begin{aligned} dx/dt &= -\sigma \cdot x + \sigma \cdot y \\ dy/dt &= -x \cdot z + r \cdot x - y \\ dz/dt &= x \cdot y - b \cdot z \end{aligned}\right\} \tag{93}$$

* It was abstracted by Lorenz in 1963 from the complicated governing equations in the weather prediction modelling among temperature variation, pressure gradient and convective motion [15]. The mathematical symbols in Eq.93 only apply to this equation and Fig.17.

where, x, y, z are unknown time-dependent variables and σ, r, b are time-independent variables. When $\sigma = 10,\ b = 8/3,\ r = 28$, found by Lorenz, this simple-looking system has the solution in Fig.17. The most significant meaning is that 3 time-dependent variables are always attracted by the "strange attractor", when σ, r, b are chosen in some ranges. The characteristics of Lorenz's system can be referred to Appendix 7.

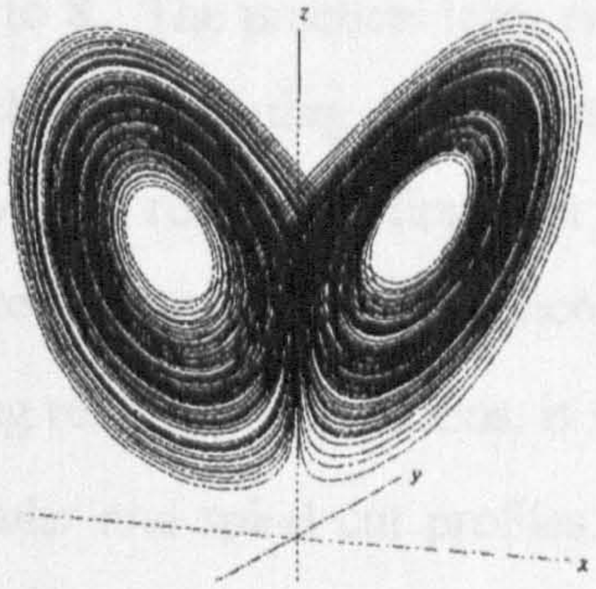

Figure 17. *Strange attractor by Lorenz's system when* $\sigma = 10,\ b = 8/3,\ r = 28$

The comparison between the differential governing equations Eqs.81-83 for the cutting system and the differential governing equations Eq.93 for Lorenz's system suggests the approach to choose the optimized operating parameters such as the laser power, P_l, and the cutting velocity, V_c, which affect the coefficients in the differential governing equations. The method to predict can be carried out in 3 steps:

- to choose the different combinations of the operating parameters;
- to run the differential governing equations with as many initial conditions as possible;
- the optimized operating parameters are discovered when the nearly periodic variation of $\delta_l(t)$ together with the smallest phase space comprised of the 5 time-dependent variables are reached.

The dynamic formation and development of the striations and kerf widths are concluded in Chapter 10, after the variable striations from the experiments are confirmed in Chapter 9.

Chapter 9. Experimental measurement

In this chapter, a practical laser cutting system is studied in comparison with the theoretical laser cutting system as shown in Fig.9, for which the differential governing equations have been constructed in chapters 2 to 8. The practical laser cutting system symbolizes practical laser cutting processes in which the operating parameters, e.g., the laser power and beam translation velocity, could vary with respect to time. In the experiments, the laser power (P_l) and the power intensity are measured. The influence of the variation of the velocity of beam translation (V_c) on cutting results, i.e., striations, is studied by designing an X-Y table which can produce linear, circular and spiral cut profiles. Typical measured striations are shown. More experimental results are included in Appendix 7.

9-1. Experimental set-up

The experimental work was carried out in CO_2 Laboratory, Laser and Optical System Engineering Centre, Department of Mechanical Engineering, Glasgow University. The arrangement is schematically shown in Fig.1. The operating parameters are set as follows:

- The laser power is provided with the industrial Ferranti MFKP CO_2 Laser with coaxial O_2 jet gas. The laser power is set at *1* (*kW.*) in continuous wave. The wavelength of the laser emission is *10.6* (*μm.*);
- The diameter of laser beam before the focusing lens is measured at around *11* (*mm.*); the transverse electromagnetic mode is Gaussian profile;
- The focal length of the focusing lens is *110* (*mm.*);
- The gap between the focal waist and the nozzle outlet is set at *0.2* to *0.5* (*mm.*);
- The diameter of the slightly convergent gas nozzle is *1* (*mm*);
- The stagnation pressure of the jet gas is set at *2* to *3* (*atm.*);
- The cutting velocity is controlled constant, at *600* to *1,400* (*mm/min*);
- The mild steel workpiece has the thickness of *5* to *8* (*mm.*).

9-2. Measurement of the focused laser power

9-2-1. The stability of laser power

The stability of laser power is measured with a Power Sticker; the irradiation time is about *20* seconds.

	At $t = 0$ (*min.*)	At $t = 5$ (*min.*)	At $t = 10$ (*min.*)
Day 1	*720* (*W.*)	*750* (*W.*)	*695* (*W.*)
Day 2	*690* (*W.*)	*714* (*W.*)	*734* (*W.*)

Table 1. *The measurement of the focused laser power*

The measurement of the focused laser power, in Tab.1, shows that the laser power (P_l) used in the experiments is not constant, with respect to time.

9-2-2. The power intensity profile

The power intensity profile is measured with acrylic cubes [1].

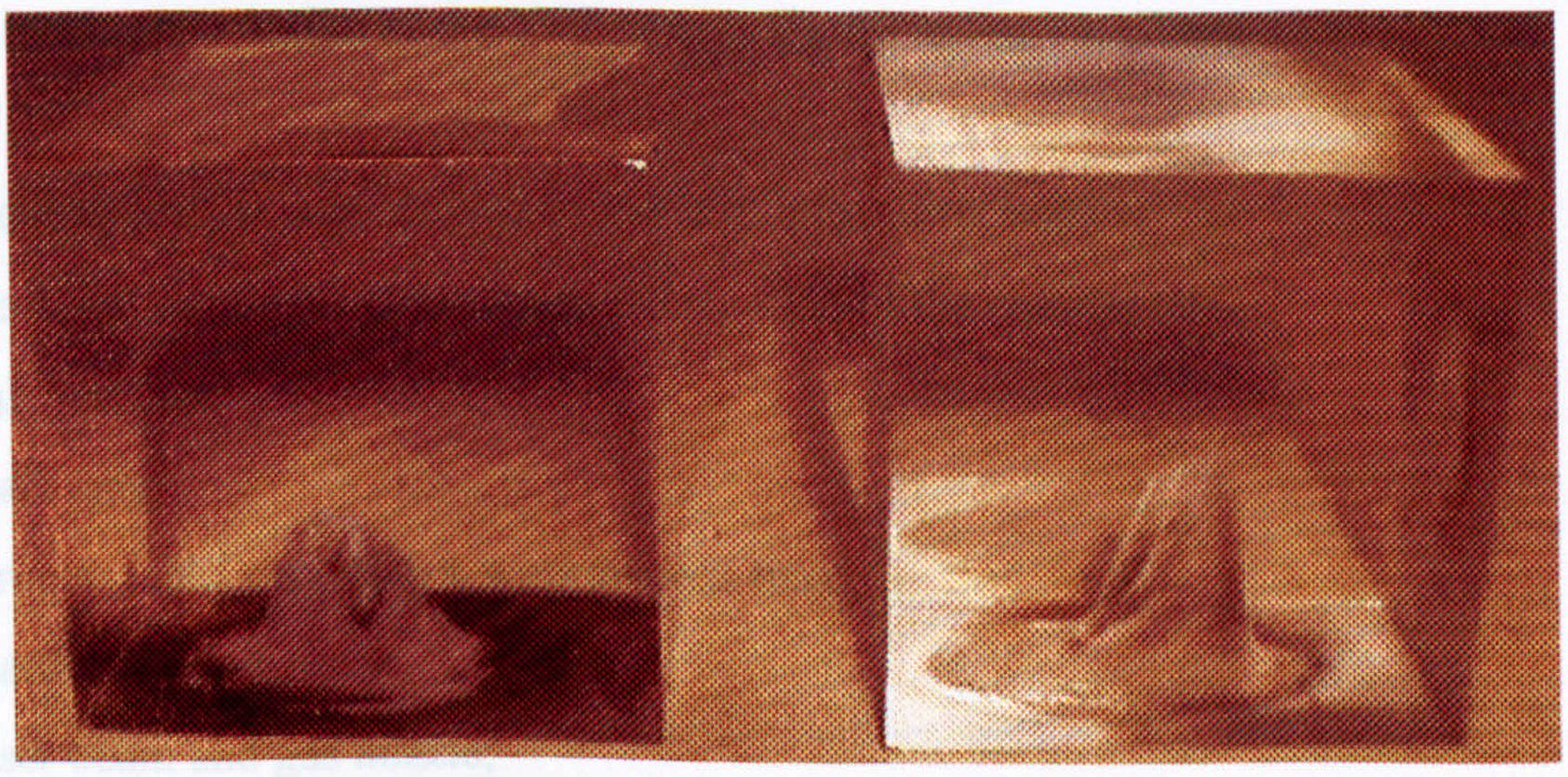

(a) the irradiation time is 6 seconds *(b) the irradiation time is 8 seconds*

Figure 18. *The measurement of the power intensity profile*

The measurement of the power intensity profile, in Fig.18, shows that the laser beam used in the experiments can only be very roughly treated as a 3-D Gaussian profile.

9-3. Artificial variation of cutting velocity

9-3-1. Design of X-Y table

The objective of the design of an X-Y table is to investigate the influence of the variation of the velocity of beam translation (V_c, in the theoretical laser cutting system) on cutting results, i.e., striations. In practical laser cutting processes in which the workpiece is fixed and the cutting velocity is produced by moving the laser beam, any mechanical vibrations can generate the oscillations of the velocity of beam translation.

In designing the X-Y table, the laser beam together with the reactive gas jet is fixed; the workpiece is fixed on the table which is controlled by two electrical motors. The cutting profiles can be chosen as linear, circular and spiral. In the case of linear and circular cutting profiles, the cutting velocity along the profile is constant with respect to time. In the case of spiral cutting profiles, the cutting velocity along the profile is artificially accelerated or decelerated with respect to time.

The mechanical design of the X-Y table is shown in Fig.19, where,

1 -- moving box. It is controlled to move in linear direction;

2 -- electrical motor A. It produces the rotation of the circular table;

3 -- ball bearings;

4 -- main axis;

5 -- circular table, on which a workpiece is fixed;

6 -- matching gears;

7 -- laser beam and gas nozzle;

8 -- roller bearings;

9 -- lead screw;

10 -- sliding track, on which the moving box slides;

11 -- electrical motor B. It produces the linear movement of the circular table;

12 -- holders, which hold the lead screw;

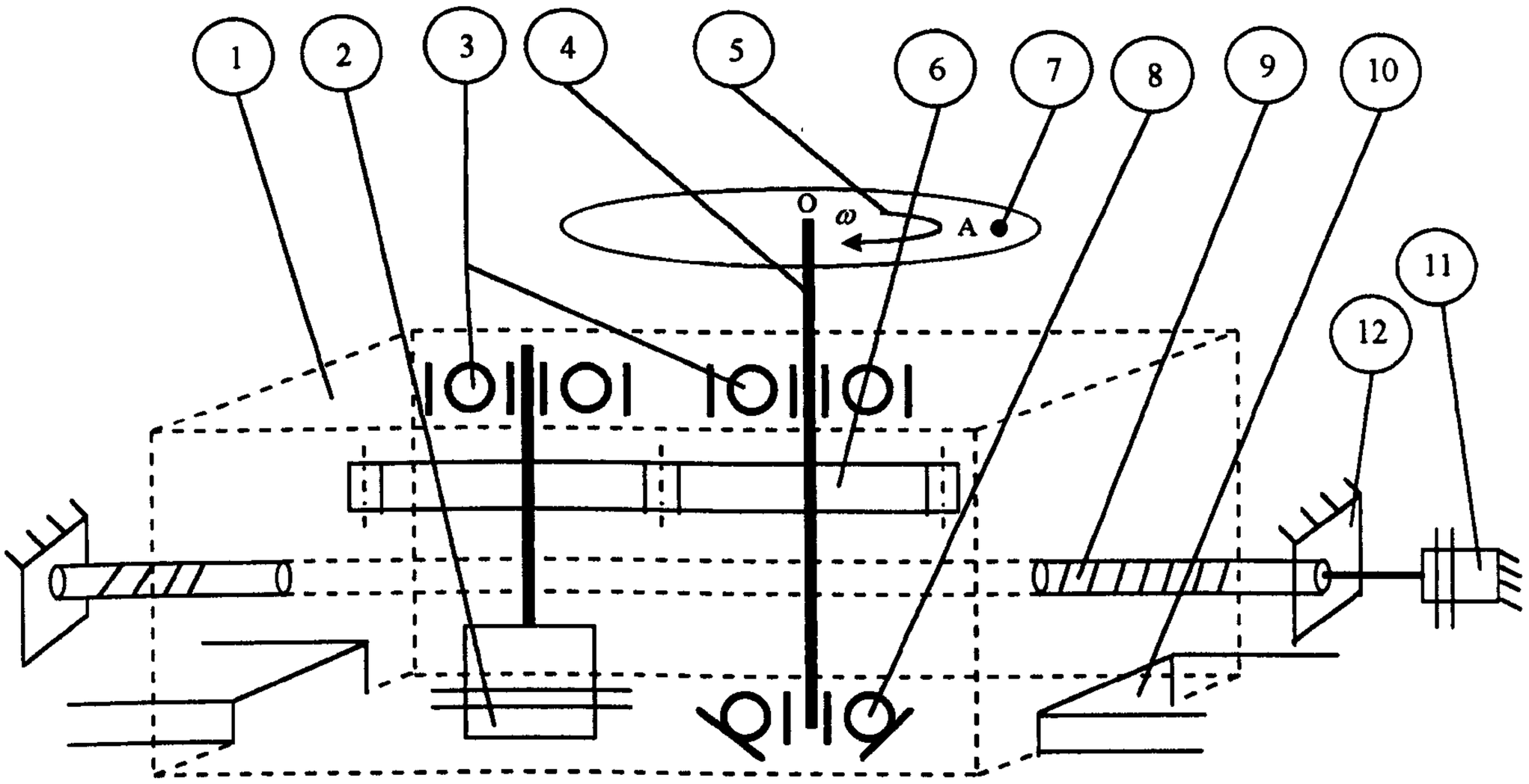

Figure 19. *The design of X-Y table. The laser beam and the gas nozzle are fixed. The cutting profiles can be chosen as linear, circular and spiral*

The local cutting velocity along the cutting profile is analyzed in Fig.20 *. Assuming that ϖ and V_R are controlled as constantly as possible; $R = R_0$, $\theta = \theta_0$ at $t = 0$, the equation of the cutting profile and the local cutting velocity are derived in Eq.94:

* The mathematical symbols for the calculations in Eq.94 based on the analyses in Fig.20 are not listed in Nomenclature. The magnitude of the velocity vector $\vec{V}_c$ has the same meaning as V_c defined in the theoretical analyses

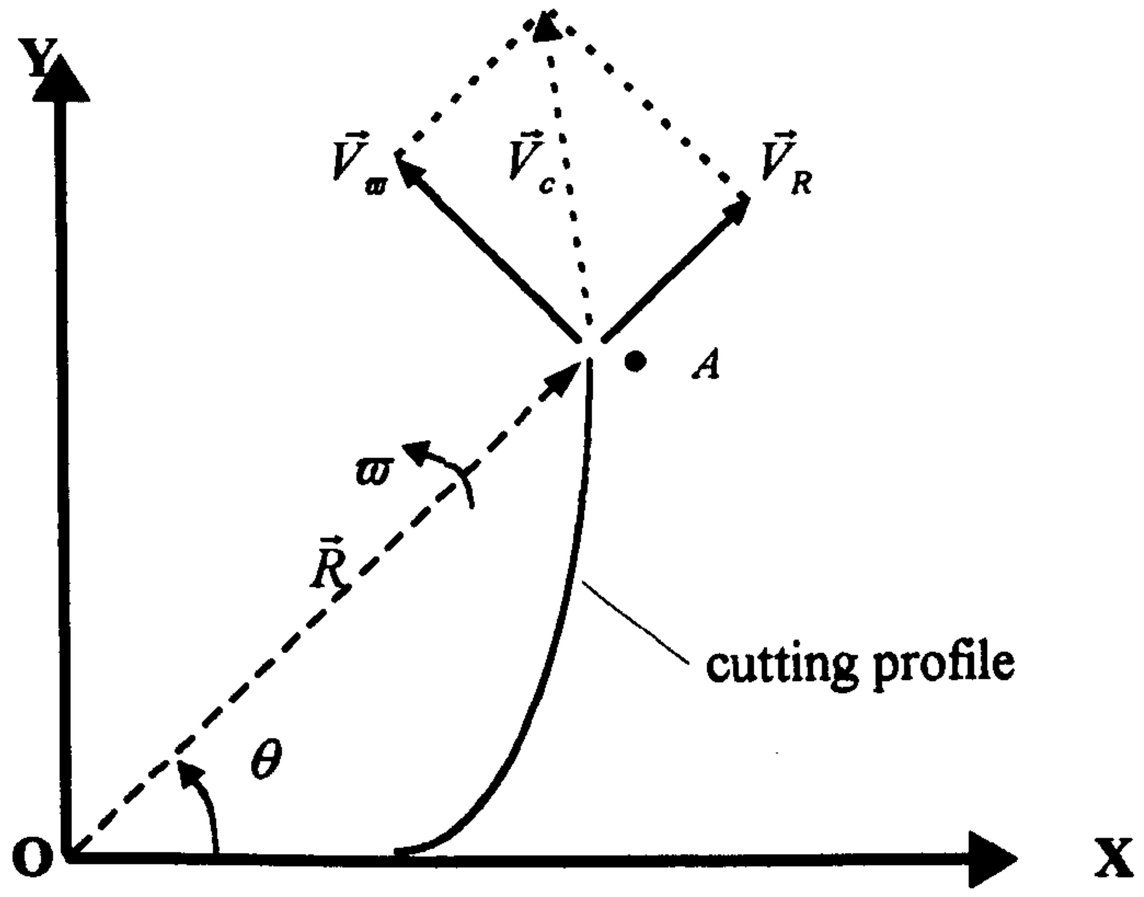

Figure 20. *In X-O-Y, the cutting profile is represented by the track of the movement of the point A. The local cutting velocity, $\vec{V}_c$, varies along the cutting profile. The origin O is at the center of the circular table; X-O-Y plane is fixed at the surface of the circular table*

$$\begin{cases} x = (V_R t + R_0)\cos(\varpi t + \theta_0) \\ y = (V_R t + R_0)\sin(\varpi t + \theta_0) \\ \vec{V}_c = \vec{V}_R + \vec{V}_\theta \ , V_c = \sqrt{(V_R)^2 + (V_R t + R_0)^2 \varpi^2} \end{cases} \tag{94}$$

where,

x, y: the coordinates of the vector $\vec{R}$, representing the equation of laser cutting profile;

R_0: the initial distance between the beam center and the axis of the circular table at $t = 0$;

θ_0: the initial angle between $\vec{R}$ and X at $t = 0$;

$\vec{V}_R$: the velocity vector in the direction of $\vec{R}$;

$\vec{V}_\varpi$: the velocity vector vertical to $\vec{R}$;

ϖ: the angular velocity;

$\vec{V}_c$: the local cutting velocity vector;

t: the cutting time.

Based on the design above, the experimental set-up is shown in Fig.21.

- if $\varpi = 0$, a linear cutting profile is available at constant V_c;
- if $V_R = 0$, a circular cutting profile is available at constant V_c;
- if $\varpi \neq 0, V_R \neq 0$, a spiral cutting profile is available at variable V_c;

By varying both ϖ and V_R, V_c should be controlled within *10* to *22* (*mm/s*) for a possible cut of *6* (*mm.*) thickness of mild steel.

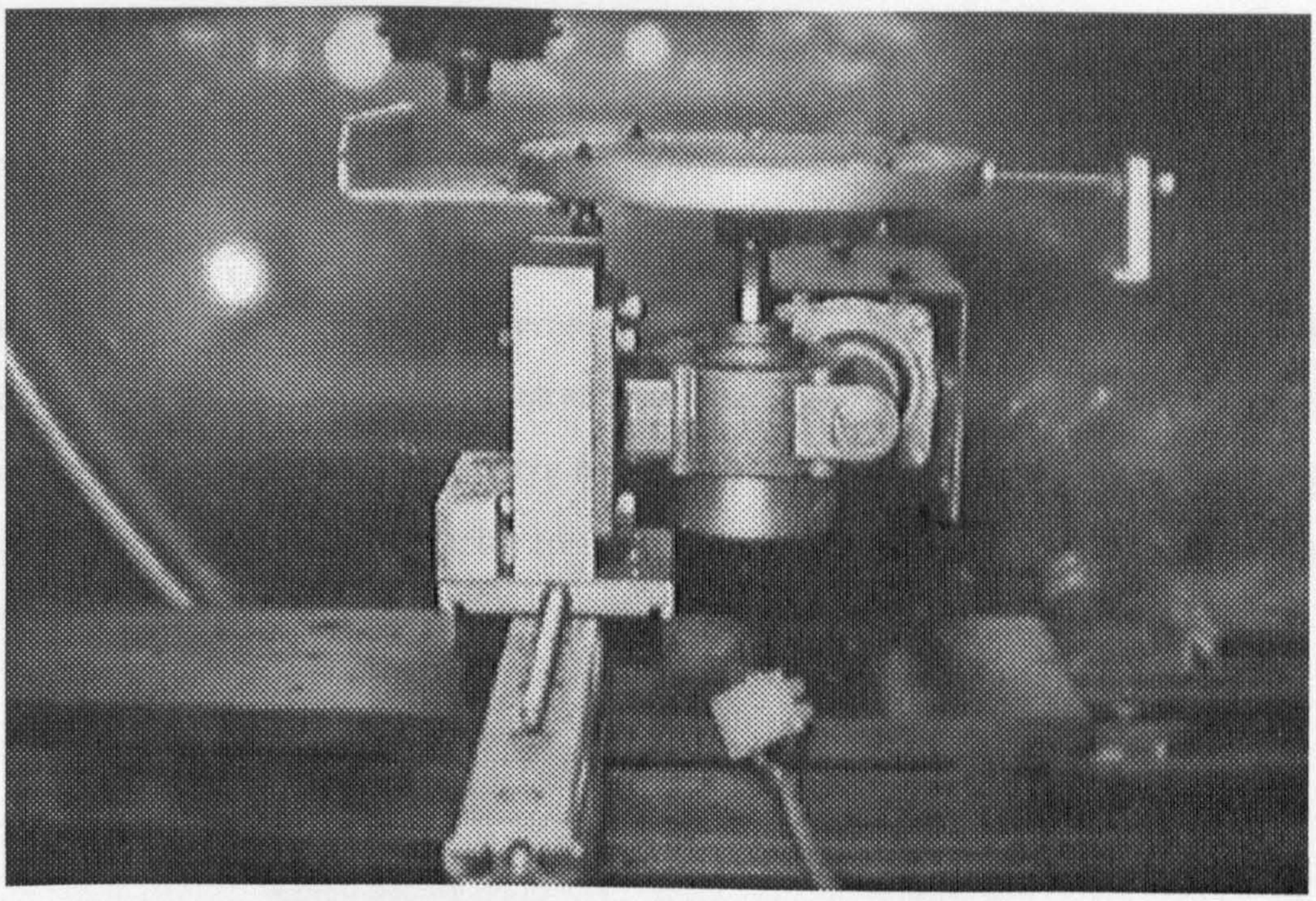

Figure 21. *The experimental set-up of X-Y table*

9-3-2. Calculation of variable laser cutting velocity

Given $\theta_0 = 0$; $R_0 = 85\ (mm.)$; $V_R = 1.5\ (mm/s)$; $\varpi = 0.11\ (radi/s)$, Fig.22 shows an example of the variation of V_c along the spiral cutting profile:

- the cutting time, *80* seconds;
- the dimension of the workpiece, $400 \times 400 \times 6\,(mm^3)$;
- the local cutting velocity, $V_c \in [9.47,\ 22.6]\ (mm/s)$.

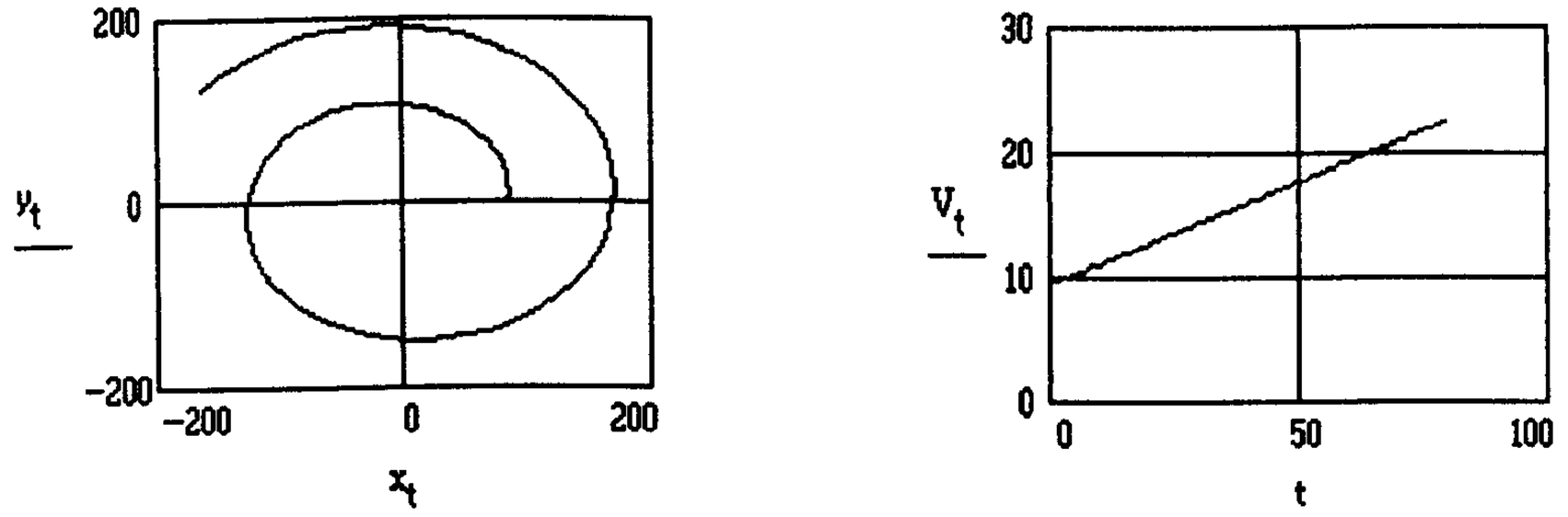

(a.) The laser cutting profile *(b.) The local cutting velocity*

***Figure 22.** An example of the laser cutting profile and the local cutting velocity*

9-4. Experimental results

Massive cuts are achieved in the experiments, using both the original CNC control system and the designed X-Y table. The objective is to examine the finish quality by checking the striations. Usually, striations are closely associated with kerf widths, for example, bigger kerf widths approximately correspond to coarser local striations. Scientifically, however, the measurement of striations can not be precisely carried out. This is shown in Fig.23.

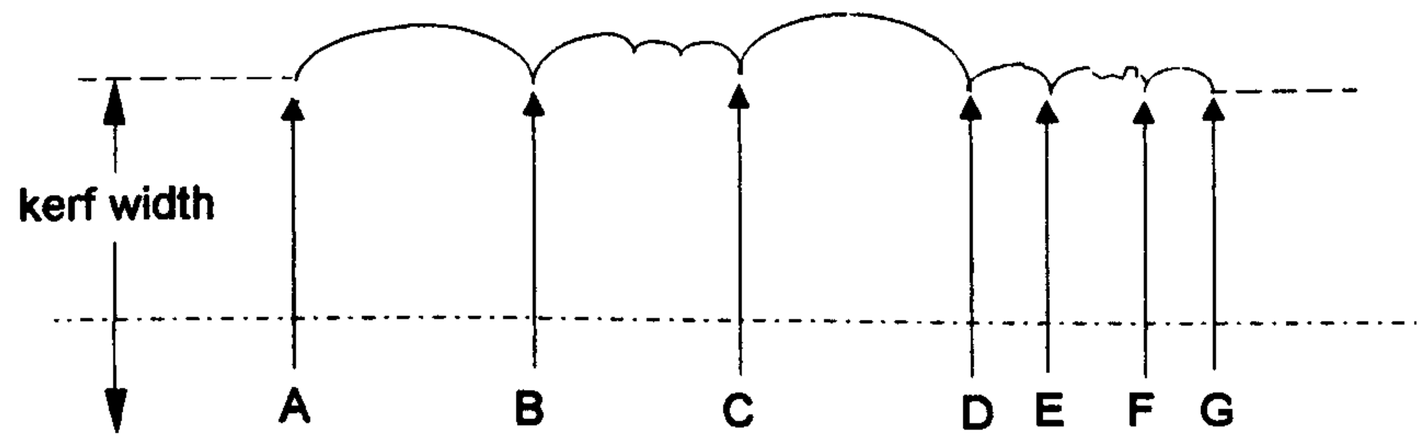

***Figure 23.** Appearance of striations (top view or bottom view). The spacing gaps between the points A to G, at the half depth of the thickness of workpiece, can be measured. The spacing gaps between B / C and E / F cannot be measured*

Due to the fact shown in Fig.23, it is intended to choose the original pictures of striations to present different types of cuts. In the case of circular and spiral cuts, the top and bottom view pictures of workpieces are shown. The measured spacing gaps of striations are used to help, quantitatively, understand good cuts and bad cuts.

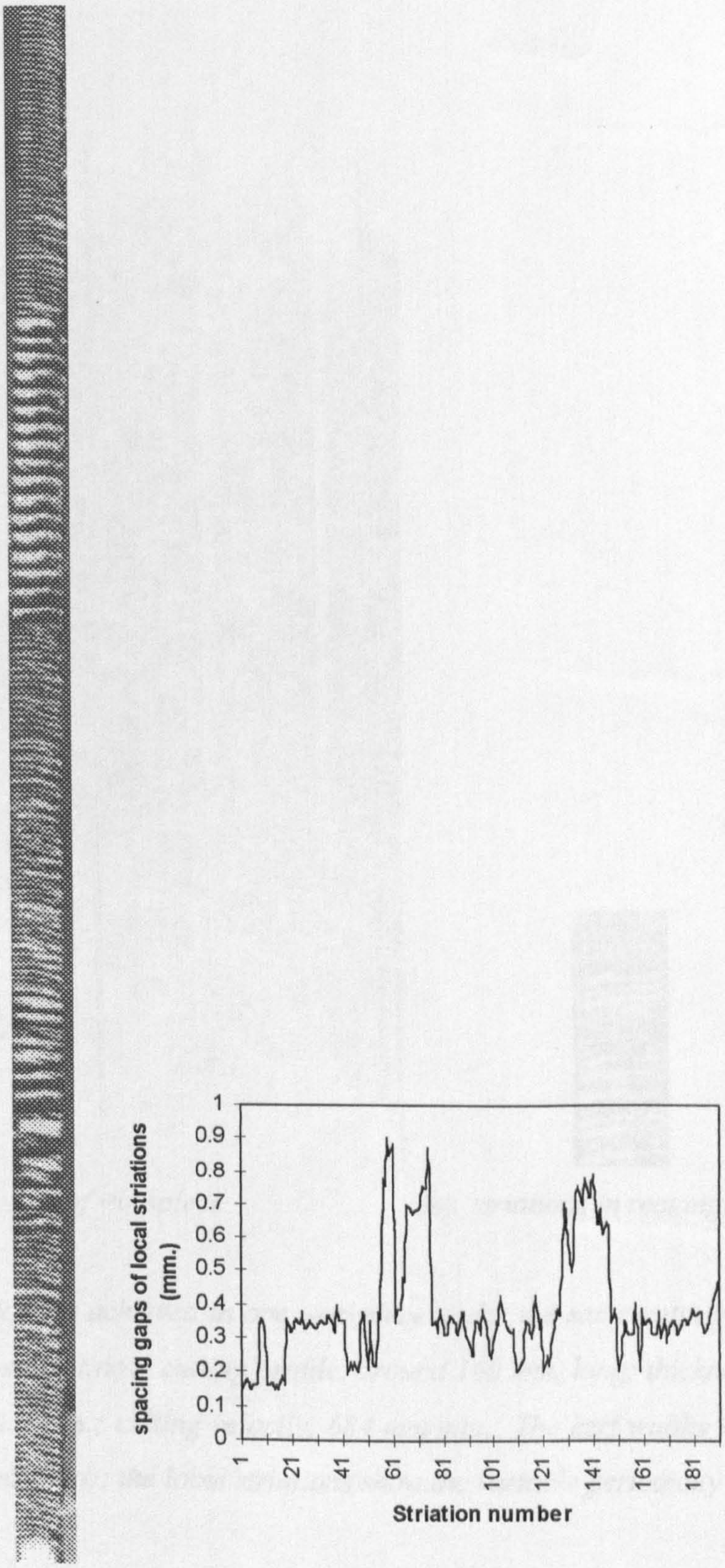

Figure 24. *Striations with variable periodicity. The sample is achieved using CNC control system. Cutting condition: mild steel; linear cutting profile, 120 mm. long; stagnation pressure, 2.5 atm.; thickness, 6 mm.; cutting velocity, 865 mm/min.*

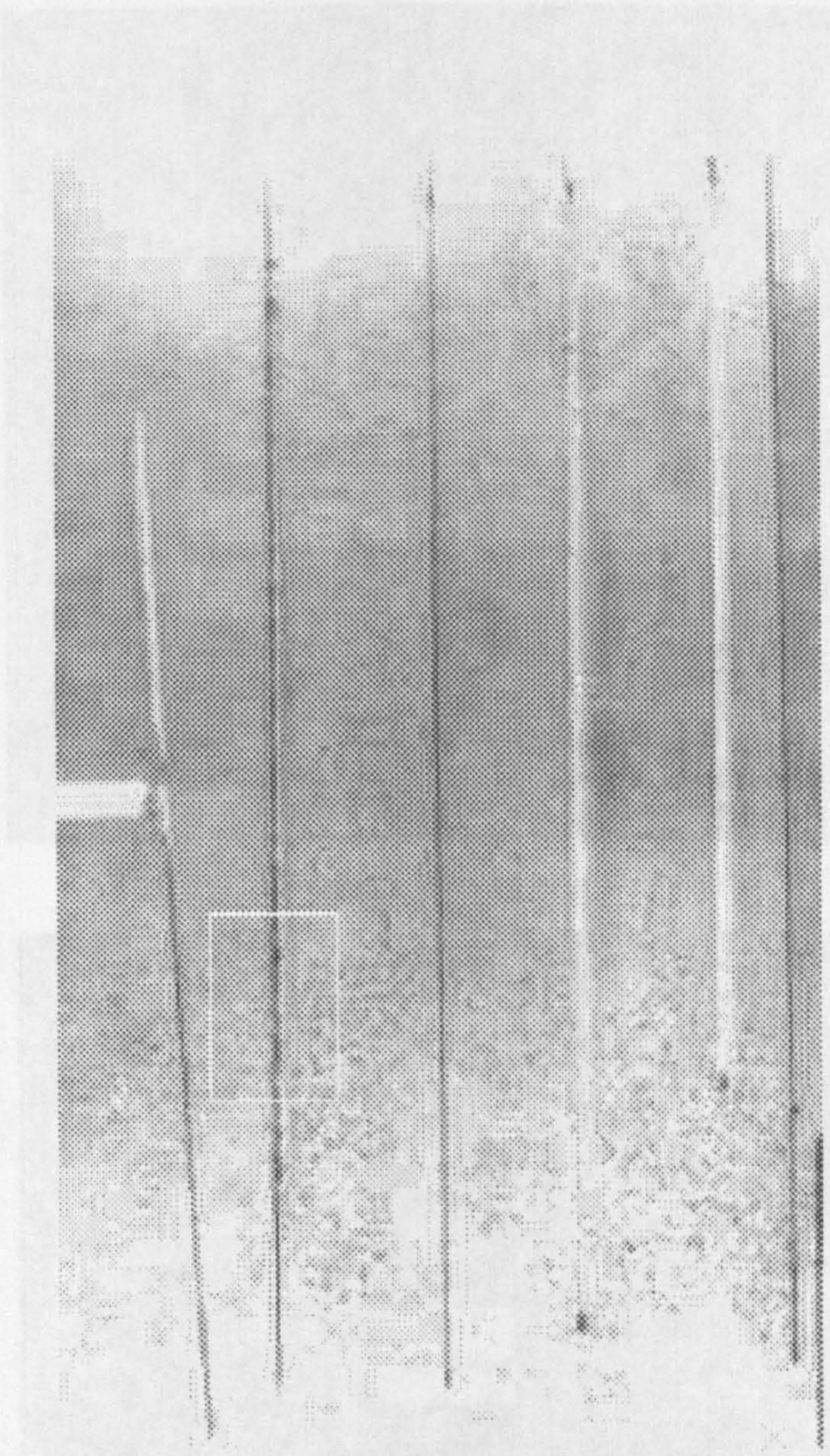

(a) top view of workpiece

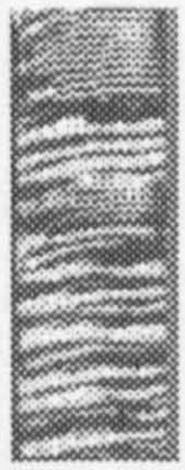

(b) striations in rectangle in (a)

Figure 25. *6 cuts in (a) are achieved in one workpiece under the same cutting condition, using X-Y table: mild steel; linear cutting profile, around 160 mm. long; thickness, 6 mm.; stagnation pressure, 3.0 atm.; cutting velocity, 684 mm/min. The kerf widths vary in one cut and in different cuts in (a); the local striations show the variable periodicity in (b)*

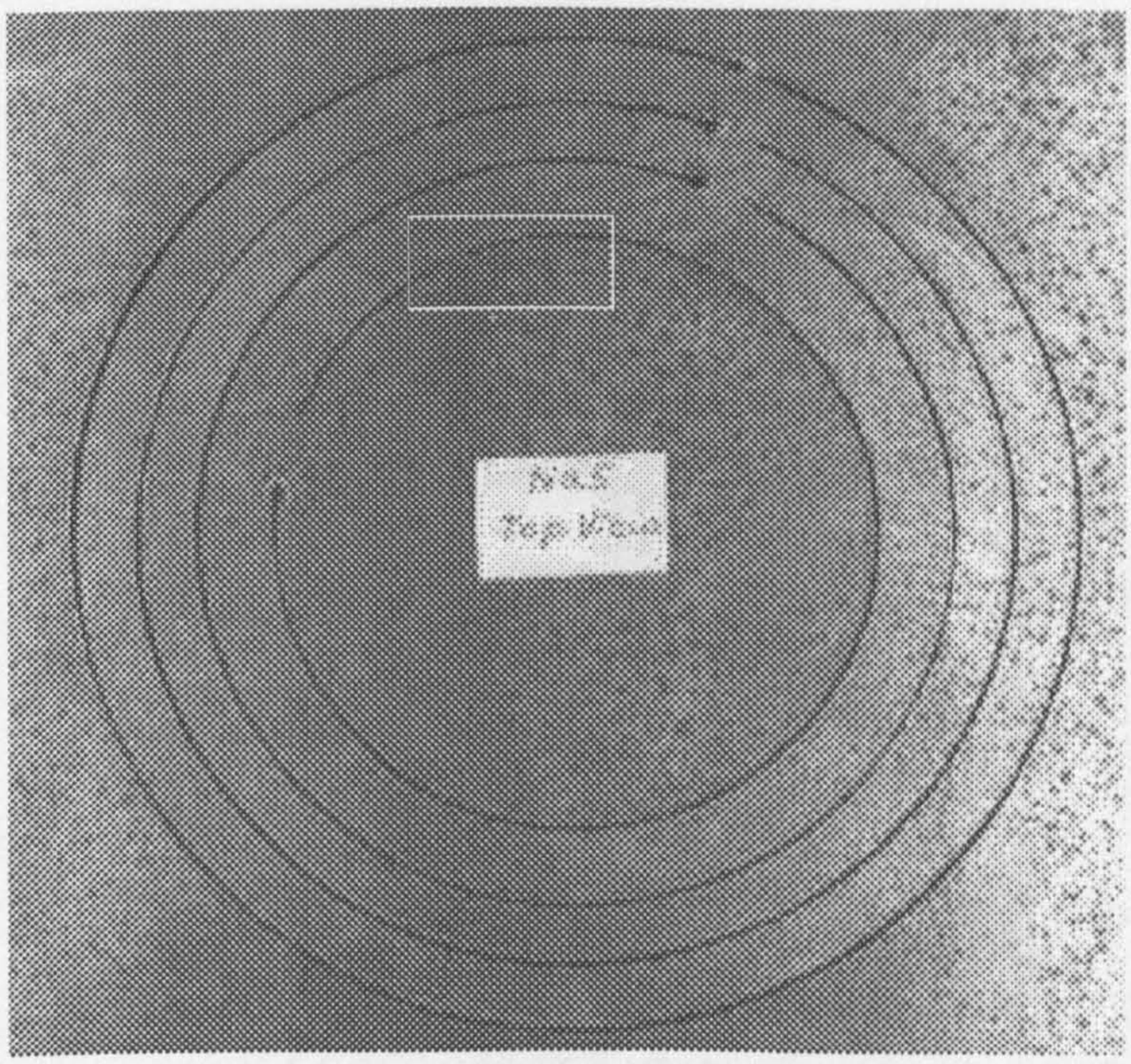

(a) top view of workpiece

(b) striations in rectangle in (a)

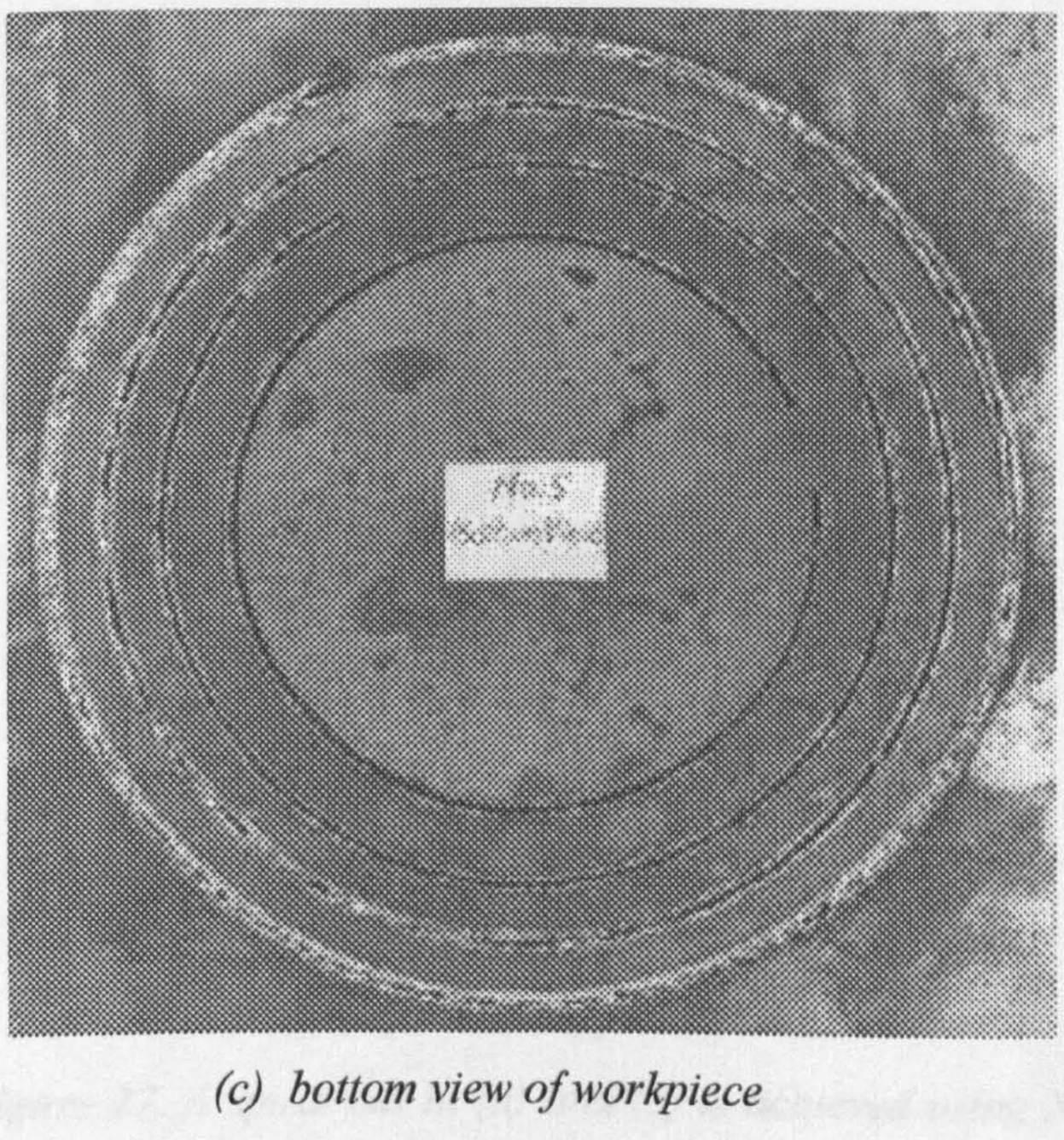

(c) bottom view of workpiece

Figure 26. *4 cuts in (a) and (c) are achieved in one workpiece using X-Y table. Except for the cutting velocities, the cutting conditions are the same: mild steel (400 × 400 mm²); circular cutting profile; stagnation pressure, 2.5 atm.; thickness, 6 mm. The cutting velocities are constant along each cutting profile, varying from 688 to 1123 mm/min. The kerf widths vary in one cut and in different cuts in (a) and (c); the local striations show the variable periodicity in (b)*

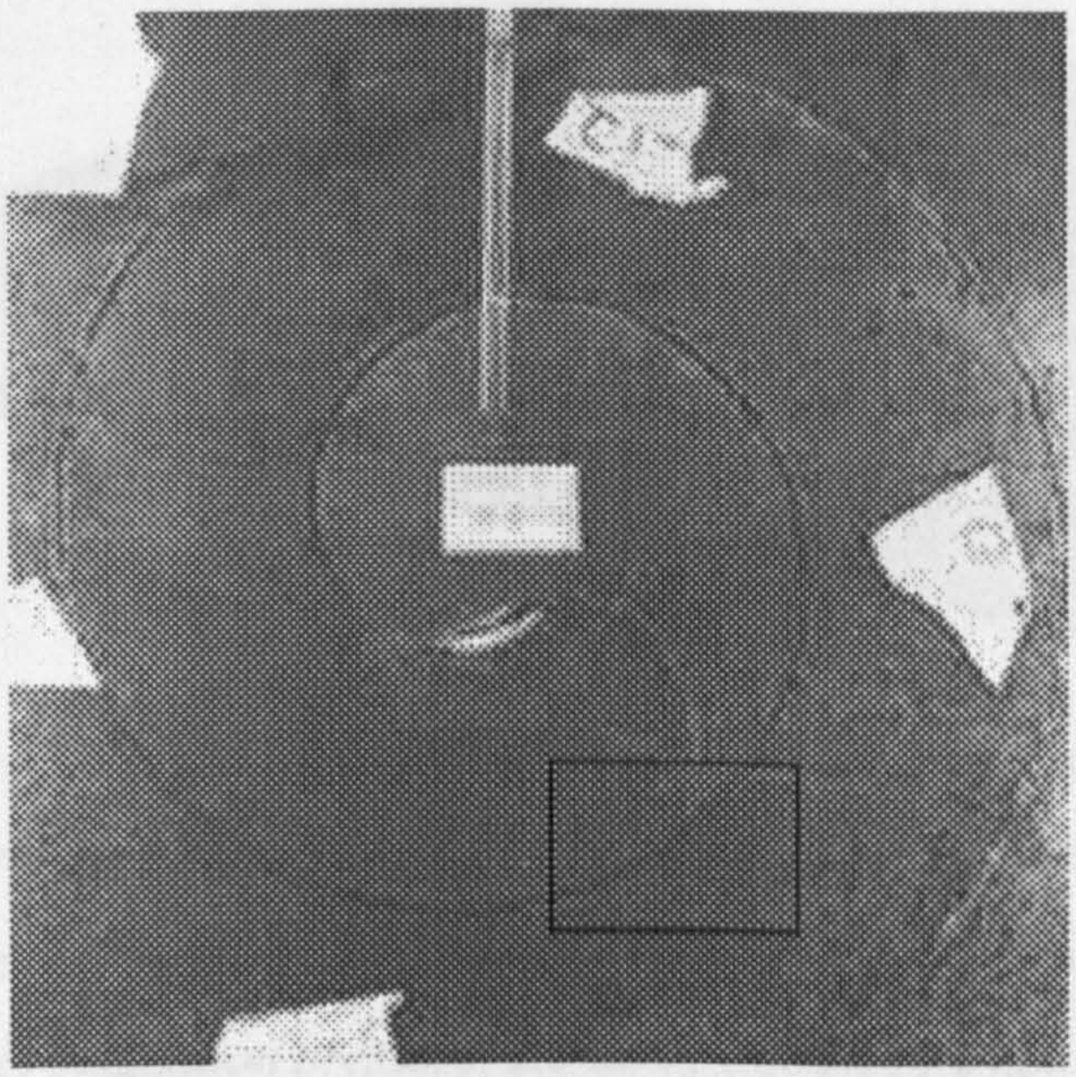

(a) top view of workpiece

(b) striations in rectangle in (a)

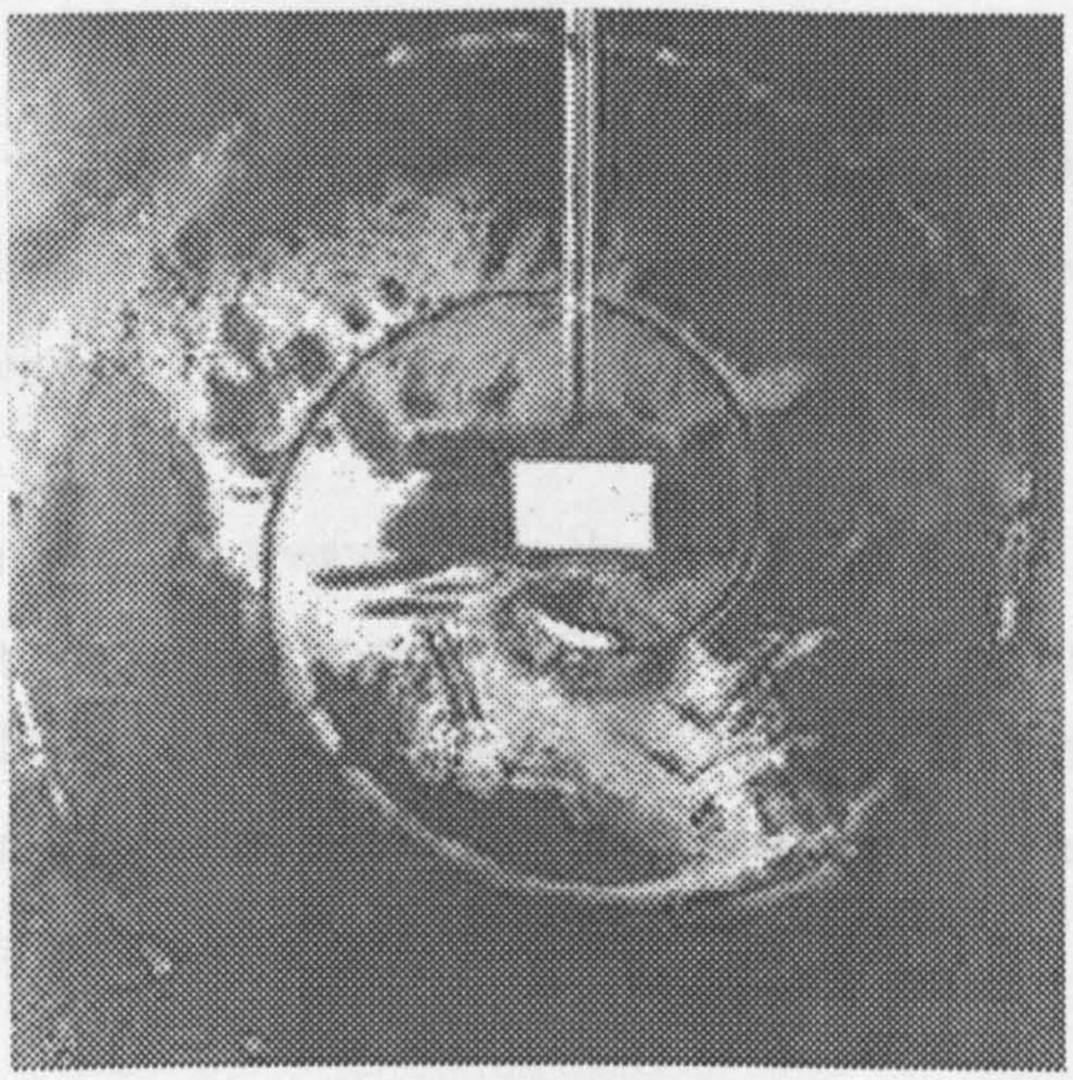

(c) bottom view of workpiece

Figure 27. *A spiral cut in (a) and (c) is achieved using X-Y table. The local kerf widths vary in (a) and (c); the local striations show the variable periodicity in (b). The local cutting velocities continuously vary along the cutting profile from 460 to 1403 mm/min. The cutting conditions: mild steel (400 × 400 mm^2); spiral cutting profile; stagnation pressure, 2.5 atm.; thickness, 6 mm.*

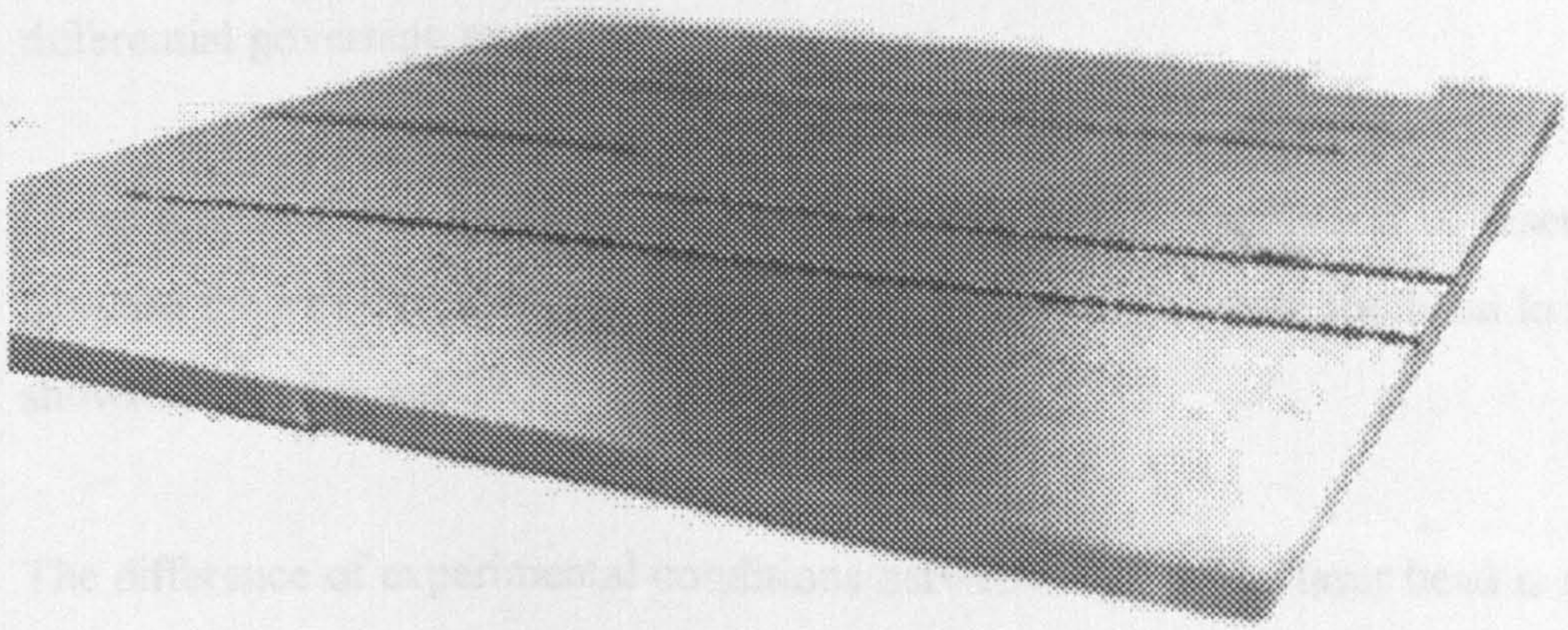

Figure 28. *Experimental tests on the importance of exothermic reaction between oxygen gas and metallic liquid, using X-Y table. By substituting the oxygen gas with argon gas, no cuts are possible. The cutting conditions: mild steel (400 × 400 mm^2); linear cutting profile; stagnation pressure, 2.5 atm.; thickness, 6 mm. The cutting velocities are constant along each cutting profile; it varies from one cut to another, 328 to 1102 mm/min.*

Figs.24-27 exhibit the typical laser cutting finishes with linear, circular or spiral cutting profiles. Both qualitative observation and quantitative measurement lead to the following conclusions:

- The striations always exit in the kerf except in the case of fusion cut (the example of fusion cut can be seen in Fig.27(a) where the finish near the center is extremely of poor quality and totally unacceptable). They can be very fine or very coarse. Essentially, the existence of striations do not come from the oscillation of laser scanning velocity or the mechanical vibration.

- The intermittence of the striations with different periodicity often exists. This phenomenon does not qualitatively be changed even when the laser scanning velocity is artificially decreased, as shown in Fig.27.

- Along the certain striation, the local kerf width at the surface of a specimen is always narrower than that at the bottom (Figs.26, 27). This phenomenon strongly supports the argument: the thicker the local thickness of the liquid, the wider the local kerf width. In

Chapter 8, the local thickness of the liquid can quantitatively be calculated with the differential governing equations.

- Given anything else is the same except the velocity of translation of laser beam, to increase the velocity will to a greater or lesser extent decrease the local kerf width, as shown in Figs.26 and 27.

- The difference of experimental conditions between Fig.24 (the laser head is moved) and Fig.25 (the specimen is moved by the designed X-Y table) demonstrates: the possible mechanical vibration in laser cutting practices is not the first important factor to produce the striations in the kerf. In Fig.25, it is seen that the same cutting conditions even produce dramatically different cutting finishes on the same specimen.

In addition, Fig.28 qualitatively demonstrates the significance of the exothermic reaction in the reactive gas assisted laser cutting process. In the experiment, there are no possible cuts at all if the oxygen gas is substituted with the argon gas.

In Appendix 8, more pictures of different types of cut finish are included for reference, including the type characterized by the intermittence of cut and no cut.

9-5. Characteristics of cut finish

Based on over *1000* cuts on around *300* workpieces, the conclusions for a practical laser cutting system are as follows.

- The quality of a cut finish is determined by local kerf widths and local spacing gaps of striations. Smaller kerf widths require that the mechanism of removal of the thin liquid film is by the shear stress applied by the fast-flowing gas. In this case, striations are unavoidable due to the dynamic nature of the development of the metallic liquid layer. The dynamics of striations, i.e., the intermittence of variable periodicity, reflect the fact that the metallic liquid layer is removed layer by layer while the thickness of the layer is variable with respect to time.

- In the case of fusion cut, kerf widths become too big with big spacing gaps of striations. This situation is not expected.

- A good cut is characterized by small kerf widths and homogeneously fine striations. A practical cut is always characterized by the striations with variable periodicity. In a practical laser cutting system, the oscillations in the laser power and the cutting velocity would affect the cutting surface quality, to a greater or lesser extent.

- The worst situation exists, i.e., the intermittence of cut and no cut. This fact is well explained by the theoretical conclusions: if the molten metal layer in the kerf can not satisfy the differential governing equations, in Eqs.81-83, the cut simply stops. Numerically, this is monitored by checking $y(t)$ within a certain range.

Chapter 10. Discussions

In this chapter, the rationality of the dynamic modelling is first generalised. The dynamic formation and development of striations is analysed based on the quantitative calculations of the differential governing equations for the theoretical laser cutting system. The method to choose the optimised operating parameters in practical laser cutting processes is predicted, theoretically. Two challenging research directions are recommended for future work.

10-1. Rationality of the dynamic modelling

The dynamic modelling for the reactive jet gas assisted laser cutting of metals is focused on the dynamic formation and development of the flow of the molten metal layer in the kerf and its multiple interactions with the laser beam, the gas jet and the substrate metallic solid. The most relevant physical mechanisms have mathematically been modelled:

- Dynamic balance equations of mass, momentum and energy for the molten metal layer;
- Dynamic absorption of the laser power by the workpiece;
- Momentum interaction between the gas jet and the liquid at the gas / liquid interface;
- Oxidisation reaction at the gas / liquid interface;
- Energy loss producing the heat affect zone (HAZ) at the liquid / solid interface;

These individual physical processes do not exist separately. The construction of the differential governing equations for the theoretical laser cutting system, as shown in Fig.9, reflects the fact that they interact with each other through the time-dependent variables. The 5 most concerned variables have been treated as time-dependent,

- $\delta_l(t)$, the thickness of metallic liquid film at the bottom of the kerf;
- $T_l(t)$, the surface temperature of metallic liquid film at the gas / liquid interface;
- $V_e(t)$, the fusion front velocity at the liquid / solid interface along cutting direction;

- $y(t)$, the displacement between the fusion front and the laser beam front;
- $P_{l,abs}(t)$, the laser power absorbed by the heated workpiece.

Consequently, the objective is to discover how the dynamic characteristics in the laser cutting system are generated due to the internal time-dependent variables of the system, rather than external variables such as the laser power, P_l, and the cutting velocity, V_c. By numerically solving the set of differential governing equations in Eqs.81,82,83 and the physical boundary conditions identified in Eq.89, which should be satisfied in each step of time evolution (otherwise the cutting process stops), the dynamic characteristics such as the thickness of molten metal layer, $\delta_l(t)$, can be quantitatively analysed. The local kerf widths and the local striations are closely associated with the variation of $\delta_l(t)$, as shown in Fig.29.

The type of the derived governing equations belongs to the 5 (or 4) coupled, 1st-order, non-linear, ordinary differential equations. In the set of differential governing equations, the coefficients are characteristic of the combinations of time-independent variables, i.e., the operating parameters and the thermophysical properties (thermodynamic properties and transport properties) of the oxygen gas (at around T_a and T_m), the metallic liquid (iron) and the metallic solid (iron). Chaos theory proves that systems such as these are often chaotic for some choices of the coefficients.

Relation of the theoretical laser cutting system and the practical laser cutting system

In practical laser cutting processes, any unstable factors in laser operating parameters, e.g., oscillations in laser power or cutting velocity, would to a greater or lesser extent affect the surface quality characterised by striations. A practical laser cutting system symbolizes general laser cutting processes, e.g., the experimental set-up introduced in Chapter 9.

A theoretical laser cutting system is abstracted from the reality. It is defined as the system into which the inputs (p_0, T_0, P_l, V_c) are time-independent variables. It symbolizes ideal laser cutting processes in which the operating parameters (p_0, T_0, P_l, V_c) are controlled as constantly as possible. The physical model of the theoretical laser cutting system is shown in Fig.9; the dynamic laser cutting model in Chapters 2-8 in this thesis is constructed from

it. In this case, the possible effects of the unstable factors in P_l, V_c and so on in the practical laser cutting system are theoretically isolated from the analyses of the dynamic formation and development of striations. The attention is thus focused on discovering the respective variations of the most relevant time-dependent variables, which are the internal unstable factors in the system.

Dynamic balance equations of mass, momentum and energy for the molten metal layer

Except for the fusion cutting that produces very poor surface quality, the molten metal layer in the kerf exists as a extremely thin film flow, which is continuously produced from the substrate solid and ejected off the kerf at the same time. To trace the dynamic variations of the liquid in the kerf, the application of the concept of Control Volume (CV) is essential. The control volume is defined as such that it always encloses the molten metal layer in the kerf, with respect to time. With CV, the 3 dynamic balance equations of mass, momentum and energy for the flow of molten metal layer can be constructed macroscopically.

The continuity is constructed, in Eq.1, assuming that the vaporisation of the molten metal from the left side of the CV, at the gas / liquid interface, is ignored in comparison with the liquid ejected at the bottom of the kerf. The momentum conservation in the CV describes the fact that the velocity profile of the molten metal layer, u_l, is controlled by the forces applying at its two surfaces. Treating the flow of the molten metal layer as a quasi-shear-stress boundary-layer flow, the momentum equation is expressed in Eq.7. Assuming the energy loss associated with the vaporisation of the molten metal from the left side of the CV is ignored, the energy conservation in the CV is interpreted in Eq.9.

The 3 balance equations in the CV must be satisfied simultaneously, with respect to time, as long as the laser cutting continues. In the derivations of the related quantities identified, some of them can directly be expressed in association with the 5 time-dependent variables, i.e., $\delta_l(t)$, $T_l(t)$, $V_e(t)$, $y(t)$ and $P_{l,abs}(t)$. This is carried out in Chapter 3. The others are discovered to be in association with the 5 time-dependent variables only when the relevant physical mechanisms are dealt with in Chapters 4-7, respectively.

Momentum interaction between the gas jet and the liquid at the gas / liquid interface

At the gas / liquid interface, the interaction between the cold, fast-flowing gas jet and the hot, slow-moving metallic liquid film exists. During the interaction, the momentum of the gas is transferred to the liquid, through the shear stress, $\tau_{l,w}$, that drives the liquid to flow out of the kerf; at the same time, the heat is convected from the liquid into the gas, making the gas cooling effect unavoidable.

The gaseous boundary layer develops at the gas / liquid interface. The physics is analysed by solving the 2-D differential governing equations for a laminar boundary layer flow, based on Howarth-Dorodnitsyn's method and Von Karman's skin friction relationship. The shear stress applied at the gas side at the gas / liquid interface ($\tau_{g,w}$) and the gas cooling effect ($\dot{e}_{cool}$) are derived. The shear stress applied at the liquid side at the gas / liquid interface is thus derived, by $\tau_{l,w} = -\tau_{g,w}$.

The maximum surface velocity of the liquid at the bottom of the kerf, $u_{0,max}$, is analysed with Lock's solution for the momentum interaction of 2 parallel laminar boundary layer flows. $u_{0,max}$ occurs only when there is "no slip" between 2 interacting flows at the gas / liquid interface. It is used to discover the physical boundary condition for $\delta_l(t)$, i.e., $\delta_{l,max}$. $\delta_l(t) \in (0, \delta_{l,max}]$ must be abided by for every step of time evolution.

The derived quantities are tested with the typical data in Appendices 1-3. The possible range of $\delta_l(t)$, e.g., $0 < \delta_l(t) \leq 0.105\,(mm)$, very well justifies that the flow of the molten metal layer, in Chapter 3, has been treated as a quasi-shear-stress boundary-layer flow with linear velocity profiles at every section of the flow (except $x = 0$). The magnitude of $\delta_l(t)$ is also supported by several researchers [2,3,5,8,10].

The fact that $\delta_l(t)$ in Y is far less than the average measured kerf width, w, in Z, certifies that the 2-D modelling, in X-Y plane, is very effective in describing the 3-D practical laser cutting system.

Oxidisation reaction at the gas / liquid interface

It is generally accepted that, in the oxygen jet gas assisted CO_2 laser cutting of mild steel, the energy of the exothermic reaction entering the molten metal layer, $\dot{e}_{exo}$, is at the same magnitude as the focused laser power [P.213, reference 1], [3,5]. This is supported by the experimental test in Fig.28. The exothermic reaction mechanism between the oxygen gas and the molten metal liquid is vital in calculating $\dot{e}_{exo}$. Two possible chemical reactions are analysed, i.e., the reaction between O_2 and liquid Fe with the product in liquid phase, by the experimental findings by Powell et al [1,28,29], in Eq.41,

$$\frac{1}{2}\times(O_2)+1\times\{Fe\}=1\times\{FeO\}+\Delta H\big|_T,$$

and the reaction between O_2 and gaseous Fe with their product in gaseous phase, derived by Dutta [P.84, reference 3], in Eq.42,

$$\frac{1}{2}\times(O_2)+1\times(Fe)=1\times(FeO)+\Delta H\big|_T.$$

By comparing the tested value of $\dot{e}_{exo}$ with the focused laser power, P_l, using the data in Appendices 1-3, the exothermic energy generated due to the chemical reaction of O_2 and vapour Fe, is ignored. The method of calculation is listed in Appendix 4 for reference.

For the chemical equilibrium identified in Eq.41, the enthalpy of reaction, $\Delta H\big|_T$, is calculated with Hess' principle using the respective heats of formation from standard tables. $\Delta H\big|_T$ is essentially dependent on $T_l(t)$ at which the oxidisation reaction exists, at the gas / liquid interface. However, the tests of $\Delta H\big|_T$ at $T_l(t) = 1808-2300\ (^oK)$ show that it is scientifically precise enough to take $\Delta H\big|_{T_l(t)}$,

$$\Delta H\big|_{T_l(t)} = \Delta H\big|_{2000K} = -4.613\times10^6\ (J/kg\ of\ liquid\ Fe),$$

when $T_l(t)$ practically varies around $2000\ (^oK)$. The negative sign simply means that the chemical reaction system releases energy.

The mass rate of the liquid entering exothermic reaction, $\dot{m}_{exo}$, is vital in calculating $\dot{e}_{exo}$, too. It is derived on the assumption that all of the particles of liquid Fe existing only at the

surface of the molten metal layer, at the gas / liquid interface, are oxidised; the exothermic heat generated enters the metallic liquid. The derivation of $\dot{m}_{exo}$ yields the initial-condition-dependent and time-independent variable, C_{exo}, which is called the combustion efficiency coefficient. Given any initial conditions, i.e., $\delta_l(0)$, $P_{l,abs}(0)$, $V_e(0)$, $y(0)$ and $T_l(0)$, the determination of C_{exo} are shown in Eqs.90-92, respectively.

The introduction of C_{exo} reflects the fact that the ratio of the metallic liquid entering the exothermic reaction to the metallic liquid leaving the kerf, k_{exo},

$$k_{exo} = \frac{\dot{m}_{exo}}{\dot{m}_{out}},\ 0 < k_{exo} \le 1$$

is variable with respect to time. The relation of k_{exo} and C_{exo} is shown in Eq.54: k_{exo} is inversely proportional to the thickness of the molten metal layer, $\delta_l(t)$. It is seen that the dilemma in evaluating k_{exo} in the previous work [1, 5], for example, $k_{exo} = 0.5$ or $k_{exo} = 1$, is overcome by the derivation of C_{exo}.

Knowing $\Delta H\big|_T$ and $\dot{m}_{exo}$, the energy rate of the exothermic reaction entering the molten metal layer, $\dot{e}_{exo}$, is calculated by $\dot{e}_{exo} = \Delta H\big|_{T_l} \times \dot{m}_{exo}$, which is essentially associated with $\delta_l(t)$ and $T_l(t)$, in Eq.55.

Energy loss producing the heat affect zone (HAZ) at the liquid / solid interface

In a practical laser cutting system, the energy loss from the molten metal layer into the substrate solid at the liquid / solid interface, identified as $\dot{e}_{loss}$, is responsible for the phenomenon of heat affected zone (HAZ) in the solid. The mechanisms of the heat transfer on two sides of the liquid / solid interface are essentially different, as shown in Fig.12. On the liquid side of the liquid / solid interface, the heat is convected to the interface due to the temperature difference of $\left[T_l(t) - T_m\right]$, identified as $\dot{e}_{conv}$. On the solid side of the liquid / solid interface, the same amount of heat is conducted from the interface into infinity due to the temperature difference of $\left[T_m - T_a\right]$, identified as $\dot{e}_{cond}$. The relation is shown by Newton's law, in Eq.56:

at $y = 0$, $T = T_m$,

$$\dot{e}_{loss} = \dot{e}_{conv} = \dot{e}_{cond} = -(wD)K_s(\frac{dT}{dy})_{y=0}.$$

The analyses of the heat transfer through the liquid / solid interface, making the heat loss ($\dot{e}_{loss}$) unavoidable, suggest that $\dot{e}_{loss}$ can be approached by either calculating $\dot{e}_{conv}$ or calculating $\dot{e}_{cond}$. In major previous work [3,5,23,35], the heat conduction characteristics are focused, shown in Appendix 5. The calculating methods are usually associated with the moving heat source theory [33,34]. The fundamental theory derived by Carslaw and Jaeger [Section 10.7, reference 34] is expressed in X-O-Y in Fig.13,

$$T_{(y)} = \frac{\dot{e}_{cond}}{2\pi K_s D} \cdot exp(\frac{V_e y}{2k_s}) \cdot K_0(\frac{V_e y}{2k_s}) \quad \text{when } y \neq 0.$$

It is essential to notice that it requires,

$y \neq 0$, mathematically. Physically, however, the application requires that:

$T_{(y \to 0)} = T_m$,

because T_m only exists at the liquid / solid interface, i.e., $y = 0$.

Theoretically, the smaller the y, the more accurate the $\dot{e}_{cond}$. Because K_0 is extremely sensitive when $y \to 0$, the evaluation of $\dot{e}_{cond}$ is not scientifically accurate.

For this reason, the calculation of $\dot{e}_{loss}$ in this thesis is carried out by evaluating $\dot{e}_{conv}$, in Eq.57''. The test of $\dot{e}_{loss}$ with the typical data in Appendices 1-3, by Eq.57'', supports the reasonability of the theoretical treatment, simply by comparing $\dot{e}_{loss}$ with $P_l = 800(W)$.

Dynamic absorption of the laser power by the workpiece

The dynamic absorption of the laser power (P_l) by the workpiece, identified as $P_{l,abs}(t)$, is studied by analysing the relative displacement between the laser beam front and the fusion front at the liquid / solid interface, identified as $y(t)$. In Fig.9, $y(t)$ can vary with respect to time, because there is a lack of physical bond between the laser beam at V_c and the fusion front velocity at $V_e(t)$. The analyses of the mechanism of dynamic absorption of laser

power are therefore to identify the interrelations between the time-dependent variables, i.e., $y(t)$, $P_{l,abs}(t)$, $V_e(t)$. The "non-contact" interaction between the focused laser beam and the workpiece is shown in Fig.14.

It is seen that, assuming that P_l and the absorptivity of the heated workpiece to the CO_2 laser light are constant, $P_{l,abs}$ only depends upon the intersecting area of the focused laser beam and the workpiece.

In the simulation of $P_{l,abs}(t)$, the angle of the fusion front to horizontal plane, α, is taken into account. This is because, although the thickness of molten metal layer is negligible in comparison with a, the quantity of $(D \cdot cot\,\alpha)$ can not be neglected, in comparison with a. This is proved by the tests with the typical data in Appendix 1. Even in the situation that $\alpha = 89\ (^o)$, for example, the quantity of $(D \cdot cot\,\alpha)$ can reach $0.105 \times 10^{-3}\ (m.)$.

The ideal 3-D laser power with Gaussian profile is transformed into the 2-D model to fit the interest in X-O-Y plane: along Y, the power intensity is in Gaussian profile; along Z, it is even, as shown in Fig.9.

The comparison between the steady-state considerations in the previous work where the assumptions ($V_e(t) = V_c$; $P_{l,abs}(t) = P_l$) were always made, and the dynamic analyses in this thesis has been made in Chapter 7. It is seen that, in order to better model the reality in the laser cutting of metals, the dynamic approach as in Fig.14 is necessary. Practically, it is easy to understand that, if $y(t)$ is out of certain limits, symbolising the laser beam / the gas nozzle far behind or far ahead of the fusion front, there is no laser power or even no oxidisation reaction energy can be absorbed by the molten metal layer. In this case, the cutting stops. This explains the worst cutting situation, as shown in Fig.A7 in Appendix 8, where the cutting profile is intermittent between cut and no cut.

10-2. Possible solutions of differential governing equations

The complicated interactions of the molten metal layer with the laser beam, the gas jet and the substrate metallic solid are governed by the differential governing equations. 3 sets of differential governing equations for the theoretical laser cutting system shown in Fig.9 have been derived, by Eqs.81,82,83, depending on the scope of $y(t)$, respectively. They are bounded, in each step of time evolution, by the physical boundary conditions identified in Eq.89. Given any initial conditions, i.e., $\delta_l(0)$, $P_{l,abs}(0)$, $V_e(0)$, $y(0)$ and $T_l(0)$, C_{exo} is determined by Eqs.90,91,92, depending on the scope of $y(t)$, respectively.

The type of the governing equations are generalised in Eqs.81',82',83', corresponding to Eqs.81,82,83, respectively. It is seen that Eq.81 belongs to the 5 coupled, 1st-order, non-linear, ordinary differential equations; Eq.82 and Eq.83 belong to the 4 coupled, 1st-order, non-linear, ordinary differential equations, respectively.

To solve the differential governing equations, a feasible numerical approach is necessary. A well-structured program coded in C is designed to solve Eqs.81,82,83 bounded by Eq.89, in Appendix 6. The algorithm is based on the 4th-order Runge-Kutta method. The program has been tested with several simpler 1st-order non-linear differential equations.

Chaos theory has proved that systems such as these are often chaotic for some choices of the coefficients in the equations [P.3, reference18]. A good analogy for understanding the chaotic nature of the cutting system may be the well studied Lorenz's system [15]. The butterfly effect has become one of the icons of Chaos theory. The numerical calculations in Figs.15,16 suggest that the respective variations of the 5 time-dependent variables with respect to time are extremely sensitive to the initial conditions. The experimental results in Figs.24-27 and Figs.A3-A5 suggest that the intermittence of the striations with different periodicity often exists. By Chaos theory [P.507-P.766, reference 16], it is concluded that the practical laser cutting system, which is theoretically governed by Eqs.81,82,83 and bounded by Eq.89, is chaotic.

The chaotic nature of the laser cutting system matches the fact that the dynamic striations always exist on the kerf surface. This is because, theoretically, the thickness of the molten metal layer, $\delta_l(t)$, always varies with respect to time and the local kerf width, w, varies with respect to time, correspondingly. It is impossible to have a constant $\delta_l(t)$ even when the system starts from the special initial point at which the 1st-order derivatives of the time-dependent variables are equal to zero, respectively.

The chaotic nature of the laser cutting system also suggests the approach to choose the optimized operating parameters such as the laser power, P_l, and the cutting velocity, V_c. It is seen that they affect the coefficients in the differential governing equations. The method to predict is carried out in 3 steps:

- to choose the different combinations of the operating parameters;
- to run the differential governing equations with as many initial conditions as possible;
- the optimized operating parameters are discovered when the nearly periodic variation of $\delta_l(t)$ accompanied by the smallest phase space made up of the 5 time-dependent variables is reached.

10-3. Nature of striations

The dynamic formation and development of the striations is demonstrated in Fig.29, where the increased local thickness of the molten metal layer corresponds to the wider local kerf width at any time. The assumption is experimentally certified by the fact that the local kerf width at the bottom of the kerf is always bigger than that at the top of the kerf, along the depth of the same striation, e.g., in Figs.26,27. Fig.29 explains this very well:

- the molten metal is removed layer by layer. This is because the measured spacing gaps of the striations are around *0.2 - 1 mm.*; the calculated maximum thickness of the liquid is *0.105 mm.*. Therefore, the formation of one observable striation requires at least more than one liquid layer to be removed. Theoretically, the locations at which the local striations can be measured satisfy the condition: $\frac{d}{dt}\left[\delta_l(t)\right] = 0$.

• A good cut is characteristic of the nearly periodic variation of the thickness of the liquid layer with the smallest varying range. In this case, the nearly homogeneous fine striations are developed, producing the smaller kerf width and the smoother cutting surface.

• The intermittence of the striations with variable periodicity and the intermittence of the cut and no cut along the cutting direction are not strange, because of the chaotic variations of the thickness of the molten metal layer together with the other time-dependent variables, with respect to time. They produce bad cuts.

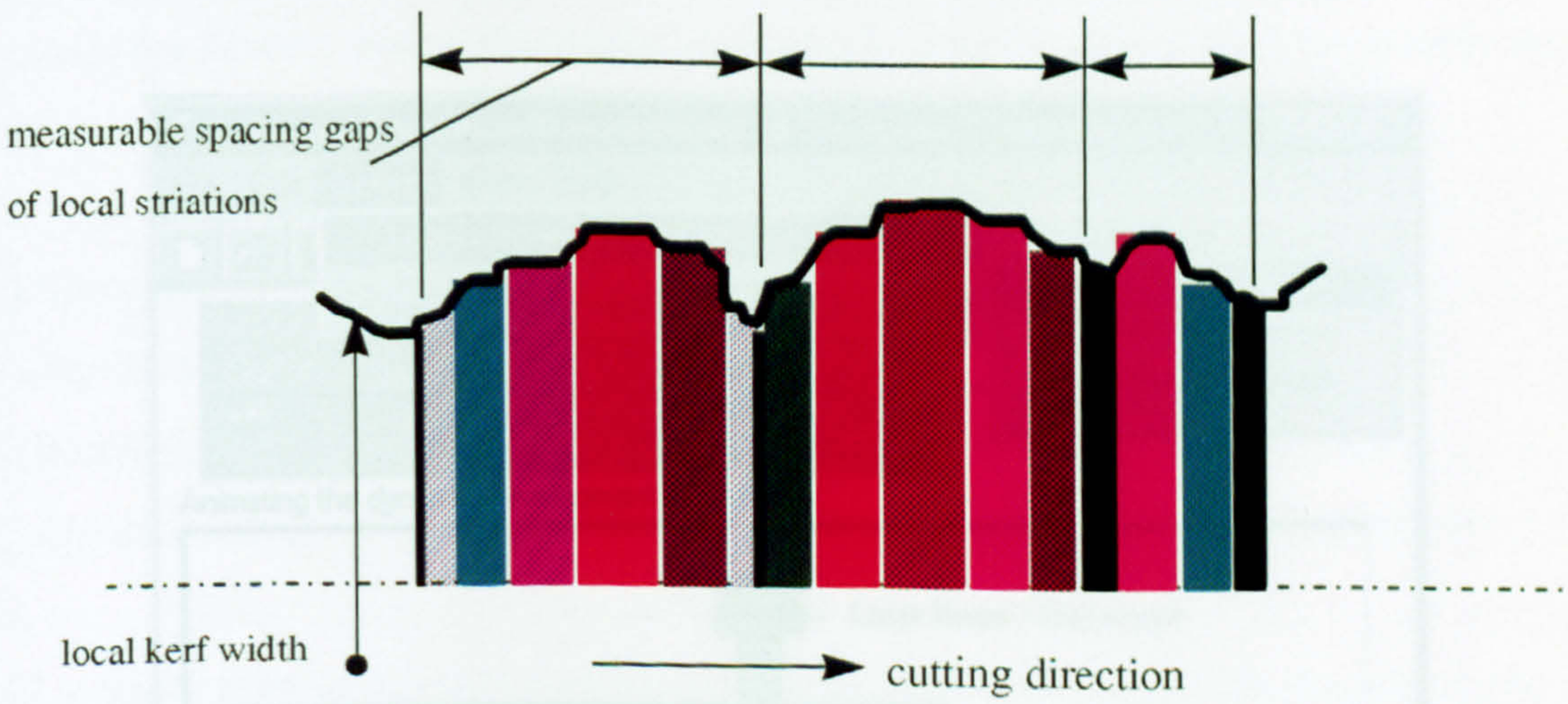

Figure 29. *The dynamic development of the local striations due to the chaotic variations of the thickness of the molten metal layer (top view). The thicker the local thickness of the liquid, the wider the local kerf width. The local thickness of the liquid can quantitatively be calculated with the differential governing equations*

10-4. Future work

To complete this thesis, 2 prospective research directions are recommended.

Chaotic analysis for the differential governing equations

Detailed theoretical work on the chaotic nature of the differential governing equations are necessary, especially in the long run. Because the laser cutting system is essentially chaotic,

by Chaos theory, there must be windows in which the periodic points, nearly periodic points and period-doubling points exist. The systematic examination of the operating parameters is worthwhile in order to try to achieve the stable, optimized cutting surface quality.

10-4-2. Animation of dynamic development of striations

In applying the differential governing equations, a user-friendly interface can help both numerical simulations and industrial practices. The following Window95 based interface will make it more comfortable to theoretically predict the optimized operating parameters.

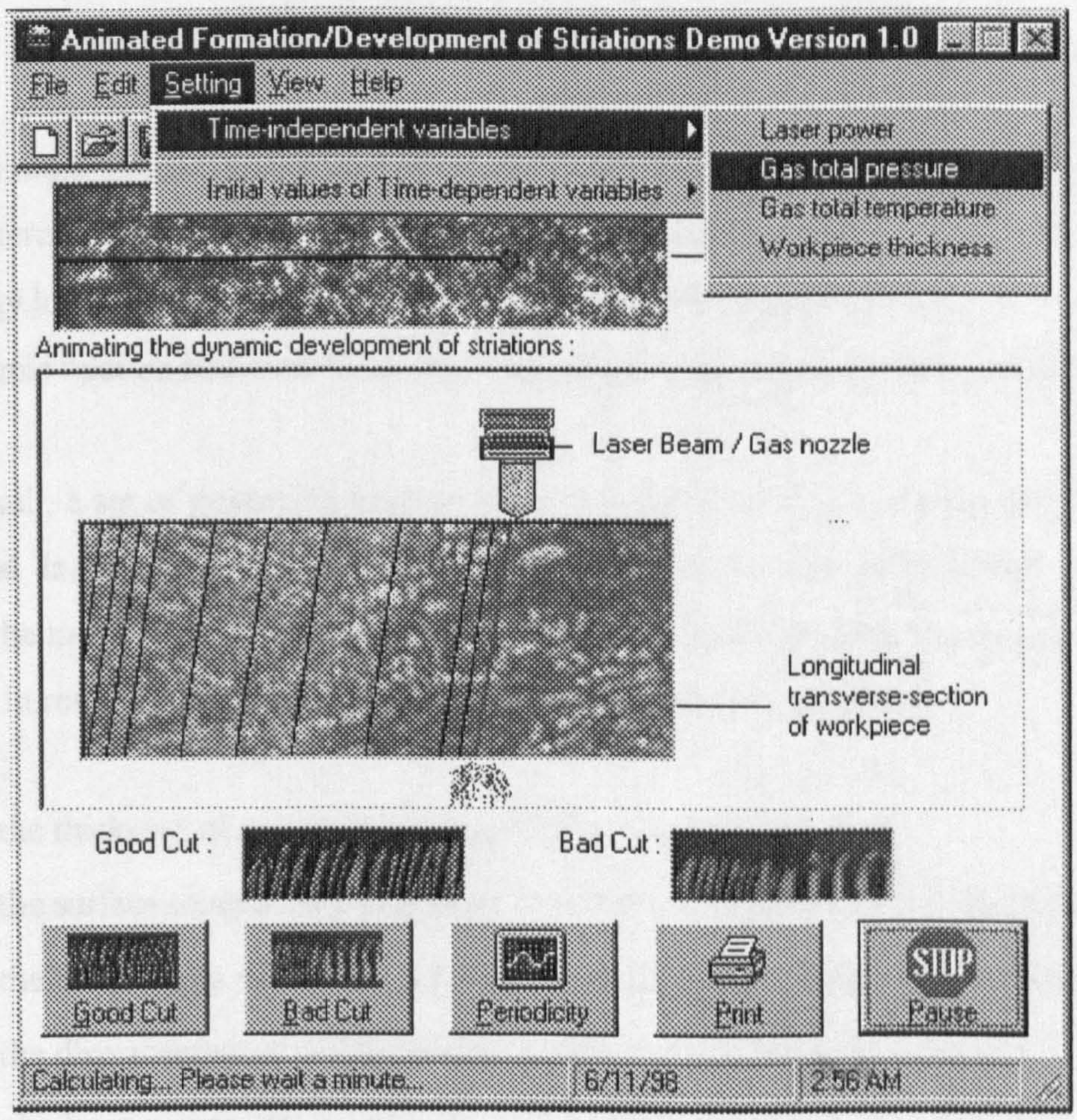

Figure 30. *A user-friendly interface making it more efficient to theoretically predict the optimized operating parameters*

The author of this thesis truly believes that this work will be useful.

Chapter 11. Conclusions

To generalise predictions of the laser cutting performance, in particular, of the kerf surface quality, the interest of this thesis has been focused at the dynamic formation / development of the flowing molten metal layer in the kerf. By defining a theoretical laser cutting system and applying the concept of control volume, it is expected to dynamically construct the balance equations of mass, momentum and energy in the control volume which always encloses the flowing molten metal layer in the kerf. In order to ascertain the specific entries into the 3 balance equations, 4 individual physical processes have been modelled:

(1) Momentum interaction between the gas and metallic liquid flows;
(2) Exothermic reaction between the gas and metallic liquid flows;
(3) Energy loss from the metallic liquid into the substrate metallic solid;
(4) Dynamic relation between the fusion front velocity and the beam front velocity.

As a result, a set of governing equations are built up to be able to dynamically model this theoretical laser cutting system in which the multiple interactions of the metallic liquid with the gas, the metallic solid and the laser beam occur. Mathematically, the 5 most concerned variables in respect with time, as follows, can numerically be calculated.

$\delta_l(t)$: the thickness of molten metal layer at the bottom of the kerf;
$T_l(t)$: the surface temperature of molten metal layer at the gas / liquid interface;
$V_e(t)$: the fusion front velocity at the liquid / solid interface along cutting direction;
$y(t)$: the displacement of the fusion front relative to the laser beam front;
$P_{l,abs}(t)$: the laser power absorbed by the workpiece.

The time evolution of the thickness of the molten metal layer, $\delta_l(t)$, reflects the dynamic nature of the theoretical laser cutting system and the frequency of $\delta_l(t)$ is closely related with that of striations in the kerf, as shown in Fig.29.

To solve the differential governing equations, a feasible numerical approach is necessary. Commercially, several software packages, e.g., *Mathematica*, *MathCad* and *NAG routine*, are able to numerically solve the sets of 1st-order differential equations. However, these software packages are difficult to incorporate with the special requirement, which is the physical boundary conditions for the 5 time-dependent variables, in Eq.89, in this thesis. It is essential to keep in mind that Eq.89 must be satisfied in each step of time evolution, as long as the simulation of the laser cutting process continues ($a-b \le y(t) \le a+b$). In Appendix 6, a well-structured program coded in C has been designed to solve Eqs.81,82,83 bounded by Eq.89.

The dynamic modelling has resulted in 3 sets of differential governing equations for the theoretical laser cutting system. These are found to be in the form of 5 or 4 coupled, 1st-order non-linear differential equations (Eqs.81-83) along with their specific boundary conditions (Eq.89) for the 5 time-dependent variables. To analyse the characteristics of so many possible solutions, it is important to understand the type of the differential governing equations. Mathematician Baker concluded that the dynamic systems such as Eqs.81-83 are often chaotic for some choices of the coefficients in the equations [P.3, reference 18]. The recent findings from Chaos theory help predict the optimised operating parameters.

In addition to the dynamic modelling, objective-oriented experimental tests are carried out. An X-Y table which can produce both constant cutting velocity (linear and circular cutting profiles) and accelerated / decelerated cutting velocity (spiral cutting profile) is designed to study the influence of the cutting velocity on the formation of striations in a practical laser cutting system.

The major conclusions are summarised as follows:

(1) The dynamic modelling has resulted in 3 sets of differential governing equations for the theoretical laser cutting system. These are found to be in the form of 5 or 4 coupled, 1st-order non-linear differential equations along with their specific boundary conditions for the 5 time-dependent variables. By simultaneously solving those equations, the dynamic nature of the laser cutting system can be clearly demonstrated.

(2) The type of the differential governing equations itself suggests that any practical laser cutting process is essentially chaotic. The recent amazing findings from Chaos theory can thus be employed to explain and predict the chaotic characteristics of kerf surface finishes, in particular, when the cutting time is long.

(3) The most concerned physical mechanisms underlying practical laser cutting processes can be concluded as follows:

- Two boundary layer flows exist and interact with each other at the gas / liquid interface. The shear stress is thus produced at the gas / liquid interface and it is predominantly responsible for the removal of the molten metal layer.

- The exothermic reaction contributes a considerable amount of energy, in addition to the absorbed laser power, to help heat up the workpiece. The exothermic energy entering into the metallic liquid film comes predominantly from the oxidisation reaction of the gas (O_2) and the metallic liquid (Fe), rather than that of the gas (O_2) and the metallic vapour (Fe).

- The molten metal layer, acting as a linear moving heat source, will incur the unavoidable heat conduction loss. It is also responsible for the retrieval of part of the heat conduction loss when it advances. Theoretically, however, due to the invalidity of pre-conditions when applying the moving heat source theory in the modelling, the heat conduction loss can be evaluated by the heat convection theory, i.e., the heat convected from the flowing molten metal layer into the liquid / solid interface can instead be calculated.

- Keeping V_c (cutting velocity) constant does not guarantee the constant value of V_e (fusion front velocity at the liquid / solid interface), simply because there is no physical bond between V_c and V_e in reality. The oscillation of V_e with respect to time is confirmed. This consequently changes the interacting area of the laser beam and the workpiece and thus influences the absorption of laser power by the workpiece.

The structure of this thesis has been rooted in the following 3 respects:

(1) to describe as comprehensively as possible the physics in the laser cutting process. In this respect, it is worthwhile to refer to the previous laser cutting models and endeavours [1-14].

(2) to abstract as reasonably as possible the so-called theoretical laser cutting system from the reality. By doing so, the differences between the theoretical laser cutting system and the practical laser cutting system are crystal clear, as analysed in Chapter 2.

(3) to generalise the calculated results and optimise the laser operating parameters. In this respect, the author of this thesis has not furthered too deep during limited PhD period. 2 prospective research directions in Chapter 10-4 are thus strongly recommended.

At the completion of this thesis, the originality of this thesis is emphasised as follows, not for the author to be proud of but for the reader to be aware where he or she may start.

(1) A 2-dimensional-based, dynamic model concerning the reactive jet gas assisted laser cutting of metals has been constructed in this thesis. As far as the author is aware, to date, this is the first, most comprehensive, dynamic model in the research communities of laser materials processing. Dynamic solutions rather than static ones are thus naturally expected, i.e., the 5 most concerned time-dependent variables, $\delta_l(t)$, $T_l(t)$, $V_e(t)$, $y(t)$ and $P_{l,abs}(t)$, as defined above, can be simultaneously simulated in respect of cutting time. For example, the periodicity of striations can be calculated by analysing the periodicity of $\delta_l(t)$.

(2) The sets of differential governing equations for the theoretical laser cutting system have been derived and they are comprised of 5 or 4 coupled, 1st-order, non-linear differential equations. The detailed boundary conditions for the governing equations have been derived based on both physical and mathematical grounds; they must be satisfied in every step of time evolution. Chaos theory certifies that the theoretical laser cutting system, governed by the differential governing equations, is essentially chaotic.

(3) The measured striations demonstrate that the chaotic nature is embedded in a practical laser cutting system where any unstable factors in, for example, the laser power and cutting velocity will add to more complexity in the laser cutting mechanism. Essentially, the chaotic striations are unavoidably generated (including nearly periodic striations) regardless of how constant all the operating parameters are adhered to. Both the theoretical calculations and the experimental measurements reveal the dynamic nature of the striations: the variable $\delta_i(t)$ with respect to time produces the local striations with variable periodicity and thus variable local kerf widths. The optimised operating parameters for good cuts (nearly periodic fine striations) can be theoretically predicted by achieving the nearly periodic variation of $\delta_i(t)$ together with the smallest phase space comprised of the 5 time-dependent variables.

The End

Appendix 1. Typical operating parameters used in the experiment

In this appendix, a set of typical operating parameters used in the experiment, introduced in Chapter 9, are listed for reference throughout this thesis. Theoretically, they are taken as time-independent variables in the modeling. Practically, any unexpected unstable factors contribute to a greater or lesser extent into the dynamic development of striations.

- The ambient pressure, p_a:

$p_a = 1\ (atm) = 1.015 \times 10^5\ (N/m^2)$;

- The ambient temperature, T_a :

$T_a = 300\ (^oK)$;

- The stagnation pressure of the gas, p_0 :

$p_0 = 2\ (atm) = 2.03 \times 10^5\ (N/m^2)$;

- The stagnation temperature of the gas, T_0:

$T_0 = 300\ (^oK)$;

- Mach number of gas jet in the exit plane of the nozzle, M_g :

$M_g = 1$;

- The velocity of translation of laser beam along Y, V_c:

$V_c = 900\ (mm/min) = 1.5 \times 10^{-2}\ (m/sec)$;

- The total power of laser radiation in the beam waist, P_l:

$P_l = 800\ (W)$;

- The thickness of metallic sheet to be cut, D:

$D = 6\ (mm.) = 6 \times 10^{-3}\ (m.)$;

- The average measured kerf width, w *:

$w = 2\ (mm.) = 2 \times 10^{-3}(m.)$

- The dimension of focused laser power with Gaussian profile intensity, $2a \times 2a$,

$2a = w = 2 \times 10^{-3}(m.)$; $a = \frac{1}{2}w = 1 \times 10^{-3}(m.)$;

- The width of nozzle of gas jet in Y, $2b$,

$2b = 4 \times 10^{-3}(m.)$;

- The average measured angle of the fusion front to horizontal plane, α,

$\alpha = 85\ (^{o})$;

* The value of w is used in the evaluations of derived quantities for the theoretical laser cutting system. The dynamic modeling in this thesis only concerns the variations in X-O-Y or X-O-S planes, as shown in the physical model in Fig.9. Therefore, w in Z can be essentially taken as any constant, as long as it is much larger than the thickness of the molten metal film.

Appendix 2. Calculation for gas flow

In this appendix, the flow parameters in the free stream of the gas are calculated with the data in Appendix 1. The pure oxygen gas is used and it is treated as an ideal gas. The data are used in this thesis wherever required. They are time-independent in the modeling.

- The specific heat ratio for O_2, $\gamma = 1.401$ [20];
- The relative molar mass of O_2, $M_{O_2} = 32 \times 10^{-3}$ $(kg / mole)$;
- The universal constant for ideal gases: $\Re = 8.3144$ $(J / mole \cdot {}^{o}K)$

- The gas pressure in free stream, p_g, is calculated [24]:

$$p_g = p_0 \cdot (1 + \frac{\gamma - 1}{2} \cdot M_g^2)^{\frac{\gamma}{1-\gamma}} = 2.03 \times 10^5 \times (1 + \frac{1.401 - 1}{2} \times 1^2)^{\frac{1.401}{-0.401}} \quad \text{(A2-1)}$$
$$= 1.072 \times 10^5 \ (N / m^2)$$

- The gas temperature in free stream, T_g:

$$T_g = T_0 \cdot (1 + \frac{\gamma - 1}{2} \cdot M_g^2)^{-1} = 300 \times (1.2005)^{-1} = 249.9 \ ({}^{o}K) \quad \text{(A2-2)}$$

- The stagnation density, ρ_0, and the gas density in free stream, ρ_g, respectively:

$$\rho_0 = \frac{p_0 \cdot M_{O_2}}{T_0 \cdot \Re} = \frac{2.03 \times 10^5 \times 32 \times 10^{-3}}{300 \times 8.3144} = 2.6 \ (kg / m^3) \quad \text{(A2-3)}$$

and,

$$\rho_g = \rho_0 \cdot (1 + \frac{\gamma - 1}{2} \cdot M_g^2)^{\frac{1}{1-\gamma}} = 2.6 \times (1.2005)^{\frac{1}{-0.401}} = 1.65 \ (kg / m^3) \quad \text{(A2-4)}$$

- The free stream velocity of the gas, U_g:

$$U_g = M_g \cdot (\gamma \cdot \frac{\Re}{M_{O_2}} \cdot T_g)^{\frac{1}{2}} = 1 \times (1.401 \times \frac{8.3144}{32 \times 10^{-3}} \times 249.9)^{\frac{1}{2}} = 301.6 \ (m / sec) \qquad \text{(A2-5)}$$

- The gas temperature at the gas / liquid interface, $T_{g,w}$, is expected:

$$T_{g,w} = T_l \geq T_m = 1808 \ (^{o}K) \qquad \text{(A2-6)}$$

where T_l: the surface temperature of molten metal layer at gas / liquid interface (^{0}K);

T_m: the temperature of fusion of Fe at around p_a, $T_m = 1808 \ (^{0}K)$;

- The gas pressure at the gas / liquid interface, $p_{g,w}$, is taken as:

$$p_{g,w} = p_g \qquad \text{(A2-7)}$$

- The gas density at the gas / liquid interface, $\rho_{g,w}$:

$$\rho_{g,w} = \frac{p_{g,w} \cdot M_{O_2}}{T_{g,w} \cdot \Re} \leq \frac{1.072 \times 10^5 \times 32 \times 10^{-3}}{1808 \times 8.3144} = 0.228 \ (kg / m^3) \qquad \text{(A2-8)}$$

Appendix 3. Thermophysical properties

- thermodynamic and transport properties

In this appendix, the thermophysical properties (thermodynamic and transport properties) for the gas, the liquid and the solid are listed for reference. Although they are all treated as time-independent variables in the modeling, their temperature-dependencies are considered.

In particular, the thermophysical properties of the gas are strongly associated with the local temperature. Fig.A1 demonstrates the principle to choose the temperature-dependent thermophysical properties for the gas.

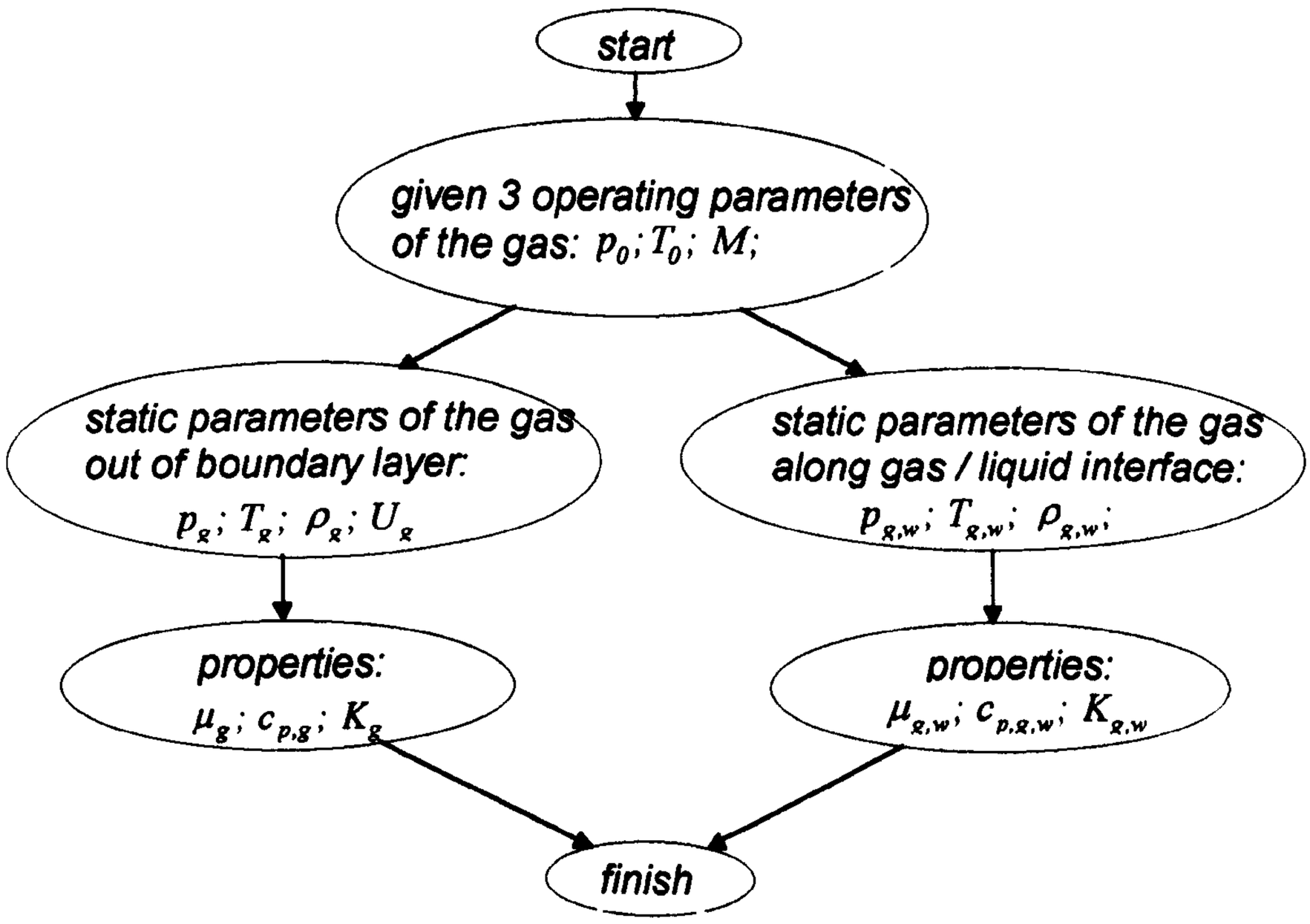

Figure A1. *The principle to choose the temperature-dependent thermophysical properties for the gas. The local temperatures in the free stream, T_g, and at the gas / liquid interface, $T_{g,w}$, are listed in Appendix 2*

- The dynamic viscosity for oxygen gas, μ_g, at around T_g and $p_g = 1\ (atm)$ [20]:

$\mu_g = 178.63 (micropoises) = 1.79 \times 10^{-5}\ (N \cdot s / m^2)$;

- The dynamic viscosity for oxygen gas, $\mu_{g,w}$, at around T_m and $p_g = 1\ (atm)$:

$\mu_{g,w} = 7.03 \times 10^{-5}\ (N \cdot s / m^2)$;

- Prandtl number for oxygen gas, $(Pr)_g$:

at T_g, $(Pr)_g = 0.691$;

at T_m, $(Pr)_g = 0.704$;

It justifies the theoretical treatment in solving the boundary layer equations for the gas in Section 4-1, where $(Pr)_g$ is treated as constant. For the calculation, it is taken as:

$(Pr)_g = 0.698$;

- The specific heat for oxygen gas, $c_{p,g}$, at T_g [20]:

$c_p / \Re = 3.534$,

$c_{p,g} = 8.3144 \times 3.534 = 29.38\ (J / mole \cdot {}^\circ K) = 918 (J / kg \cdot {}^\circ K)$;

- The specific heat for oxygen gas, $c_{p,g,w}$, at around T_m :

$c_p / \Re = 4.483$,

$c_{p,g,w} = 8.3144 \times 4.483 = 37.27\ (J / mole \cdot {}^\circ K) = 1164.7 (J / kg \cdot {}^\circ K)$;

- The thermal conductivity for liquid Fe, K_l, at around $1808 - 2000\ ({}^\circ K)$ [23]:

$K_l = 41.8\ (W / m \cdot {}^\circ K)$;

- The specific heat for liquid Fe, $c_{p,l}$, at around $T_m = 1808\ ({}^\circ K)$:

$c_{p,l} = 664.8\ (J / kg \cdot {}^\circ K)$;

- The dynamic viscosity for liquid Fe, at $T_m = 1808\ (^oK)$ [27]:

$\mu_l = 3.9 \times 10^{-3} (N \cdot m / (m^2))$;

- The density for liquid Fe at around $T_m = 1808\ (^oK)$:

$\rho_l = 7.86 \times 10^3\ (kg / m^3)$;

- The density for solid Fe at around $T_m = 1808\ (^oK)$ [28]:

$\rho_s = 7.874 \times 10^3\ (kg / m^3)$;

- The thermal conductivity for solid Fe, K_s, at around $T_m = 1808\ (^oK)$ [23]:

$K_s = 0.35\ (W / cm \cdot ^oK) = 35\ (W / m \cdot ^oK)$;

- The specific heat for solid Fe, $c_{p,s}$, at around $T_m = 1808\ (^oK)$:

$c_{p,s} = 557\ (J / kg \cdot ^oK)$;

- The enthalpy of fusion for Fe, h_f, at $T_m = 1808\ (^oK)$ [28]:

$h_f = 65.0\ (Cal / g) = 2.72 \times 10^5\ (J / kg)$;

The enthalpy of evaporation for Fe, h_v, at $T_v = 3133\ (^0K)$ [30]:

$h_v = 6.65 \times 10^6\ (J / kg)$

- The relative molar mass of Fe,

$M_{Fe} = 55.85 \times 10^{-3}\ (kg / mole)$;

- The temperature of fusion and of vaporization of Fe, at around p_a, respectively,

$T_m = 1808\ (^0K)$;

$T_v = 3133\ (^0K)$;

- The relative molar mass of FeO,

$M_{FeO} = 71.85 \times 10^{-3}$ $(kg / mole)$;

Appendix 4. Chemical reaction between oxygen gas and metallic vapour

-The method to calculate the rate of exothermic energy into the molten metal layer

In this appendix, the method to calculate the rate ($\dot{q}_{LJ}$) of heat transfer from the boundary layer of the gas mixture into the molten metal layer for the oxidisation reaction between the oxygen gas and metallic vapour of iron with the product of FeO in gaseous phase, is listed for reference. This method of calculation was derived by Dutta [P.84-P.88, reference 3]. $\dot{q}_{LJ}$ reflects the combined effect of the chemical reactions, the cooling and the evaporation. The mathematical symbols used here are the same as in the original work for the convenience of check-up. Since the calculation is based on the steady-state analysis, the typical data listed in Appendixes 1-3 are used wherever required. Consequently, the mathematical symbols used in the domain of this thesis are converted into the ones used in this appendix, by the same definitions, respectively. Some modifications of the formulas are made by the author of this thesis.

The oxidisation reaction is assumed as the chemical equilibrium:

$$1\times(O)+1\times(Fe)=1\times(FeO)+\Delta Q_{FeO} \tag{A4-1}$$

The objective is to evaluate the rate of heat transfer flux, $\dot{q}_{LJ}$, from the boundary layer of the gas mixture into the liquid metal, derived as:

$$\dot{q}_{LJ}=C_H\cdot\rho_e\cdot U_e\cdot[(I_f)_e-(I_f)_g+\frac{G(\infty,P)}{G(\infty,S)}\cdot h_c-B_3\cdot L_V] \tag{A4-2}$$

Chemical reaction enthalpy, h_c

$$h_c=\Delta Q_{FeO}[(1+B_4)\cdot(C_{FeO})_g] \tag{A4-3}$$

(1) Enthalpy of reaction at the temperature of gas / liquid interface, ΔQ_{FeO}

At $T = 298\,(^{\circ}K)$, ΔQ_{FeO} is calculated with Hess' principle using the respective heats of formation from the standard tables [30]. It is then modified by Kirchhoff's equation to the temperature of the reaction in Eq.A4-1. The method can be referred to in Chapter 5-2.

(2) Species mass fraction for FeO at gas / liquid interface, $(C_{FeO})_g$

$$C_i = \frac{\rho_i}{\rho} = \frac{\rho_i}{\sum \rho_i} = \frac{M_i \times p_i}{\sum (M_i \times p_i)} \qquad \text{(A4-4)}$$

where, the subscript i denotes the 3 species, respectively, which are treated as ideal gases; M_i is the relative molar mass for i. The calculation of p_i is as follows.

The mass action constant for the chemical equilibrium identified in Eq.A4-1 is defined by the mass action law *:

$$K_{p,1} = \frac{p_{FeO}}{p_{Fe} \cdot p_O} \qquad \text{(A4-5)}$$

the mass action constant for the vaporisation of Fe:

$$K_{p,2} = p_{Fe} \qquad \text{(A4-6)}$$

By Dalton's law of partial pressure:

$$p_e = p_{Fe} + p_O + p_{FeO} \qquad \text{(A4-7)}$$

---

* In Dutta' thesis, the mass action constant for the reaction was defined as: $K_{p,1} = \frac{p_{Fe} \cdot p_O}{p_{FeO}}$. In accordance with the definition of mass action constant for the vaporisation of Fe: $K_{p,2} = p_{Fe}$, it should be defined as Eq.A4-5 [P.2 - P.18, reference 30]

where, p_e is the static pressure of the gas mixture at the edge of the boundary layer flow.

Combining Eqs.A4-5, A4-6, and A4-7, p_i are discovered *:

$$p_{Fe} = K_{p,2}$$
$$p_O = \frac{(p_e - K_{p,2})}{1 + K_{p,1} \cdot K_{p,2}} \qquad \text{(A4-8)}$$
$$p_{FeO} = \frac{(p_e - K_{p,2})}{1 + K_{p,1} \cdot K_{p,2}} \cdot K_{p,1} \cdot K_{p,2}$$

In Eq.A4-8, $K_{p,1}$ is calculated from:

$$\Delta G^o = -4.574 \cdot T \cdot \log(K_p) \qquad \text{(A4-9)}$$

where, for $K_{p,1}$, ΔG^o is the standard Gibbs energy of reaction (*Cal.*); $K_{p,1}$ and $K_{p,2}$ are calculated when partial pressures are in the unit of atmosphere (*atm.*). ΔG^o is found out as [Table E, reference 30], with the unit of *Cal / mole of iron* **:

$$\Delta G^o_{T_l} = -55620 + 10.83 \times T_l \qquad \text{(A4-10)}$$

For $K_{p,2}$, ΔG^o is the standard Gibbs energy of vaporisation of liquid Fe. Here, $K_{p,2}$ is calculated by assuming p_{Fe} is the saturated vapour, $P_{Fe,sat}$, [Table D, reference 30] ***:

---

* Eq.A4-8 is here derived by the author of this thesis.

** Due to availability of data, ΔG^o used here is precisely for the practical chemical equilibrium [30]:
$\frac{1}{2} \times (O_2) + 1 \times \{F_e\} = 1 \times \{F_eO\}$

*** The calculation of $K_{p,2}$ here is carried out by the author of this thesis, alternatively. In Dutta' s original work, it was suggested by finding ΔG^o from the thermochemical tables. ΔG^o of the vaporisation of liquid iron is essentially related with the saturated vapour pressure [30].

$$\log p_{Fe,sat} = -19710 \times T_l^{-1} - 1.27 \times \log T_l + 13.27 \ (mmHg) \tag{A4-11}$$

$$p_{Fe} = p_{Fe,sat} \tag{A4-12}$$

(3) Mass transfer parameter B_4

B_4 is calculated by,

$$(\overline{C}_O)_g = \frac{(\overline{C}_O)_e}{1+B_4} \text{ and } (\overline{C}_{Fe})_g = \frac{B_4 + (\overline{C}_{Fe})_e}{1+B_4} \tag{A4-13}$$

$$(\overline{C}_i) = \Sigma(r_{i,k} \cdot C_k) \tag{A4-14}$$

where, $\overline{C}_i$ denotes the element mass fraction for the chemical elements of O and Fe, respectively. The subscripts *e* and *g* denote the situations at the edge of boundary layer and the surface of gas / liquid interface, respectively. The subscript *k* denotes 3 species. $r_{i,k}$ is the fraction of mass of species *k* which is contributed by element i .

Quantity of $\frac{G(\infty,S)}{G(\infty,P)}$

$$G(\infty,S) = \int_0^{\eta} \frac{S}{C} \cdot exp(-\int_0^{\eta'} \frac{S}{C} \cdot f \cdot d\eta'')d\eta' \text{ when } \eta = \infty$$

and ,

$$G(\infty,P) = \int_0^{\eta} \frac{P}{C} \cdot exp(-\int_0^{\eta'} \frac{P}{C} \cdot f \cdot d\eta'')d\eta' \text{ when } \eta = \infty \tag{A4-15}$$

where, S : Schmidt number; P : Prandtl number. The ratio is evaluated by analysing Lewis number: $L = \frac{P}{S}$. In the derivation of the differential governing equations for the "frozen" boundary layer approximation, Lewis number has been taken as unity, $P = S$. Therefore,

$$\frac{G(\infty,S)}{G(\infty,P)} = 1 \tag{A4-16}$$

Mass transfer parameter, B_3

$$B_4 = \frac{G(\infty,S)}{G(\infty,P)} B_3 \tag{A4-17}$$

Heat transfer coefficient, C_H

The heat transfer coefficient, C_H, is calculated *:

$$C_H = \frac{1}{B_3} \frac{(\rho v)_g}{\rho_e U_e} \tag{A4-18}$$

where, the density, ρ_e, and the velocity, U_e, at the edge of the boundary layer of the gas mixture are assumed the same as those in the free stream of oxygen gas. They are listed in Appendix 2.

Because FeO has been treated as an ideal gas, the density of gas mixture at the interface of liquid / gas, ρ_g, can be calculated by Eq.A4-4:

$$\rho_g = \frac{\rho_{FeO}}{C_{FeO}} = \frac{1}{C_{FeO}} \cdot \frac{M_{FeO} \cdot p_{FeO}}{\Re \cdot T_l} \tag{A4-19}$$

* The calculation of C_H which appears in Eq.A4-2 was not mentioned in Method of Calculation in Dutta's PhD thesis. $B_3 = \frac{(\rho v)_g}{C_h \rho_e U_e}$ was defined in the Nomenclature of Chapter 5 of his work.

For the velocity of gas mixture at the interface of liquid / gas along Y in Fig.4, v_g, it is taken as the velocity of translation of laser beam (V_c) as shown in Appendix 1.

The difference of partial enthalpies, $(I_f)_e - (I_f)_g$

The partial enthalpies, $(I_f)_g$ and $(I_f)_e$, are defined as:

$$I_f = \Sigma C_i \cdot (\int_0^T C_{p,i} dT) + \frac{u^2}{2} \qquad \text{(A4-20)}$$

$$[(I_f)_e - (I_f)_g] =$$

$$[(C_O)_e C_{p,O} T_e + \frac{U_g^2}{2}] - [(C_{Fe})_g C_{p,Fe} T_g + (C_O)_g C_{p,O} T_g + (C_{FeO})_g C_{p,FeO} T_g + \frac{u_g^2}{2}] \qquad \text{(A4-21)}$$

where, u denotes the velocity along s co-ordinate as shown in Fig.4; $C_{p,i}$ is the specific heat at constant pressure for i. They are calculated through the following procedures:

u_e is taken as the same as U_e shown in Appendix 2. u_g is taken as $u_{0,max}$ calculated by Eq.38 where μ_l is taken as: $\mu_l = (\mu_{FeO})_g = 1.437 \times 10^{-4}$ *(kg/m s)* *. The other properties in Eq.38 are listed in Appendix 3.

At the liquid / gas interface, C_i can be calculated by Eq.A4-4; at the liquid / gas interface, C_i are:

---

* Due to $(C_{FeO})_g = 0.8357$, it is justified that the physical properties of gas mixture at the liquid / gas interface such as the dynamic viscosity are dominated by those of gaseous FeO. The value of $(\mu_{FeO})_g$ is approximately evaluated by the author of this thesis since the transport properties of gaseous FeO are not available from major reference books. It is estimated with the empirical relations of data for the gases: Ar, O_2, N_2, CO and air at $1800(^oK)$ [20].

$(C_{FeO})_e = 0,\ (C_{Fe})_e = 0$ and $(C_O)_e = 1$ (A4-22)

This is due to the assumption of "frozen" boundary layer. $C_{p,i}$ is approximately taken as *:

$$C_{p,O} = 1.2 \times 10^3\ ;\ C_{p,Fe} = 7.5 \times 10^2;\ C_{p,FeO} = 9.5 \times 10^2\ \ (J/kg\cdot^oK) \quad \text{(A4-23)}$$

Enthalpy of evaporation of liquid iron, L_V

It is listed in Appendix 3. $L_V = 6.65 \times 10^6\,(J./kg)$.

In conclusion, under the condition of typical data in Appendixes 1-3, all the quantities involved in the derivations identified above are listed for reference:

$p_e = 1.056(atm.);\ T_e = 249.9(^oK);\ \rho_e = 1.65\ (kg/m^3);\ U_e = u_e = 301.6\ (m/s);$

$(C_{FeO})_e = 0;\ (C_{Fe})_e = 0;\ (C_O)_e = 1;$

$(C_{FeO})_g = 0.8357;\ (C_{Fe})_g = 2.55 \times 10^{-4};\ (C_O)_g = 0.164;$

$(p_{FeO})_g = 0.5610(atm);\ (p_{Fe})_g = P_{Fe,sat} = 2.2 \times 10^{-4}(atm);\ (p_O)_g = 0.4947(atm);$

$K_{p,2} = 2.2 \times 10^{-4};\ K_{p,1} = 5.156 \times 10^3;$

$(C_{FeO})_g = 0.8357;\ (C_{Fe})_g = 2.55 \times 10^{-4};\ (C_O)_g = 0.164;$

$(\overline{C}_{Fe})_g = 0.6496;\ (\overline{C}_{Fe})_e = 0;$

$\rho_g = 0.294\ (kg/m^3);\ \mu_g \approx (\mu_{FeO})_g = 1.437 \times 10^{-4}\,(N\cdot s/m^2);\ T_g = 2000(^oK);$

$v_g = 1.5 \times 10^{-2}(m./s.);\ u_g \le 3.35\ (m./s.);$

$C_{p,O} = 1.2 \times 10^3\ ;\ C_{p,Fe} = 7.5 \times 10^2\ ;\ C_{p,FeO} = 9.5 \times 10^2\,(J/kg\cdot^oK);$

$[(I_f)_e - (I_f)_g] = -1.636 \times 10^6\,(J/kg);$

---

* The data chosen by the author of this thesis are from [Tables C1, C2, reference 30], where, (O_2) is used for (O), $\{Fe\}$ for (Fe) and $\{FeO\}$ for (FeO) at the temperature of $1800 - 2000\,(^oK)$

$L_V = 6.65 \times 10^6 (J./kg)$;

$C_H \leq 7.744 \times 10^{-6}$;

$B_3 = B_4 = 1.8539$;

$\frac{G(\infty, S)}{G(\infty, P)} = 1$;

$\Delta Q_{FeO}\big|_{2000K} = -1.325 \times 10^7 (J./kg\ of\ gaseous\ FeO)$ when $1808 \leq T_g \leq 2000 (^oK)$;

$h_c = -3.16 \times 10^7 (J./kg\ of\ gaseous\ FeO)$;

By contributing the relevant data above into Eq.A4-2, $\dot{q}_{LJ}$ is:

$\dot{q}_{LJ} = -1.08 \times 10^5 (W/m^2)$.

With $D = 6 \times 10^{-3} (m.)$; $w = 2 \times 10^{-3} (m.)$ in Appendix 1, the total heat rate from the gas mixture into the molten metal layer is calculated by knowing $\dot{q}_{LJ}$ above:

$q_{LJ} = D \times w \times \dot{q}_{LJ} = -1.30\ (W)$,

where, the negative sign means that the chemical reaction system releases the energy.

Appendix 5. The moving heat source theory for heat conduction in solids

In this appendix, 3 types of calculation method to evaluate the conductive heat rate, $\dot{e}_{cond}$, at the liquid / solid interface, are introduced. The evaluations of the derived quantities are analysed in association with Chapter 6. The first method of calculation is derived assuming that the molten metal layer is extremely thin and it flows extremely slowly. The other 2 are derived based on the heat conduction theory for a moving heat source in solids. They are evaluated with the typical data in Appendices 1-3. The mathematical symbols used here are the same as in the main contents, except those only related with the local derivations. Because they only seek steady-state solutions, the 5 time-dependent variables are denoted without *(t)* wherever they are used, e.g., T_l for $T_l(t)$ and so on.

The method by Dutta

Assuming that the molten metal layer is extremely thin and it flows extremely slowly, the heat convection in the liquid reduces to the heat conduction [3]. In X-O-S in Fig.13, $(\frac{dT}{ds})$ at the liquid / solid interface, i.e., $s = 0$, is calculated,

$$(\frac{dT}{ds}) = \frac{T_m - T_l}{\bar{\delta}_l} \quad \text{at } s = 0 \tag{A5-1}$$

$\bar{\delta}_l$: the average thickness of molten metal layer, $\bar{\delta}_l = \frac{1}{2}\delta_l$;

Contributing Eq.A5-1 into Eq.57 gives:

$$\dot{e}_{loss} = \dot{e}_{cond} = 2(wD)K_l \frac{T_l - T_m}{\delta_l} \tag{A5-2}$$

Let: $T_l = 2000\,(^oK)$; $T_m = 1808\,(^oK)$; $\delta_l(t) = \delta_{l,max} = 0.105 \times 10^{-3}\,(m.)$;

$\dot{e}_{loss}$ can be found: $\dot{e}_{loss} = 1834.4\,(W.)$.

The method by Schuocker

Taking the molten metal layer as a linear heat source moving in the solid, the steady-state solution, derived by Carslaw and Jaeger [Section 10.7, reference 34], can be expressed, in X-O-Y system in Fig.12:

$$T_{(r)} = \frac{\dot{e}_{loss}}{2\pi K_s D} \cdot exp(\frac{V_e y}{2k_s}) \cdot K_0(\frac{V_e r}{2k_s}) \quad \text{when } r = \sqrt{y^2 + z^2} \neq 0 \qquad \text{(A5-3)}$$

where, k_s: the thermal diffusivity of the solid, $k_s = \frac{K_s}{\rho_s c_{p,s}}$. Z is vertical to X-O-Y plane. It is noted that the formula by Eq.A5-3 is invalid if $r = \sqrt{y^2 + z^2} = 0$. To apply Eq.A5-3 to the evaluation of $\dot{e}_{loss}$ at the liquid / solid interface, in X-O-Y plane, the crucial point is to determine the situation when $y \to 0$ *. The method by Schuocker [5] is listed as follows:

By approximately assuming $y = \frac{w}{2}$, $T_{(\frac{w}{2})} = T_m = 1808\,(^oK)$, where w is the kerf width, $\dot{e}_{loss}$ is expressed by Eq.A5-3:

---

* In abiding by this critical condition, assuming $T_{(\frac{\delta_l}{2})} = T_m = 1808\,(^oK)$, Eq.A5-3 becomes:

$$\dot{e}_{loss} = \frac{2\pi K_s D T_m}{exp(\frac{V_c \delta_l}{4k_s}) K_0(\frac{V_c \delta_l}{4k_s})}$$

By taking $V_e = V_c$; $\delta_l = \delta_{l,max}$, $\dot{e}_{loss}$ is found: $\dot{e}_{loss} = 725.9\,(W.)$.

$$\dot{e}_{loss} = \frac{2\pi K_s D T_m}{exp(\frac{V_e w}{4k_s}) K_0(\frac{V_e w}{4k_s})} \tag{A5-4}$$

Using the data in Appendixes 1-3 and letting $V_e = V_c = 1.5 \times 10^{-2}\,(m/s)$,

$\dot{e}_{loss}$ is found: $\dot{e}_{loss} = 2030.2\,(W.)$.

The method by Schulz

The work proposed by Schulz [35] is listed as follows:

$$\dot{e}_{cond} = 4 \cdot K_s \cdot D \cdot (T_m - T_a) \cdot (\frac{P_e}{2})^{\gamma} \tag{A5-5}$$

Eq.A5-5 is valid when Peclet number,

$$P_e = \frac{r_0 \cdot V_c}{k_s} \tag{A5-6}$$

is between 0.2 and 4. γ is slightly dependent on the aperture ratio: $\frac{r_k}{r_0}$, where r_k is the half of the kerf width. When $\frac{r_k}{r_0}$ is within the interval $\frac{r_k}{r_0} \in (0, 0.9)$, γ varies within the interval: $\gamma \in (0.30, 0.36)$.

With the typical data in Appendix 3,

$r_k = \frac{1}{2} w = 1 \times 10^{-3}\,(m.)$; $r_0 = \frac{1}{0.9} r_k = 1.11 \times 10^{-3}\,(m.)$;

$\gamma = 0.33$;

$V_c = 1.5 \times 10^{-2}\,(m./s.)$;

$K_s = 35\,(W/m \cdot {}^{o}K)$; $k_s = 7.98 \times 10^{-6}\,(m^2/s)$;

$T_a = 300\ (^oK)$;

$D = 6 \times 10^{-3}\ (m.)$;

In this case, for example, $\dot{e}_{loss}$ is found: $\dot{e}_{loss} = \dot{e}_{cond} = 1284.5\,(W.)$.

Appendix 6. Differential governing equations program

This appendix demonstrates the program for numerically solving the differential governing equations for the theoretical laser cutting system. This program is coded in C with *Turbo C / C++ 3.0*; it can be successfully executed under *MS-DOS*. A test is shown to prove the applicability of the program.

Program

```
/* Copyright 1998-  All Rights Reserved! */

#include <stdio.h>

#include <nr.h>
#include <nrutil.h>

#include <math.h>
#include <graphics.h>
#include <conio.h>
#include <stdlib.h>

#define MAXSTP 1.0e10
#define TINY 1.0e-3

#define PGROW -0.20
#define PSHRNK -0.25
#define FCOR 0.06666666
#define SAFETY 0.9
#define ERRCON 6.0e-4

#define N 2

float dxsav, *xpp, **ypp ;
int kount, kmax ;

/*=============================================================================
  Definition of all the variables :
  y[0] - thickness of metallic liquid layer, δ_l(t);
  y[1] - displacement of fusion front and laser beam front, y(t);
  y[2] - absorption of laser power by metallic liquid film, P_{l,abs}(t);
  y[3] - fusion front velocity at liquid / solid interface, V_e(t);
  y[4] - surface temperature of metallic liquid at gas / liquid interface, T_l(t);
  x - cutting time, t;
=============================================================================*/
void derivs ( x , y , dydx )
   float x, y[] , dydx[];
   {
```

```
        dydx[0] = 2*sin(y[0]) ;
        dydx[1] = 4*cos(y[1]) ;
        dydx[2] = 474.593*(14-y[3])/exp(fabs(y[1]-1)) ;
        dydx[3] = 2512.2*y[0]*y[3]-1.583*pow(10,6)*pow(y[0],3) ;
        x = x/1. ;
    }
/*=============================================================================*/
void ouydbc ( y , dy_dx )
    float *y, *dy_dx;
    {
            int i;
            for (i=0 ; i<N ; i++)
                {
                    if (y[0]<0.0)    {y[0]=eps    ; dy_dx[0]=0.0;}
                    if (y[0]>0.21)   {y[0]=0.21   ; dy_dx[0]=0.0;}
                    if (y[1]<0.0)    {y[1]=eps    ; dy_dx[1]=0.0;}
                    if (y[1]>1.0)    {y[1]=1.0    ; dy_dx[1]=0.0;}
                    if (y[2]<0.0)    {y[2]=eps    ; dy_dx[2]=0.0;}
                    if (y[2]>600.0)  {y[2]=600.0  ; dy_dx[2]=0.0;}
                    if (y[3]<0.0)    {y[3]=eps    ; dy_dx[3]=0.0;}
                   if (y[4]>1808.0) {y[4]=1808.0  ; dy_dx[4]=0.0}
                }
        }
/*=============================================================================
  Here starts main() : following parameters need to be customerized to
meet specific needs.
  vector2[] and matri[][] should be allocated memory enough to accommodate
                          *xp and ** yp, i.e., larger than kmax, which will
                          determine dxsav.
  dxsav  is the pre-set gap of points; when x is a bit larger than it, the
           x and corresponding y[1..4] will be stored within *xp and **yp.
           two-level pointers will really contain memory : xp[N] and
           yp[N][kmax]; and kount++ will turn out to be kmax to make sure.
  x2  is the end of x
  x1  = 0.
=============================================================================*/

void main()
    {
            int i;
            float eps, h0, hmin, x1, x2, *ystart;
            float vector1[N], vector2[50], matri[N][50]; /* less than [4][3000] */
            void ouydgraph ();

            ystart = vector1;
            xpp = vector2;
            ypp = matri;

            x1 = 0.0;   /* time starts from 0 (sec) to ? (sec) */
            x2 = 50.;

            kmax = 50;
            dxsav = (x2-x1)/kmax;  /* minimum dx is stored in *xp */

            ystart[0] = 0.;    /* (mm) */
            ystart[1] = 1.;     /* (mm) */
            ystart[2] = 200.0;   /*  w   */
            ystart[3] = 11.0;    /*  mm/sec */
```

```
eps = 1.0e-6;
h0 = 0.0001;        /* control one step quality  */

hmin = 0.0;         /* (sec) */

odeint(ystart, N, x1, x2, eps, h0, hmin, derivs, rkqc);

printf("\n%s %3d\n","stored intermediate values number :  ",kount);
printf("\n%8s %18s \n","xpp[]","ypp[3][]");

for (i=0;i<kount;i++)
   printf("%10.4f %16.6f\n",xpp[i],ypp[0][i]);
        ouydgraph();
   }

/*=============================================================================*/

void odeint(ystart, nvar, x1, x2, eps, h0, hmin, derivs, rkqc)
   float ystart[], x1, x2, eps, h0, hmin;
   int nvar;
   void (*derivs)();
   void (*rkqc)();
   {
        int nstp, i;
        float xsav, x, hnext, hdid, h;
        float *yscal, *y, *dydx;
        float vector3[N],vector4[N],vector5[N];

yscal = vector3;
y = vector4;
dydx = vector5;
x = x1;
h = fabs(h0);
kount = 0;

for (i=0 ; i<nvar ; i++)
   {
        y[i] = ystart[i];
        xpp[0] = x1;
        ypp[i][0] = ystart[i];
   }

for (nstp=1 ; nstp <= MAXSTP ; nstp++)
   {
        (*derivs)(x,y,dydx);

for (i=0; i<nvar; i++)
   yscal[i] = fabs(y[i])+fabs(dydx[i]*h)+TINY;

(*rkqc)(y, dydx, nvar, &x, h, eps, yscal, &hdid, &hnext, derivs);

x = x + hdid;

if ( x >= dxsav*(kount+1))
  {
        xpp[++kount] = x;
        for (i=0 ; i< nvar ; i++)
           ypp[i][kount] = y[i];
```

```
                h = hnext;
            }
        else
            h = hnext;

        if (fabs(hnext) <= hmin)
            printf("Step size too small in main() !");

        if (x >= x2)
            break;

    }
}

/*=============================================================================*/

void rkqc(y, dydx, n, x, htry, eps, yscal, hdid, hnext, derivs)
    float y[], dydx[], *x, htry, eps, yscal[], *hdid, *hnext;
    void (*derivs)(); /* ANSI : void (*derivs)(float, float *, float *); */
    int n;
    {
        int i;
        float xsav, hh, h, temp, errmax;
        float *dysav, *ysav, *ytemp;
        float vector6[N], vector7[N],vector8[N];
        void rk4();
        void ouydbc();

        dysav = vector6;
        ysav = vector7;
        ytemp = vector8;
        xsav = (*x);

        for (i=0 ; i<n ; i++)
            {
            ysav[i] = y[i];
            dysav[i] = dydx[i];
            }

        h = htry;

        for (;;)
            {
                hh = 0.5 * h;

                ouydbc(ysav,dysav);

                rk4(ysav, dysav, n, xsav, hh, ytemp, derivs);
                *x = xsav + hh;
                (*derivs)(*x, ytemp, dydx);

                ouydbc(ytemp, dydx);

                rk4(ytemp, dydx, n, *x, hh, y, derivs);
                *x = xsav + h;

                ouydbc(ysav, dysav);

                rk4(ysav, dysav, n, xsav, h, ytemp, derivs);
```

```
        errmax = 0.0;

        for (i=0 ; i<n ; i++)
           {
             ytemp[i] = y[i] - ytemp[i];
             temp= fabs(ytemp[i]/yscal[i]);
             if (errmax < temp)
                    errmax = temp;
           }

        errmax /= eps;

                    if (errmax <= 1.0)
                      {
                        *hdid = h;
                        *hnext = ( errmax > ERRCON ?
                                        SAFETY*h*exp(PGROW*log(errmax)) : 4.0*h );
                        break;
                      }

                    h = SAFETY*h*exp(PSHRNK*log(errmax));
                }

            for (i=0 ; i<n ; i++)
               y[i] += ytemp[i] * FCOR;
    }

/*=============================================================================*/

void rk4(y, dydx, n, x, h, yout, derivs)
    float y[], dydx[], x, h, yout[];
    void (*derivs)(); /* ANSI : void (*derivs)(float, float *,float *); */
    int n;
    {
            int i;
            float xh, hh, h6, *dym, *dyt, *yt;
            float vector9[N], vector10[N], vector11[N];

            dym = vector9;
            dyt = vector10;
            yt = vector11;

            hh = h * 0.5;
            h6 = h / 6.0;
            xh = x + hh;

for (i=0 ; i<n ; i ++) yt[i] = y[i] + hh*dydx[i];

(*derivs)(xh, yt, dyt);

for (i=0 ; i<n ; i ++)
   yt[i] = y[i] + hh*dyt[i];

(*derivs)(xh, yt, dym);

for (i=0 ; i<n ; i ++)
   {
     yt[i] = y[i] + h*dym[i];
     dym[i] += dyt[i];
```

```
            }

        (*derivs)(x+h, yt, dyt);

        for (i=0 ; i<n ; i++)
            yout[i] = y[i] + h6*( dydx[i] + dyt[i] + 2.0*dym[i] );
    }

/*=============================================================================
  Graph routine, which is coded to graphically show all the
variables y[1], y[2], y[3], y[4] and y[5] along with time x.
The input of the function is the global variable, from the function
 odeint, *xp and **yp, starting from x1 to x2.
 It is firstly to enter graph mode; to scale the screen; to set up coordinates;
 put in the scaled data by *xp and **yp.
=============================================================================*/

void ouydgraph()
    {
        int i, j;
        int nva;
        float xmin, xmax, ymin = 5000., ymax = -5000. ;
        char ch;
        int gmode, maxx, maxy, gdriver = DETECT ;
        float a, b, c, d;

        /*  Choose which variable to be shown graphically, nvar,
            i.e., x[nvar] against y[nvar][1 .. kmax] */

for(;;)
  {
    printf("Choose a variable to be graphically shown against time :\n");
    printf("0 - thickness of liquid boundary layer at kerf bottom (m)\n");
    printf("1 - relative displacement of fusion front and laser beam front (m)\n");
    printf("2 - absorption of laser power by workpiece (w)\n");
    printf("3 - fusion front velocity (m/sec)\n");
    printf("4 - surface temperature of liquid  (k)\n");
    ch = getche();
    if (ch == '0') {nva=0; break;}
    if (ch == '1') {nva=1; break;}
    if (ch == '2') {nva=2; break;}
    if (ch == '3') {nva=3; break;}
 /*  if (ch == '4') {nva=4; break;}    not use at moment */
    printf("Please key in a correct number corresponding to the variable you want : ");
  }

initgraph(&gdriver, &gmode, "\\backup\\tc\\bgi");

maxx = getmaxx();
maxy = getmaxy();

outtextxy(maxx/4, maxy/10, "Variables in respect with Time");

line(0,0,0,maxy);
line(0,maxy,maxx,maxy);
line(0,0,maxx,0);
line(maxx,0,maxx,maxy);

for (i=1; i<=20 ; i++)
```

```
    {
     line((maxx+1)/20*i , maxy , (maxx+1)/20*i , maxy-5);
    }

for (j=1; j<=20 ; j++)
    {
     line(0, maxy-(maxy+1)/20*j , 6 , maxy-(maxy+1)/20*j);
    }

/* Determine the maximum / minimum values of xp[1, 2, .., kmax] and
   yp[nvar][1, 2, ..kmax] in order to graph the points within the
   whole screen */

for (i=0 ; i<kmax ; i++)
   {
     xmax = xpp[kmax];
     xmin = xpp[0];
     if (ypp[nva][i] > ymax) ymax = ypp[nva][i];
     if (ypp[nva][i] < ymin) ymin = ypp[nva][i];
   }

/* Scale the coordinates between real world and specific screen */

   a = maxx / (xmax - xmin);
   b = -a * xmin;
   c = -maxy / (ymax - ymin);
   d = maxy - c*ymin;

/* Draw points in graph by *xp and **yp, when nvar is certain
                for variable          */

                for (j = 1 ; j < kmax ; j++)
                   {
                          putpixel ( (a*xpp[j]+b) , (c*ypp[nva][j]+d), GREEN);
//                        line((a*xpp[j-1]+b) , (c*ypp[nva][j-1]+d) ,
//                                (a*xpp[j]+b) , (c*ypp[nva][j]+d) );
                          line((a*xpp[j-1]+b) , (c*ypp[nva][j-1]+d) ,
                                (a*xpp[j]+b) , (c*ypp[nva][j]+d) );
                   }

                getch();
                closegraph();

   }
```

A test for the program

2 coupled 1st-order differential equations,

$$\begin{cases} \dfrac{d}{dt}[x_1(t)] = -0.2x_1(t) - x_2(t) - \left[(x_1(t))^2 + (x_2(t))^2\right]x_1(t) \\ \dfrac{d}{dt}[x_2(t)] = -0.2x_2(t) - x_1(t) - \left[(x_1(t))^2 + (x_2(t))^2\right]x_2(t) \end{cases}$$

are numerically solved with the program and *MathCad6* [P363, reference 64], respectively. The comparison demonstrates the applicability of the program.

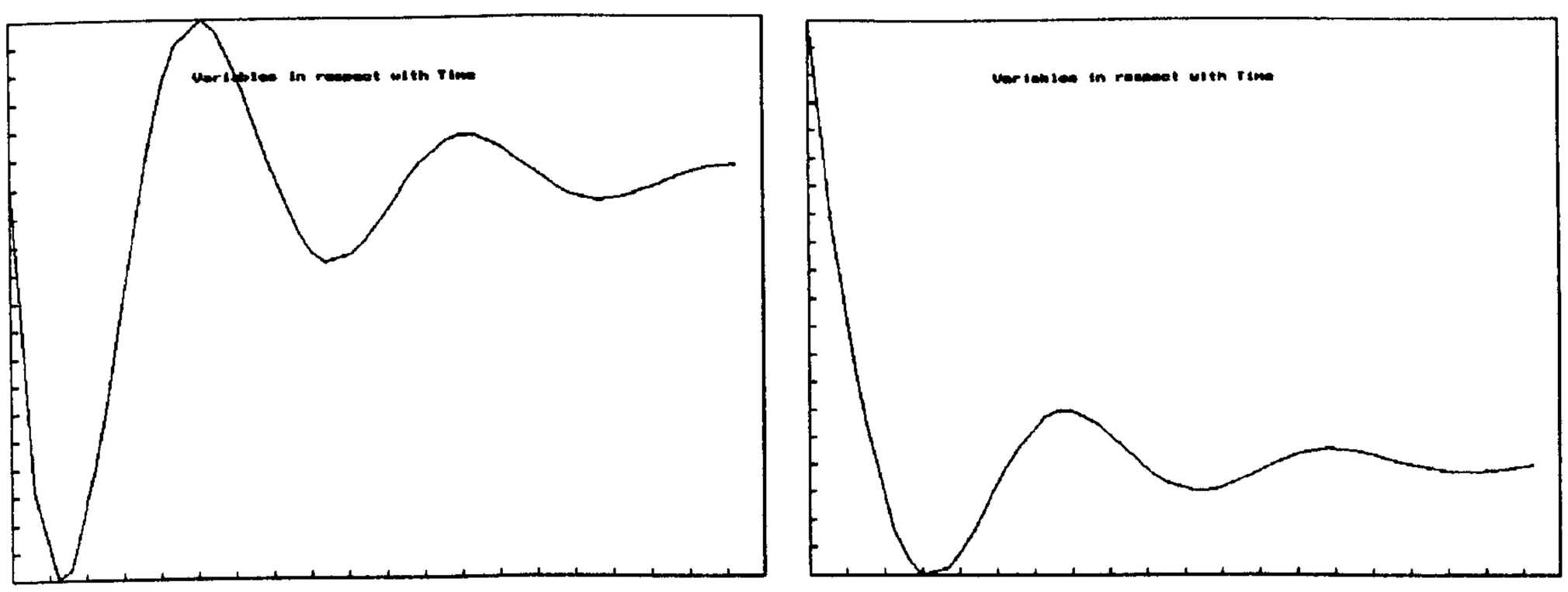

(a.) the coupled equations are solved by the program

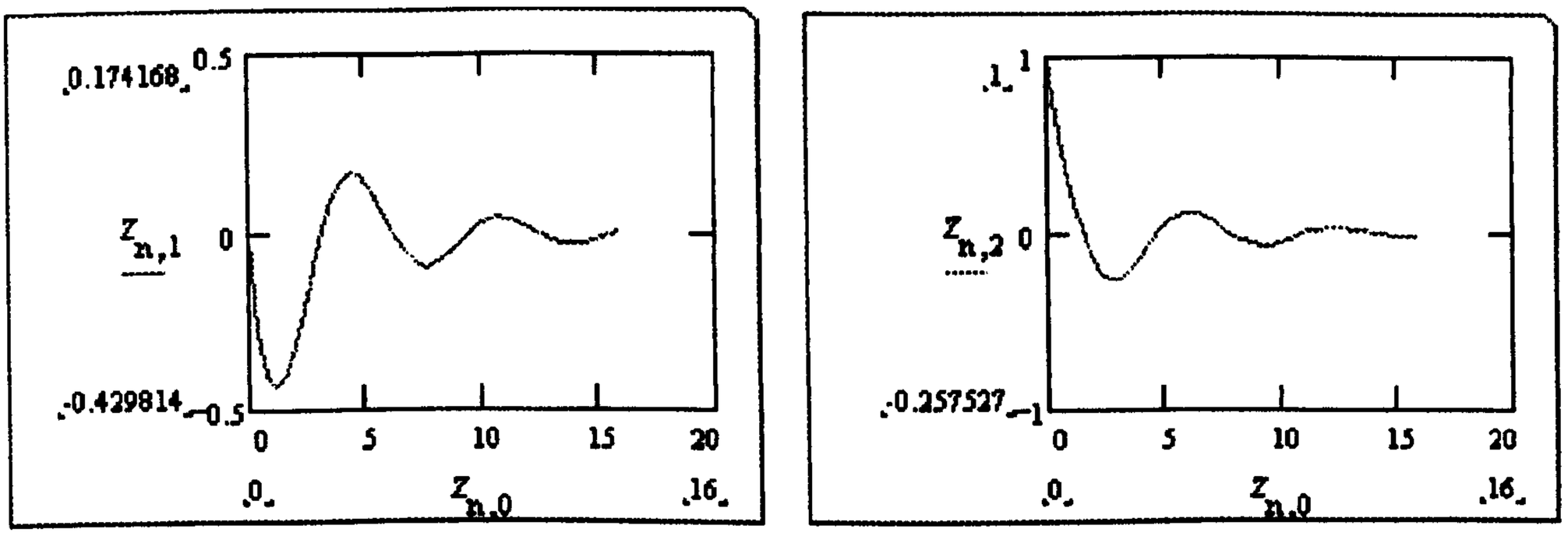

(b.) *the coupled equations are solved by MathCad6*

Figure A2. A test of the program

Appendix 7. Characteristics of Lorenz's attractor

This appendix is associated with Chapter 8 where the possible solutions of the differential governing equations for the theoretical laser cutting system can qualitatively be predicted by observing the well-studied Lorenz's system. In comparison with the differential governing equations as shown in Eqs.81-83, Lorenz's system may be solved with the program listed in Appendix 6 without any boundary conditions (mathematically and physically).

The Lorenz's system is mathematically expressed as follows:

$$\left.\begin{aligned} dx/dt &= -\sigma \cdot x + \sigma \cdot y \\ dy/dt &= -x \cdot z + r \cdot x - y \\ dz/dt &= x \cdot y - b \cdot z \end{aligned}\right\} \qquad \text{(A7-1)}$$

where, x, y, z are unknown time-dependent variables and σ, r, b are time-independent variables. When $\sigma = 10,\ b = 8/3,\ r = 28$, chosen by Lorenz, this simple-looking system has the solution in Fig.A3 (initial conditions: $x = 1;\ y = 1;\ z = 1$ at $t = 0$).

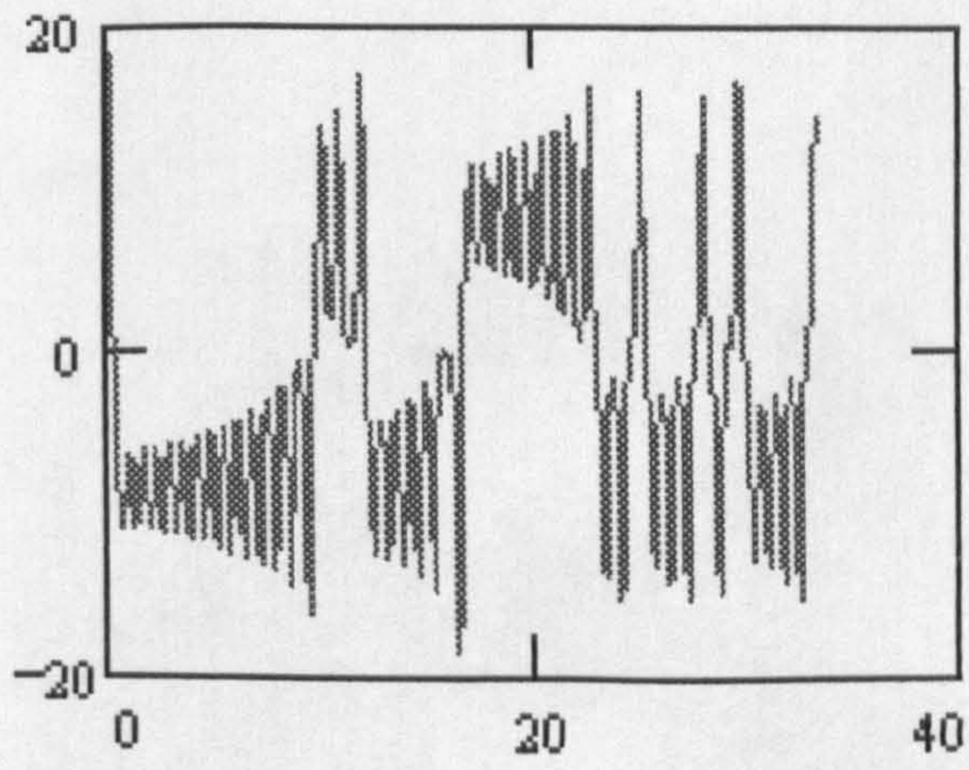

Fig.A3 (a) *Time-dependent variable, x, varies with time t*

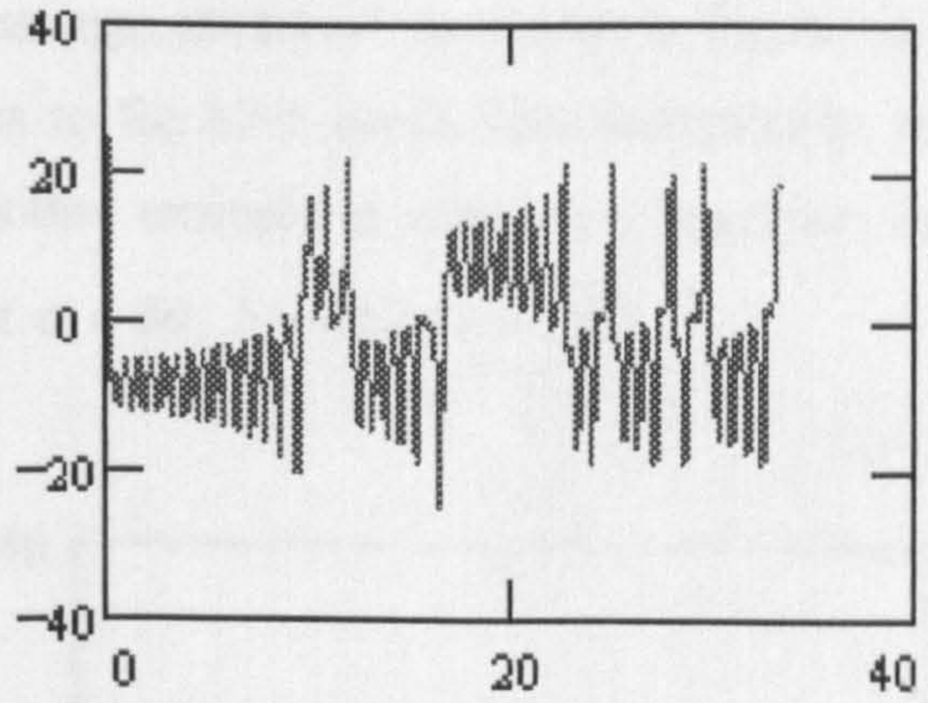

Fig.A3 (b) *Time-dependent variable, y, varies with time t*

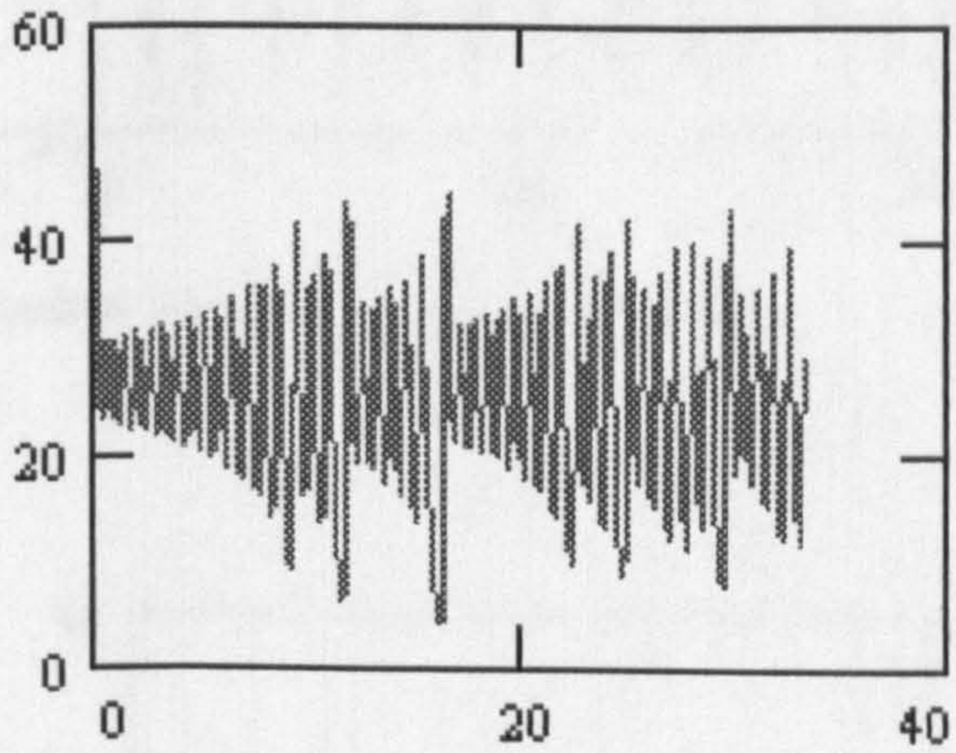

Fig.A3 (c) *Time-dependent variable, z, varies with time t*

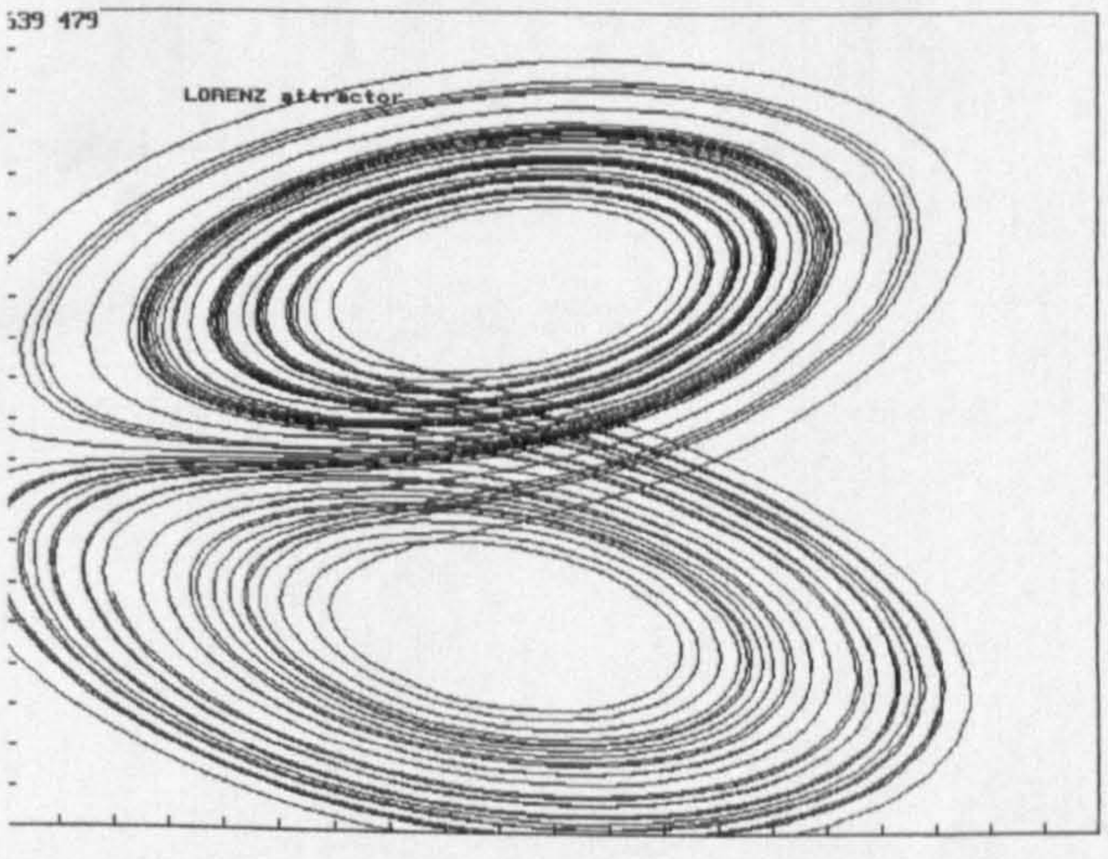

Fig.A3 (d) *3-D Phase-space comprised of 3 time-dependent variable, x, y and z*

The phenomenon of "strange attractor" as shown in Fig.A3 is only one of the solutions. Normally, the solutions to Eq.A7-1 could vary dramatically, due to the combinations of σ, r, b. Fig.A4 is another example in which the long-term variation gradually becomes periodic. In Fig.A4, let $\sigma = 30,\ b = 0.67,\ r = 33.3$.

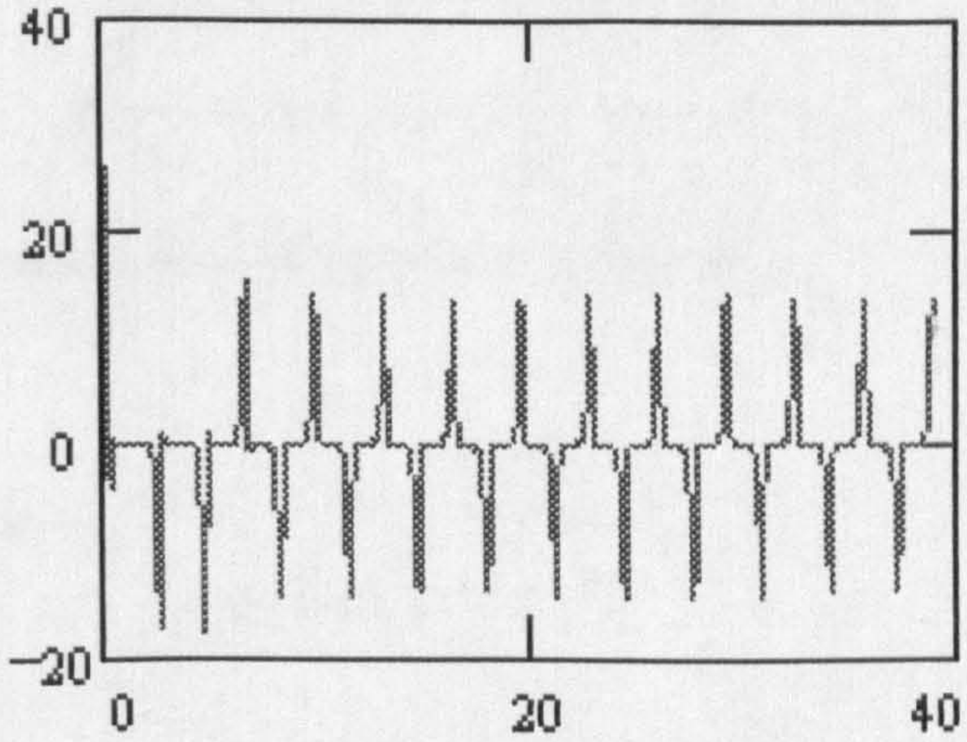

Fig.A4 (a) *Time-dependent variable, x, varies with time t*

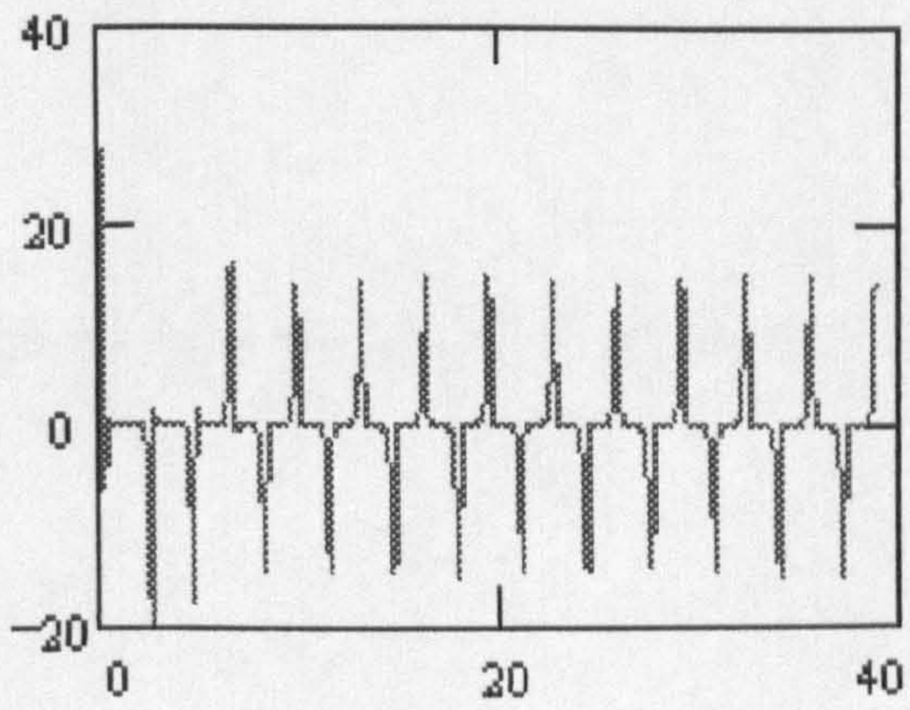

Fig.A4 (b) *Time-dependent variable, y, varies with time t*

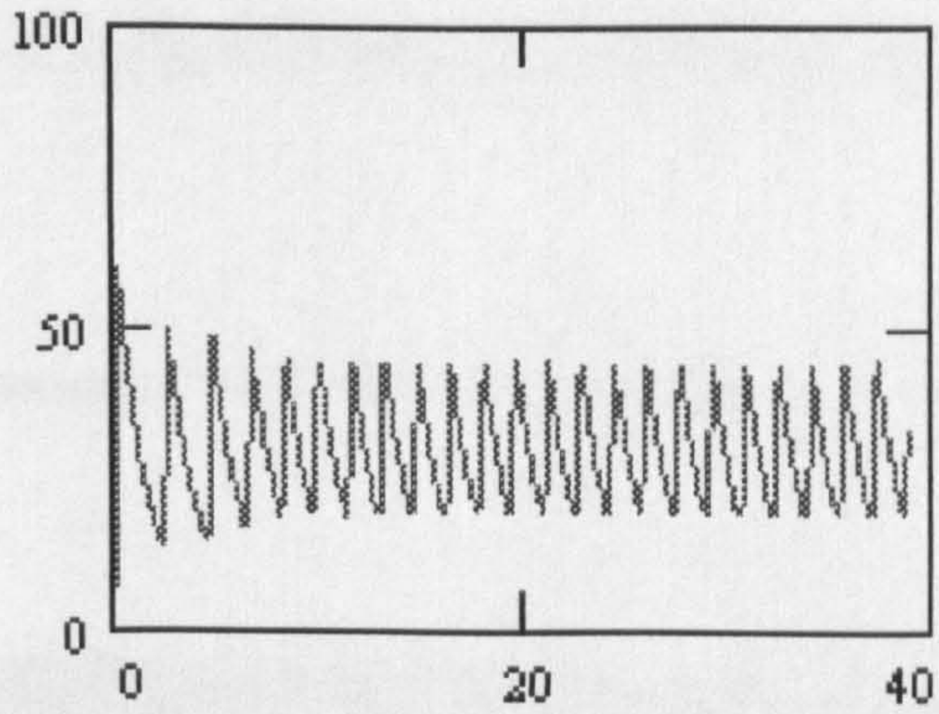

Fig.A4 (c) *Time-dependent variable, z, varies with time t*

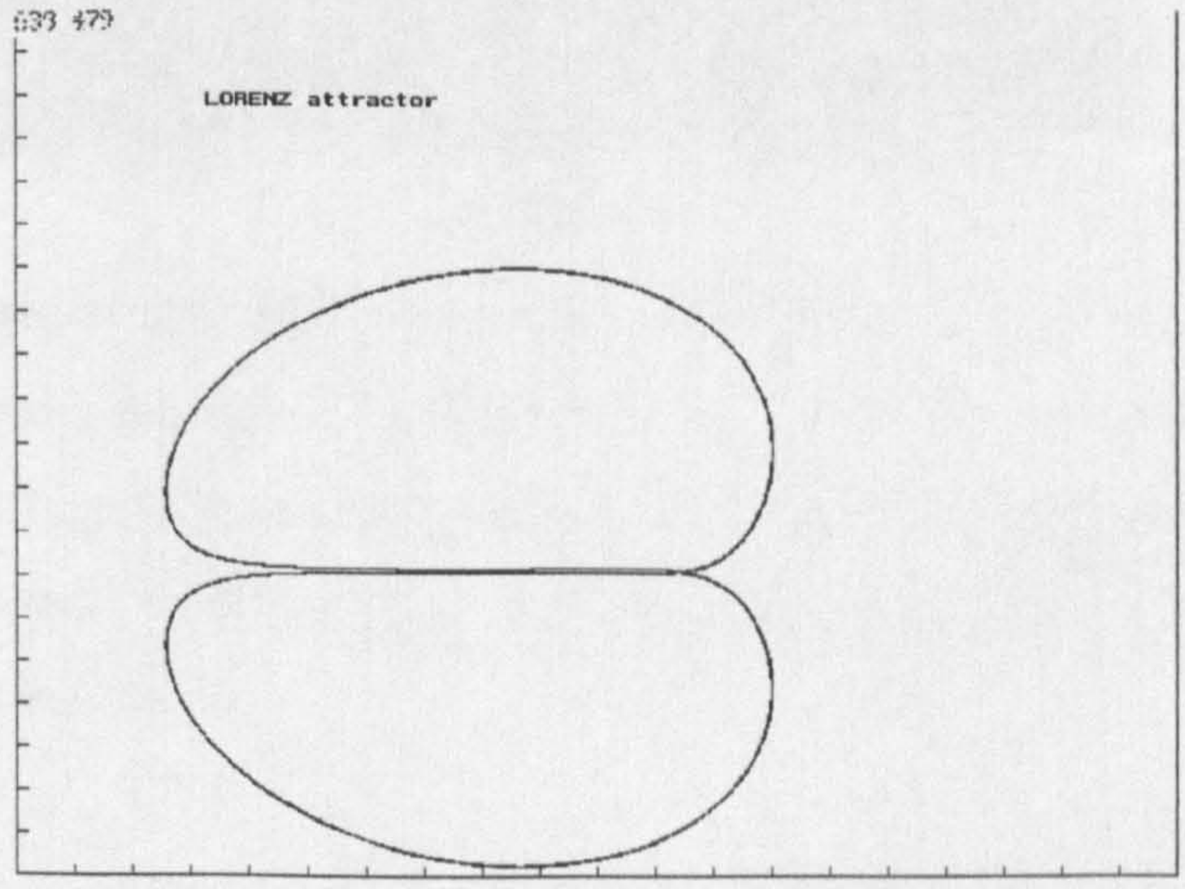

Fig.A4 (d) *3-D Phase-space comprised of 3 time-dependent variable, x, y and z*

Appendix 8. Collections of cutting results

This appendix is associated with Chapter 9 where the experimental details are introduced.

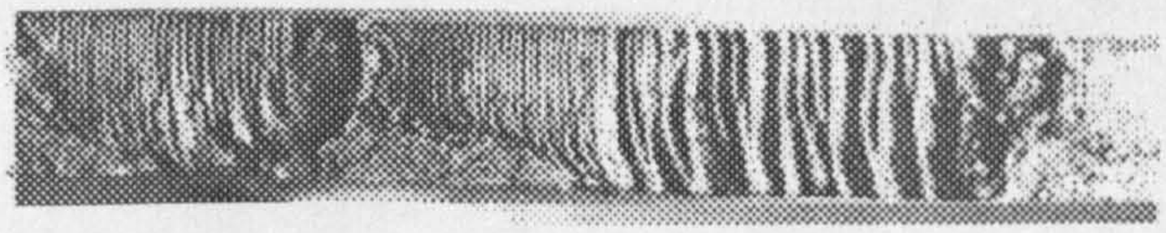

(a) cut 1

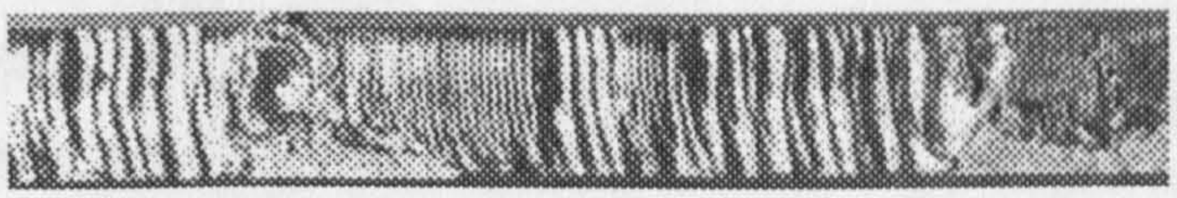

(b) cut 2

Figure A5. *The striations are different in 2 cuts even when the cutting conditions are the same, using CNC control system. The local striations show the variable periodicity; the local kerf widths vary accordingly. The cutting conditions in both (a) and (b): mild steel; thickness, 6 mm.; linear cutting profile, 120 mm. long; stagnation pressure, 2.5 atm.; cutting velocity, 940 mm/min.*

(a) cut 1

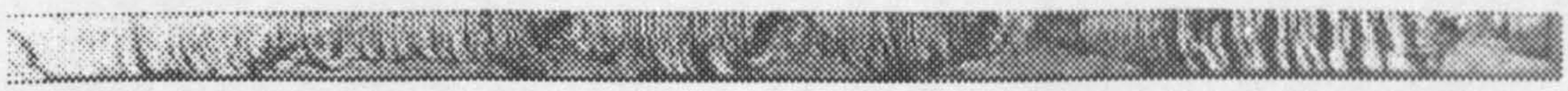

(b) cut 2

Figure A6. *The striations are different in 2 cuts even when the cutting conditions are the same, using X-Y table. The local striations show the variable periodicity; the local kerf widths vary accordingly. The cutting conditions in both (a) and (b): mild steel; thickness, 6 mm.; linear cutting profile, 320 mm. long; cutting velocity, 812 mm/min; stagnation pressure, 2.5 atm.*

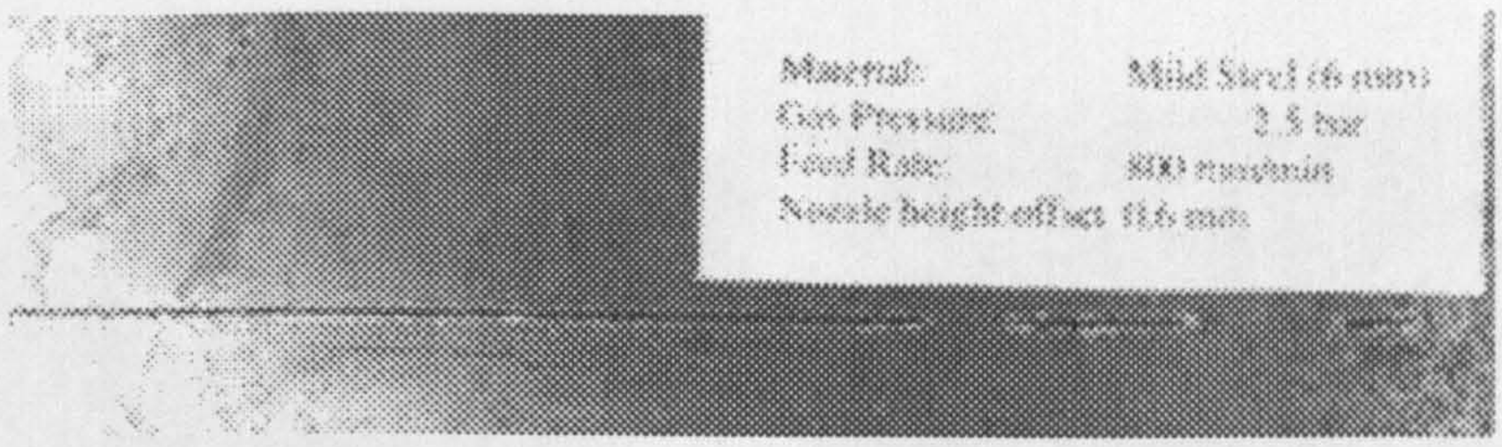

(a) Top view of the workpiece 1

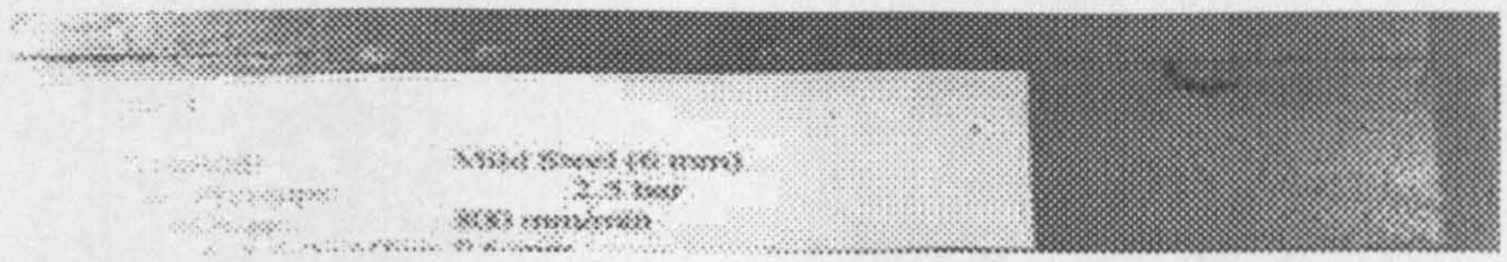

(b) Top view of the workpiece 2

Figure A7. *2 cutting profiles are characterised by the intermittence of cut and no cut under the same cutting conditions, using CNC control system. The local kerf widths vary. The cutting conditions: mild steel; thickness, 6 mm.; linear cutting profile, 120 mm. long; stagnation pressure, 2.5 atm.; cutting velocity, 800 mm/min.*

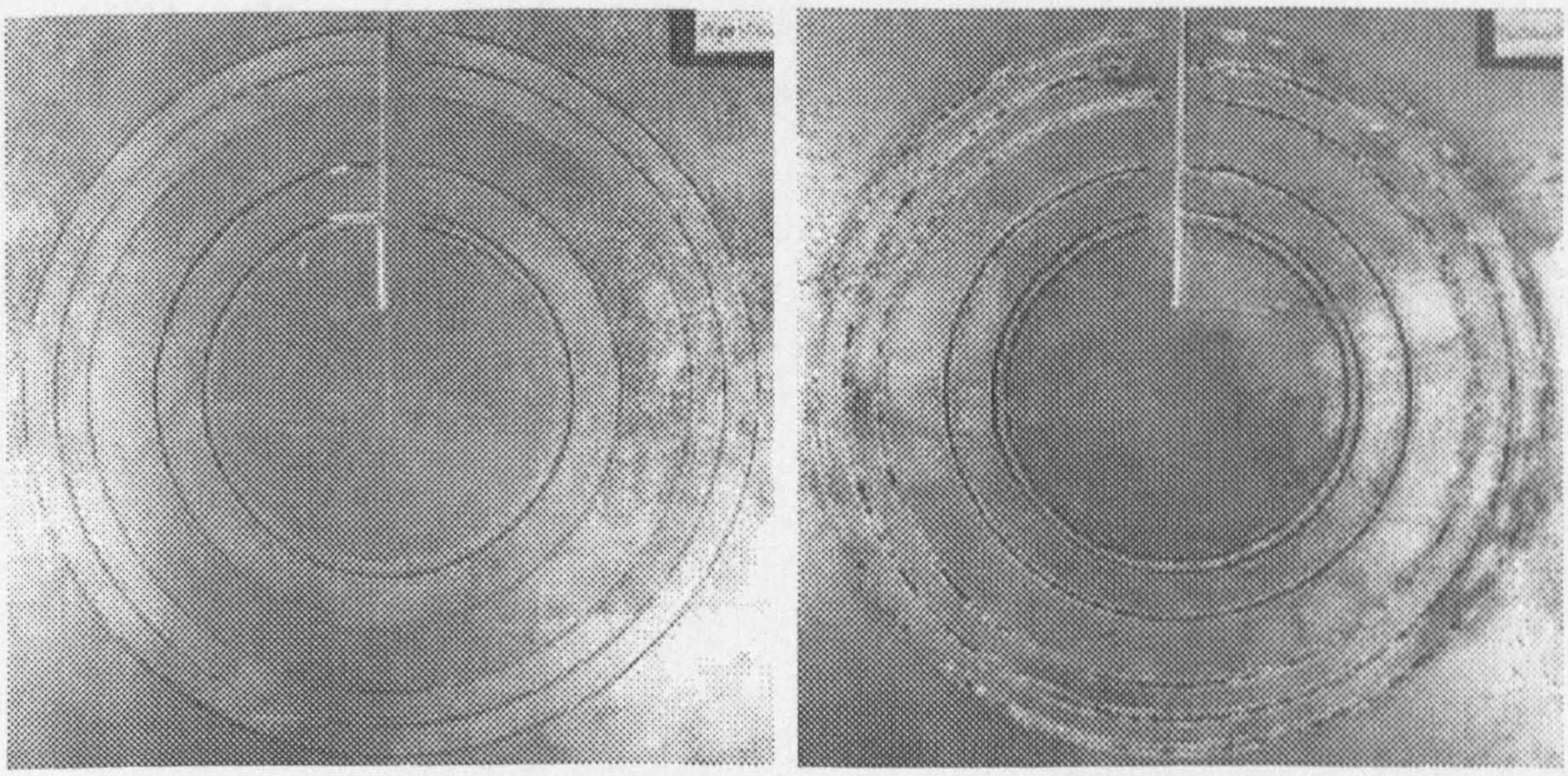

(a) Top view of the workpiece *(b) Bottom view of the workpiece*

Figure A8. *5 cuts in (a) and (b) are achieved in one workpiece using X-Y table. The kerf widths vary in one cut and in different cuts and the periodicity of the local striations varies accordingly. Except for the cutting velocities, the cutting conditions are the same: mild steel (400 × 400 mm^2); circular cutting profile; stagnation pressure, 2.5 atm.; thickness, 6 mm. The magnitudes of the cutting velocities are constant along each cutting profile, varying from 650 to 1123 mm/min*

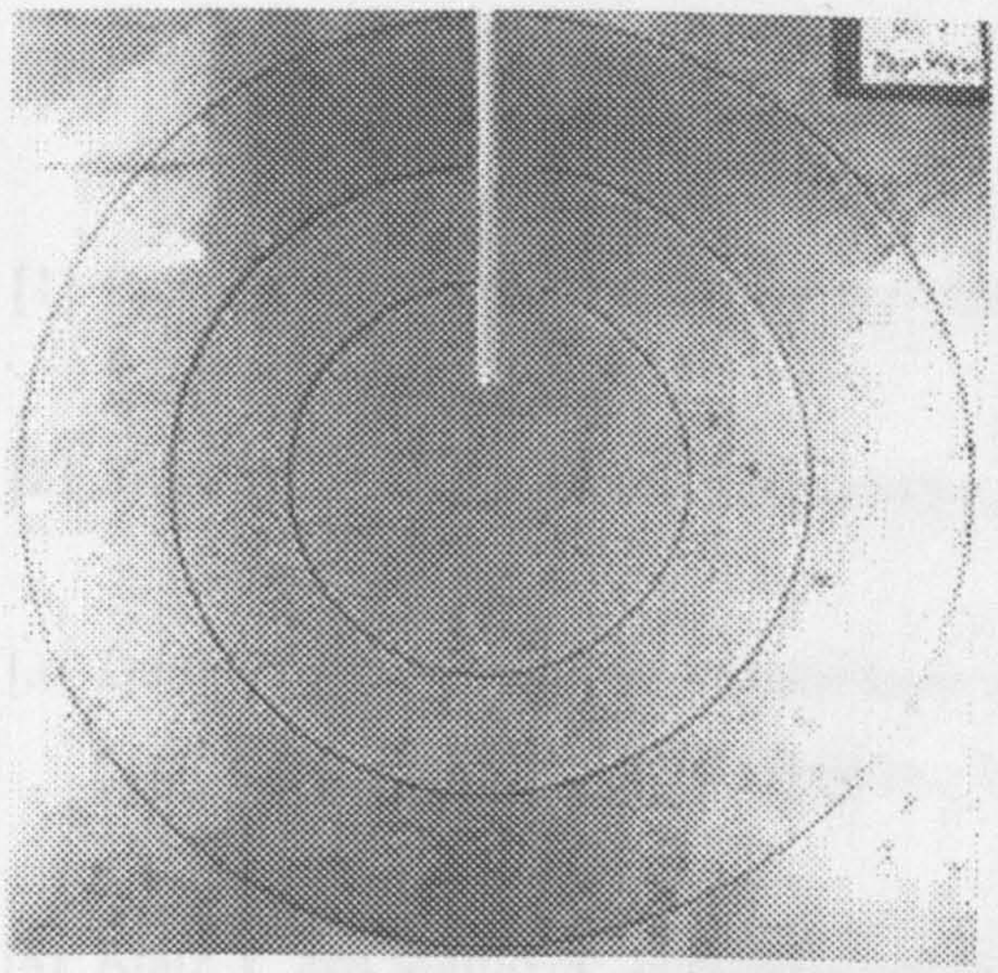

(a) Top view of the workpiece

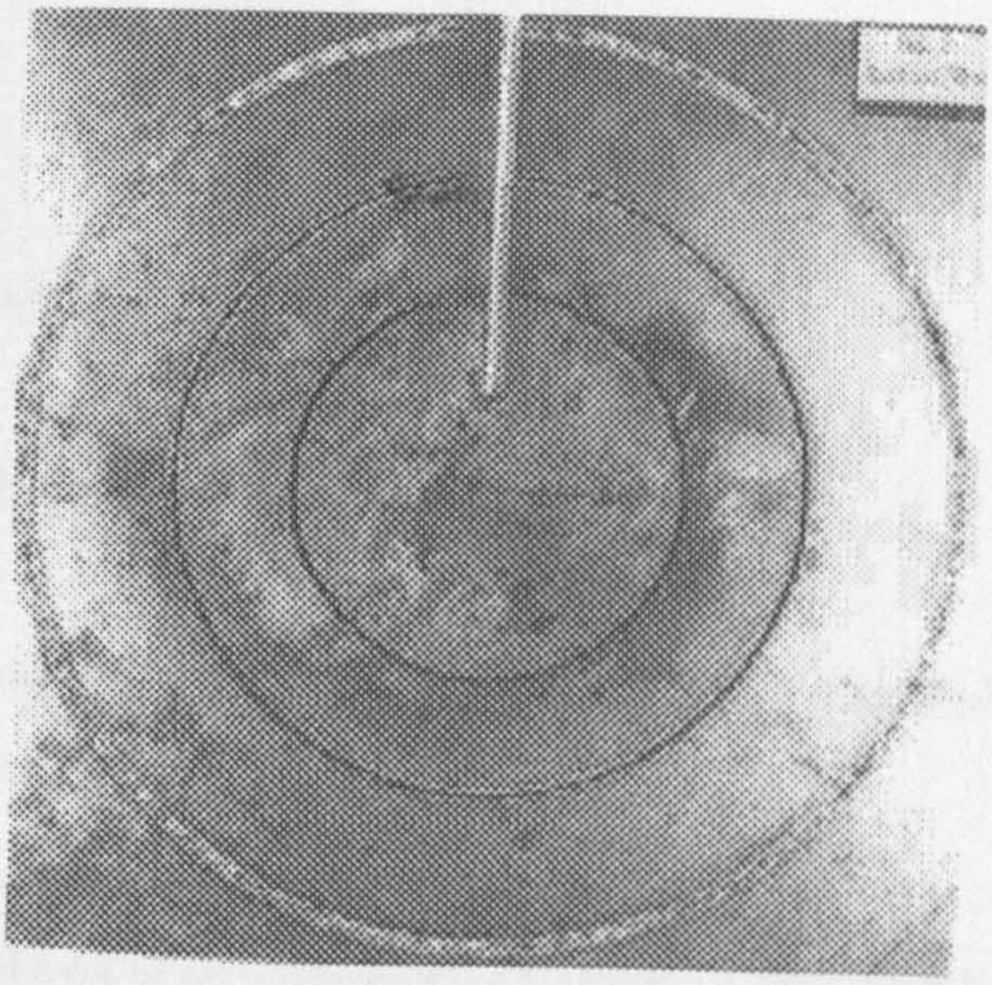

(b) Bottom view of the workpiece

Figure A9. *3 cuts in (a) and (b) are achieved in one workpiece using X-Y table. The kerf widths vary in one cut and in different cuts and the periodicity of the local striations varies accordingly. Except for the cutting velocities, the cutting conditions are the same: mild steel (400 × 400 mm^2); circular cutting profile; stagnation pressure, 3.5 atm.; thickness, 6 mm. The cutting velocities are constant along each cutting profile, varying from 620 to 1220 mm/min.*

References

[1] Powell J., *CO_2 laser cutting*, Spring-Verlag, Germany, 1993

[2] Steen W. M., *Laser material processing*, Spring-Verlag, Germany, 1991

[3] Dutta P., *Reactive gas jet assisted laser cutting*, PhD thesis, Department of Mechanical Engineering, University of Birmingham, 1975

[4] Arata Y. and Maruo H., *Dynamic behaviour in laser cutting of mild steel*, Tans. JWRI, No.8(2), 1979

[5] Schuocker D., *Reactive gas assisted laser cutting - physical mechanism and technical limitations*, Industrial Applications of Laser Technology (editor: Fagan W), SPIE Proc., No.398, 1983

[6] Schuocker D., *Dynamic phenomena in laser cutting and cut quality*, J. Appl. Phys. B, vol.40, p9-14,1986

[7] Schuocker D., *Theoretical model of oxygen assisted laser cutting*, Inst. Phys. Conf. Ser., No.72, Bristol, 1985

[8] Vicanek M., Simon G., Urbassek H. M. and Decker I., *Hydrodynamical instability of melt flow in laser cutting*, J. Phys. D: Appl. Phys., No.20, 1987

[9] Vicanek M. and Decker I., *Momentum and heat transfer of an inert gas jet to the melt in laser cutting*, J. Phys. D: Appl. Phys., No.20, 1987

[10] Tsai M. J. and Weng C. I., *Linear stability analysis of molten flow in laser cutting*, J. Phys. D: Appl. Phys., No.26, 1993

[11] Huang C. C. and Weng C. I., *Non-linear stability analysis of film flow down a heated inclined plane with viscosity variation*, Int. J. Heat Mass Transfer, No.31(9), 1988

[12] Lim S. Y., *An AI approach to the tasking and control of an industrial laser system*, PhD thesis, Department of Mechanical Engineering, Glasgow University, 1993

[13] Lim S. Y. and Chatwin C., *Chaos in laser material processing*, Laser in Engineering, No.3, 1994

[14] Lim S. Y. and Chatwin C., *Spatial chaos aspects of laser material interaction*, Optics and Laser in Engineering, No.20, 1994

[15] Lorenz E. N., *Deterministic nonperiodic flow*, J. Atmospheric Science, No.20, 1963

[16] Peitgen H. O., Jurgens H. and Saupe D., *Chaos and Fractals*, Springer-Verlag, New York, 1992

[17] Weiss C. O. and Vilaseca R., *Dynamics of Laser*, VCH, 1991

[18] Baker G. L. and Gollub J. P., *Chaotic dynamics*, Cambridge University Press, UK, 1990

[19] Slivsgaard E. and True H., *Chaos in railway-vehicle dynamics*, Nonlinearity and Chaos in Engineering Dynamics (editors: J.M.T. Thompson and S. R. Bishop), John Wiley and Sons Ltd., 1994

[20] Rohsenow W. M. and Hartnett J. P., *Handbook of heat transfer*, McGraw-Hill Inc., USA, 1973

[21] Lock R. C., *The velocity distribution in the laminar boundary layer between parallel streams*, Quat. J. Mech. and Appl. Math. Vol.4.1, 42-63, 1951

[22] Chapman A. J., *Heat transfer* (3rd), Macmillan Publishing Co., USA, 1974

[23] Duley W. W., *CO_2 lasers: effects and applications*, Academic Press, USA, 1976

[24] Boxer G., *Fluid mechanics*, Macmillan Education Ltd., London, 1991

[25] Allmen M. V., *Laser-beam interactions with materials*, Springer-Verlag Berlin, 1987

[26] Prandtl L., *Motion of fluids with very little viscosity*, NACA Tech. Mem. 452, 1928

[27] *Liquid metal handbook (2nd)*, Government Printing Office, Washington DC

[28] Touloukian Y. S., *Thermophysical properties of high temperature solid Materials*, Vol.1-3, The Macmillan Co., USA, 1967

[29] Howarth L., *Concerning the effect of compressibility in laminar boundary layer and their separation*, Proc. Roy. Soc., A194 (16), London, 1948

[30] Kubaschewski O. and Alcock C. B., *Metallurgical Thermochemistry*, Pergamon Press Ltd, UK, 1979

[31] Ivarson I., Powell J. and Magnusson C., *The role of oxidation in laser cutting stainless and mild steel*, J. of Laser Appli. 3(3), 1991

[32] Ivarson I., Powell J. and Magnusson C., *Laser cutting of steels: analysis of the particles ejected during cutting*, Welding in the World, 30(5/6), 1992

[33] Rosenthal D., *The theory of moving sources of heat and its application to metal treatments*, Transactions of the ASME, Detroit, USA, 1946

[34] Carslaw H. S. and Jaeger J. C., *Conduction of heat in solids*, Oxford University Press, UK, 1959

[35] Schulz W., *Heat conduction losses in laser cutting of metals*, J. of Physics D: Applied Physics, 26, 1993

[36] Mazumder J. and Steen W. M., *Heat transfer for cw laser material processing*, J. Appl. Phys., 51(2), P.941, 1980

[37] Kim M.J., et al, *Finite element modelling of laser cutting process*, Computer and Structure, 49(2), P.231-241, 1993

[38] Yilbas B.S. and Sahin A.Z., *Oxygen assisted laser cutting mechanism - a laminar boundary layer approach including the combustion process*, Optics and Laser Technology, Vol.27 No.3, 1995

[39] Huang M-Y, *Characterisation of laser cutting for an adaptive control environment*, PhD thesis, Department of Mechanical Engineering, Glasgow University, 1994

[40] Press W.H., Teukolsky S. A., Vetterling W.T. and Flannery B. P., *Numerical recipes in C , 2n edi.*, Cambridge University Press, USA, 1992

[41] Heard H. G., *Laser parameters handbook*, John Wiley & Sons Inc., New York, 1968

[42] Frenkel J., *Kinetic theory of liquids*, The Clarendon Press, Oxford, 1946

[43] Bolton W., *Newnes engineering materials pocket book*, Heinemann-Newnes, Oxford, UK, 1990

[44] Brokaw R. S., *Approximate formulas for viscosity and thermal conductivity of gas mixtures*, NASA TN D-2502, USA, 1964

[45] Wilke C. R., *A viscosity equation for gas mixtures*, J. Chem. Phys., 18: 517, 1950

[46] Molian P. A., *Dual-beam CO_2 laser cutting of thick metallic materials*, J. of Material Science, 28, 1993

[47] Kaplan A. and Schuocker D. (edi.), *Proceedings of modelling of laser material processing*, 9th Meeting Innsbruck, 27/28, 01, 1994

[48] Schulz W., et al, *On laser fusion cutting of metals*, J. of Physics D: Applied Physics, 20, 481-488, 1987.

[49] Huang A.M.Y. and Chatwin C., *Spark cone characterisation for the control of laser cutting*, Laser in Engineering, 3, 125-140, 1994

[50] Roth W. A., *Thermochemie,* Berlin: Goschen, 1947

[51] Edwards D. K., Denny V.E. and Mills A. F., *Transfer process*, Hemisphere Publishing Corporation, USA, 1976

[52] Taylor G., *The dynamics of thin sheets of fluid*, Proc. Roy. Soc., 253A, 289-312, 1959

[53] Dorrance W. H., *Viscous hypersonic flow, Theory of reacting and hypersonic boundary layers*, McGraw Hill Co., NY, 1962

[54] Patel B. S., *Photo-drag Ge tetector for CO_2 laser*, Proceedings of IEEE, 1973

[55] Wolf A., Swift J. B., Swinney H. L. and Vastano J. A., *Determining lyapunov exponents from a time series*, Physica 16D, 285-317, North-Holland, Amsterdam, 1985

[56] Dooley D., *Measuring CO_2 lasers with pyroelectric detectors*, Lasers and Applications, February 1987

[57] Jackson F., *Moving heat sources with change of phase*, J. Heat Transfer, P.329, August 1965

[58] Abramowitz M. and Stegun I. A., *Handbook of mathematical functions*, Dover Publications Inc., New York, 1970

[59] Schildt H., *Using Turbo C++*, Osborne McGraw-Hill, USA, 1990

[60] Bauerle D., *Chemical processing with lasers*, Springer-Verlag, Germany, 1986

[61] Beck C. and Schlogl F., *Thermodynamics of chaotic systems*, Cambridge University Press, 1993

[62] Jaluria Y. and Torrance K. E., *Computational heat transfer*, Hemisphere Publishing Corporation, USA, 1980

[63] Ready J. F., *Industrial applications of lasers*, Academic Press, USA, 1978

[64] *User's guide, Mathcad 6.0*, MathSoft Inc., USA, 1995